AD-A232 972

REPORT DOCUMENTATION PAGE

Form Approved
OMB No. 0704-0188

1b. RESTRICTIVE MARKINGS	
2b. DECLASSIFICATION / DOWNGRADING SCHEDULE	3. DISTRIBUTION / AVAILABILITY OF REPORT Approved for Public Release; Distribution Unlimited
4. PERFORMING ORGANIZATION REPORT NUMBER(S)	5. MONITORING ORGANIZATION REPORT NUMBER(S) AFOSR-TR· 9 1 0 1 1 7

6a. NAME OF PERFORMING ORGANIZATION Massachusetts Institute of Technology	6b. OFFICE SYMBOL (If applicable)	7a. NAME OF MONITORING ORGANIZATION AFOSR/NA
6c. ADDRESS (City, State, and ZIP Code) 77 Massachusetts Ave., Cambridge, MA 02139		7b. ADDRESS (City, State, and ZIP Code) Bldg. 410 Bolling AFB, DC 20332-6448
8a. NAME OF FUNDING / SPONSORING ORGANIZATION AFOSR	8b. OFFICE SYMBOL (If applicable) NA	9. PROCUREMENT INSTRUMENT IDENTIFICATION NUMBER AFOSR-89-0060
8c. ADDRESS (City, State, and ZIP Code) Bldg. 410 Bolling AFB, DC 20332-6448		10. SOURCE OF FUNDING NUMBERS

10. SOURCE OF FUNDING NUMBERS			
PROGRAM ELEMENT NO. 6.1102F	PROJECT NO. 2302	TASK NO C1	WORK UNIT ACCESSION NO.

11. TITLE (Include Security Classification) (U)

INTERPRETATION OF IN SITU TESTING OF COHESIVE SOILS USING RATIONAL METHODS

12. PERSONAL AUTHOR(S)
Whittle, A.J., Aubeny, C.P., Rafalovich, A., Ladd, C.C. & Baligh, M.M.

13a. TYPE OF REPORT ANNUAL	13b. TIME COVERED FROM 15Oct'89 TO 15Oct'90	14. DATE OF REPORT (Year, Month, Day) 89-11-15	15. PAGE COUNT 229

16. SUPPLEMENTARY NOTATION

17. COSATI CODES			18. SUBJECT TERMS (Continue on reverse if necessary and identify by block number)
FIELD	GROUP	SUB-GROUP	IN SITU TESTING, COHESIVE SOILS, PIEZOCONE, DILATOMETER, FIELD VANE, PRESSUREMETER, STRAIN PATH METHOD, SOIL MODELS

19. ABSTRACT (Continue on reverse if necessary and identify by block number)

This research uses theoretical analyses to investigate the fundamentals controlling the performance of common in-situ penetration tests (piezocone, pressuremeter, dilatometer, field vane etc.) which are used to estimate the engineering properties of cohesive soils. The mechanics of penetration processes are modeled using the Strain Path Method together with generalized effective stress soil models. The analytical predictions provide a rational basis for establishing how soil properties are related to in situ measurements. Comparisons with field data from well documented sites are used to evaluate the analytical predictions and provide a basis for more reliable interpretation of engineering properties. Research during the second year of the project focused on the following topics: 1) the development of analytical methods to predict pore pressures around three-dimensional penetrometers; 2) fundamental analytical studies of the mechanics of flat plate penetration; 3) application of analytical predictions for interpreting the undrained shear strength and preconsolidation pressure from piezocone data; 4) evaluation of contact pressures measured by the dilatometer; and 5) prediction of the disturbance caused by field vane insertion.

20. DISTRIBUTION / AVAILABILITY OF ABSTRACT ☒ UNCLASSIFIED/UNLIMITED ☐ SAME AS RPT ☐ DTIC USERS	21. ABSTRACT SECURITY CLASSIFICATION UNCLASSIFIED
22a. NAME OF RESPONSIBLE INDIVIDUAL Lt. Col. Steven C. Boyce	22b TELEPHONE (Include Area Code) (202) 767-6963 / 22c. OFFICE SYMBOL AFOSR/NA

DD Form 1473, JUN 86 Previous editions are obsolete.

SECURITY CLASSIFICATION OF THIS PAGE
UNCLASSIFIED

ANNUAL TECHNICAL REPORT

INTERPRETATION OF IN-SITU TESTING OF COHESIVE SOILS USING RATIONAL METHODS

by

Andrew J. Whittle

Charles P. Aubeny

Alexander Rafalovich

Charles C. Ladd

Mohsen M. Baligh

Constructed Facilities Division

Department of Civil Engineering

Massachusetts Institute of Technology

submitted to:

Lt. Col. Steven C. Boyce

Program Manager, Civil Engineering

Air Force Office of Scientific Research,

Bolling AFB, Washington D.C. 20322-6448

November 1990

TABLE OF CONTENTS: Page

1. INTRODUCTION

The principal objective of this research is to provide a more fundamental understanding of the results obtained by in-situ 'penetration' tests in cohesive soils. Devices of special interest include flat blade penetrometers (such as the dilatometer), cone penetrometers (such as the piezocone), pressuremeter and field vane tests. The data from these tests are currently used to estimate essential engineering properties of clay soils including, a) the in-situ horizontal stress, b) undrained shear strength, c) preconsolidation pressure, d) permeability, and e) coefficient of consolidation.

Current interpretations of these tests rely largely, or solely, on empirical correlations which relate the in-situ measurements to some (known) property of the given soil. Such approaches can be reasonably reliable if the measurement is indeed closely linked to the property of interest, or for those soil types which were used to establish the correlation. More often, the correlation involves minimal measurement-property dependence, a poor quality data base and/or extrapolation to quite different soil types.

This research aims to develop more reliable methods for selecting and interpreting in-situ tests based on a fundamental understanding of the factors which control test results. The work focuses on the following tasks:

1. Theoretical analyses to develop a predictive framework for interpreting the performance of existing types of in-situ test (the piezocone, pressuremeter, dilatometer and field vane). The analyses are based on two recent developments at MIT: i) the Strain Path Method (Baligh, 1985; 1986a, b), an analytical tool for quantifying the disturbance effects in the soil due to penetrometer installation; and ii) the MIT-E3 model (Whittle, 1987; 1989a, b), a generalized effective stress soil model for describing the behavior of overconsolidated clays and clays under cyclic loading.

2. Comparison of predicted versus measured field performance using data from well documented field studies. This work will identify limitations in the analyses and in the experimental data base.

3. Improvements in the existing analytical techniques to include, i) the effects of partial drainage on in-situ measurements, and b) the effects of strain rate on the stress-strain behavior of cohesive soils.

This report summarizes the principal research findings for the period November 1989

to November 1990:

• Section 2 describes the development and evaluation of a new method for estimating the pore pressures which develop around penetrometers during undrained penetration in low permeability clays. In the Strain Path Method, pore pressures are obtained by integrating the equations of static equilibrium using the predicted fields of effective stresses. Due to the analytical approximations in the Strain Path Method, the equilibrium conditions are not satisfied uniquely and the pore pressures are found to be integration path dependent. In previous studies, pore pressures ahead of the penetrometer tip were estimated from conditions of vertical equilibrium only, while conditions around the shaft of long axisymmetric penetrometers were found from radial equilibrium. However, this preferential selection of integration path cannot be used reliably to establish the distribution of pore pressures around a penetrometer. In this work, the equlibrium equations are expressed in the form of a single Poisson type equation which is then solved numerically by finite element methods. The Poisson formulation represents an essential tool a) for unifying the prediction of disturbance caused by penetrometers of different geometries (piezocone, dilatometer, field vane etc.), and b) for estimating the distribution of pore pressures around a penetrometer.

• Section 3 presents a complete analysis of the stresses, strains and pore pressures caused by penetration of flat plate penetrometers in clay. The main aim of this section is to compare and contrast the effects of penetrometer geometry on the disturbance due to undrained penetration. Strain path analyses are presented for 'simple plate' geometries which are fully characterized by dimensions of length and width. Solutions are presented for simple plates with aspect ratios (length/width) similar to existing plate penetrometers (dilatometer, earth pressure cells and the field vane). Generalized effective stress soil models (Modified Cam Clay and MIT-E3) are used to predict effective stresses around the plate penetrometers, while pore pressures are estimated from finite element solutions of the the Poisson equation described in section 2. Further effects of penetrometer geometry are clarified from the dissipation of excess pore pressures after installation.

• The Piezocone is widely used in geotechnical practice for estimating site stratigraphy and spatial variability based on simultaneous measurements of tip resistance and pore pressures

obtained during steady penetration. Application of these data to interpret engineering properties of clays (undrained shear strength and preconsolidation pressure) has been based almost exclusively on empirical correlations. In previous research, Whittle et al. (1989) describe a centerline analysis, using the strain path method, which provides a rational basis for estimating undrained shear strength from either the measured tip resistance or tip pore pressure[1]. However, in practice, the design of the piezocone is not standardized and pore pressures are often not measured at the tip of the cone. In section 4, more comprehensive strain path analyses are used to predict distributions of stresses and pore pressures for piezocone penetration in normally and lightly overconsolidated clays (OCR≤4). The analyses are based on generalized effective stress soil models (MCC and MIT-E3) and use the Poisson formulation developed in section 2. The analytical predictions provide a rational basis: a) for establishing which soil properties (undrained shear strength, preconsolidation pressure) can be interpreted from piezocone measurements; b) for evaluating the relative merits of different locations for pore pressure filters; and c) for providing an independent assessment of the centerline analysis proposed previously. A detailed evaluation of the analytical predictions is achieved by direct comparison with field data obtained in Boston Blue Clay at two well documented sites.

• The Marchetti Dilatometer has gained considerable popularity since it was first introduced into the United States in the early 1980's. One of the major applications of the test is the empirical interpretation of undrained shear strength in clays using the 'contact pressure' measured by a circular steel diaphragm located on the flat face of the device. Section 5 describes a comprehensive analysis of the contact pressure for dilatometer installation in clays. The analyses are based on the solutions described for the simple plate geometry in section 3 and include full descriptions of effective stresses and pore pressures acting on the dilatometer membrane. A systematic interpretation of the analytical results is used to evaluate whether the contact pressure can be reliably correlated with engineering properties (undrained shear strength, preconsolidation pressures and/or K_0). The results also a) provide valuable insight into how the location of the dilatometer membrane influences the measured data, and b) enable dilatometer measurements to be compared with lateral stress data obtained around the shaft of axisymmetric penetrometers (measured by devices such as

---

[1]This work is described fully in the PhD Thesis of Elghaib (1989).

the full displacement pressuremeter test and the Piezo-Lateral Stress cell). The analytical predictions are evaluated by direct comparison with field data obtained in Boston Blue Clay (BBC). Field data from other well documented sites are used to confirm trends observed in the predictions for BBC.

• The field vane is the most widely used test for estimating the in-situ undrained shear strength in clays. It has long been recognized that the insertion of the vane causes disturbance of the soil and can affect the measured shear strength. Section 6 describes the first analytical predictions of disturbance (stresses and pore pressures) caused by installation of a standard field vane. The analyses are based on strain path solutions for the simple plate geometries (section 3) and include a) detailed studies of the effective stresses and excess pore pressures around the vane prior to rotation, and b) calculations of partial drainage of excess pore pressures due to time delays between vane insertion and rotation.

2. PENETRATION PORE PRESSURES FROM STRAIN PATH METHOD

2.1 INTRODUCTION

The undrained penetration of intrusive test devices (e.g. piezocone, field vane, dilatometer etc.) in low permeability clay deposits leads to the development of excess pore pressures in the soil. For normally and moderately overconsolidated clays, these pore pressures are large and dominate other soil stresses and hence hold the key to the understanding of penetration mechanisms (Baligh, 1986b). Reliable analytical predictions of penetration pore pressures are essential if engineering properties of soils are to be interpreted rationally from in-situ measurements, both during penetration and in subsequent activities such as dissipation and holding tests, membrane expansion, vane rotation etc.

Using the Strain Path Method (SPM), the effective (or deviatoric) stresses around a penetrometer are determined from the strain paths of soil elements using an appropriate soil model. The pore pressures can then be estimated by integrating the equilibrium equations from the known field of effective (or deviatoric) stresses. Due to the approximate nature of the strain and stress fields computed from the SPM, equilibrium will not be satisfied uniquely. This chapter discusses the implementation of a method which gives an 'averaged' pore pressure field obtained by solving the complete set of equilibrium equations in the form of a Poisson solution.

The method outlined in this chapter has two advantages: 1) it is rational and minimizes the need for subjective judgement to estimate the distribution of pore pressures; and 2) it can be used for penetrometers of general shape, and hence can be used to unify the interpretation of installation disturbance for different types of in-situ tests used in geotechnical practice, including axisymmetric and flat plate penetrometers.

2.2 BACKGROUND

Deep penetration problems are commonly modelled as the undrained expansion of spherical or cylindrical cavities. For cylindrical cavity expansion (Soderberg, 1962; Ladanyi, 1963; Butterfield and Bannerjee, 1970; and Randolph et al., 1978), the soil is assumed to deform under plane strain and axisymmetric conditions, and displacements occur only in the radial direction. In this case the strain components can be obtained solely

by the kinematics of deformation and are given by:

$$\varepsilon_{rr} = \frac{1}{2} \ln \left[1 + (\frac{R}{r_0})^2 \right]; \quad \varepsilon_{\theta\theta} = - \varepsilon_{rr}; \quad \varepsilon_{zz} = \varepsilon_{rz} = 0 \tag{2.1}$$

Stresses in the soil mass can then be estimated from the known strain field using an appropriate constitutive model.

Baligh (1975, 1984) suggests that the Cavity Expansion Method (CEM) is too simplistic to describe the two-dimensional nature of the problem. Baligh (1985, 1986a, b) also proposed the Strain Path Method (SPM), which provides a general analytical framework for describing the mechanics of quasi-static, steady, undrained deep penetration in saturated clay. The method assumes that, due to the severe kinematic constraints in deep penetration problems, deformations and strains are essentially independent of the shearing resistance of the soil, and can be estimated with reasonable accuracy based only on kinematic considerations and boundary conditions. By considering the two-dimensional deformations of soil elements, SPM analyses provide a more realistic framework for describing the mechanics of deep penetration problems than one-dimensional (cylindrical or spherical) cavity expansion methods, and can account properly for the effects of non-linear and inelastic soil behavior. On the other hand, the assumptions of strain-controlled behavior used in the Strain Path Method greatly simplify the problem of steady deep penetration and avoid the complexity of large scale numerical (finite element) analyses.

The analysis of steady deep penetration problems using the Strain Path Method (Baligh, 1985, 1986a, b) includes the following steps (Figure 2.1):

Step 1. Soil deformations are considered in terms of the steady flow of soil around a static penetrometer. Approximate velocity fields are estimated from potential theory (i.e., treating the soil as an incompressible, inviscid and irrotational fluid) and are differentiated with respect to the spatial coordinates in order to obtain strain rates ($\dot{\varepsilon}_{ij}$). For the case of a penetrometer generated by a point source of incompressible material in a uniform flow field (the simple pile), solutions can be obtained in closed form (Baligh, 1985; Teh & Houlsby, 1989). More complex geometries require numerical methods such as the method of sources and sinks (Weinstein, 1948; Rouse, 1959) or boundary element methods (Williamson, 1989).

Step 2. Integration of the strain rates along the streamlines defines the strain paths (histories) for individual soil elements moving around the penetrometer. Baligh (1985) shows

that soil elements are subject to complex histories of straining involving reversals of individual strain components, as illustrated in Figure 2.2, which shows the strain paths in the triaxial compression (E_1), the pressuremeter (E_2), and the simple shear (E_3) shearing modes during simple penetration, where E_1, E_2, and E_3 are defined in the figure. In this case both the E_1 and E_3 components experience reversals, while E_2 increases monotonically. SPM predictions by Levadoux and Baligh (1980) showed that during penetration of 18^0 and 60^0 cones reversal of the E_2 component also occur. It can also be seen from this figure that the absence of a particular deformation mode at the end of penetration does not imply that the soil element did experience that deformation mode during penetration.

Step 3. Stress fields around the penetrometer estimated from the strain paths using either a) an effective stress approach in which the effective stresses, σ'_{ij}, are determined using a generalized effective stress soil model to characterize the constitutive behavior of the soil; or b) a total stress approach in which the deviatoric stresses, s_{ij}, and the shear-induced pore pressures, Δu_s, are determined separately using two constitutive models of soil behavior (Levadoux and Baligh, 1980; Baligh, 1985, 1986a, b). The effective stress approach has the advantage that the same model can be used to study the consolidation process after installation. Input parameters for models (for both effective stress analysis and total stress analysis) include initial total stresses and pore pressures in the ground (σ^0_{ij}, u_0), together with (model specific) material properties. Baligh (1986a,b) shows that ahead of the penetrometer tip the soil is loaded primarily in a triaxial compression mode with no strain reversals ; consequently, the predicted stress components, s_{ij}, are not sensitive to inelastic effects. By contrast, soil elements located near the penetrometer boundary above the tip have experienced extensive reversals of individual strain components and are therefore most sensitive to inelastic effects. Predictions in this region therefore require more realistic soil models incorporating the effects of anisotropy and strain softening. Previous studies (Baligh, 1986b; Whittle & Baligh, 1990) have shown that realistic predictions of effective stresses acting at the indenter-soil interface can be achieved using comprehensive soil models (Whittle, 1987, 1990) which incorporate strain softening, small strain non-linearity and anisotropic properties of clay.

Step 4. Baligh (1985) shows that, since the effects of gravity on stress changes in deep

foundation problems are negligible, the equilibrium equations in a cartesian frame can be expressed in terms of total stresses as:

$$\frac{\partial \sigma_{ij}}{\partial x_j} = 0 \qquad (2.2)$$

in which x_i (=x_1, x_2, x_3) are the coordinates of a material point and repeated indices imply summation over 1, 2, and 3. By invoking the effective stress principle, $\sigma_{ij} = \sigma'_{ij} + \delta_{ij} u$, [1] he shows that

$$\frac{\partial u}{\partial x_i} = - \frac{\partial \sigma'_{ij}}{\partial x_j} = g_i \qquad (2.3)$$

Alternatively, from a known field of deviatoric stresses, the changes in mean total stress, $\Delta\sigma$, is determined from:

$$\frac{\partial \sigma}{\partial x_j} = - \frac{\partial s_{ij}}{\partial x_j} \qquad (2.4)$$

whereupon, the excess pore pressure can be computed from:

$$\Delta u = \Delta\sigma + \Delta u_s \qquad (2.5)$$

For axisymmetric problems, the equilibrium equations in terms of effective stresses can be expressed in a cylindrical coordinate frame as:

$$-\frac{\partial u}{\partial r} = - g_r = \frac{\partial \sigma'_{rr}}{\partial r} + \frac{\partial \sigma'_{rz}}{\partial z} + \frac{\sigma'_{rr} - \sigma'_{\theta\theta}}{r} \qquad (2.6a)$$

$$-\frac{\partial u}{\partial z} = - g_z = \frac{\partial \sigma'_{zz}}{\partial z} + \frac{\partial \sigma'_{rz}}{\partial r} + \frac{\sigma'_{rz}}{r} \qquad (2.6b)$$

---

[1] where δ_{ij} is the Kronecker defined by:

$$\delta_{ij} = \left\{ \begin{array}{ll} 1 & i=j \\ 0 & i \neq j \end{array} \right\}$$

In principle, the pore pressures can be calculated by integrating in either the radial or vertical (z) direction (using the known distributions g_r, g_z, respectively). If the stress fields are exact, the predicted pore pressure will be independent of the path of integration and the stress gradients will satisfy the relation:

$$\frac{\partial g_r}{\partial z} = \frac{\partial g_z}{\partial r} \qquad (2.7)$$

This condition is only satisfied if the strain paths are compatible with the model used to determine the stresses. However, from step 1, the strains are approximated using potential flow theory and are not compatible with the soil model used in step 3.

Figure 2.3 illustrates the potential differences in predictions of pore pressures that can arise by satisfying equilibrium in different directions. The figure shows the distribution of excess pore pressures, $(u-u_0)/\sigma'_{v0}$, at points along the surface of 18 and 60^0 cone penetrometers and at vertical locations ahead of the penetrometer tip. The initial fields of effective stresses were predicted using the Modified Cam Clay soil model (MCC; Roscoe & Burland, 1968) with material properties selected to represent the behavior of K_0-normally consolidated Boston Blue Clay (Whittle, 1987). This model has the advantage that it is formulated in terms of effective stresses; and it is isotropic and has a well defined critical state condition, so it can be readily interpreted. Unless otherwise stated, this case is used in subsequent analyses illustrated in this chapter. The results show the following:

1. At the tip of the penetrometers, the excess pore pressures from vertical equilibrium (Δu^z) are approximately 50% higher than those from radial equilibrium (Δu^r). Ahead of the tip, the distributions of excess pore pressures show similarly large variations due to integration path. It should also be noted that the vertical equilibrium pore pressures at the tip of the penetrometer are not affected significantly by the apex angle of the cone.

2. Differences between radial and vertical integration paths are especially significant as soil elements move past the level of the base of the cone. Vertical equilibrium pore pressures, Δu^z, decrease rapidly and become unbounded (i.e., continue to decrease with distance along the penetrometer), while Δu^r reach a steady state solution at a distance, z/R=10-20 above the tip of the cone.

Non-uniqueness of pore pressure (or octahedral stress) fields was first observed by Levadoux and Baligh (1980) by integrating the equilibrium equations along isochrones and

streamlines, where isochrones are lines describing the deformed geometry of originally horizontal lines in the soil and streamlines correspond to orthogonal lines of the undeformed mesh of soil. Their results for isochronic and streamline integration showed differences similar to those shown in figure 2.3 for vertical and radial integration. They attributed the differences, in large part, to unrealistic predictions in σ_{rz}, which contributes significantly to equilibrium in the vertical direction. Subsequent fields of pore pressure reported by Levadoux and Baligh (1980) were based on isochronic integration only.

The nature of the uncertainty in σ_{rz} predictions and its impact on vertical integration solutions are illustrated by considering region far above the penetrometer tip, where $\partial\sigma_{ij}/\partial z$ = 0. In this case Equation 2.6b reduces to

$$-\frac{\partial u}{\partial z} = -g_z = \frac{\partial\sigma'_{rz}}{\partial r} + \frac{\sigma'_{rz}}{r} \qquad (2.8)$$

For a steady condition ($\partial u/\partial z =0$), $\partial\sigma'_{rz}/\partial r$ must equal $-\sigma'_{rz}/r$; however, SPM predictions (Levadoux, 1980) of σ'_{rz} indicate both $\partial\sigma'_{rz}/\partial r$ and σ'_{rz}/r to be positive near the penetrometer boundary far above the tip. This implies that pore pressures will decrease indefinitely in the vertical direction far above the penetrometer tip. This unreasonable result shows that vertical integration solutions are unreliable above the cone tip.

To mitigate discrepancies between vertical and radial integration solutions, Chin (1986) integrated the equilibrium equations in a polar direction (the ϕ-direction) in spherical coordinates, using deviatoric stress fields based an elastic-perfectly-plastic soil model. His results showed that for $(z/R)>0$ polar integration provides a smooth and continuous transition between the vertical and radial integration. But far above the tip, polar integration did not match the steady-state radial integration solutions and should therefore be considered unreliable.

Subsequent studies have shown that:

1. In the region ahead of the cone tip, since the soil is subject to triaxial compression modes of shearing only, vertical equilibrium can reliably be used to estimate pore pressures at the tip of a piezocone (Baligh , 1986b; and Elghaib, 1989).

2. Far behind the penetrometer tip, predictions of excess pore pressures can be obtained from radial equilibrium. Predicted stresses in this region are very susceptible to inelastic effects (Baligh 1986a) due to reversal of individual strain components. Consequently, predicted pore pressures will be strongly influenced by complex aspects of soil behavior

including anisotropy, strain softening and rate dependence.

2.3 EQUILIBRIUM CORRECTION

As discussed above, vertical equilibrium controls the pore pressures ahead of the cone tip, while radial equilibrium controls the shaft pore pressures on the shaft far above the tip. For other locations around the cone, the path dependence in the predicted pore pressures represents a major source of uncertainty in the analysis. Equilibrium imbalance can be dealt with by two possible approaches: a) applying corrections to the initial SPM stress and strain fields to reduce disequilibrium, or b) adoption of a scheme which satisfies the two equilibrium equations (equations 2.6a and b) predicted from the SPM in an 'average' sense.

Iterative schemes for correcting the equilibrium imbalance have been proposed by a number of authors (Baligh, 1985; Teh, 1987). Teh (1987) proposed a number of iterative corrections including:

1. Newton-Raphson Correction.- Using an error term defined in terms of the curl of **g** such that

$$H = \nabla \times g \qquad (2.9)$$

the SPM stream functions ψ are successively corrected to approximately eliminate H, using a Newton-Raphson iteration scheme. This scheme was found to converge very rapidly in regions where no plastic deformations occur, but convergence could not be achieved in regions of plastic deformation. Since realistic solutions for penetration must consider plastic deformations, this approach cannot provide useful corrections.

2. Finite Element Correction.- Using stress fields from SPM predictions, out-of-balance nodal forces are computed based on equilibrium equations. These out-of-balance forces are eliminated by incrementally applying equal but opposite nodal forces in a conventional finite element analysis. Convergence could not be achieved by this scheme. Teh (1987) attributed the lack of convergence to be due, in part, to numerical difficulties involved in interpolation of stresses from the SPM grid to the finite element grid.

Another equilibrium correction approach has been to include the strain path solutions as initial conditions in a finite element analysis (Teh & Houlsby, 1989). In this method, the

deviatoric stresses during an increment of penetration are computed based on a SPM solution. The out-of-balance forces occurring during this penetration increment are then computed based on equilibrium considerations. While holding the cone fixed, the initial SPM displacements are modified by incrementally applying nodal forces equal and opposite to the out-of-balance forces. This process is then repeated for the next increment of cone penetration. Some disadvantages to this approach include:

1. The large strains involved in this analysis require a large strain formulation, which increases the complexity of the analysis.

2. Computation of the out-of-balance forces requires an arbitrary selection regarding which equilibrium equation is correct (radial or vertical). In situations where vertical and radial equilibrium solutions differ significantly from one another, such an arbitrary selection can conceivably have a significant effect on the final result. The arbitrary selection of one equilibrium equation to be correct is particularly unattractive when the SPM is extended to penetrometers of general geometry (plates, vanes,etc.), as a different set of assumptions will be required for each different geometry that is analyzed.

2.4 PROPOSED POISSON FORMULATION

An alternative approach (Baligh, 1985), which can ameliorate the difficulties associated with path dependent pore pressures, is to solve both equlibrium equations by taking the divergence of eqn. 2.3:

$$\nabla^2 u = - \nabla \cdot g = - q \qquad (2.10)$$

In this case the scalar pore pressure field is determined as the solution of a Poisson equation using standard finite element techniques. In general, Poisson pore pressure fields will not satisfy either equilibrium equation exactly. However, the Poisson solution does not rely upon an arbitrary selection of an integration path; it therefore provides a flexible method for extending SPM solutions to penetrometers of general shape.

The Poisson solution was first implemented by Chin and Whittle (1984) for simple pile penetration in a bilinear soil model. They reported results which were in reasonable agreement with radial integration solutions, except near at the tip and face of the pile. The

inaccuracies near the tip were probably due to a) innacuracies of the numerical differentiation in regions of high stress gradients, and b) an improperly formulated boundary condition at the indenter interface. Teh (1987) subsequently implemented a Poisson solution (also using a bilinear model) with a properly formulated boundary condition; however, his predicted distribution of mean stress ahead of the tip was much too low, being much less than his predicted mean stress distributions obtained by radial and vertical integration.

In principle, the flux term, q, is calculated by numerical differentiation (first and second derivatives) of the stress components from the strain path method. However, accurate numerical evaluation of second derivatives is very difficult to achieve, especially in regions of high stress gradients. Considerable simplifications in computing can be achieved using the divergence theorem to estimate an average flux within a given finite element:

$$\int_V q \, dV = \int_A \mathbf{g} \cdot \mathbf{n} \; dS \qquad (2.11)$$

$$\overline{q} \, V = \sum_{i=1}^{n} (\mathbf{g} \cdot \mathbf{n})_i \, \Delta S_i \qquad (2.12)$$

where; $\overline{q}$ = average q within element

V = volume of element

$\mathbf{g}$ = pore pressure gradient vector on side i
   of the n-sided element

$\mathbf{n}$ = unit vector normal to side i of the element

S_i = Surface area of side i of the element

The numerical procedure for evaluating derivatives of stress components ($\mathbf{g}$) is based on the construction of nine node isoparametric elements (Bathe, 1982),where three closely spaced streamlines are used to define a nine-node element around the point of interest. An isoparametric differentiation scheme permits data points from the streamlines (see Section 2.2, steps 2 and 3) to be used directly without intermediate interpolation onto a finite difference grid. A natural coordinate system (s,t) is introduced to enable standard isoparametric interpolation of the stress derivatives at the point (Bathe, 1982):

$$\frac{\partial \sigma'_{ij}}{\partial s} = \frac{\partial h_n}{\partial t} \sigma'^n_{ij} \; ; \; \frac{\partial \sigma'_{ij}}{\partial t} = \frac{\partial h_n}{\partial t} \sigma'^n_{ij} \qquad (2.13)$$

where h_n are the interpolation functions shown in Appendix A, and σ'^n_{ij} are the effective stresses computed at the nodal points. The derivatives in the (r,z) coordinate frame are obtained through a Jacobian transformation:

$$\begin{pmatrix} \dfrac{\partial}{\partial r} \\ \dfrac{\partial}{\partial z} \end{pmatrix} = \begin{bmatrix} \dfrac{\partial r}{\partial s} & \dfrac{\partial z}{\partial s} \\ \dfrac{\partial r}{\partial t} & \dfrac{\partial z}{\partial t} \end{bmatrix} \begin{pmatrix} \dfrac{\partial}{\partial r} \\ \dfrac{\partial}{\partial z} \end{pmatrix} \qquad (2.14)$$

Boundary conditions for the Poisson equation (locations A,B,C,D are shown schematically in fig. 2.3) include: 1) $\partial u/\partial r=0$, due to symmetry, along the centreline (OD); 2) $u=0$, along BCD (assuming soil behavior is linear far from the penetrometer); and 3) $\partial u/\partial z=0$, to satisfy steady state conditions along AB. The most difficult boundary condition is that at the penetrometer boundary (OA), as it has no simple physical interpretation and there is no reason to assume that no pore pressure gradients normal to this boundary ($\partial u/\partial n \neq 0$). This boundary is treated in an approximate manner by computing the gradients adjacent to the indenter interface (g_r and g_z) and imposing the condition:

$$g_n = g_r n_r + g_z n_z \qquad (2.15)$$

Poisson solutions for normalized excess pore pressure, $(u-u_0)/\sigma'_{v0}$, during 18^0 and 60^0 cone penetration in the K_0-normally consolidated BBC described in section 2.2.1 are shown in figure 2.3. These solutions show:

1. At the base of the cones the normalized excess pore pressures predicted from the Poisson solutions are 10 to 20% greater than those predicted from radial integration. As a steady state is approached, the Poisson solutions match the radial integration solutions.

2. The excess pore pressures at the tip of the 60^0 cone predicted from the Poisson solution is approximately 25% less than that predicted by the vertical integration solution. On the centerline ahead of the cone tip the differences between the Poisson solution and the vertical integration solution become more significant.

3. For the 18^0 cone, there are large differences between the Poisson pore pressures and vertical integration solutions both at the tip of the penetrometer and in the soil ahead of the tip.

These observations suggest the following conclusions:

1. Far above the cone tip, the Poisson solutions match the radial integration solutions. Since radial integration solutions are considered to be very reliable in this region, the Poisson solutions can accordingly be considered to be reliable in this area.

2. On the cone face and on the centerline ahead of the cone tip, the Poisson solutions differ substantially from the vertical integration solutions. The differences between the Poisson solutions and the vertical intregration solutions increase with decreasing cone angle. The discrepancies between Poisson and vertical integration solutions ahead of the tip are serious for two reasons: a) the vertical equilibrium equation is considered to be reliable ahead of the tip, and b) the Poisson solutions imply that tip angle has a major influence on magnitudes of tip pore pressures, which is contrary to measured data (Levadoux and Baligh, 1980). Accordingly, the excess pore pressures on the cone face and ahead of the cone tip predicted from the Poisson solution cannot be considered reliable, particularly for sharp cone angles.

2.5 THE MODIFIED POISSON FORMULATION

Since the vertical equilibrium equation is considered to be more reliable ahead of the cone tip, the Poisson solutions described in the previous section can be improved by considering only the vertical equilibrium equation in the region ahead of the tip. If the pore pressure field u^z is computed based on vertical integration using Equation 2.6b, the flux term q based solely on vertical equilibrium can then be determined by computing the Laplacian of u^z

$$q = \nabla^2 u^z \tag{2.16}$$

For implementation in a finite element solution, the equivalent nodal loads corresponding to Equation 2.16 are required. These can be computed by a simple matrix multiplication

$$\{ q_e \} = [K] \{ u^z \} \tag{2.17}$$

where [K] is the system conductivity matrix which is used in the solution of the Poisson equation.

To implement the modified Poisson solution, a rational means is required for identifying the extent of the zone ahead of the tip which is dominated by vertical equilibrium equation. To assess the contribution of the radial and vertical equilibrium equations to the total value of q defined in equation 2.10, the following scalar terms were defined

$$\text{Radial Equilibrium Contribution:} \quad q^r = \frac{g_r}{r} + \frac{\partial g_r}{\partial r} \tag{2.18a}$$

$$\text{Vertical Equilibrium Contribution:} \quad q^z = \frac{\partial g_z}{\partial z} \tag{2.18b}$$

where $q=q^r+q^z$. A simple measure of the relative contribution of the vertical equilibrium equation can be defined as:

$$R_z = q^z / (|q^z| + |q^r|) \tag{2.19}$$

When vertical equilibrium dominates R_z will be unity, and when radial equilibrium predominates, R_z will be zero. Contours of R_z for 18^0 and 60^0 cone penetration are shown in Figure 2.4. These results indicate three regions:

1. Below line OA the vertical equilibrium is dominant ($R_z \approx 1$); except near the tip ($z/R<3$).
2. Above line OB radial equilibrium the radial equilibrium is dominant ($R_z \approx 0$).
3. The area between OA and OB is a transition region where both equilibrium equations influence the solution ($0<R_z<1$).

In order to eliminate the influence of the unreliable radial equilibrium equation near the face and tip of the cone, the following modified Poisson procedure was adopted:

1. Subdivide the problem into two regions, which are separated by a line OA.
2. In the upper region compute q based on both equilibrium equations using Equation 2.10.
3. In the lower region compute q based solely on the vertical equilibrium equation using Equation 2.16.

Modified Poisson solutions for 18^0 and 60^0 cone penetration in K_0-normally consolidated BBC based on effective stress fields from the MCC soil model are shown in Figure 2.5. Comparison to the integration solutions described in Section 2.2 and the modified Poisson solution described in Section 2.5 indicates:

1. For both cone angles, the normalized excess pore pressure near the cone tip predicted from the modified Poisson solution matches the vertical integration solution to within

5%. On the centerline ahead of the cone tip the modified Poisson solution agrees very well with the vertical integration solution.

2. On the shaft above the base of the cone the modified Poisson solutions are quite similar to the Poisson solutions, with the normalized excess pore pressures predicted from the modified Poisson solutions being a maximum of 15% greater than those predicted from the Poisson solutions. Far above the cone tip (z/R>15-20), the modified Poisson solutions closely match the radial integration solutions.

The modified Poisson solutions therefore agrees with integration solutions in two important areas:

1. Ahead of the the cone tip they agree with solutions based on the vertical equilibrium equation, which have proved reliable in past studies (Elghaib, 1989).

2. Far above the cone tip they agree with radial integration solutions, which are most reliable in the steady state region far above the cone tip.

2.6 FORMULATION FOR THREE-DIMENSIONAL GEOMETRIES

Plate penetration problems can be described in a three-dimensional cartesian frame as shown in Figure 2.6, where the z-direction is vertical, the y-direction is parallel to the major (wide) axis of the plate, and the x-direction is parallel to the minor (thin) axis of the plate. Strain and stress field predictions during plate penetration are discussed in detail in Sections 3.3 and 3.4 respectively. In a three-dimensional cartesian frame the equilibrium equations are

$$-\frac{\partial u}{\partial x} = -g_x = \frac{\partial \sigma'_{xx}}{\partial x} + \frac{\partial \sigma'_{xy}}{\partial y} + \frac{\partial \sigma'_{xz}}{\partial z} \qquad (2.20a)$$

$$-\frac{\partial u}{\partial y} = -g_y = \frac{\partial \sigma'_{xy}}{\partial x} + \frac{\partial \sigma'_{yy}}{\partial y} + \frac{\partial \sigma'_{yz}}{\partial z} \qquad (2.20b)$$

$$-\frac{\partial u}{\partial z} = -g_z = \frac{\partial \sigma'_{xz}}{\partial x} + \frac{\partial \sigma'_{yz}}{\partial y} + \frac{\partial \sigma'_{zz}}{\partial z} \qquad (2.20c)$$

In principle, Equations 2.20 can be substituted into Equation 2.12, and pore pressures can be determined as the solution of a Poisson equation in three dimensions; however, the complexity and cost of three-dimensional finite element analyses can be avoided by using

simplified two-dimensional analyses in two orthogonal planes ; namely: a) the y=0 plane, and b) z=constant planes. The y=0 plane corresponds to a vertical plane on the centerline of a blade penetrometer. Physical measurements are often made in this plane during plate penetration; for example, the center of the membrane of the dilatometer and the pore pressure filter in the piezoblade are located in this plane. Predictions in this plane are accordingly quite important for validation of predictions and for assessing the vertical variation in pore pressures and total stresses along the dilatometer membrane during penetration. Predictions in z=constant (horizontal) planes are important for predicting the horizontal variation in pore pressures and total stresses along the blade; for example, in assessing the horizontal variation in total horizontal stress along the membrane of a dilatometer.

2.6.1 Formulation in the y=0 Plane

In the y=0 plane, the two relevant equilibrium equations become equations 2.20a and c. Derivatives of stress components in the x and z directions can be computed numerically using Equations 2.13 and 2.14. The y=0 plane is a plane of anti-symmetry with respect to the σ_{xy} and σ_{yz} stress components, therefore, the partial derivatives with respect to these stress components cannot be assumed to be zero and must be evaluated numerically. Partial derivatives of these stress components with respect to y at a point (x^*, z^*) can be evaluated by the following steps:

1. Compute the stresses along three streamlines whose initial positions far ahead of the tip are offset a distance Δy from the y=0 plane. Δy is selected to be equal to the initial streamline spacing within the y=0 plane. This is typically $\Delta y/w = \Delta x/w = 0.1$, where w=plate half-thickness.

2. Evaluate the stress components $(\sigma_{ij})_{y=\Delta y}$ at x^*, z^* by interpolation.

3. Evaluate the partial derivative by a first order finite difference approximation

$$\frac{\partial \sigma'_{ij}}{\partial y} \approx \frac{(\sigma'_{ij})_{y=\Delta y} - (\sigma'_{ij})_{y=0}}{\Delta y} \qquad (2.21)$$

With g_x and g_z thus evaluated, excess pore pressures in the y=0 plane can be predicted by direct integration of the equilibrium equations as discusssed in section 2.2 or by the

modified Poisson solution discussed in section 2.5. Figure 2.7 illustrates the potential differences in predictions of pore pressures that can arise amongst these three solutions. The figure shows the distribution of excess pore pressures, $(u-u_0)/\sigma'_{v0}$, at points along the surface and at vertical locations ahead of the tip of a simple plate penetrometer having an aspect ratio B/w=6.8; where B is the half-length and w is the half-thickness of the plate. The simple plate is the penetrometer geometry defined by a line source of incompressible material of length 2B in a uniform flow field. The geometry of the simple plate is described in detail in section 4.2. This aspect ratio corresponds to the aspect ratio of the Marchetti dilatometer described in Chapter 5. The results show the following:

1. At the tip of the plate, excess pore pressures predicted from the modified Poisson solution match the vertical solution to within 10%. On the centerline ahead of the tip the modified Poisson solution closely matches the vertical integration solution. The horizontal integration solution underpredicts the vertical integration solution by approximately 20% at the plate tip. The horizontal integration solution substantially underpredicts the vertical integration and modified Poisson solutions on the centerline ahead of the plate tip.

2. Far above the plate tip the Poisson solution matches the horizontal integration solution. The two solutions begin to converge at approximately z/w=40-50.

3. Above the plate tip, vertical equilibrium pressures, Δu^z, decrease rapidly and become unbounded (i.e. continue to decrease with distance along the penetrometer), while horizontal equilibrium pressures reach a steady state solution at z/w=40-50.

These observed trends are qualitatively quite similar to the trends observed for axisymmetric penetrometers which were discussed in sections 2.2 and 2.5. A major difference is the distance above the tip at which a steady condition is achieved. This is due to the fact that the plate in this example displaces a larger volume of soil than the axisymmetric penetrometers discussed in sections 2.2 through 2.5; that is, the plate has a cross-sectional area far above the tip equal to 4Bw, while the cone penetrometers have a cross-sectional area equal to πR^2. This difference can be accounted for by normalizing the plate coordinates by an equivalent radius, R_{eq}, which is defined as

$$R_{eq} = \sqrt{\frac{4Bw}{\pi}} \qquad (2.22)$$

Figure 2.8 shows predictions of excess pore pressure around a plate after normalizing the plate coordinates by R_{eq}. Figure 2.8a shows the predicted distribution in the y=0 plane

on the plate boundary and on the centerline ahead of the plate tip, and figure 2.8b shows the predicted lateral distribution of excess pore pressures far above the plate tip. Comparing the plate predictions to the predicted distribution of pore pressures during simple pile (B/w=0) penetration indicates:

1. The normalized distance above the penetrometer tip at which a steady state pore pressure distribution is reached is 10-20z/R_{eq} for both the simple pile and the simple plate.

2. The predicted pore pressures at the penetrometer tips for the two penetrometer shapes match to within 15%. The predicted pore pressure distributions ahead of the tip pore are also quite similar to one another.

3. The lateral distribution of pore pressure far above the penetrometer tip for the simple plate and simple pile match quite closely, with the predicted pore pressures at the penetrometer boundaries agreeing to within 3%.

These observations imply:

1. Penetrometer geometry (aspect ratio) has a relatively small influence on magnitudes of tip and shaft pore pressures.

2. The extent of the zone of disturbance is strongly influenced by the volume of soil displaced during penetration. Penetrometer geometry does not significantly alter the extent of the zone of disturbance.

2.6.2 Formulation in z=constant Planes

In a horizontal plane the relevant equilibrium equations are equations 2.20a and b. For the special case of a plane located far above the plate tip these equations reduce to

$$-\frac{\partial u}{\partial x} = -g_x = \frac{\partial \sigma'_{xx}}{\partial x} + \frac{\partial \sigma'_{xy}}{\partial y} \tag{2.23a}$$

$$-\frac{\partial u}{\partial y} = -g_y = \frac{\partial \sigma'_{xy}}{\partial x} + \frac{\partial \sigma'_{yy}}{\partial y} \tag{2.23b}$$

The derivatives of the stress components in Equations 2.23 were evaluated using a 4-node isoparametric interpolation scheme (Bathe, 1982), where four closely spaced streamlines are used to define an element around the point of interest. A description of numerical differentiation using isoparametric functions is contained in section 2.4, and a listing of isoparametric functions and their derivatives for four-node elements is contained in

Appendix A.

Equations 2.23 can be substituted into Equation 2.12, and pore pressures can be determined as a solution of a Poisson equation in the x-y plane. Pore pressure contours during installation of a B/w=32.5 plate as computed by integration solutions and the Poisson equation are shown in Figure 2.9. This figure indicates significant (on the order of 25%) differences between the two integration solutions. It further shows that the Poisson solution generally provides an 'average' between the two integration solutions in the vicinity of the penetrometer; although, in the far field in the x-direction, the Poisson solution predicts a greater zone of disturbance than either the x- or y-integration solutions. Table 2.1 compares Poisson pore pressure predictions to integration solutions far above the plate tip (large z/w) at the plate center and at the edge of penetrometers having an aspect ratios B/w=6.8, 20, and 32.5. This table indicates that at the plate center the pore pressure predicted from the Poisson solution is intermediate between the two integration solutions. The predicted pore pressures at the edge of the plate also lie between the two integration solutions at the higher aspect ratios of 20 and 32.5. For B/w=6.8 the Poisson prediction is slightly lower (approximately 5-10%) than both integration solutions. In general, the Poisson solution appears to provide a reasonable 'average' of the two integration solutions at the penetrometer boundary for a wide range of aspect ratios.

Uncoupled dissipation (see Chapter 3.5) solutions at the plate center is shown in Figure 2.10. It can be seen that the dissipation solutions based on the pore pressure distribution predicted from the Poisson equation gives a reasonable average in all cases. The practical implication of this result is that, although the Poisson installation pore pressures are not an 'average' of the two integration solutions at all points within the field (note the reference above to the zone of disturbance in the x-direction), the dissipation curves for Poisson pore pressures at the plate center nevertheless lie intermediate between the dissipation curves for the two integration solutions.

The Modified Poisson solutions presented in Section 2.6.1 were based on equilibrium in the x-z plane, while the Poisson solutions presented in this section are based on equilibrium in the x-y plane. To assess the consequences of the simplification of the analyses from a three-dimensional problem to a 2-dimensional problem within a particular plane of interest, these two solutions are compared to one another in Figure 2.11, which shows the predicted distributions of pore pressure along the x-axis (on the plate centerline) far above the tip of a simple plate having an aspect ratio B/w=6.8. This figure indicates that the pore pressure distributions along the x-axis are in good agreement, with the predicted excess pore

pressures at the plate boundary agreeing to within 10%.

2.7 CONCLUSIONS

1. The Poisson solution provides a reliable means for predicting pore pressure distribution without requiring arbitrary assumptions regarding the path of integration. This makes the method particularly suitable for application to more complex penetrometer geometries such as the field vane, the dilatometer, spade cells, etc.

2. The Poisson solution was evaluated by comparing it to: a) the radial integration solution far above the tip, where radial integration provides the most reliable solution, and b) the vertical integration solution ahead of the tip, where vertical integration provides the most reliable solution. It was found that: a) far above the tip, the Poisson solution matches the reliable radial integration solution, and b) ahead of the tip, the Poisson solution seriously underpredicts the vertical integration solution.

3. The Modified Poisson solution, which a) considers only vertical equilibrium ahead of the tip (below line OA in Figure 2.4) and b) considers both equilibrium equations above line OA , provides excellent agreement with vertical integration solutions. Line OA in Figure 2.4 was established by assessing the relative contribution of the gradient terms g_r and g_z to the flux term q in the Poisson equation.

4. The modified Poisson formulation enforces the more reliable vertical equilibrium equation ahead of the tip; therefore, in this study, it will be used to make predictions for the following types of penetration problems in which vertical equilibrium is important: 1) piezocone penetration, 2) the push-in pressuremeter test (based on open-ended pile solutions), and 3) the Marchetti dilatometer test (based on plate solutions in a vertical plane). Analysis of pore pressure distribution in horizontal planes far above the penetrometer tip do not involve the vertical equilibrium equation; therefore, the originally proposed Poisson formulation described in Section 2.4 should be implemented for such cases. In this study, such cases will include predictions of pore pressure distribution in horizontal planes around: 1) single plates, and 2) the field vane (i.e. superpostion of two plates rotated at 90^0).
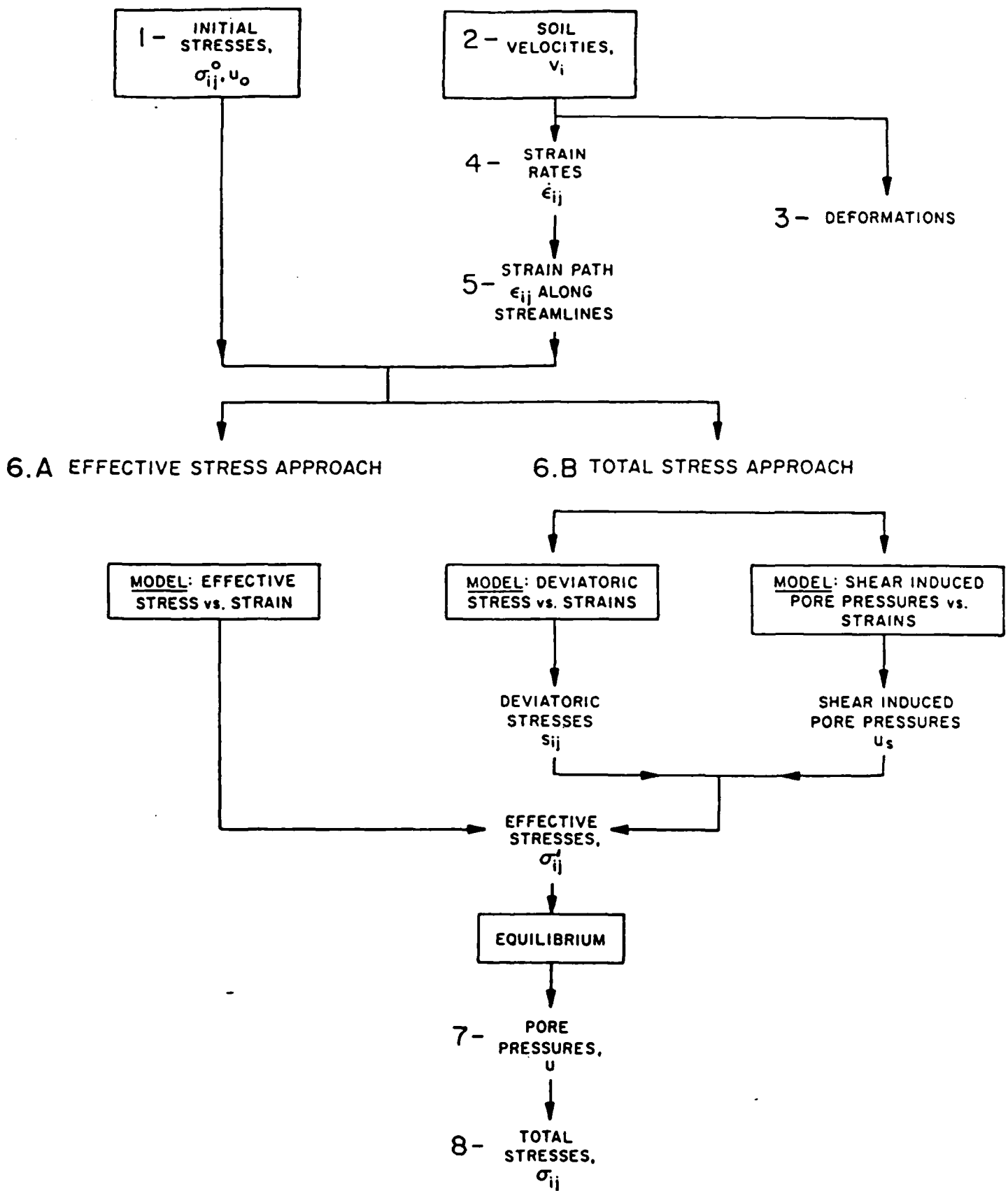
Fig. 2.1 The Strain Path Method (Baligh, 1985)
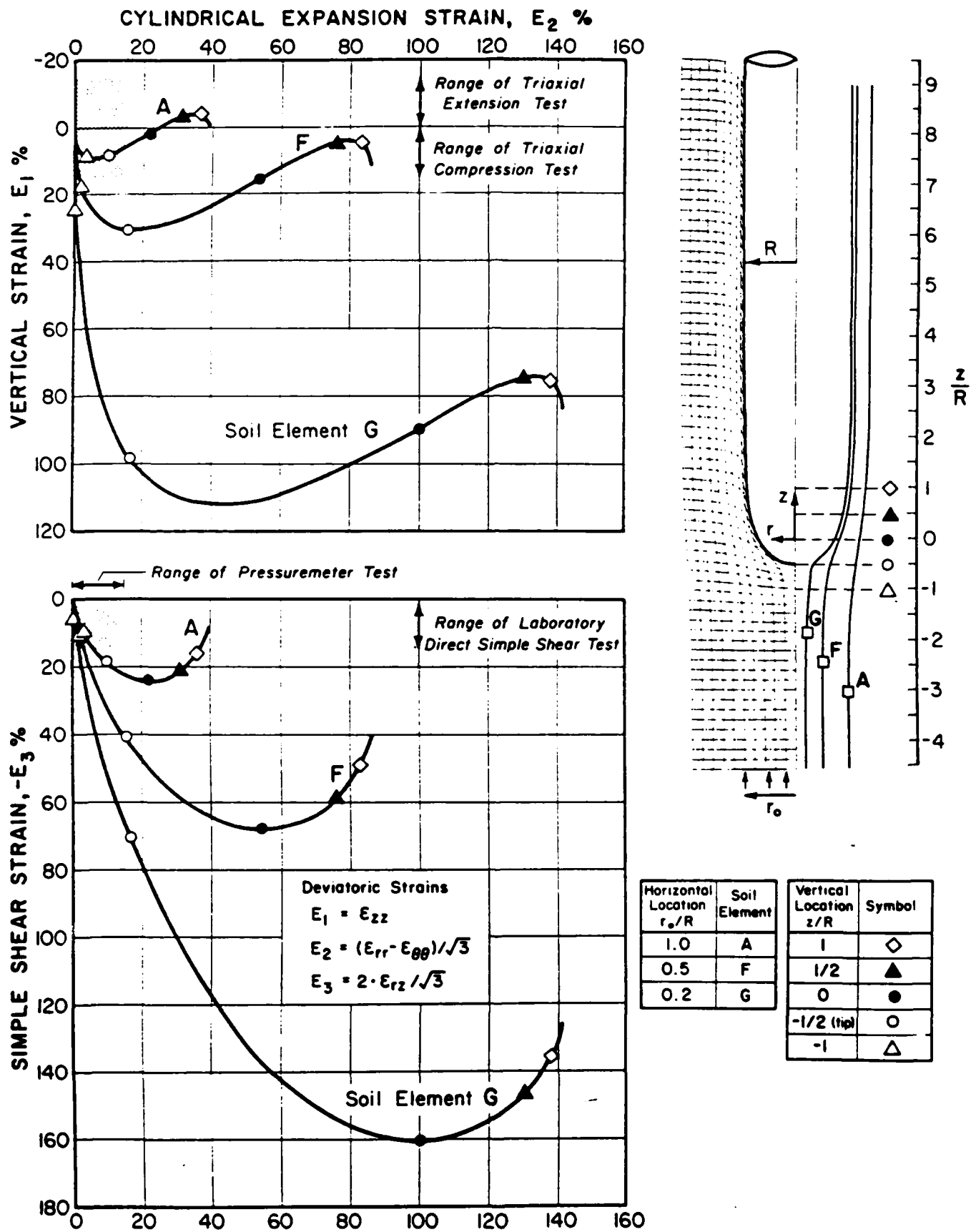
Figure 2.2 Strain Paths During Simple Pile Penetration (Baligh, 1985)
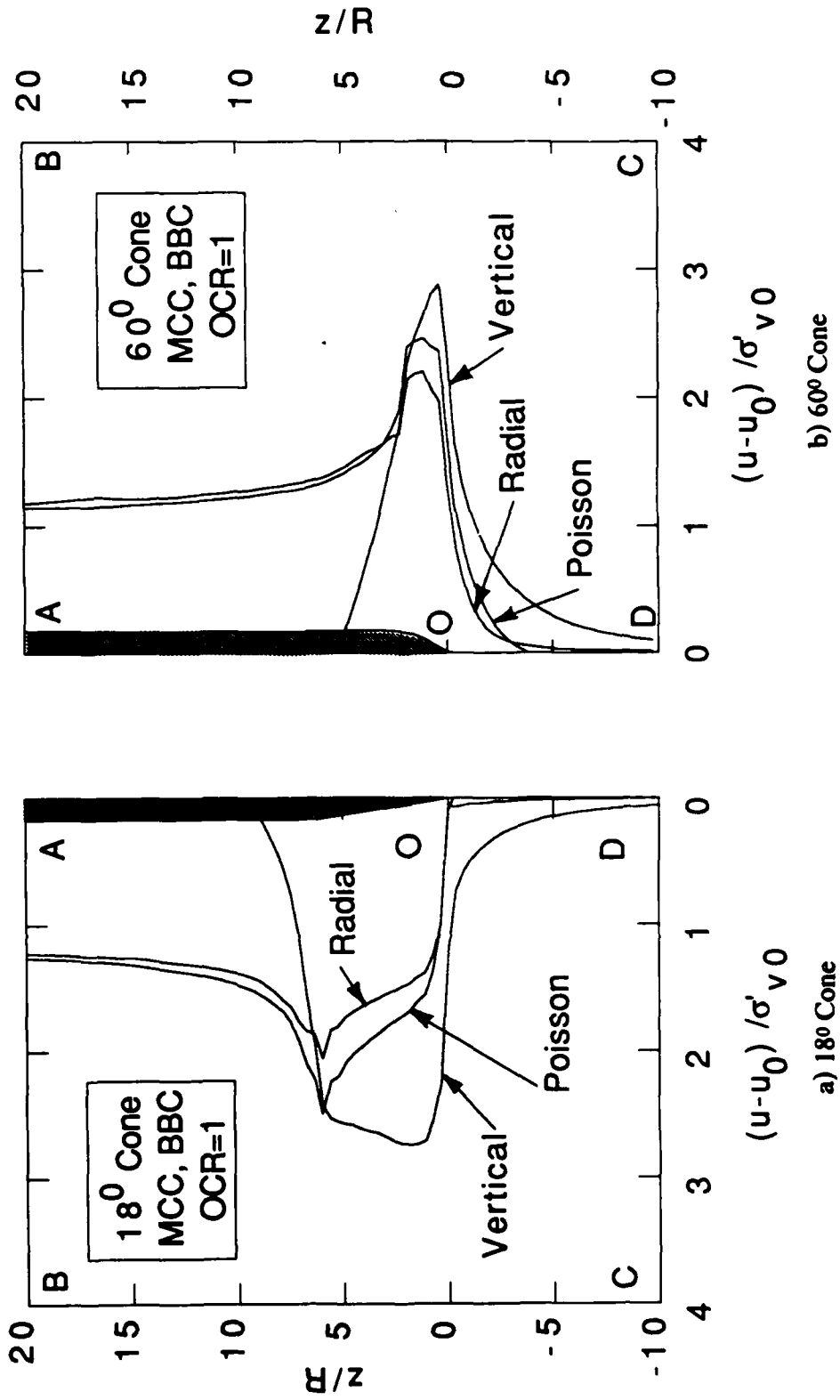
Figure 2.3. Excess Pore Pressures Around Cones Predicted by Different Equilibrium Equations Using MCC Soil Model for K_0-Normally Consolidated BBC
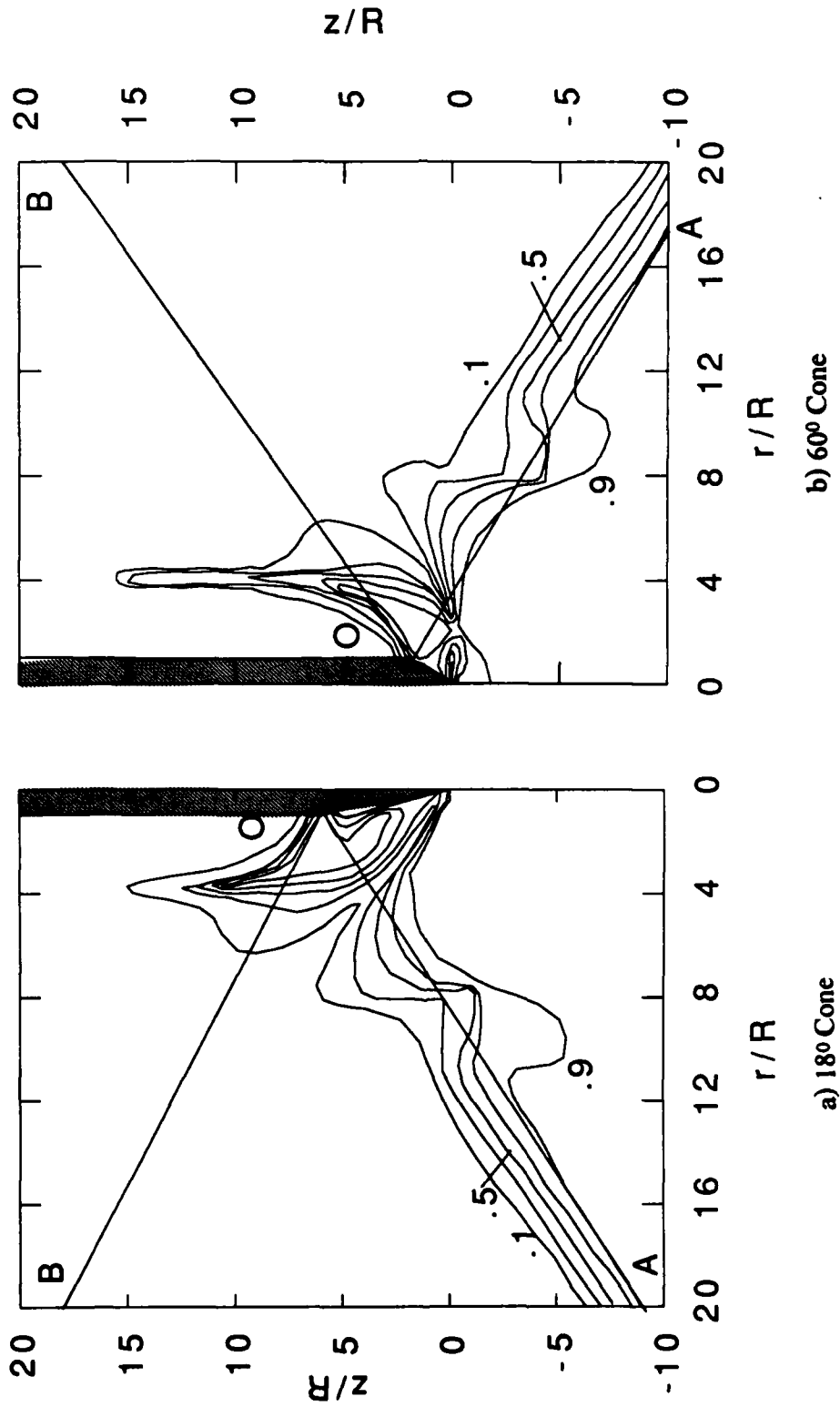
Figure 2.4 Relative Contribution of Vertical Equilibrium Equation During Cone Penetration
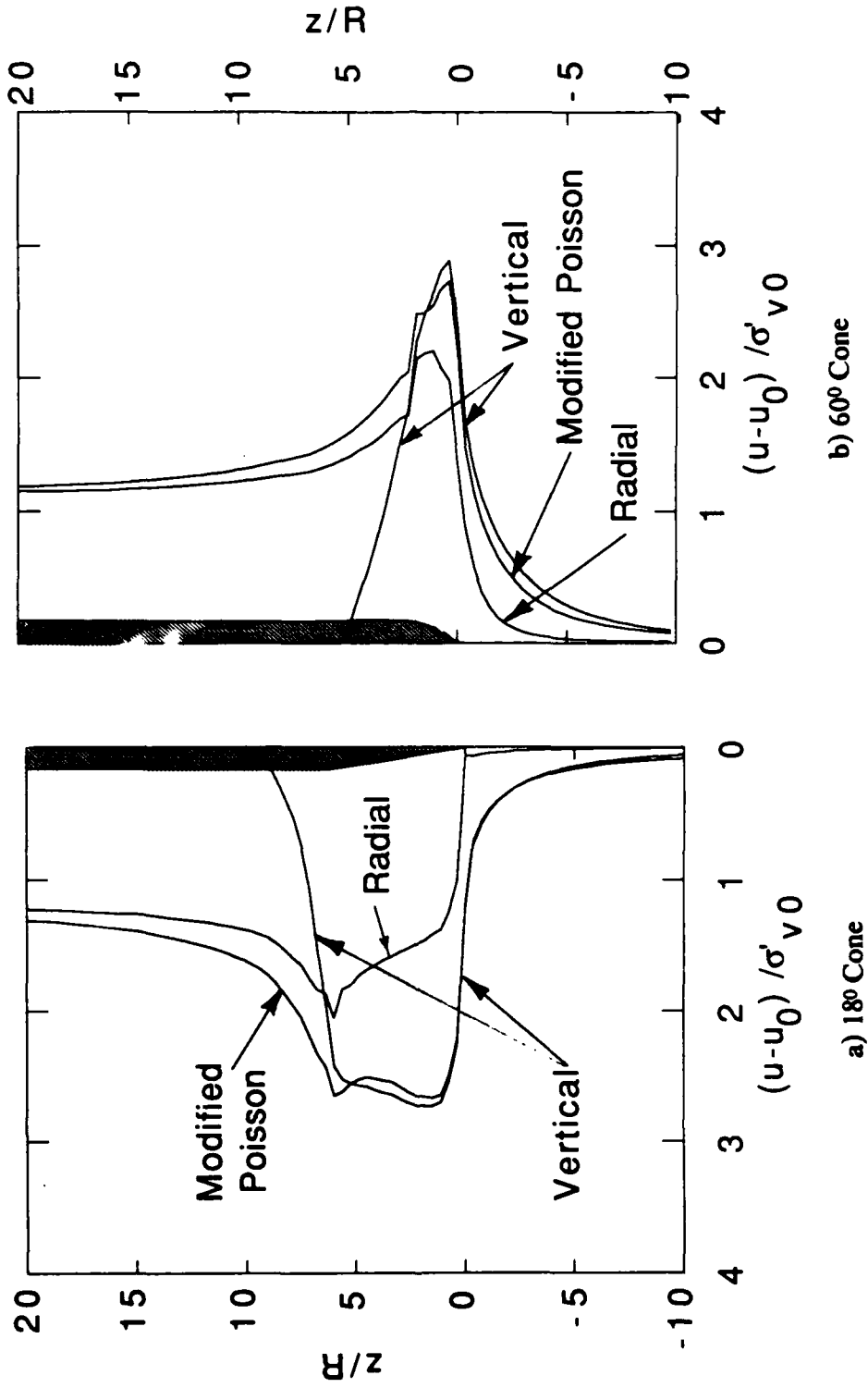
Figure 2.5 Excess Pore Pressures Around Cones Predicted by Modified Poisson Solution Using MCC Soil Model for K_0-Normally Consolidated BBC
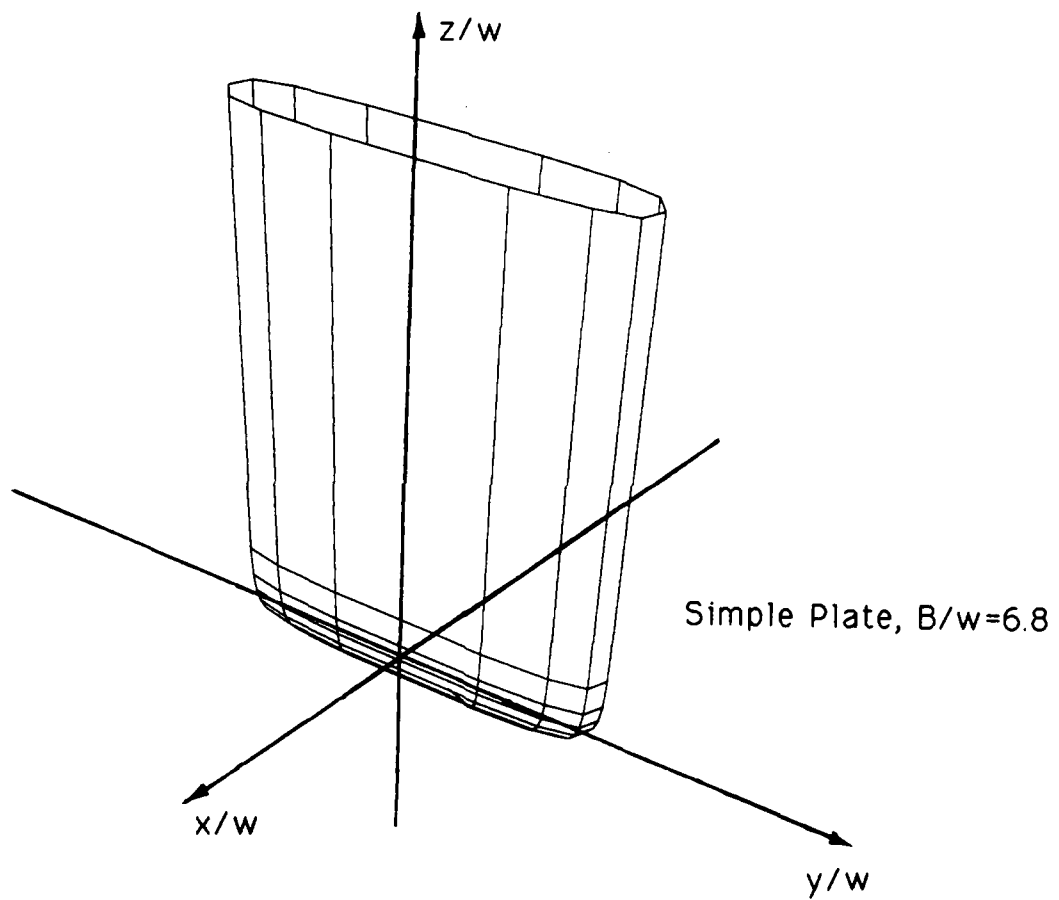
Figure 2.6 Definition of Coordinate Frame for Plate Penetration Problems
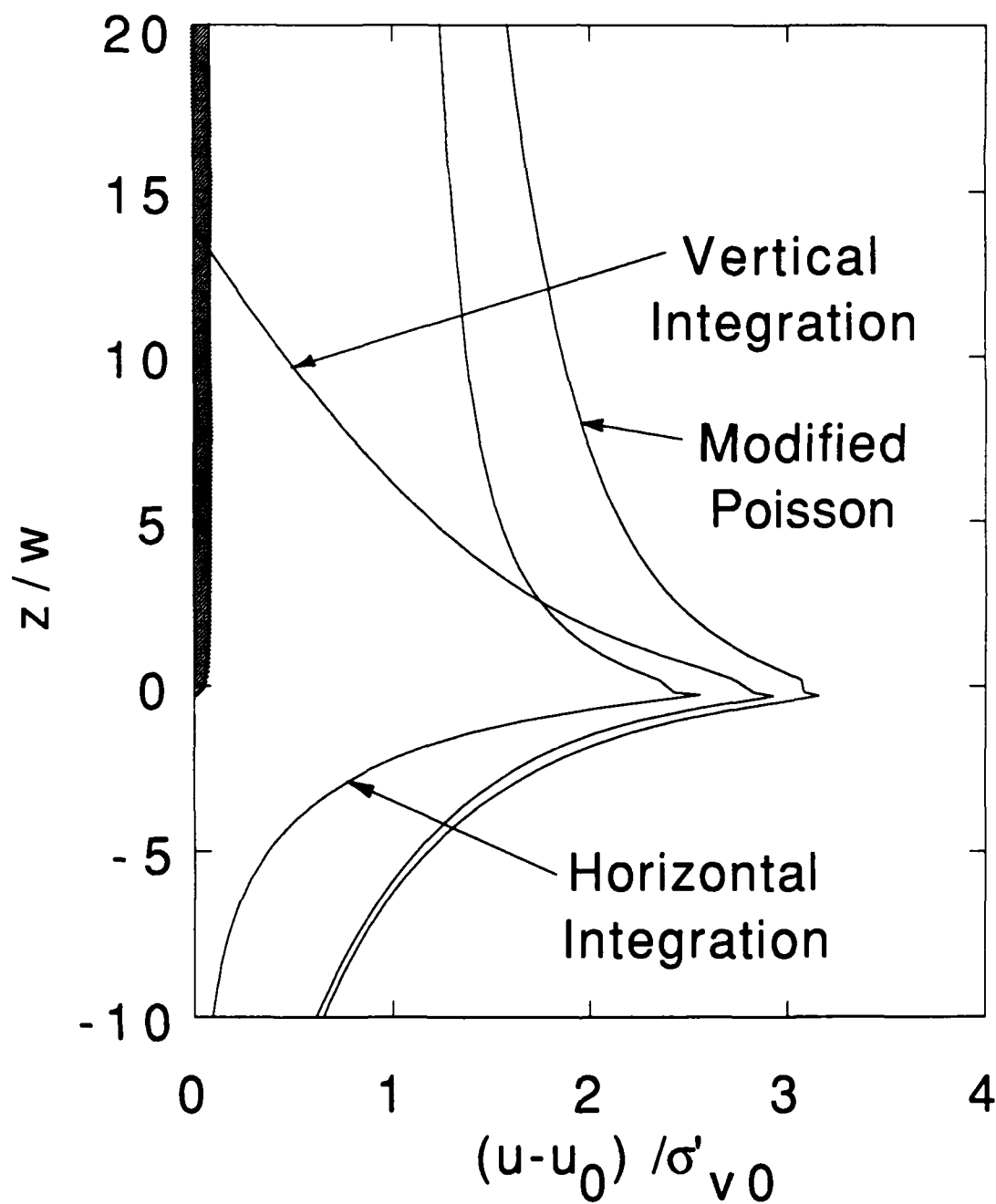
Figure 2.7 Excess Pore Pressures at Plate Center by Different Equilibrium Equations

b) Lateral Distribution far above Tip

a) Along Centerline and Plate Boundary
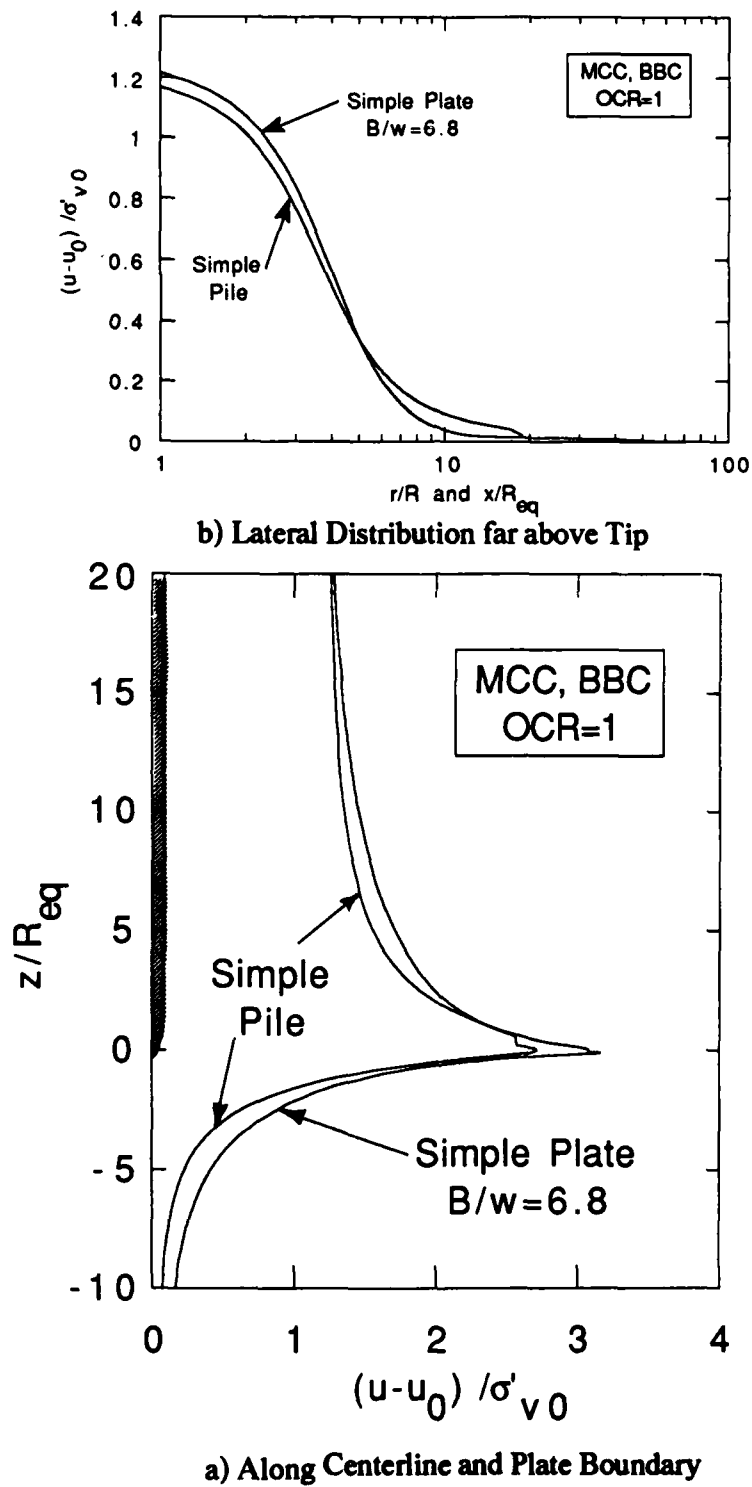
Figure 2.8 Comparison of Simple Plate, B/w=6.8, and Simple Pile Excess Pore Pressures
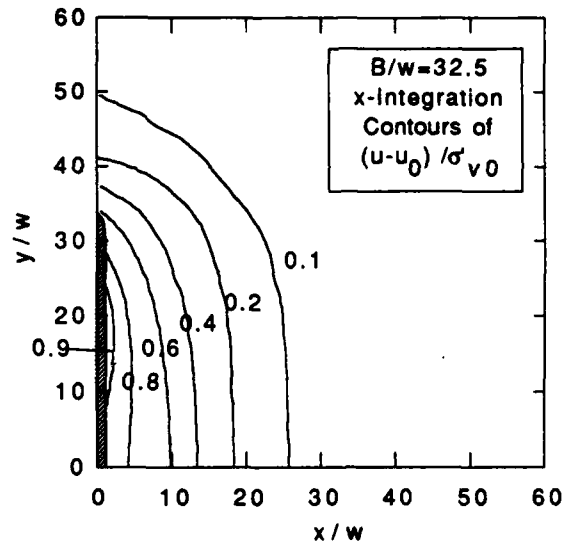
a) x-Direction integration
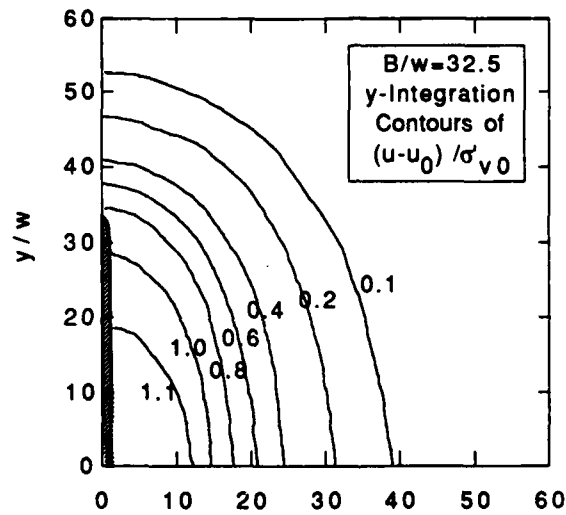
b) y-Direction Integration
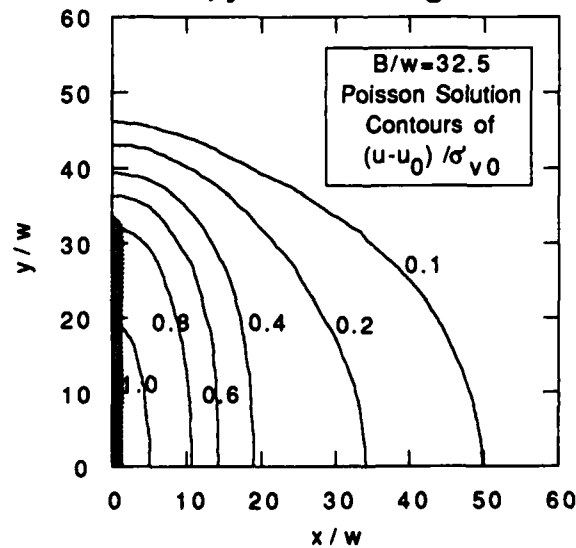
c) Poisson Solution

2.9 Pore Pressures in Horizontal Plane Far Above Tip for Simple Plate, B/w=32.5
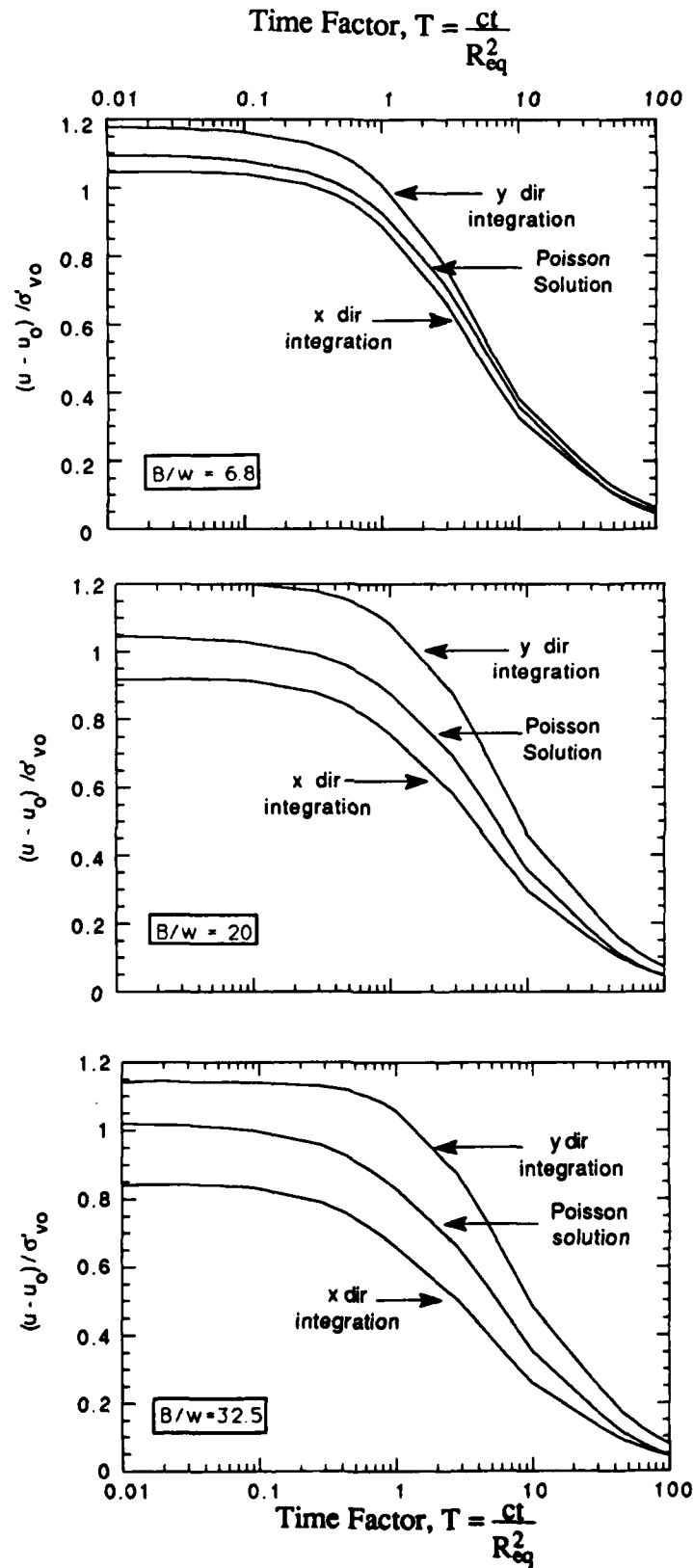
Figure 2.10 Dissipation of Excess Pore Pressures for Different Initial Conditions at Plate Center
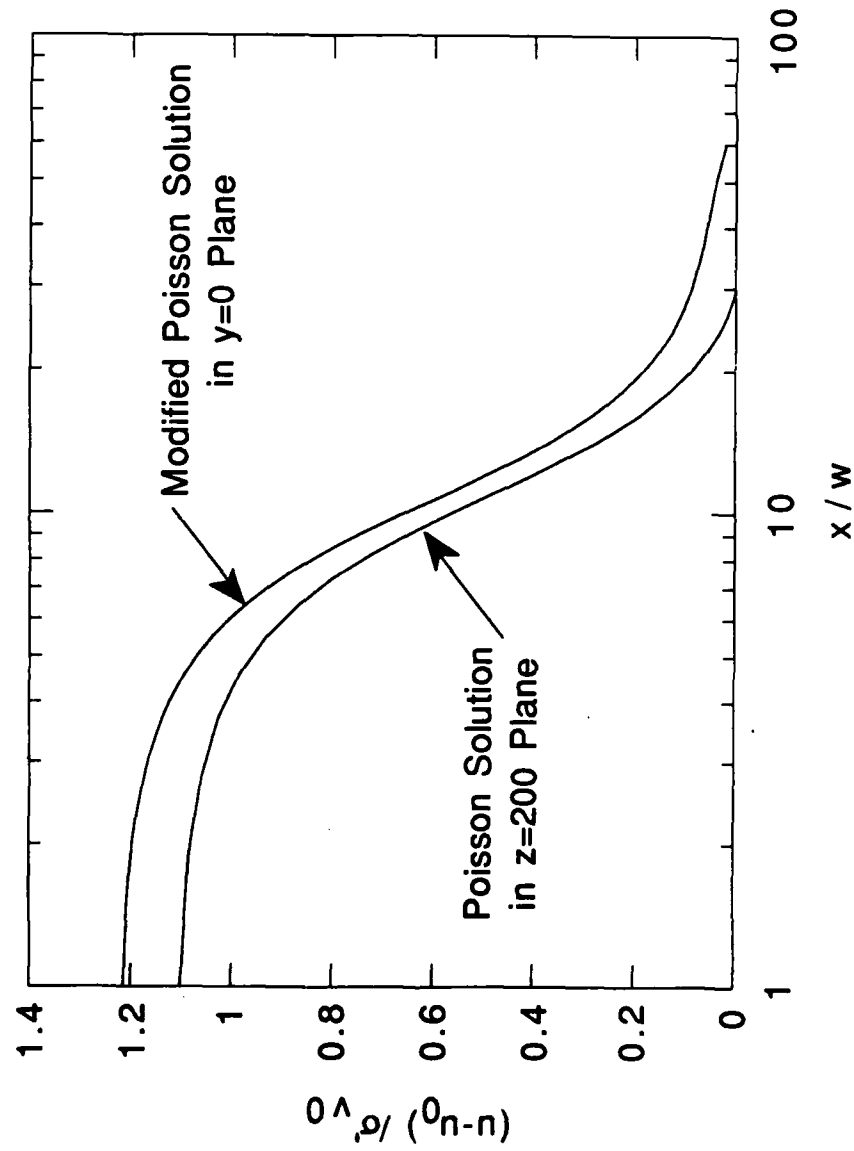
Figure 2.11 Comparison of Excess Pore Pressures Predicted in z/w=200 and in y/w=0 Planes Using Proposed Poisson Formulations

3. MECHANICS OF PLATE PENETRATION

3.1 INTRODUCTION

There are a variety of penetrometer devices, currently used to estimate in-situ engineering properties of clays, whose geometry can be characterized by a flat plate (or plates; Fig. 3.1). These include: a) the dilatometer (Marchetti, 1980), which measures total lateral stresses acting on a membrane inflated against the soil; b) earth pressure (spade) cells (Tedd and Charles, 1982; Germaine, 1980; Tavenas et al. 1975); c) Iowa stepped blade (Handy et al. 1982); and d) field vanes (Chandler, 1988), which are inserted and then rotated against the soil. In this chapter, the Strain Path Method (SPM; Baligh, 1985a) is used to describe the mechanics of flat plate penetration. The analyses are based on a 'simple' plate geometry which is characterized by a width to thickness 'aspect ratio', B/w. The analyses provide a complete framework for predicting the stresses and pore pressures around penetrometers of different aspect ratio (B/w ≈ 6 to 30). The results are then used: a) to estimate how in-situ penetration measurements are related to soil properties (e.g. for the dilatometer, chapter 5), and b) estimate initial stress conditions in the soil prior to subsequent testing operations (e.g. prior to field vane rotation, chapter 6). The results have further applications in other areas of geotechnical practice, *including the disturbance due to* H-pile, sheet pile, and wick drain mandrel installation (Fig. 3.2).

3.2 PREVIOUS STUDIES USING THE STRAIN PATH METHOD

The strain path method was introduced by Baligh (1985) to provide an approximate analytical framework for describing the deep, quasi-static penetration of a rigid penetrometer in a saturated, homogeneous clay. The key assumption of the analysis is that the deep penetration problem is heavily kinematically constrained such that the deformation and strain fields can be estimated from a velocity field which satisfies the conservation of volume requirement and boundary conditions (i.e. strains are obtained independent of the shearing resistance of the soil). Figure 2.1 describes the necessary steps to obtain solutions by means of the Strain Path Method:

1. *Estimate the in-situ stress and pore pressure conditions before penetration.*
2. Estimate a velocity field that satisfies the conservation of mass requirement and the boundary conditions. The velocity field describes the velocity of soil particles relative to the indenter.
3. Determine soil deformations by integrating the velocity field.

4. Compute strain rates by differentiating the velocity field:

$$\dot{\varepsilon}_{ij} = \frac{1}{2}(\frac{\partial v_i}{\partial x_j} + \frac{\partial v_j}{\partial x_i}) \tag{3.1}$$

5. Integrate the strain rates to determine the strain paths of different soil elements.

6. At this stage, the effective stresses can be determined from the strain path (or history) of various elements by either a) an effective stress approach utilizing an effective stress vs. strain model, or b) a total stress approach utilizing two models: the first model determines the deviatoric stresses, and the second estimates the shear induced pore pressures. In this chapter the effective stress approach is used throughout. This is because a) the effective stress models used herein are based on fundamental concepts of soil behavior, b) in subsequent studies the effective stresses will control the soil's consolidation and strength behavior, and c) to evaluate differences in predictions from different soil models (which capture different aspects of measured soil behavior).

7. Given the effective stresses (σ'_{ij}) the excess pore pressures are computed from equilibrium considerations. In this chapter, approximate fields of excess pore pressures are obtained using the finite element solutions of the Poisson equation presented in chapter 2.

In the simplest application of the strain path method, the velocity field is estimated from the steady, irrotational (potential) flow of an incompressible, inviscid fluid around the penetrometer. Simple penetrometer geometries are obtained by combining fundamental solutions for singularities with uniform flows. For example, Baligh (1985a) describes a blunt axisymmetric penetrometer, referred to as a "simple pile", which is obtained by combining the solution of a 3-D point source with a uniform flow (Fig. 3.3). Table 3.1 summarizes other basic geometries that have been reported previously, including a) the open ended pile or hollow sampling tube, and b) the "simple wall" (Chin, 1986). In each case the geometry is defined using a singularity (infinite line source, ring source etc; Tab. 3.1) with a uniform flow. The major advantage of these simple solutions is that closed form expressions can be derived for the velocity, strain rate and strain fields during steady penetration (Baligh, 1985a, 1986a; Teh, 1987; Teh & Houlsby, 1987).

More realistic penetrometer geometries can be developed from the basic solutions using methods of superposition. The "method of sources and sinks" (Weinstein, 1948; Rouse, 1959) enables the geometry of axisymmetric bodies to be simulated by a distribution of sources and sinks along the centerline of the body. In this case, the total potential flowfield, Φ, is written as a linear combination of the potentials for each of the sources, ϕ_i :

$$\Phi = \sum c_i \, \phi_i \tag{3.2}$$

where, c_i are constant coefficients and correspond to the strengths of the individual sources. For specified source locations and penetrometer geometry, the values of c_i are determined (by an inversion process) from the boundary conditions of zero flux normal to the solid boundary.

Using the method of sources and sinks, the contribution of the individual sources/sinks to the overall velocities and strain rates in the soil can be expressed analytically. However, the method has a number of limitations:

1. The number of possible source configurations to describe a given geometry (i.e., the number and locations of sources along the penetrometer axis) is infinite and numerous trials are necessary to establish reliable and accurate solutions for a specified geometry. Also, numerical instability can result if the sources are too closely spaced.

2. The method is best suited to slender bodies and becomes numerically inaccurate when the geometry includes discontinuities of slope[1]. The 60^0 cone probably represents the maximum cone angle that can be treated by this method without the need for a ring source located at the slope of the discontinuity (Levadoux and Baligh, 1980).

Levadoux and Baligh (1980) report results for 18^0 and 60^0 degree cone penetrometers using the method of sources and sinks. Figure 3.4 compares the deformation paths for soil elements located at radial distances, $1 \leq r_0/R \leq 5$, described by the strain path method for a) the simple pile, b) 60^0 cone, and c) 18^0 cone. Radial displacements of the soil elements are controlled primarily by the conservation of volume requirement (due to soil incompressibility during penetration) and are not significantly influenced by tip geometry. In the vertical direction, the soil is initially pushed downwards in the direction of penetration and is then squeezed upwards after passage of the base of the penetrometer. The magnitude of vertical soil deformations reduces with increasing sharpness of the tip. This reflects differences in the shearing mechanism in the immediate vicinity of the tip that can be described as "pushing" of the soil for the simple pile (blunt penetrometer) and "cutting" of the soil for the 18^0 (sharp) cone.

For axisymmetric penetration, the strain path (history) of soil elements around the penetrometer is fully described by three independent components of shear strain, E_1, E_2,

---

[1] For example, at the transition between the cone and the shaft of the penetrometer, Levadoux and Baligh (1980) introduce a circular arc approximation to the geometry. Tumay et al. (1985) propose the use of conformal mapping using Schwartz-Cristoffel transformations to alleviate the problem.

E_3[2] that correspond to shearing in triaxial, pressuremeter and simple shear modes respectively. Figure 3.5 shows the strain paths of soil elements close to the centerline ($0.2 \leq r_0/R \leq 1.0$) for the three axisymmetric penetrometers. These results show the following:

1. Tip geometry does not have a significant effect on, a) the overall magnitudes of the E_2 strain experienced by soil elements close to the penetrometer, or b) the reversals of strain direction experienced by the soil elements.

2. The magnitudes of the E_1 and E_3 strain components reduce significantly with increasing tip sharpness for soil elements located close to the penetrometer ($r_0/R < 1.0$).

Two possible approaches can be considered in the study of penetration mechanics for flat plate penetrometers (such as the dilatometer, spade cells, field vane, etc.) to obtain the velocity field in step 2 of the strain path method:

1. Numerical methods that model the surface geometry of the penetrometer. For three dimensional penetrometer geometries, boundary element formulations such as the panel method are widely used by aeronautical engineers and hydrodynamicists. The first use of the panel method within the framework of the strain path method was proposed by Huang (1989) using the formulation of Hess and Smith (1962, 1964). In previous work, Williamson (1989) (Whittle et al., 1989) also implemented a potential based panel method to study the disturbance due to dilatometer installation. However, due to the complexities associated with modeling real surface geometries, it is difficult to gain insight about the basic penetration mechanics. Williamson (1989) (Whittle et al., 1989) used a potential based panel method to study the strain paths due to dialtometer penetration. These studies showed that results from panel method computations require very careful evaluation in order to establish their reliability and accuracy for a given surface discretization.

2. Simple solutions using fundamental analytical solutions. These analyses provide considerable insight into the basic mechanics of penetration but do not closely model the surface geometry of a particular penetrometer. In this chapter fundamental solutions are presented for a "simple plate" geometry in order to study the effects of plate aspect ratio on strains, effective stresses, and pore water pressures during installation.

3.3 THE SIMPLE PLATE

---

[2] Where, $E_1 = \varepsilon_{zz}$; $E_2 = (\varepsilon_{rr}-\varepsilon_{\theta\theta})/\sqrt{3}$; $E_3 = 2\varepsilon_{rz}/\sqrt{3}$. These measures are transformed deviatoric strains that were originally introduced by Levadoux and Baligh (1980) in order to gain physical insights into the mechanics of penetration.

Analytical solutions for the fields of velocity and strain rate due to steady penetration are established by considering the flow of soil elements around a stationary penetrometer using fundamental potential flow solutions (Tab. 3.1). This chapter introduces a 'simple plate' geometry which is characterized by the length of a finite line source, 2B, and its strength, Q' (rate of volume discharged per unit length), superimposed in a uniform flowfield (of velocity, u_z). For the particular case when B=>0, the simple plate reduces to a simple pile geometry (Baligh, 1985a), while for B=>∞, the simple wall is obtained. The following sections describe the mechanics of flat plate penetration based on the simple plate geometry.

3.3.1 Fundamental Solution for a Finite Line Source

A single point source, discharging volume at a rate, V (volume per unit time), produces a velocity that acts radially away from the source (Fig. 3.6). Assuming that the emitted fluid occupies a spherical cavity, the radius of the cavity, R(t), can be related to the rate of discharge by:

$$R(t) = \frac{3Vt}{4\pi} \tag{3.3a}$$

The radial location of a soil element, r(t), is then related to its initial location, ρ_0, by the incompressibility constraint:

$$\rho(t) = \left\{ \rho_0^3 + R^3(t) \right\}^{1/3} \tag{3.3b}$$

Hence, if the radius of the cavity is defined at time, t, all deformations and strains are fully determined. The velocity of soil elements due to a point source located at the origin of the reference coordinate frame can then be written:

$$v_\rho^0 = \frac{V}{4\pi\rho^2} \qquad \text{Spherical} \tag{3.4a}$$

$$v_r^0 = \frac{V\sin\phi}{4\pi\rho^2} \; ; \; v_z^0 = \frac{V\cos\phi}{4\pi\rho^2} \qquad \text{Cylindrical} \tag{3.4b}$$

$$v_x^0 = v_r\cos\theta \; ; \; v_y^0 = v_r^0\sin\theta \qquad \text{Cartesian} \tag{3.4c}$$

where, $\rho = \left(x^2 + y^2 + z^2\right)^{1/2}$, $r = \left(x^2 + y^2\right)^{1/2}$, $\phi = \tan^{-1}\frac{r}{z}$ and $\theta = \tan^{-1}\frac{y}{x}$.

If the cartesian frame is translated (Fig. 3.6b) such that x'=x, y'=y+ξ, z'=z, then the

velocity components (x',y',z') due to a source at y'=ξ are given by:

$$v_{x'}^0 = \frac{V \sin \phi \cos \theta}{4\pi\rho^2}$$

$$v_{y'}^0 = \frac{V \sin \phi \sin \theta}{4\pi\rho^2}$$ (3.4d)

$$v_{z'}^0 = \frac{V \cos \phi}{4\pi\rho^2}$$

where, y = y'-ξ.

If the point source is then treated as a line source of elemental length, dξ; then, V = Q'dξ, where Q' is the source strength per unit length. Hence the velocity components for a line source of finite length (ξ₁ ≤ ξ ≤ ξ₂) can be obtained by direct integration:

$$v_{i'} = \int_{\xi_2}^{\xi_1} v_i^0(\xi) d\xi$$ (3.5)

where v_i^0 are the velocity components given by equation 3.4d.

For the particular case of a semi-infinite line source (0 ≤ ξ ≤ ∞) (Fig. 3.6c), the velocity components are given by:

$$v_{x'} = \frac{Q' \cos \theta'}{4 \pi r'} \left(1 + \frac{y'}{\rho'}\right)$$

$$v_{y'} = \frac{Q'}{4 \pi \rho'}$$ (3.6)

$$v_{z'} = \frac{Q' \sin \theta'}{4 \pi r'} \left(1 + \frac{y'}{\rho'}\right)$$

where, $r' = (x'^2 + z'^2)^{1/2}$, $\rho' = (x'^2 + y'^2 + z'^2)^{1/2}$, and $\theta' = \tan^{-1}\frac{z'}{x'}$

When the sign of the strength (Q') is negative, the results (eqn. 3.6) describe the flow field for a semi-infinite sink. Hence, the solution for a line source of finite length can be obtained by superposition using the fundamental solutions for a semi-infinite source.

The strain rate components of the flow field described by eqn. 3.6 are obtained by differentiating the velocities with respect to the spatial coordinates (see eqn 3.1). This leads to the following expressions for the strain rates of a semi infinite line source:

$$\dot{\varepsilon}_{x'x'} = \frac{Q'}{4\pi} \left\{ \frac{1}{r'^2}\left(1 + \frac{y'}{\rho'}\right) - \frac{2x'^2}{r'^4}\left(1 + \frac{y'}{\rho'}\right) - \frac{x'^2 y'}{r'^2 \rho'^3} \right\}$$

$$\dot{\varepsilon}_{y'y'} = -\frac{Q' y'}{4\pi \rho'^3}$$

$$\dot{\varepsilon}_{z'z'} = \frac{Q'}{4\pi} \left\{ \frac{1}{r'^2}\left(1 + \frac{y'}{\rho'}\right) - \frac{2z'^2}{r'^4}\left(1 + \frac{y'}{\rho'}\right) - \frac{z'^2 y'}{r'^2 \rho'^3} \right\} \qquad (3.7)$$

$$\dot{\varepsilon}_{x'y'} = -\frac{Q' x'}{4\pi \rho'^3}$$

$$\dot{\varepsilon}_{y'z'} = -\frac{Q' z'}{4\pi \rho'^3}$$

$$\dot{\varepsilon}_{x'z'} = -\frac{Q'}{4\pi} \left\{ \frac{2x'z'}{r'^4}\left(1 + \frac{y'}{\rho'}\right) - \frac{x'y'z'}{r'^2 \rho'^3} \right\}$$

The 'simple plate' geometry is then obtained by superimposing a uniform flow of velocity, u_z, with the semi-infinite line source result. For example, the velocity field around a line source of finite length 2B can be written:

$$v_x = v_x (+Q'; 0, -B, 0) + v_x (-Q'; 0, +B, 0)$$
$$v_y = v_y (+Q'; 0, -B, 0) + v_y (-Q'; 0, +B, 0) \qquad (3.8)$$
$$v_z = u_z + v_z (+Q'; 0, -B, 0) + v_z (-Q'; 0, +B, 0)$$

where, $v_i (Q'; x,y,z)$ describes the velocity component (v_x, v_y, or v_z) due to a semi-infinite source of strength Q' that originates at (x, y, z) and extends to (x, ∞, z). The uniform flow velocity (u_z) is equivalent to the rate of penetration of the penetrometer. Applying eqn. 3.8 to eqn. 3.6 yields the following velocity field for a 'simple plate':

$$v_x = \frac{Q' \cos\theta}{4\pi r} \left\{ \frac{\rho_1(y-B) - \rho_2(y+B)}{\rho_1 \rho_2} \right\}$$

$$v_y = \frac{Q'}{4\pi} \left\{ \frac{\rho_1 - \rho_2}{\rho_1 \rho_2} \right\} \qquad (3.9)$$

$$v_z = u_z + \frac{Q' \sin\theta}{4\pi r} \left\{ \frac{\rho_1(y-B) - \rho_2(y+B)}{\rho_1 \rho_2} \right\}$$

where, $\rho_1 = \left\{ x^2 + (y+B)^2 + z^2 \right\}^{1/2}$, and $\rho_2 = \left\{ x^2 + (y-B)^2 + z^2 \right\}^{1/2}$

Using similar superposition arguments, the strain rates for a 'simple plate' of length 2B are given by:

$$\dot{\varepsilon}_{xx} = \frac{Q'}{4\pi}\left[\left(\frac{\rho_1(y\text{-}B) - \rho_2(y\text{+}B)}{\rho_1\rho_2}\right)\left(\frac{1}{r^2} - \frac{2x^2}{r^4}\right) - \frac{x^2}{r^2}\left(\frac{\rho_1^3(y\text{-}B) - \rho_2^3(y\text{+}B)}{\rho_1^3\rho_2^3}\right)\right]$$

$$\dot{\varepsilon}_{yy} = -\frac{Q'}{4\pi}\left(\frac{\rho_1^3(y\text{-}B) - \rho_2^3(y\text{+}B)}{\rho_1^3\rho_2^3}\right)$$

$$\dot{\varepsilon}_{zz} = \frac{Q'}{4\pi}\left[\left(\frac{\rho_1(y\text{-}B) - \rho_2(y\text{+}B)}{\rho_1\rho_2}\right)\left(\frac{1}{r^2} - \frac{2z^2}{r^4}\right) - \frac{z^2}{r^2}\left(\frac{\rho_1^3(y\text{-}B) - \rho_2^3(y\text{+}B)}{\rho_1^3\rho_2^3}\right)\right]$$

$$\dot{\varepsilon}_{xy} = -\frac{Q'x}{4\pi}\left(\frac{\rho_1^3 - \rho_2^3}{\rho_1^3\rho_2^3}\right) \tag{3.10}$$

$$\dot{\varepsilon}_{yz} = -\frac{Q'z}{4\pi}\left(\frac{\rho_1^3 - \rho_2^3}{\rho_1^3\rho_2^3}\right)$$

$$\dot{\varepsilon}_{zx} = -\frac{Q'}{4\pi}\left[\left(\frac{\rho_1(y\text{-}B) - \rho_2(y\text{+}B)}{\rho_1\rho_2}\right)\left(\frac{2xz}{r^4}\right) - \frac{xz}{r^2}\left(\frac{\rho_1^3(y\text{-}B) - \rho_2^3(y\text{+}B)}{\rho_1^3\rho_2^3}\right)\right]$$

Due to the condition of incompressibility, $(\dot{\varepsilon}_{xx} + \dot{\varepsilon}_{yy} + \dot{\varepsilon}_{zz} = 0)$, there are only five independent shear strain rate components. These are conveniently expressed by transformed measures of deviatoric strain rates :

$$\dot{E}_1 = \dot{\varepsilon}_{zz} \;;\; \dot{E}_2 = \frac{1}{\sqrt{3}}(\dot{\varepsilon}_{xx} - \dot{\varepsilon}_{yy})$$
$$\dot{E}_3 = \frac{2}{\sqrt{3}}\dot{\varepsilon}_{xy} \;;\; \dot{E}_4 = \frac{2}{\sqrt{3}}\dot{\varepsilon}_{yz} \;;\; \dot{E}_{zx} = \frac{2}{\sqrt{3}}\dot{\varepsilon}_{zx} \tag{3.11}$$

These measures are introduced to enable comparisons with axisymmetric penetrometers. The overall magnitude of shear strain in the soil is described by the second invariant of the deviatoric strain rates, $\dot{E}$:

$$\dot{E} = \frac{1}{\sqrt{2}}\sqrt{\dot{E}_1^2 + \dot{E}_2^2 + \dot{E}_3^2 + \dot{E}_4^2 + \dot{E}_5^2} \tag{3.12}$$

Using the fundamental solutions for velocity and strain rate components, the framework of the strain path method can then be invoked to determine the strain paths of soil elements due to steady penetration.

3.3.2 Simple Plate Geometry

The maximum thickness of the simple plate, 2w, for a given length, 2B, is controlled

by the magnitude of the source strength Q' relative to the velocity of penetration, u_z. In order to enable comparisons of simple plate solutions with those of the simple pile, the source strength is selected so that all dimensions of the problem can be normalized by the half thickness of the plate (w). Hence the geometry of the a simple plate can be fully described by the aspect ratio, B/w. Figure 3.7 is a dimensionless plot that shows the relationship between source strength (Q') and plate aspect ratio (B/w).

Surface geometries of the simple plate are shown for three different aspect ratios in figures 3.8a-c. An aspect ratio, B/w= 6.8 was selected because of its similarity to a standard Marchetti dilatometer (Marchetti, 1980; chapter 5), while the plate with B/w=32.5 closely resembles the standard dimensions of one blade of a field vane (Chandler, 1988).

Figures 3.8a-c show three sections through each simple plate a) the longitudinal section (x=0 plane), b) the central or lateral section (y=0 plane), and c) a horizontal section far above the tip of the plates, which is subsequently referred to as the 'steady state' plane[1] (in this case z/w=200). The location of the line source is included to illustrate its relationship with the geometry of the solid body. The following aspects of the simple plate geometry should be noted:

1. The simple plate is symmetric about the x=0 and y=0 planes. Its surface exhibits a slight curvature in all directions. Soil elements that are initially located in the y=0 plane remain in that plane during shearing. Hence, these elements experience no out of plane straining and their strain histories can be described by a reduced set of 3 shear strains.

2. All of the plates exhibit actual aspect ratios (L/w) greater than the aspect ratio of the line source used to generate the plate, B/w. The ratio L/B varies as a function of B, as shown in figures 3.8a-c.

It is important to emphasize that the 'simple plate' geometry is introduced in order to elucidate basic disturbance mechanisms during flat blade penetration, but does not exactly model the physical geometry of an earth pressure cell or dilatometer.

3.3.3 Shear Strains around Simple Plate

Figures 3.8a-c also show contours of octahedral shear strain, E= 1, 5, 10 and 20% in the three cross sections of the simple plates. In the central (y=0) plane of the simple plates it can be seen that, for all of the plates, soil elements initially located at lateral distances $x_o/w < 3$ experience strain levels that are larger than those imposed in conventional

---

[1]The steady state plane is defined by the assymptotic condition that there are no further changes in the field variables (deformations, strains and stresses) with vertical elevation. The results in figure 3.8 are shown at a nominal steady state condition, z/w≈200.

laboratory tests (E ≈ 10%).

Previous results for the simple pile showed that all soil elements experienced monotonic increases in the level of octahedral shear strain, E, during steady penetration, and that contours of E were parallel to the shaft of the penetrometer (e.g. Fig. 7 of Baligh, 1985b). In contrast, for the simple plates, figure 3.9 shows that in the central (y=0) plane there is a locus of maximum lateral extent for a given strain level. Hence, it can be seen that for soil elements initially located at $x_0/w < 10$, the octahedral shear strain level decreases when the element reaches this locus.

Figures 3.9 and 3.10 show the variation of the octahedral shear strain (E) with lateral distance (in the x and y directions) in the steady state (horizontal) plane[2]. In figure 3.9, the lateral dimensions are normalized with respect to the half-thickness of the plate. The results show the following:

1. For soil elements located close to the plate interface, the simple plates with aspect ratios, $6.8 \leq B/w \leq 32.5$ all exhibit similar magnitudes of octahedral shear strain and strain levels that are less than those for the simple pile at a given lateral distance.

2. Further away from the plates the shear strain increases with B/w for a given lateral distance, indicating a greater zone of disturbance.

Figure 3.10 shows the same results for E plotted against lateral distance normalized to the equivalent radius, R_{eq}, of the plate, where:

$$R_{eq} = \sqrt{\frac{4Bw}{\pi}}$$ (3.13)

i.e. R_{eq} is the equivalent radius of an axisymmetric simple pile that has the same cross-sectional area as the simple plate. Thus, the results in figure 3.10 compare the strain field for penetrometers with similar cross-sectional areas. The figure shows the following:

1. At lateral locations far from the penetrometer ($x/R_{eq} > 10\text{-}20$; $(y\text{-}B)/R_{eq} > 30\text{-}40$), the effects of penetrometer shape (B/w) are insignificant.

2. For soil elements close to the penetrometer, the disturbance (magnitude of E) at a given lateral location decreases as the aspect ratio increases.

3.3.4 Deformation and Strain Paths During Plate Installation

Figure 3.11 shows the deformation paths for soil elements initially located in the y=0

---

[2] The distance necessary to achieve this " steady state " condition increases as the aspect ratio, B/w, increases. For B/w = 6.8, z/w =200 was sufficient, while for B/w = 20, 32.5, the z/w = 2000 plane was used to ensure steady state conditions.

plane at lateral locations, $x_0/w = 1, 2, 3, 4$, and 5 for the simple plates ($B/w=6.8, 20$ and 32.5) and simple pile geometries. It can be seen that the soil elements are displaced vertically downwards and then laterally outwards to accomodate the volume occupied by the penetrometer. As the plate aspect ratio increases, the amount of total vertical and radial movement for a given soil element (i.e. at fixed x_0/w) also increases and reflects the different volumes of soil displaced by the different geometries. In figure 3.12, the deformation paths are plotted for the same geometries for radial locations, $x_0/R_{eq} = 1, 2, 3$, 4 and 5. In this case, it can be seen that, for plates of equal displaced volume, soil disturbance reduces with increased aspect ratio.

The total amount of vertical deformation experienced by soil elements due to penetrometer installation is one measure of disturbance which has been measured in laboratory (e.g. Rourk, 1961) and field tests (e.g. Karlsrud & Haugen, 1985). In the context of the strain path method, total vertical soil deformation, or retardation, is calculated by comparing the elevations of two soil elements initially located in the same horizontal plane[3]:

$$\text{Retardation} = \Delta z = (z - z^{\infty}) \tag{3.14}$$

where z is the vertical coordinate at a lateral distance (x, y) from the center of the penetrometer and z^{∞} is the vertical coordinate of a soil element far from the penetrometer (x_{∞}, y_{∞}).

Figure 3.11 shows retardation curves for soil elements located in the $y=0$ plane at steady state conditions for the three simple plates and simple pile geometries. The retardation curves (final elevations in Fig. 3.11) are very similar for the higher aspect ratio plates ($B/w = 20, 32.5$), but differ in form from the $B/w = 6.8$ plate and simple pile curves. This suggests that for long, thin penetrometers the plate thickness (w) controls the form of the retardations. However, as the plate aspect ratio decreases (say $B/w \leq 6.8$) other factors such as plate width B exert some influence over the retardations.

The strain paths of soil elements in the central plane ($y=0$) are shown in figures 3.13a, b and c for various initial locations, x_0/w . The strain history of these elements is fully described by the following transformed measures of strain [4]:

---

[3] Isochronic lines are curves showing the location of soil elements relative to the indenter at a particular time step.

[4] Note that in the central plane $\varepsilon_{xy} = \varepsilon_{yz} = 0$.

$$E_1 = \varepsilon_{zz} \quad ; \quad E_2 = \frac{1}{\sqrt{3}}(\varepsilon_{xx} - \varepsilon_{yy}) \quad ; \quad E_{zx} = \frac{2}{\sqrt{3}}\varepsilon_{zx} \qquad (3.15)$$

For all three of the plates considered, soil elements initially located at lateral distances far away from the plate surface experience strain paths that are qualitatively similar to those of the simple pile (Fig. 3.5):

1. Ahead of the penetrometer, straining is primarily in the E_1 direction (vertical compression). As the element moves past the tip of the penetrometer, this component reverses in sign (vertical extension). The E_5 component (shear strain on the vertical plane) increases to a maximum close to the level of the penetrometer tip and then reverses direction. The E_2 component increases monotonically throughout the strain path and controls the magnitude of the shear strains behind the plate tip (where $E_5 => 0$ and $E_2 => 0$).

2. For a given x_0/w, soil elements close to the plate experience an increasing amount of negative E_2 straining as the B/w ratio increases. In fact, Whittle et al. (1989) show that for a plate with B/w = 10 and $x_0/w \leq 1$ the E_2 component remains negative during an element's entire strain path. This behavior is associated with a condition in which both the length, 2B, and width, 2w, affect the strain history of soil elements. Very similar results were reported previously for open-ended pile penetration (Chin, 1986).

For initial soil element locations that are not in the central plane the strain paths become very complex, and involve all five strain components. Figures 3.14a, b,c, and d show one example of strain paths for a simple plate with B/w = 6.8 and soil elements initially located at y_0/w = 6.8 and x_0/w =0.5, 1, 3, 5. The soil elements have three degrees of freedom (i.e., 3 components of displacement). It can be seen that, for the element furthest from the penetrometer (x_0/w = 10), the strain path is qualitatively similar to that described for the y = 0 plane (Fig. 3.13a) but includes additional shear components E_3 and E_4. For the element closest to the plate (x_0/w = 0.5) the behavior is strongly influenced by the displacement out of the y/w = 6.8 plane. This causes a reversal in the sign of the E_2, E_3 and E_5 strain components. For intermediate soil elements, the strain paths reflect directly the distortion of the soil around the edge of the plate.

3.4 INSTALLATION EFFECTIVE STRESSES AND PORE PRESSURES

In the strain path method, fields of effective stresses are determined from the strain paths of soil elements around the penetrometer using a generalized effective stress soil model. Excess pore pressures are then estimated from equilibrium considerations by finite

element solution of the Poisson equation using the methods presented in chapter 2.

Of particular interest in this section is the effect of plate aspect ratio (B/w) on the resulting stress and pore pressure solution. The analysis in this section is confined to a steady state plane where stresses and pore pressures no longer change in the vertical direction.

3.4.1 Effective Stresses

In order to establish a base case for determining the effect of aspect ratio on plate installation, effective stresses are computed using the Modified Cam Clay Model (MCC; Roscoe & Burland, 1968). The input parameters selected for this model are those for K_0-normally consolidated Boston Blue Clay (BBC) (K_0=0.48; Whittle, 1987). This base case analysis was selected for the following reasons:

1. The MCC model is relatively easy to conceptualize, making interpretation of its predictions straightforward.

2. Predictions of the model (with the same input parameters for BBC) have been extensively studied in conjunction with previous penetration studies (piles; Whittle, 1987; open-ended penetrometers; Chin, 1986). Full details and evaluation of MCC predictions for BBC are presented by Whittle (1987).

3. The model is an effective stress model, allowing results to be used directly in consolidation studies and/or subsequent test procedures involving soil drainage.

4. Boston Blue Clay is a low plasticity ($I_p \approx 21\%$) marine clay of moderate sensitivity ($s_t \approx 3$ to 7) which has been extensively studied at MIT over a period of 30 years. Input parameters to describe the clay are based on high quality laboratory test data for resedimented clay (Whittle, 1987).

Figures 3.15a, b and c show the in plane effective stresses (σ'_{xx}, σ'_{yy}, σ'_{xy}) normalized to the initial effective vertical stress (σ'_{v0}) for the axisymmetric simple pile and three plates. The pile and plate geometries are also shown on each figure for reference. Based on the plate installation results reported in previous sections, the spatial coordinates are normalized by the equivalent radius of the penetrometer ($R_{eq} = (4Bt/\pi)^{0.5}$). This provides a valuable normalization that reveals similar behavior for all plates in the far field (i.e. for $x/R_{eq} >> 1$; $y/R_{eq} >> 1$, the strain history of soil elements are independent of the plate geometry). The figures show the following:

1. In the far field, the normal stresses σ'_{xx}, σ'_{yy} approach the K_0 condition of $\sigma'_{xx}/\sigma'_{v0} = \sigma'_{yy}/\sigma'_{v0} = 0.48$.

2. For all plate aspect ratios ($1 \leq B/w \leq 32.5$) the normal effective stresses ($\sigma'_{xx}/\sigma'_{v0}$,

$\sigma'_{yy}/\sigma'_{v0}$) do not vary significantly in magnitude or direction for locations along the flat surface of the plate.

3. The effect of plate shape can be seen clearly by the increased elongation of the stress contours in the region $x/R_{eq} < 3$; $y/R_{eq} < 5$ as the aspect ratio (B/w) increases.

4. The magnitude of the peak in-plane shear stress σ'_{xy} shows no dependence on the plate's aspect ratio. However, σ'_{xy} is symmetric about the x=y plane for the simple pile, and increasingly deviates from that condition as the aspect ratio increases.

Figure 3.16 shows contours of the maximum shear stress, q_h/σ'_{v0}[5] in the horizontal (x,y) plane for these same geometries. For axisymmetric penetrometers, such as the simple pile, previous studies have shown that the peak value of q_h/σ'_{v0} occurs at $r/R_{eq} \approx 6.5$ (Whittle, 1987; Baligh, 1986a). Closer to the penetrometer the strain path method predicts reductions in q_h/σ'_{v0} due to rotations of principal stresses. With respect to the plates, figure 3.16 shows the following:

1. For all of the geometries considered, the maximum shear stress, $q_h/\sigma'_{v0} \approx 0.3$ occurs at a lateral distance x/R_{eq}=3-5 (along y=0).

2. In the near field, the shear stress reaches a local minimum on the central plane (y=0) at $x/R_{eq} \approx 1$-2 for the two thinnest plates (B/w = 20, 32.5). This trend is not noted with either the B/w=6.8 plate, or the simple pile.

3.4.2 Excess Pore Pressures

The excess pore pressures ($\Delta u = (u-u_0)/\sigma'_{v0}$) arise due to changes in a) changes in mean octahedral total stress ($\Delta\sigma$), and b) shear induced pore pressure (Δu_s), so that:

$$\Delta u = \Delta\sigma + \Delta u_s \qquad (3.16)$$

The shear induced pore pressure is solely determined by the constitutive model, and is not a function of the method of equilibrium solution[6], while changes in mean stress are dominated by equilibrium considerations. Contours of shear induced pore pressure for the base case analysis are shown in figure 3.17. It is clear from the figure that the magnitude of $\Delta u_s/\sigma'_{v0}$ does not change with plate aspect ratio, and for all cases, $\Delta u_s/\sigma'_{v0} \approx 0.16$ close

---

[5] $q_h = \frac{1}{2}\sqrt{(\sigma'_{xx} - \sigma'_{yy})^2 + 4\sigma'^2_{xy}}$

[6] In the MCC model, the shear induced pore pressures are related to changes in mean effective stress according to: $\Delta u_s = -\Delta\sigma'_{oct}$

to the shaft of the penetrometer. The shape of the $\Delta u_s/\sigma'_{v0}$ contours do become increasingly elliptical as the plate aspect ratio increases. The total excess pore pressure solutions for the simple pile and three plates are shown in figure 3.18:

1. The excess pore water pressure at the plate boundary is not affected significantly by the aspect ratio of the plate ($\Delta u_s/\sigma'_{v0}$=1.0-1.2, at y=0).

2. There is an appreciable difference in the distribution of excess pore pressures due to aspect ratio. As B/w increases, a region of small negative pore pressures develops in a zone well beyond the edge of the plate.

3. For the 'base case' analysis, the shear induced pore pressures (figure 3.17) represent a relatively small fraction (10-20%) of the total excess pore pressure.

3.4.3 Distributions Along Blade

Based on the above analyses, the distributions of pore pressure, normal effective stress (σ'_n), and normal total stress (σ_n-u_0) along the three plate blades can be summarized for the base case analysis. Figure 3.19 illustrates these distributions for the three plate aspect ratios (B/w = 6.8, 20, 32.5). The figure also tabulates values at two key locations on the plate: a) on the plate center, where measurements (u, σ_n) are typically made, and b) at the plate edge, where results are most strongly affected by the plate aspect ratio. The following comments can also be made regarding the figure:

1. The form of the distributions are similar for all three plates: Over the central section of the plate, the pore pressures and stresses do not deviate significantly from the centerline values. Near the plate tips, the pore pressures decrease by approximately 20% (independent of aspect ratio) while the normal effective stresses increase slightly. This has an interesting effect on the distribution of total normal stress which exhibits a minimum value close to the edge of the plates.

2. As the aspect ratio increases, the magnitudes of the pore pressure and normal stresses decrease slightly at the plate center. For example, the excess pore pressure varies from $(u-u_0)/\sigma'_{v0} \approx 1.1$ for B/w = 6.8 to 1.02 for B/w = 32.5 (a 10% variation).

Normalization of the pore pressures and stresses by the centerline values (location 1), and normalization of the plate coordinate by the plate width B gives some insight into the variables that control the stress and pore pressure distributions along the blade. Figure 3.20 shows that over the central half of the plate (y/B ≤ 0.5) the pore pressure and total normal stress distributions fall in a narrow band. Thus for a given centerline value of stress or pore pressure, the plate width (B) is the controlling variable over the central region.

Overall, these results show that plate shape (aspect ratio, B/w) has a relatively minor influence on the stresses measured on the surface of the blade. This result is, of course, subject to the limitations of the analysis (i.e., steady state conditions, MCC model for K_0-normally consolidated BBC). However, the implication of these results is that measurements/predictions of installation pore water pressure and total normal stress (i.e., dilatometer P_0) acting on the blade of flat penetrometers will not be significantly different from those measured/predicted for an axisymmetric penetrometer, such as the piezocone. This establishes for the first time the commonality of installation disturbance between flat blade and axisymmetric penetrometers.

3.4.4 Effect of Soil Model on Predictions

In order to show some of the possible limitations of the MCC base case analysis, a more complex effective stress model, MIT-E3 (Whittle, 1987) was used to generate effective stress and pore pressure results for the B/w = 6.8 plate. This model extends the basic concepts of the MCC model by incorporating: a) anisotropic stress-strain-strength behavior; b) small strain non-linearity; and c) strain softening. Input parameters for the model have previously been selected to describe K_0-consolidated BBC and detailed evaluations have demonstrated the predictive capabilities and limitations of the model (Whittle, 1987). Whittle and Baligh (1990) have shown that MIT-E3 is capable of making reliable predictions of effective stresses acting on a model pile shaft in BBC.

Figures 3.21 a, b, and c show the in-plane effective stresses predicted by MIT-E3. Comparison with figures 3.15 (a - c) shows that the MIT-E3 model predicts much lower (up to 50%) effective stresses than the MCC model. The MIT-E3 model also shows that the region of soil influenced by the installation, as shown by the region where stresses deviate from the K_0 condition, is larger than the region predicted by MCC.

Shear induced pore pressure ($\Delta u_s/\sigma'_{v0}$), peak in plane shear stress (q_h/σ'_{v0}) and total excess pore pressure, $(u-u_0)/\sigma'_{v0}$, predictions using the MIT-E3 model are shown in figure 3.22:

1. The shear induced pore pressures are substantially higher than the MCC predictions (Fig. 3.17), and extend over a much larger range: The MIT-E3 model predicts $\Delta u_s/\sigma'_{v0} \approx 0.5$ along the plate blade (compared to $\Delta u_s/\sigma'_{v0}=0.16$ obtained using MCC). These differences can be attributed, in large part, to strain softening behavior described by MIT-E3 in undrained shear.

2. The peak in-plane shear stress contours are slightly smaller for MIT-E3 than for MCC ($q_h/\sigma'_{v0} \approx 0.2$ compared to 0.3 for MCC; c.f. Fig. 3.16).

3. The predicted magnitude of the total pore pressure along the plate blade is similar for both models (c.f. Fig. 3.18). However, the distribution of pore pressure throughout the soil is markedly different, with MIT-E3 model predicting a much greater lateral extent of excess pore pressures around the plate[3]. It is also important to note that shear induced pore pressures account for approximately 50% of the excess pore pressures acting at the plate boundary for the MIT-E3 predictions.

3.5 UNCOUPLED DISSIPATION OF EXCESS PORE PRESSURES

Baligh and Levadoux (1980, 1986) have shown that the dissipation of excess pore pressures around cone penetrometers can be well estimated from linear-uncoupled consolidation analyses[4] in which the diffusion rate is controlled by the horizontal coefficient of consolidation, c_h, of the clay. Previous analyses (e.g. Baligh & Levadoux, 1980) have shown that the dissipation of excess pore pressures (for a given c_h) depends primarily on the initial distribution of excess pore pressures around the penetrometer, and is not related to the magnitude of the pore pressures acting at the surface of the penetrometer. In this section, linear uncoupled consolidation analyses are presented for the simple plate geometries in order to establish the effects of plate aspect ratio (B/w) on the consolidation behavior after penetrometer installation.

The linear uncoupled diffusion equation is solved in the steady state horizontal plane using the finite element program ADINAT:

$$c_h \nabla^2 u = c_h \left(\frac{\partial^2 u}{\partial x^2} + \frac{\partial^2 u}{\partial y^2} \right) = \frac{\partial u}{\partial t} \tag{3.17}$$

where the soil is assumed isotropic and homogeneous.

In order to unify the interpretation of the results for plates with different aspect ratios and for different values of c_h[5], a dimensionless time factor, T, is introduced:

$$T = \frac{c_h\, t^2}{R_{eq}^2} \tag{3.18}$$

---

[3]It is important to note that it is the distribution of pore pressure, and not the shaft pore pressure, that controls rates of pore pressure dissipation (consolidation).

[4]Kavvadas (1982) and Whittle (1987) show that modeling of soil non-linearities is essential in predicting changes in effective stresses around pile shafts. Hence non-linear, coupled consolidation analyses are required in order to estimate reliably the changes in effective stresses in the soil.

[5]The value of c_h actually depends on the soil stiffness and permeability.

where R_{eq} is the equivalent radius (eqn. 3.13) and t is the time.

Solutions of the linear-uncoupled consolidation have been obtained using the initial conditions from the base case analysis (i.e. inital excess pore pressures are obtained using the MCC model with input parameters corresponding to K_0-normally consolidated BBC; Fig. 3.18). Figures 3.23 and 3.24 show the dissipation of excess pore pressures predicted at a) the edge (locations B, C, D; Fig. 3.23), and b) the center (E; Fig. 3.24) of the three simple plate geometries (B/w=6.8, 20 and 32.5):

1. For all three plate geometries, the excess pore pressures decrease monotonically at all points around the surface of the plates.

2. Disspation occurs more rapidly at the edges of the plates (B, C, D; Fig. 3.23) than for locations at the center (E; Fig. 3.24). However, for time factors, T>1 the differences in the magnitude of excess pore pressures between the edge and center of the plate become very small.

Figure 3.25 compares the predictions of the excess pore pressure ratio, $(u-u_0)/(u_i-u_0)$ at the center of simple plates (E; Fig. 3.24), with solutions for the simple pile. The figure show that the excess pore pressure ratio is effectively independent of the shape of the plates (for B/w≤32.5) using the time factor, T (eqn. 3.18). Thus these preliminary results imply that the dissipation of excess pore pressures is controlled by the volume of soil displaced by the penetrometer (R_{eq}) and by the coefficient of consolidation, c_h. Hence, dissipation of excess pore pressures can be estimated from existing solutions for axisymmetric penetrometers. Further research is now in progress to establish the generality of these results.

Singularity	Location of Singularity	Velocity Components	Geometry & Application
Point Source	$x=0$; $y=0$; $z=0$	$v_\rho = \frac{V}{4\pi}\frac{1}{\rho^2}$ (spherical) $v_r = \frac{V}{4\pi}\frac{\sin\phi}{\rho^2}$ (cylindrical) $v_z = \frac{V}{4\pi}\frac{\cos\phi}{\rho^2}$ (cylindrical) where $\rho=(r^2+z^2)^{1/2}$ and $\phi=\tan^{-1}(r/z)$	• Spherical cavity expansion (Vesić, 1972) • with uniform flow: Simple Pile (Baligh, 1985)
Line Source	$x=0$; $-\infty \le y \le \infty$; $z=0$	$v_x = \frac{Q}{2\pi\rho}\sin\phi$ (cartesian) $v_z = \frac{V}{2\pi\rho}\cos\phi$ (cartesian) where $\rho=(x^2+z^2)^{1/2}$ and $\phi=\tan^{-1}(x/z)$	• Cylindrical cavity expansion • with uniform flow: Simple Wall (Chin, 1986)
Ring Source	$r=R$; $z=0$	$v_r = \frac{V}{4\pi^2}\frac{1}{r\sqrt{z^2+(r+R)^2}}\left\{K(k)-\left[1-\frac{2r(r-R)}{z^2+(r-R)^2}\right]E(k)\right\}$ (cylindrical) $v_z = \frac{V}{4\pi^2}\frac{2z}{\sqrt{z^2+(r+R)^2}}\frac{E(k)}{[z^2+(r-R)^2]}$ (cylindrical) where $k=\frac{4rR}{z^2+(r+R)^2}$ and $K(k)$, $E(k)$ are complete elliptic integrals of the first and second kind	• with uniform flow: Simple open ended pile (Chin, 1986); Ideal Sampler (Baligh et al., 1987)
Semi-infinite Source	$x=0$; $0 \le y \le \infty$; $z=0$	$v_x = \frac{Q}{4\pi}\frac{\sin\theta}{r}\left(1+\frac{y}{\rho}\right)$ (cartesian) $v_y = -\frac{Q}{4\pi}\frac{1}{\rho}$ (cartesian) $v_x = -\frac{Q}{4\pi}\frac{\cos\theta}{r}\left(1+\frac{y}{\rho}\right)$ (cartesian) where $r=(x^2+z^2)^{1/2}$, $\rho=(x^2+y^2+z^2)^{1/2}$ and $\phi=\tan^{-1}(z/x)$	• Superposition; simple wall field vane etc. (this report)

Table 3.1. Analytic solutions for various penetrometer geometries in the Strain Path Method.

No.	Device	B (mm)	w (mm)	Aspect ratio, B/w
A	Dilatometer (Marchetti, 1980)	47.5	7.0	6.8
B	Earth Pressure Cell (Germaine, 1980)	57.3	4.5	12.7
C	Earth Pressure Cell (Tavenas et al., 1975)	150.0	6.0	25.0
D	Field Vane (ASTM, 1972)	32.5	1.0	32.5
E	Iowa stepped blade (Handy et al., 1982)	25.5	$w_1 = 1.5$ $w_2 = 2.25$ $w_3 = 3.0$ $w_4 = 3.75$	$B/w_1 = 17.0$ $B/w_2 = 11.3$ $B/w_3 = 8.5$ $B/w_4 = 6.8$
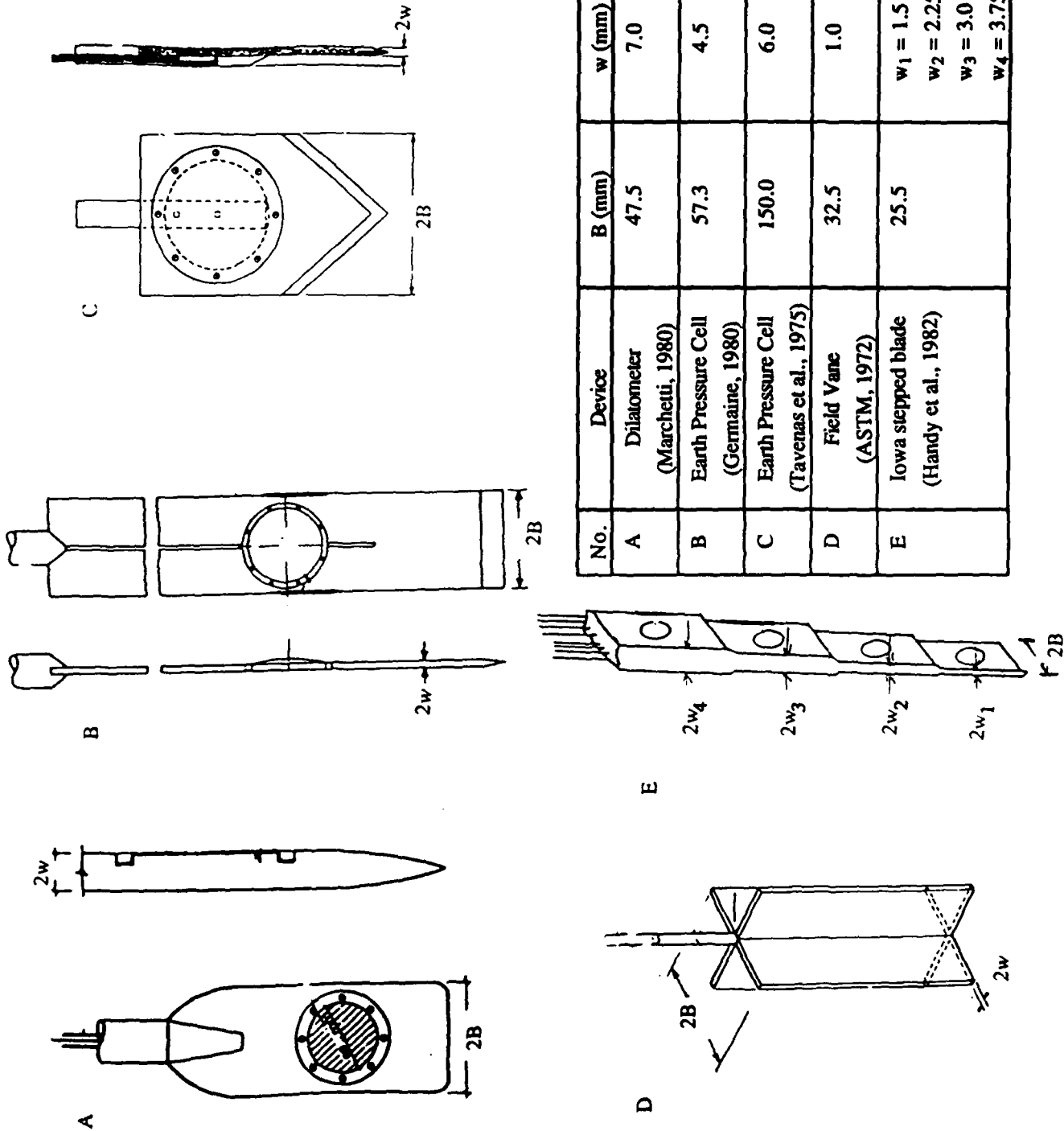
Figure 3.1. Examples of in-situ plate penetration devices
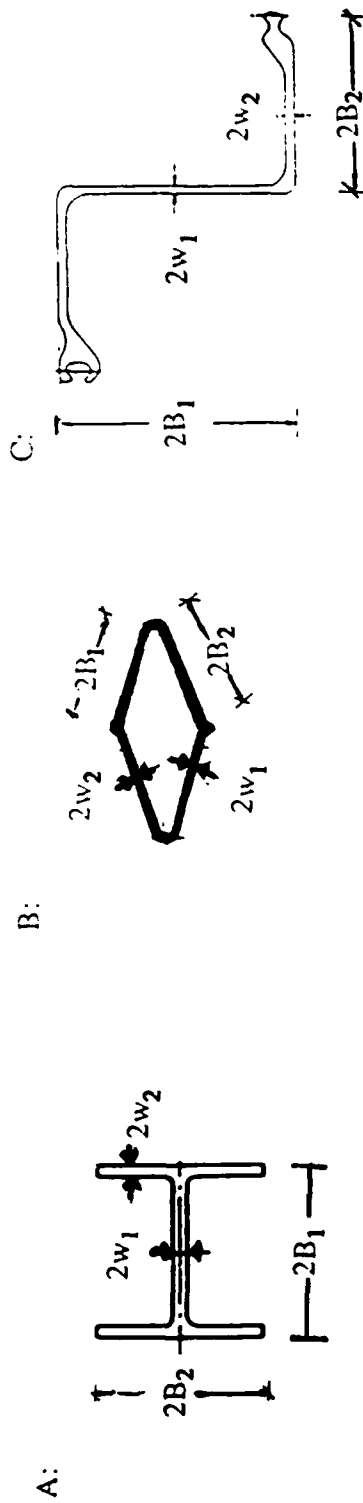
No.	Device	B_1 (in)	B_2 (in)	w_1 (in)	w_2 (in)	B_1/w_1	B_2/w_2
A	H - Pile	4.0 - 7.5	4.0 - 7.5	0.2 - 0.4	0.2 - 0.4	9.0 - 20.0	9.0 - 20.0
B	open ended Mandrel	varies	varies	varies	varies	varies	varies
C	Sheet Pile	6.0	0.375	4.5	0.5	16.0	9.0

Figure 3.2. Other plate penetration devices used in geotechnical practice
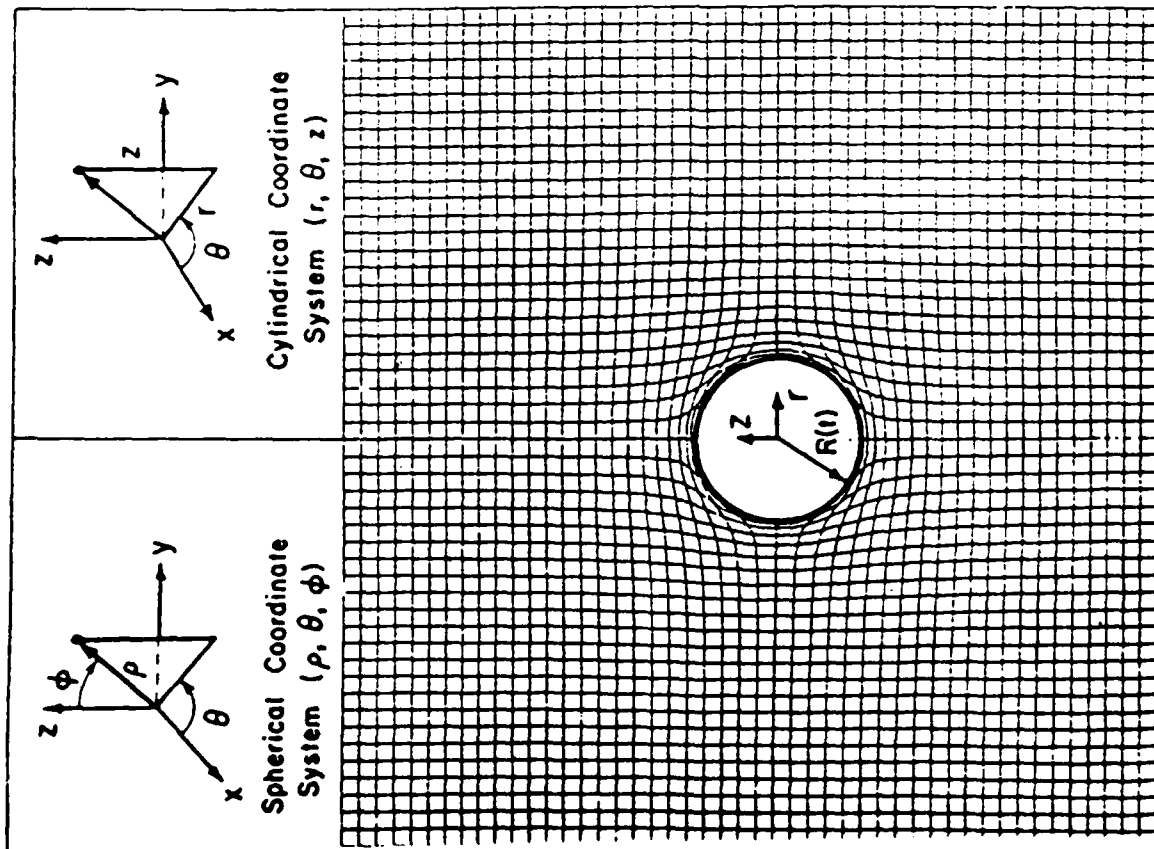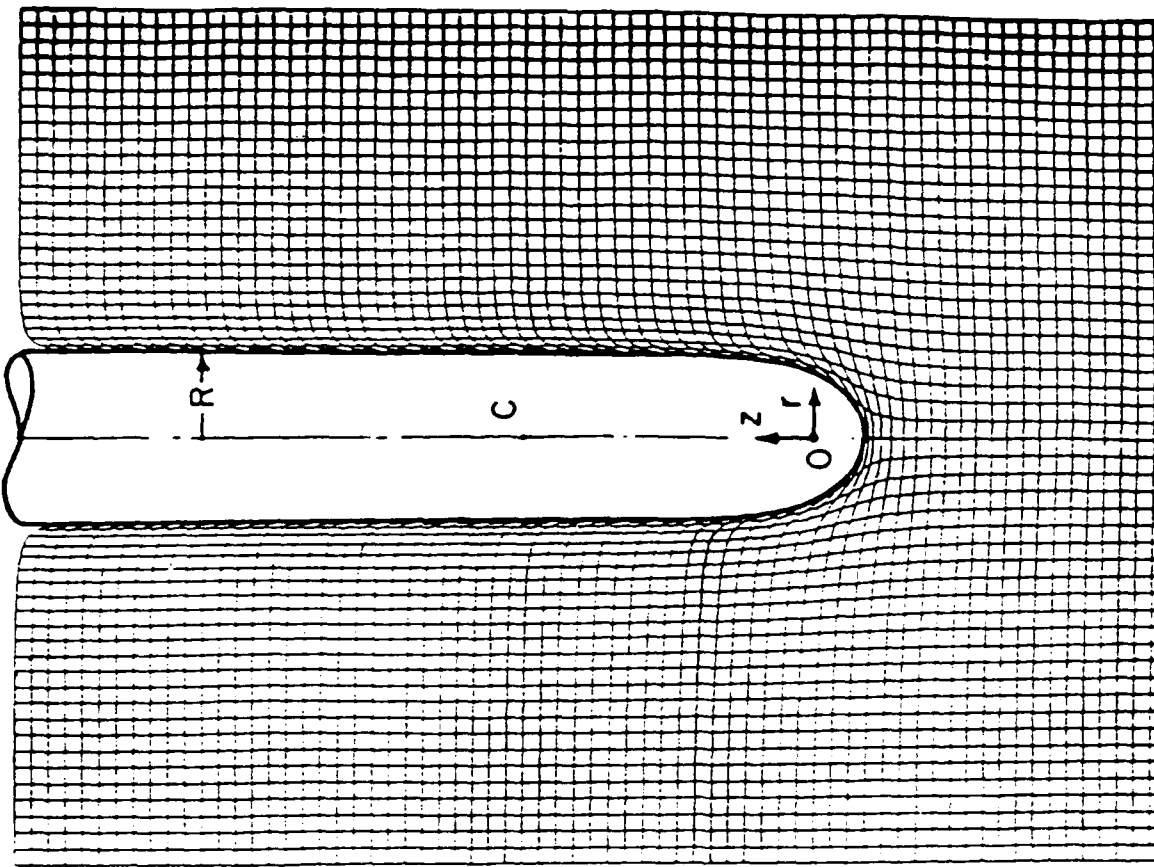
Figure 3.3. Deformation fields for a)Spherical Cavity Expansion and b) Simple Pile
(Baligh, 1985)
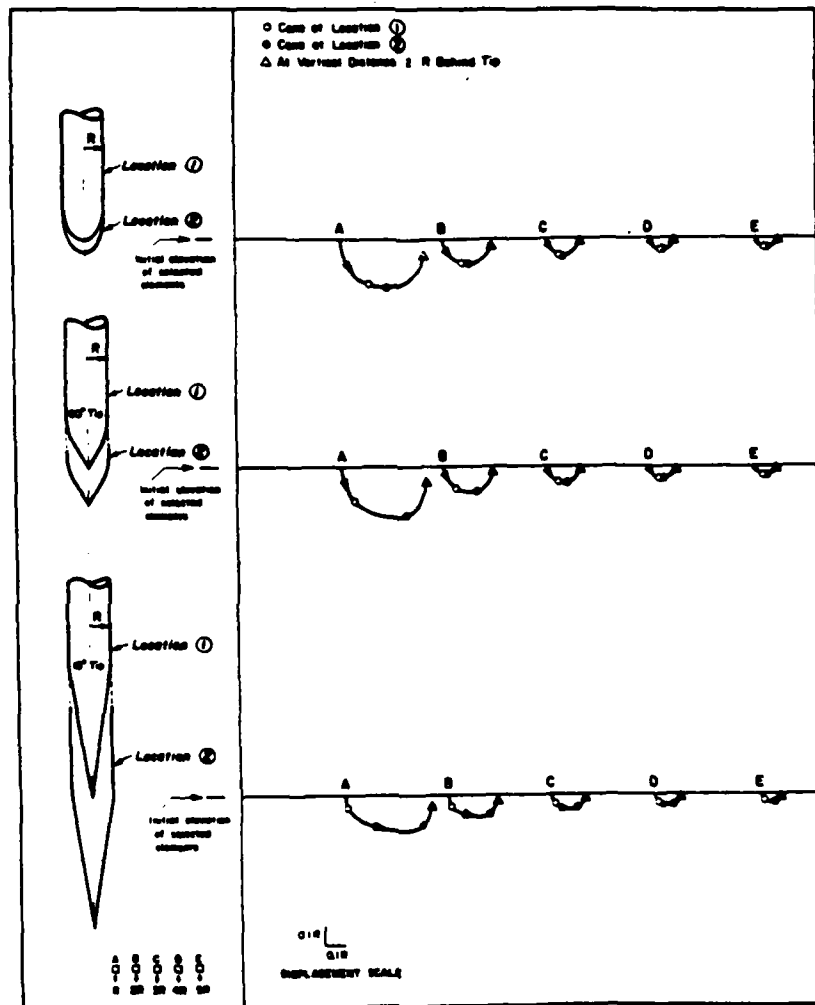
Figure 3.4. Deformation paths for axisymmetric penetrometers
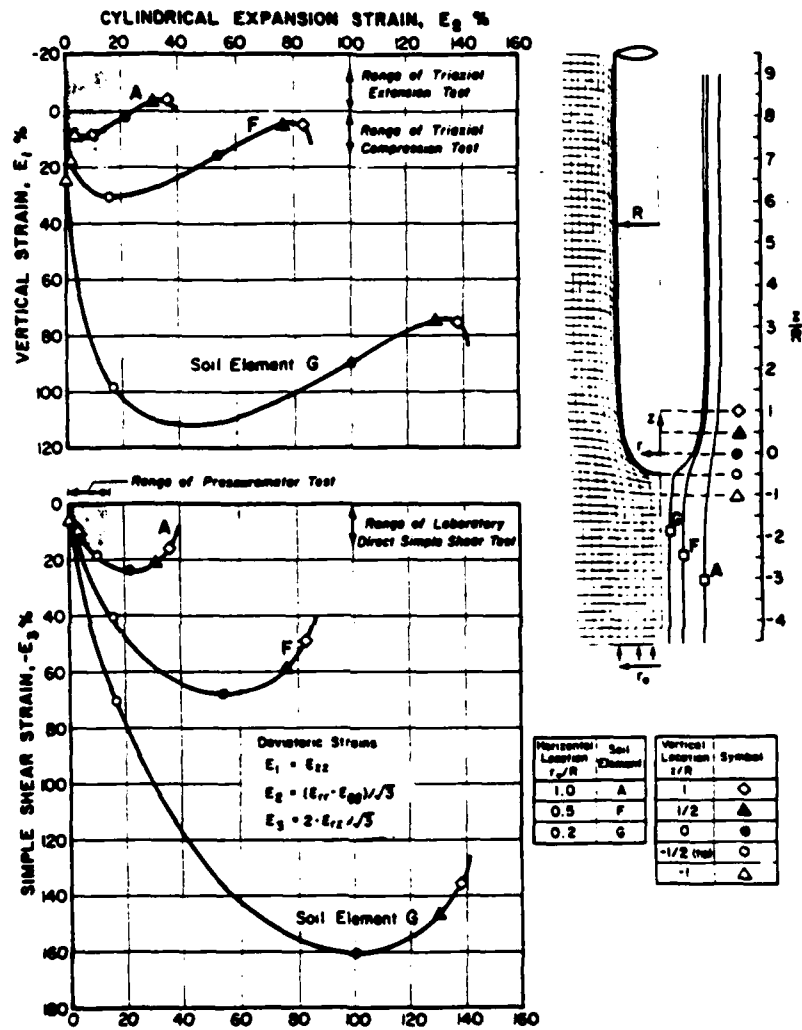
Figure 3.5a. Strain paths for axisymmetric penetrometers: Simple Pile

58
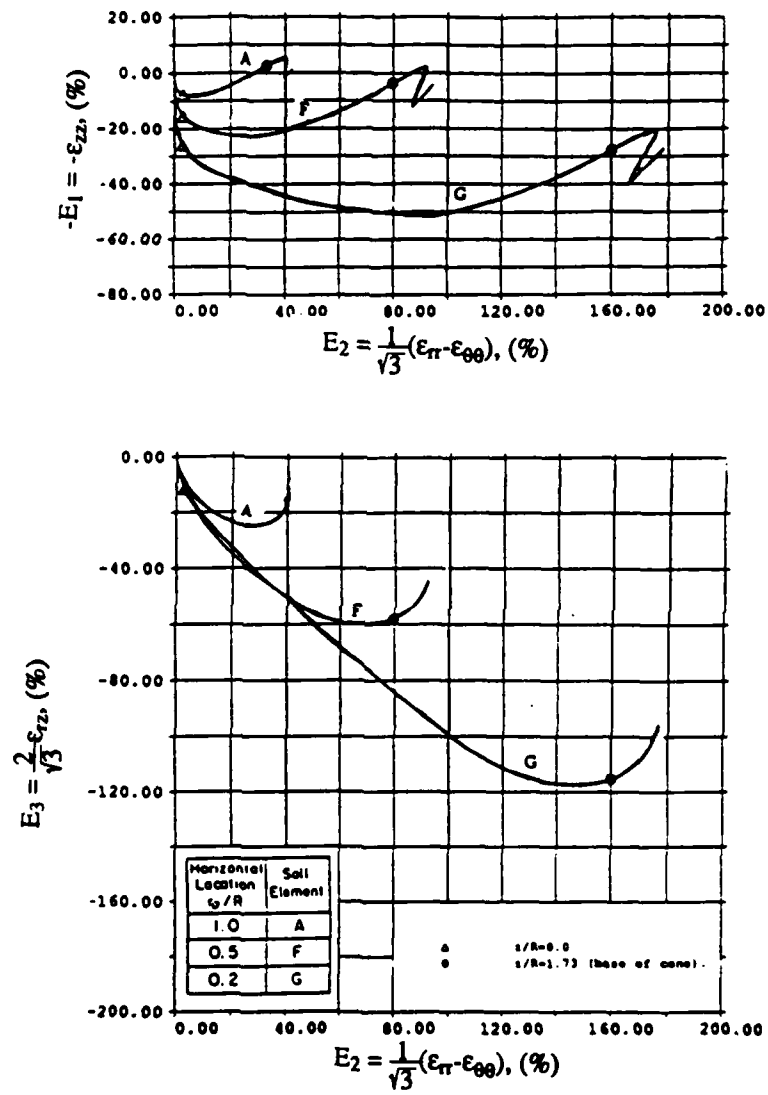
Figure 3.5b. Strain paths for axisymmetric penetrometers: 60° Cone
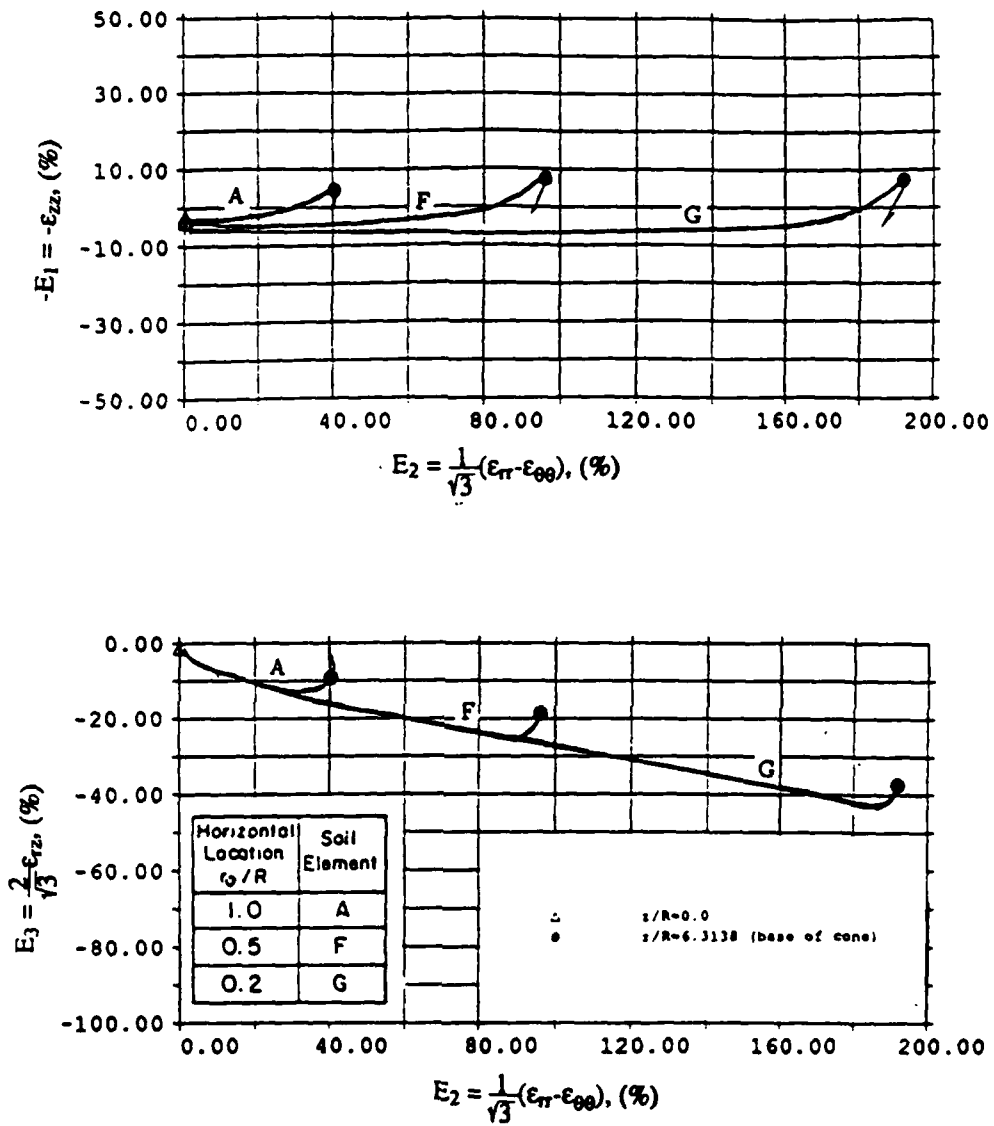
Figure 3.5c. Strain paths for axisymmetric penetrometers: 18° Cone

a) Point Source Located at Origin

b) Point Source Located at $y' = \xi$

$$x' = x$$
$$z' = z$$
$$y' = (y + \xi)$$

c) Semi-infinite Line Source, $0 \leq \xi \leq \infty$

Semi-infinite Line Source

Source Strength per Unit Length
$$v' = v/d\xi$$
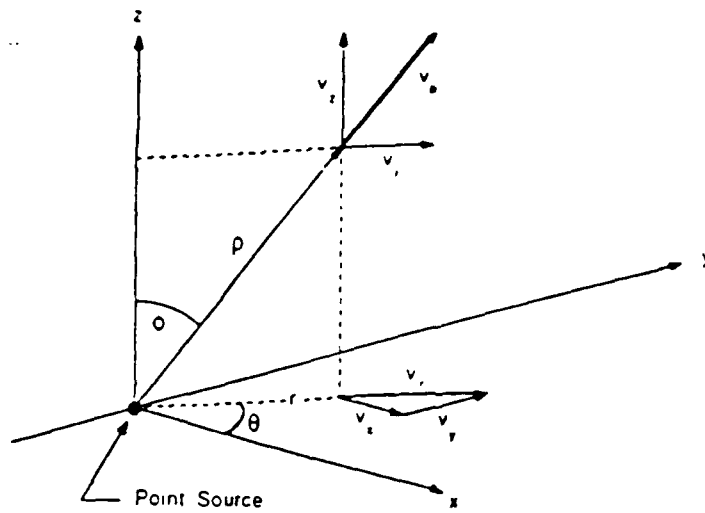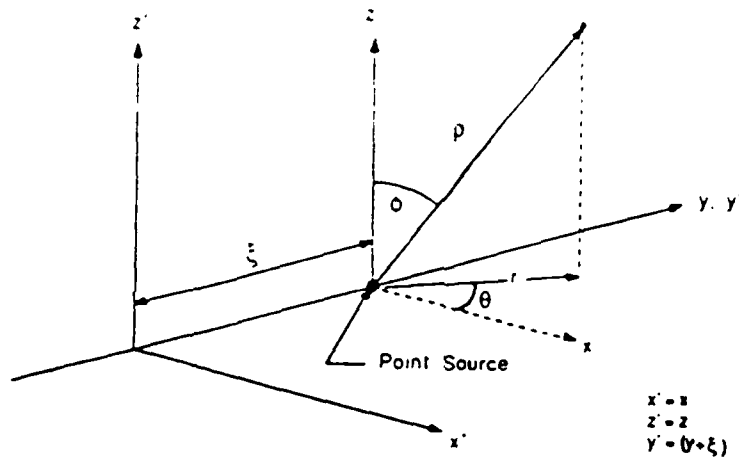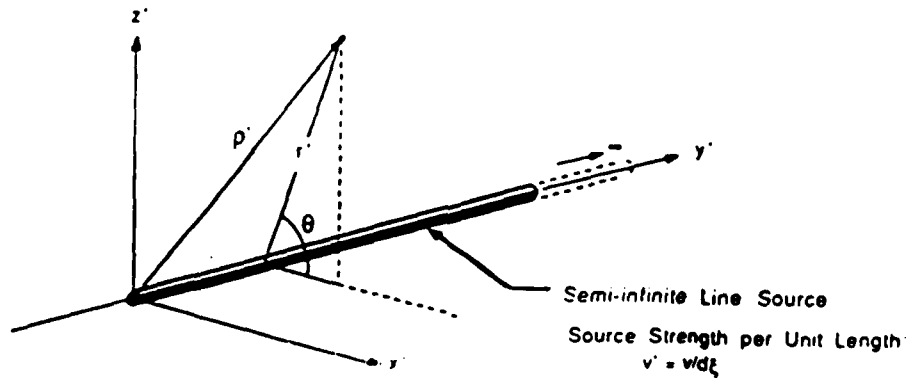
Figure 3.6. Coordinate system for the semi-infinite line source (Whittle et al. 1989)
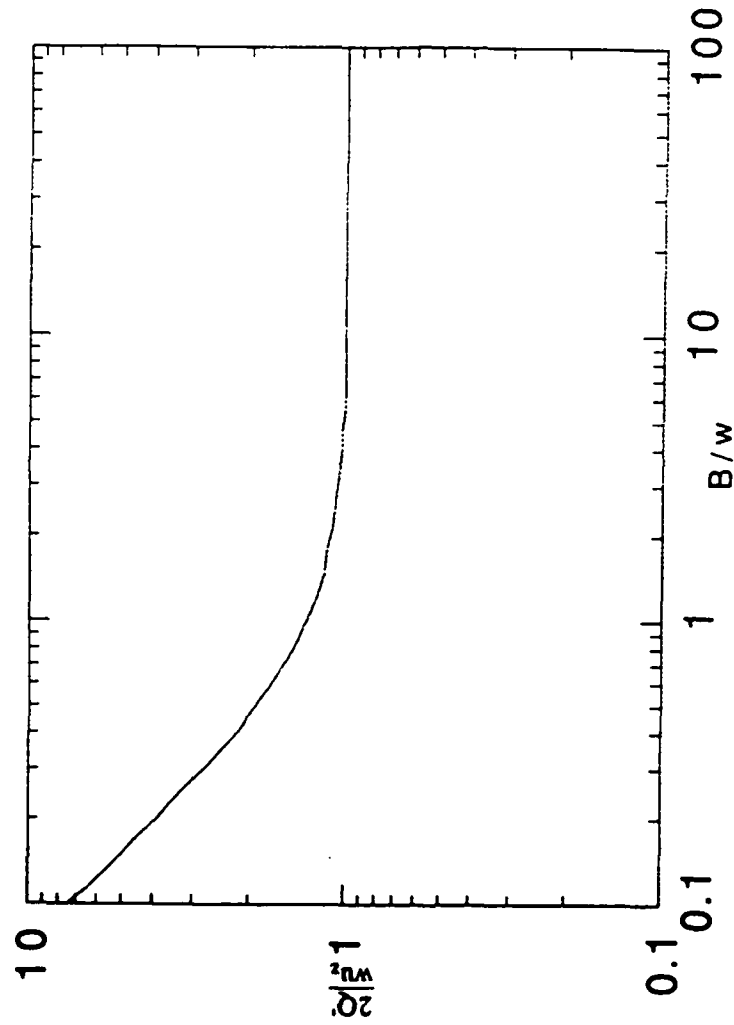
Aspect Ratio (B/w)	2Q'/wu$_z$
1	1.346
3	1.087
10	1.013
30	1.000
100	1.000

Figure 3.7. Source strength used for Simple Plate geometry
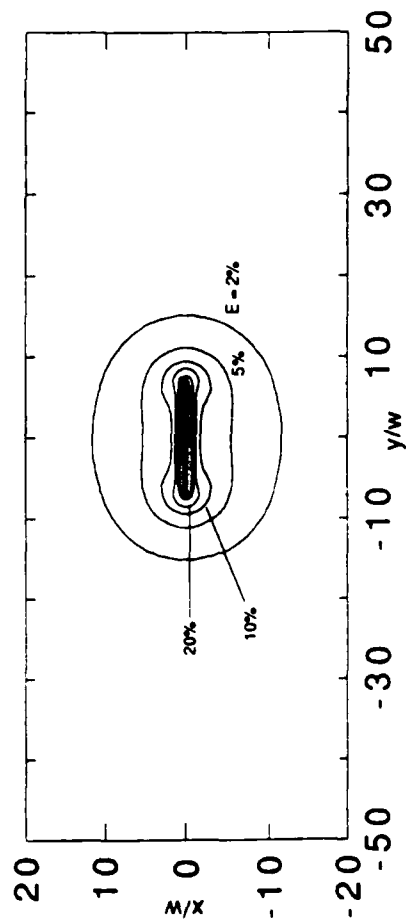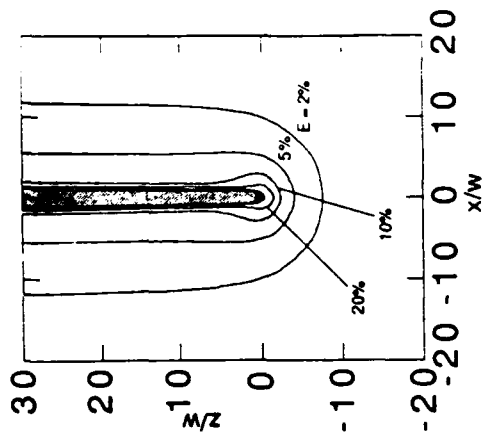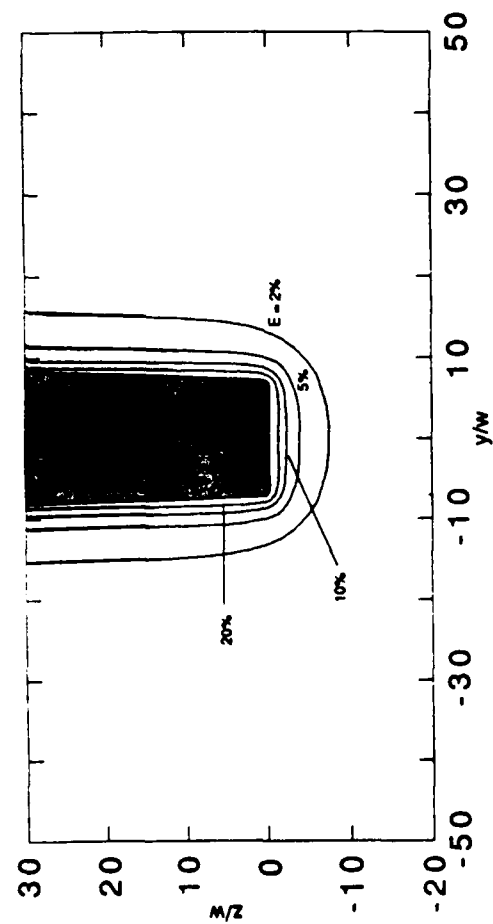
B/w	L/w	L/B
6.8	7.6	1.12

Figure 3.8a. Simple Plate with aspect ratio, B/w = 6.8

63
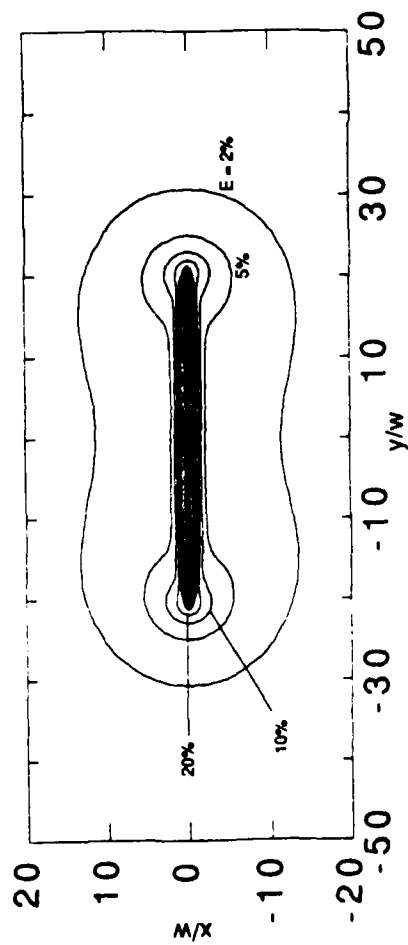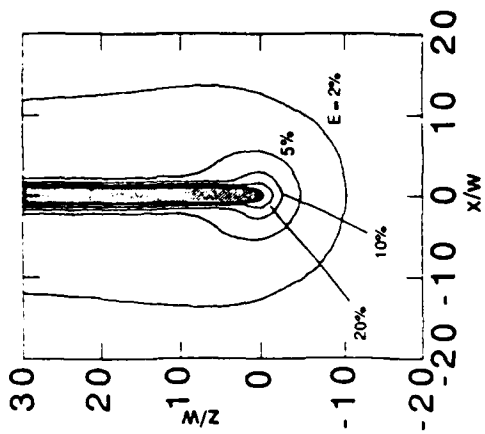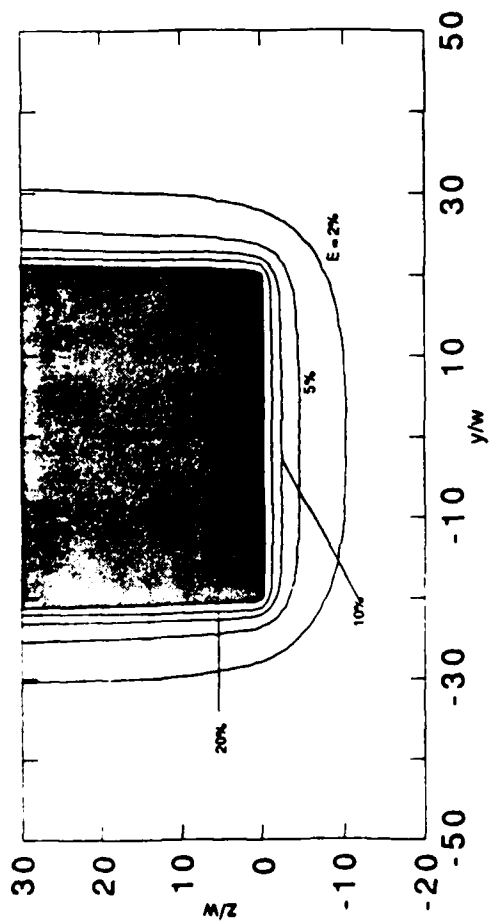
B/w	L/w	L/B
20.0	21.3	1.07

Figure 3.8b. Simple Plate with aspect ratio, B/w = 20

64
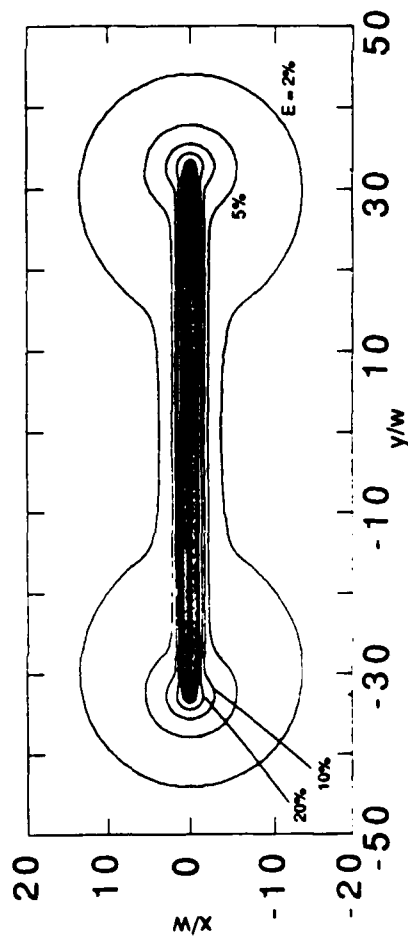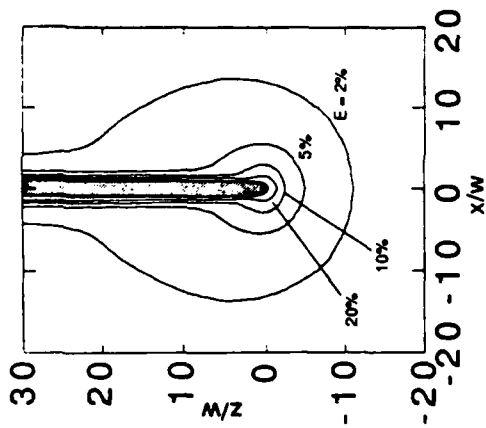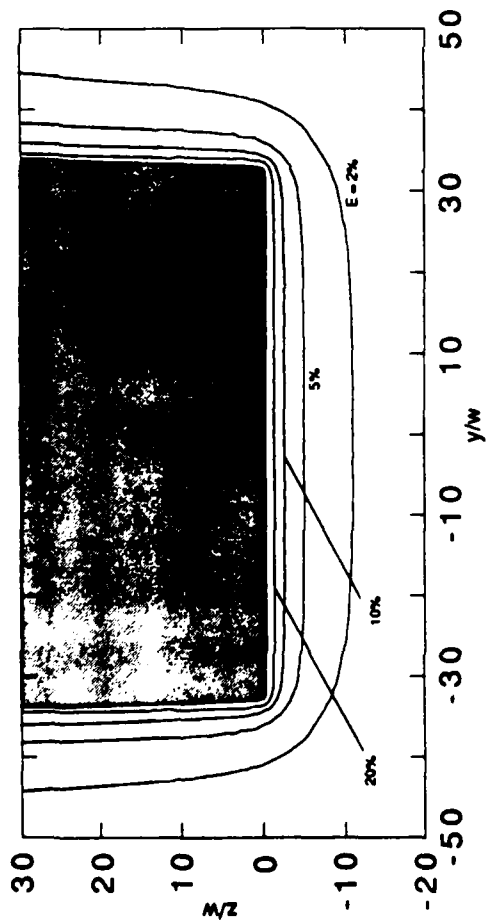
B/w	L/w	L/B
32.5	33.7	1.04

Figure 3.8c. Simple Plate with aspect ratio, B/w = 32.5
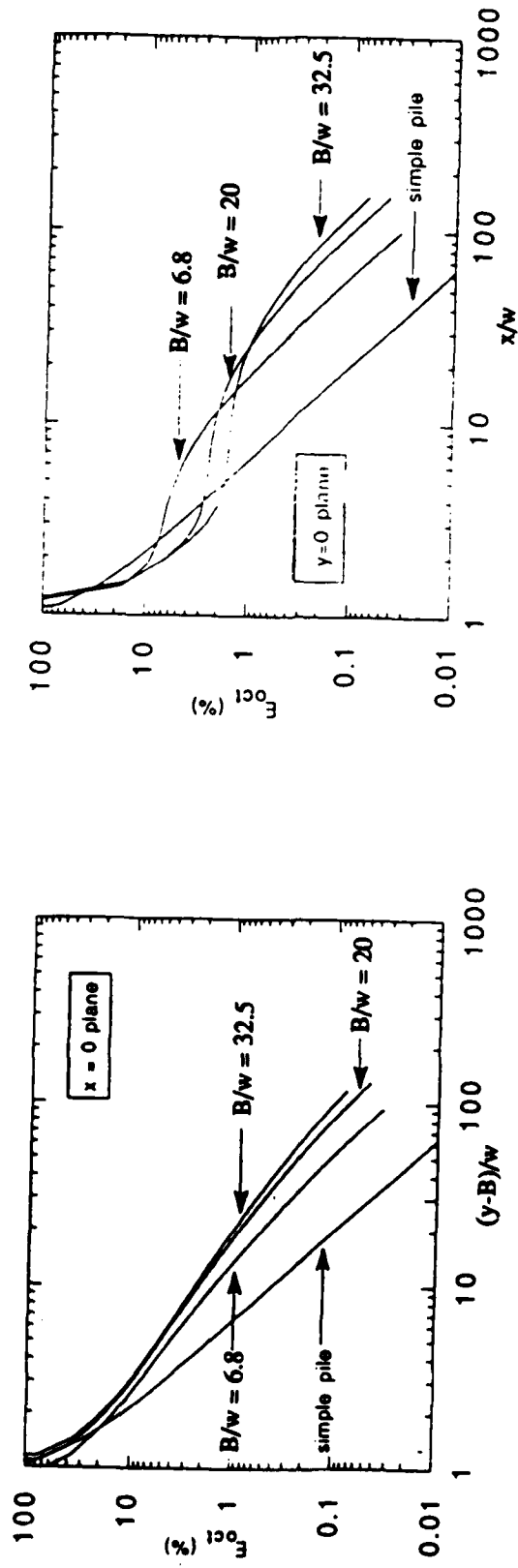
Figure 3.9. Octahedral shear strain around Simple Plates

Aspect Ratio (B/w)	R_{eq}
Simple Pile	1.00
6.8	2.94
20.0	5.05
32.5	6.43
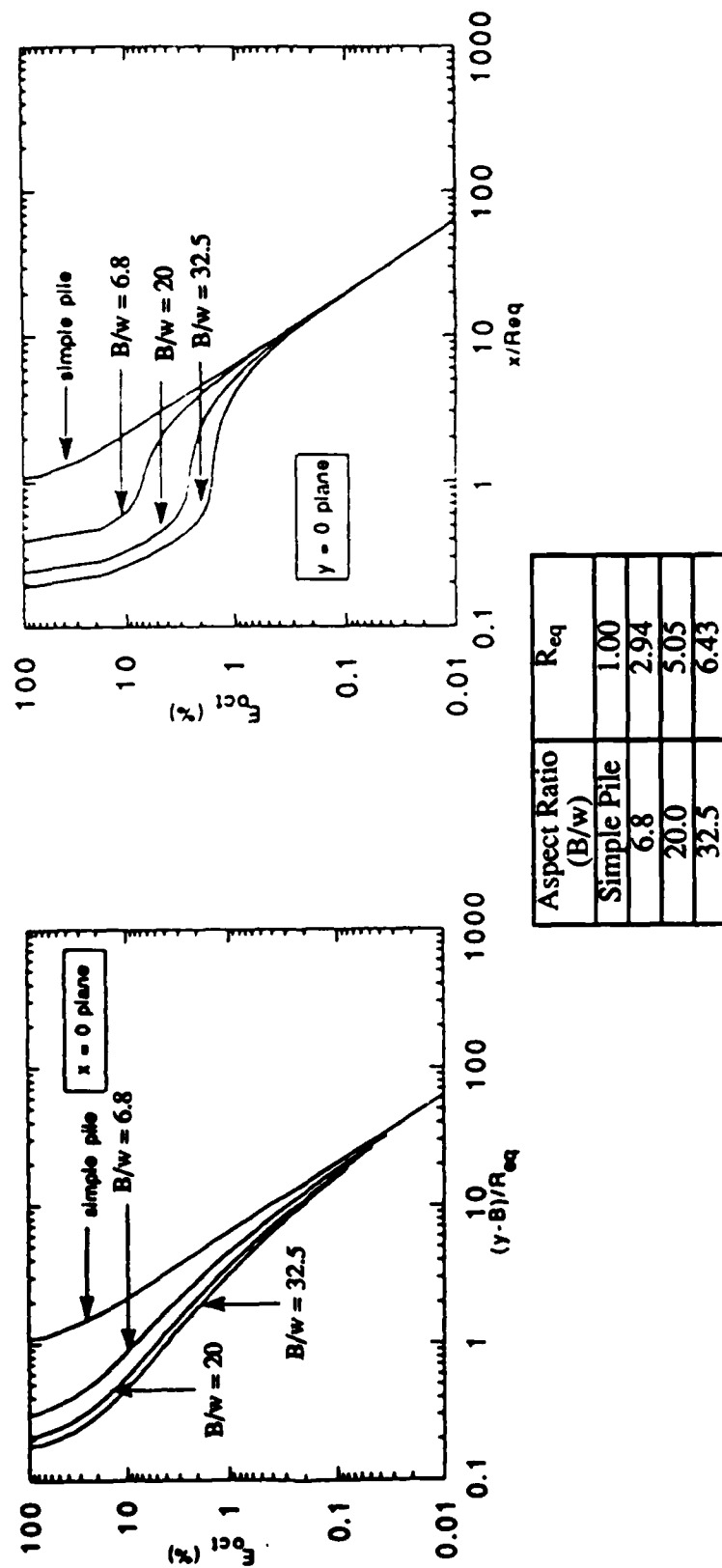
Figure 3.10. Octahedral shear strain around Simple Plates using R_{eq} normalization
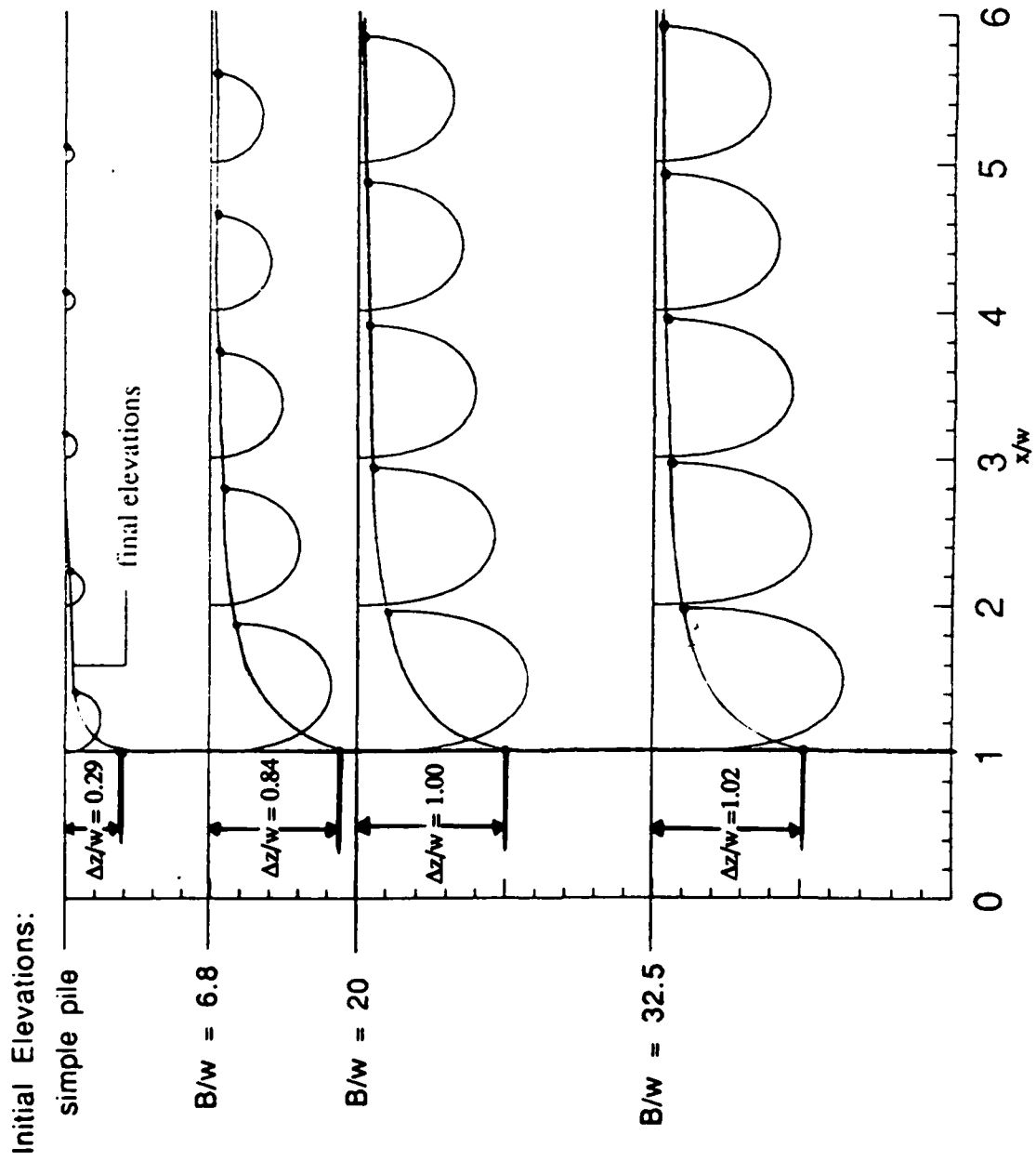
Figure 3.11. Deformation paths around Simple Plates

68
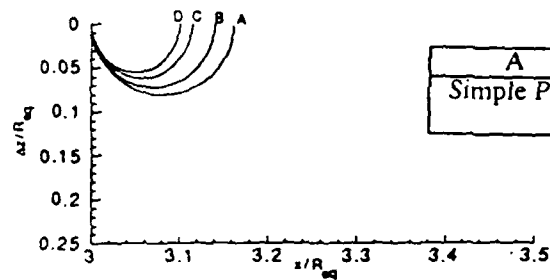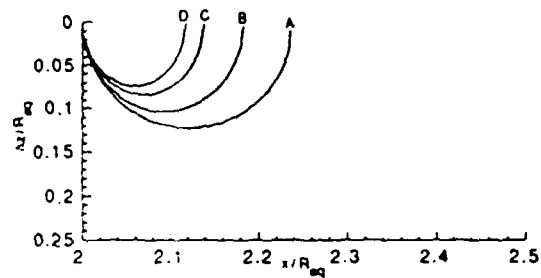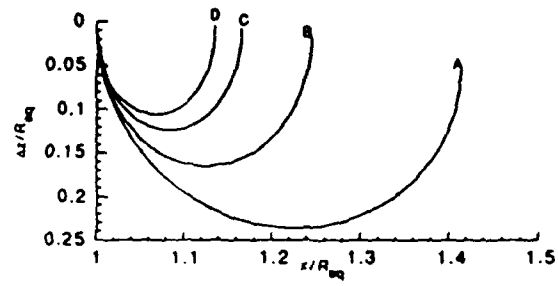
A	B	C	D
Simple Pile	B/w = 6.8 plate	B/w = 20 plate	B/w = 32.5 plate
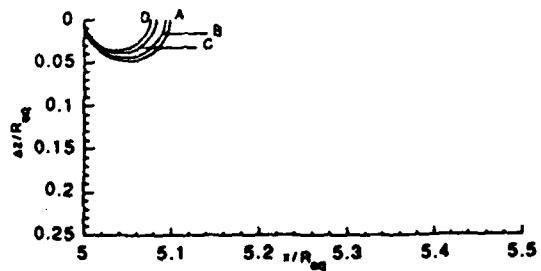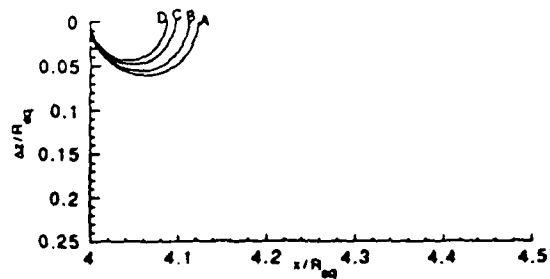
Figure 3.12. Deformation paths around Simple Plates using R_{eq} normalization
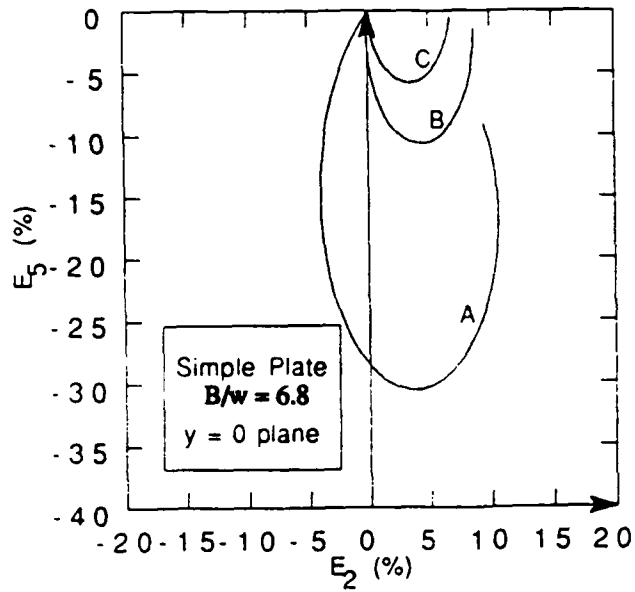
	A	B	C
x_0/w	1.0	3.0	5.0
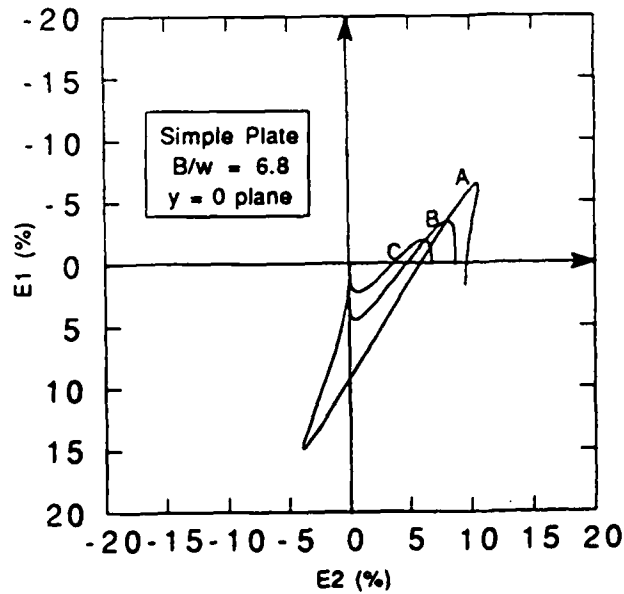
Figure 3.13a. Strain paths of soil elements around Simple Plate in the y/w = 0 plane, B/w=6.8
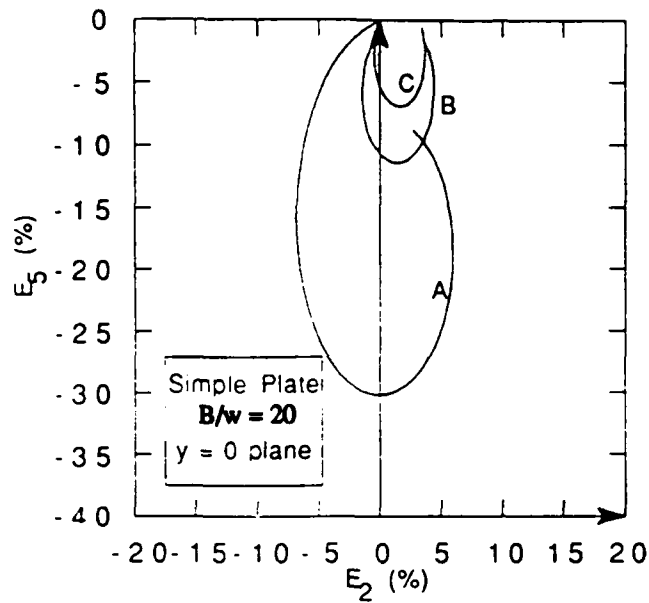
	A	B	C
x_0/w	1.0	3.0	5.0
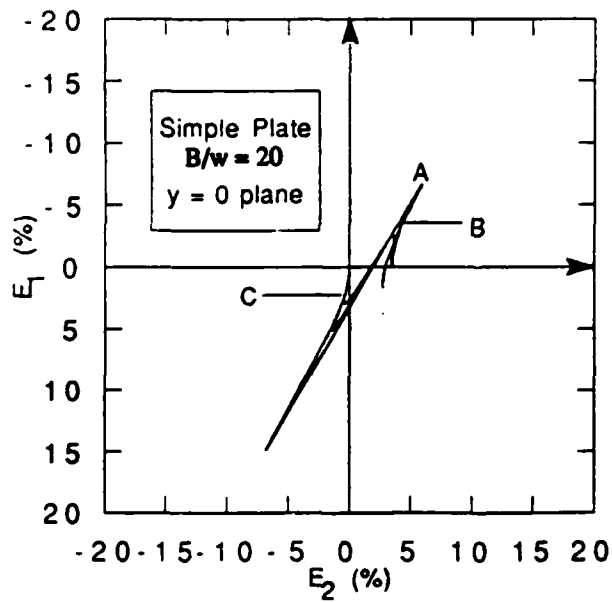
Figure 3.13b. Strain paths of soil elements around Simple Plate in the $y/w = 0$ plane, $B/w=20$
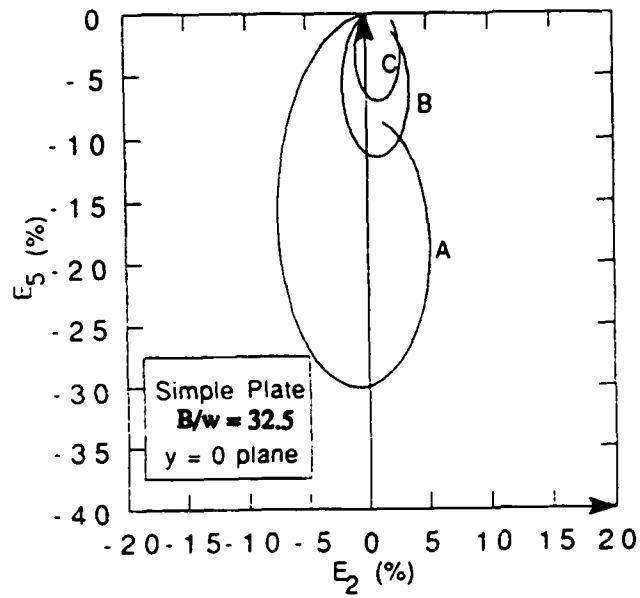
	A	B	C
x_0/w	1.0	3.0	5.0
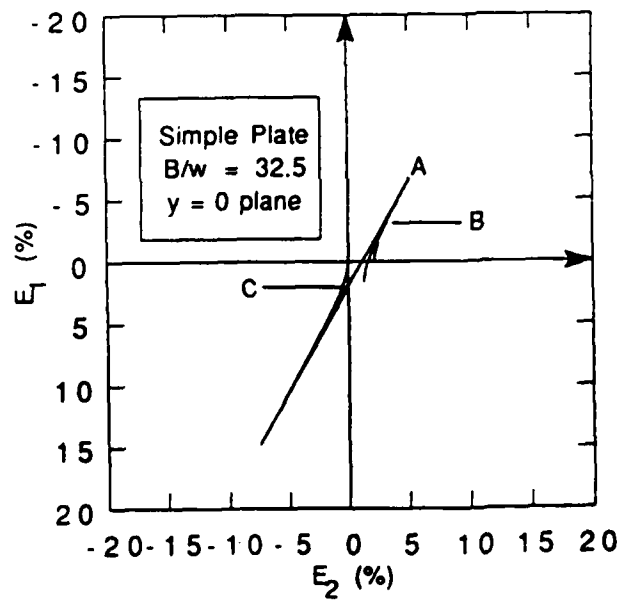
Figure 3.13c. Strain paths of soil elements around Simple Plate in the $y/w = 0$ plane, $B/w=32.5$
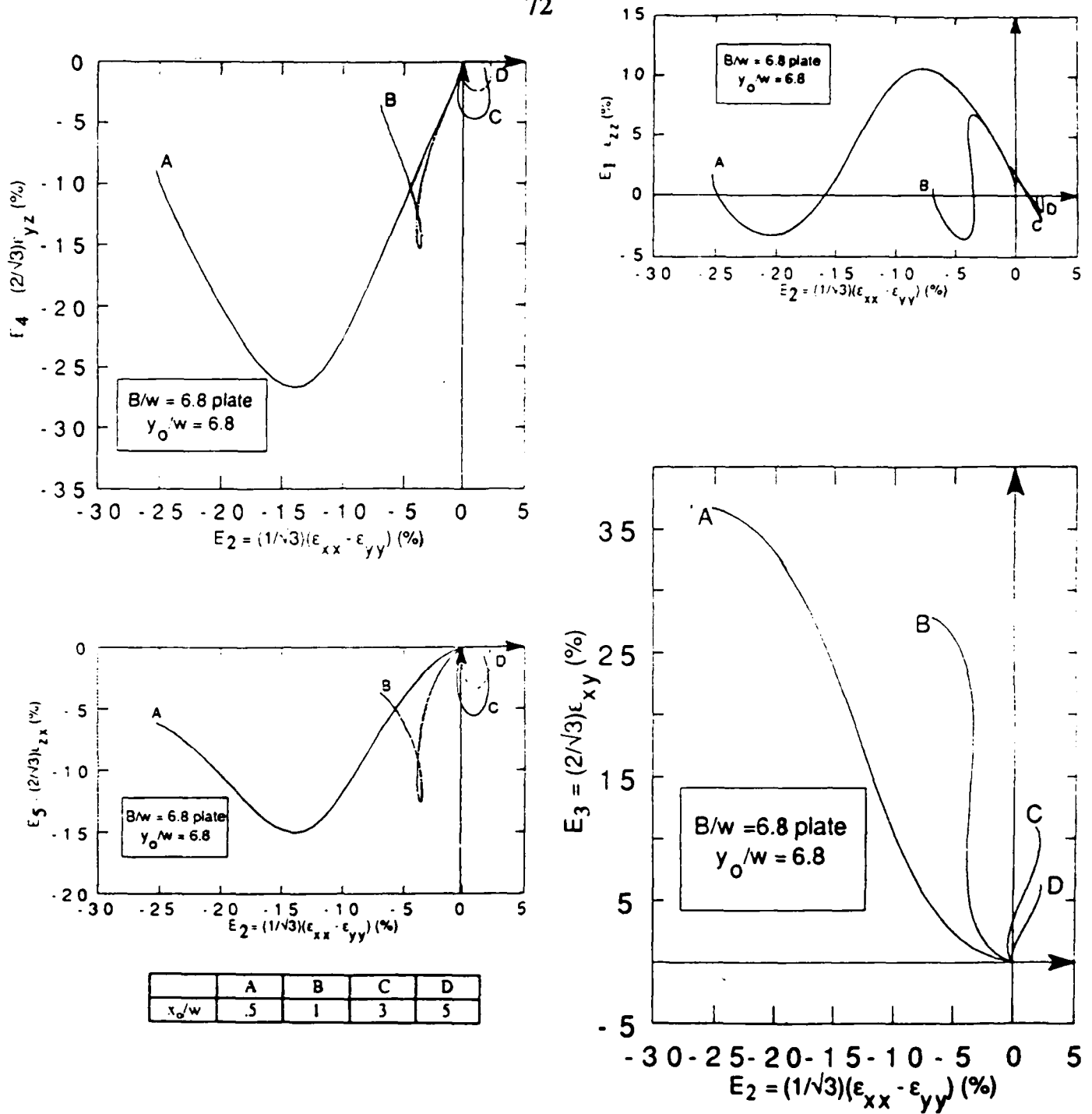
Figure 3.14   Example strain paths for soil elements around Simple Plate, B/w = 6.8, with y_o/w = 6.8.
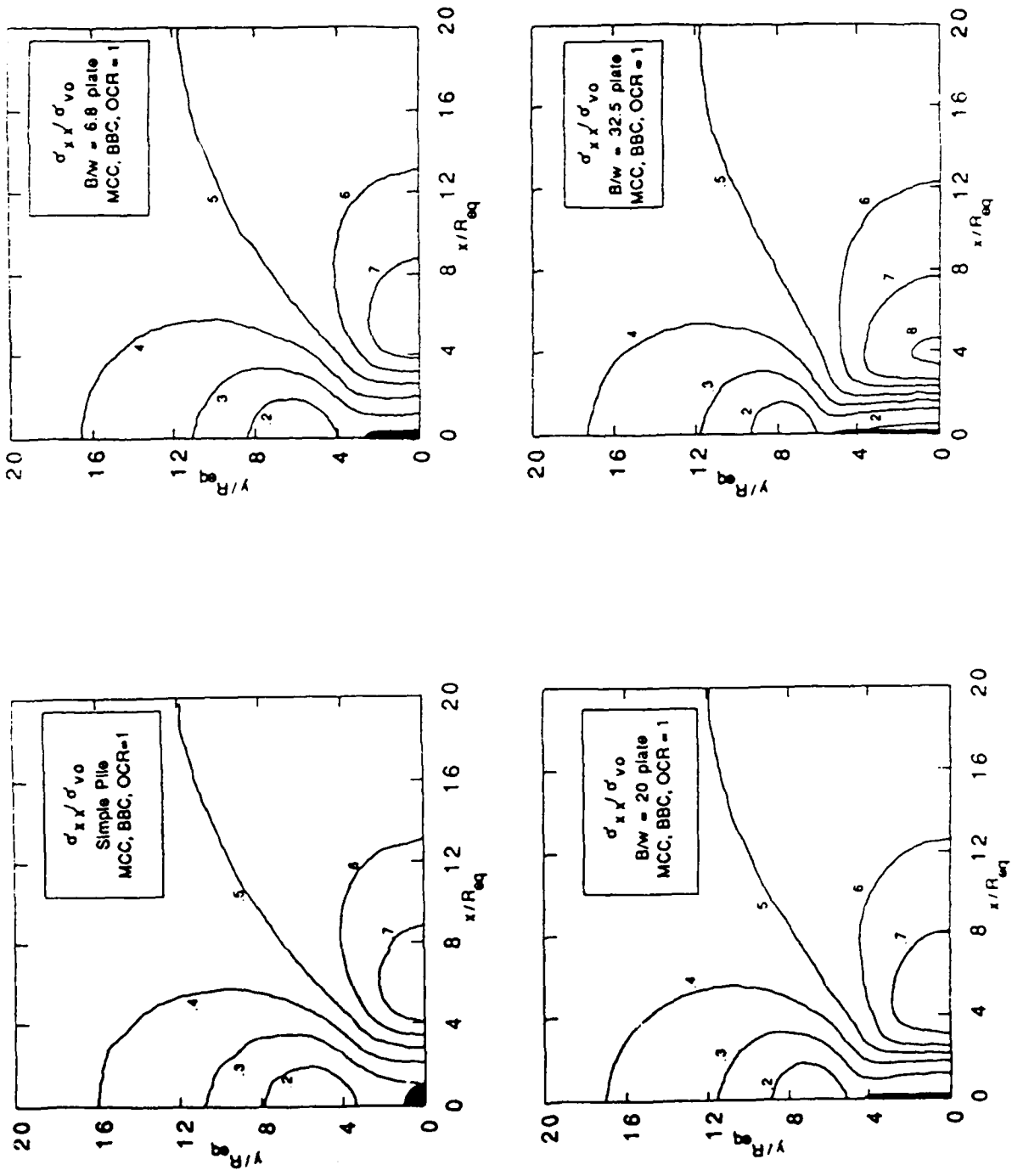
Figure 3.15a. Effect of aspect ratio on predictions of effective stresses around Simple Plates for base case analysis: Lateral effective stresses, $\sigma'_{xx}/\sigma'_{vo}$.
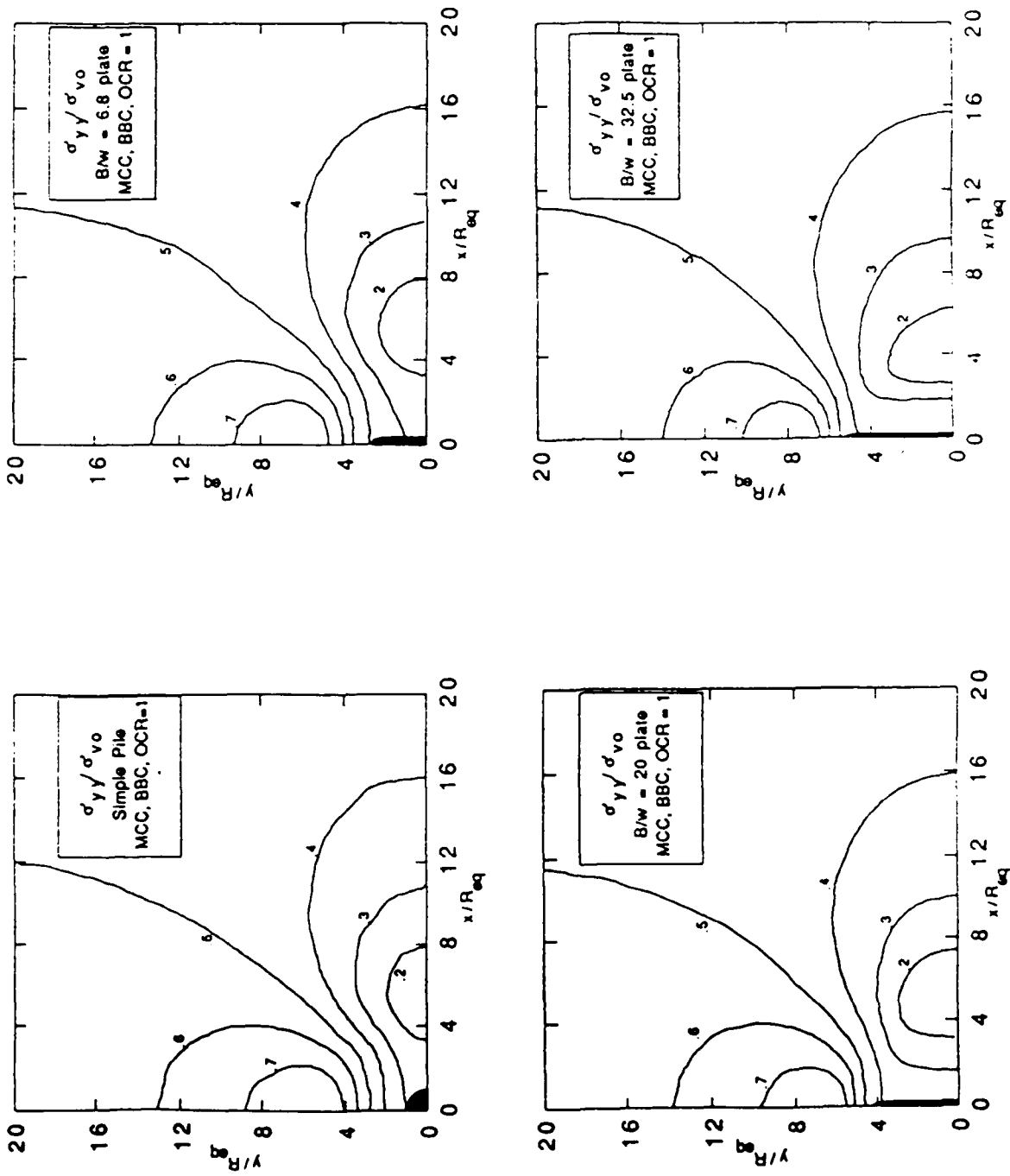
Figure 3.15b. Effect of aspect ratio on predictions of effective stresses around Simple Plates for base case analysis: Lateral effective stresses, $\sigma'_{yy}/\sigma'_{vo}$.
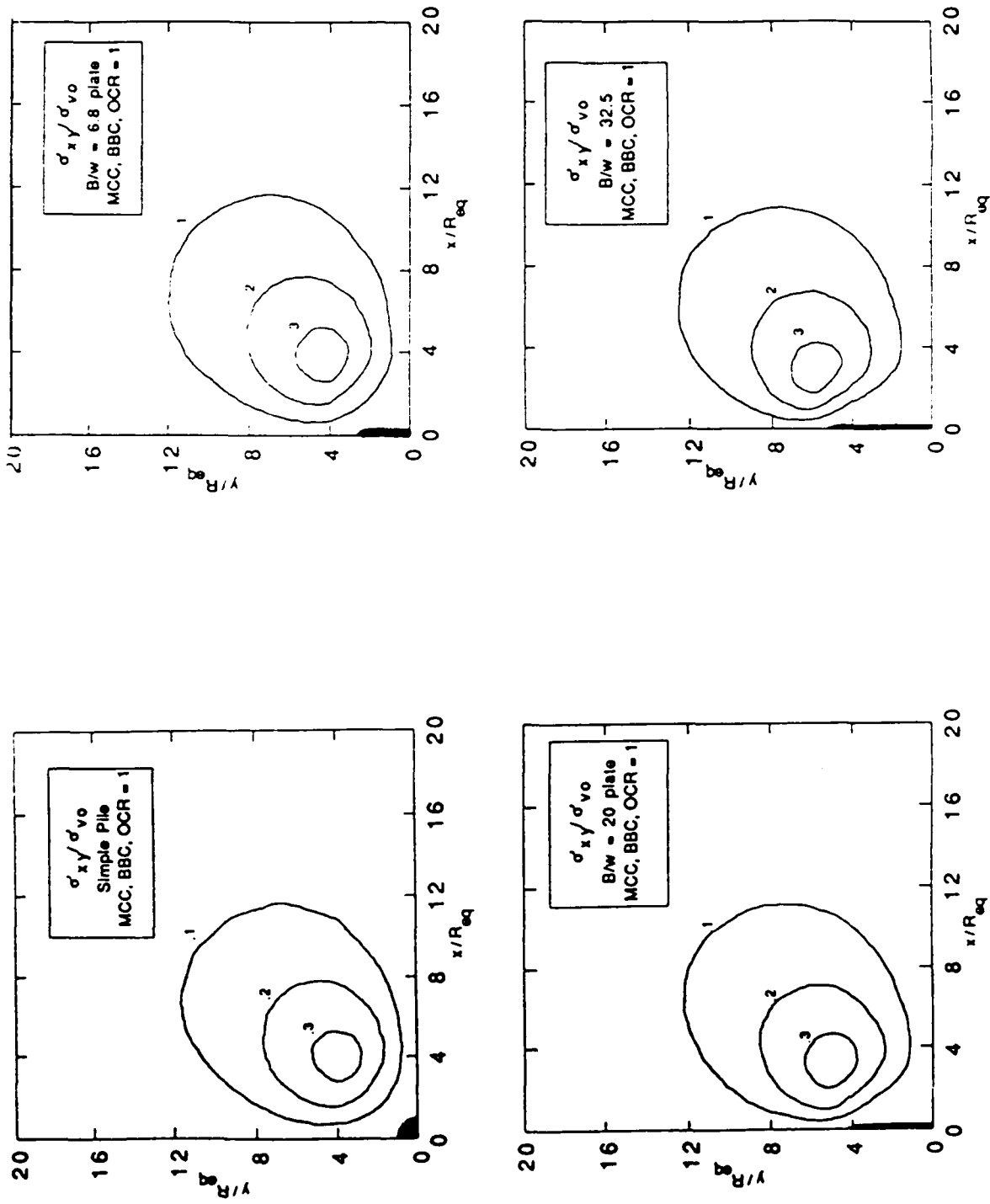
Figure 3.15c. Effect of aspect ratio on predictions of effective stresses around Simple Plates for base case analysis: Shear stresses, $\sigma'_{xy}/\sigma'_{vo}$.
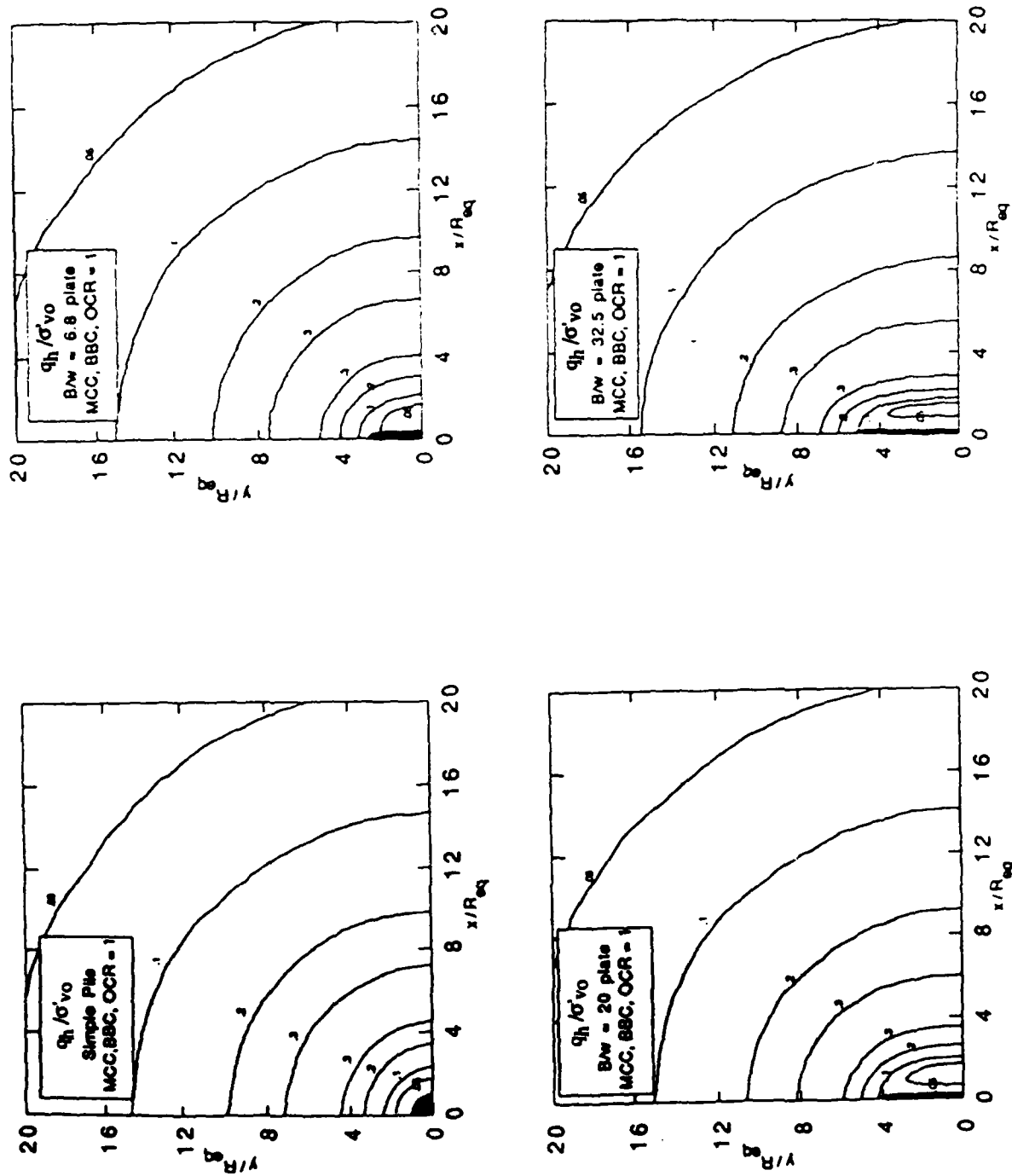
Figure 3.16. Effect of aspect ratio on predictions of maximum shear stress in the x-y plane around Simple Plates for base case analysis.
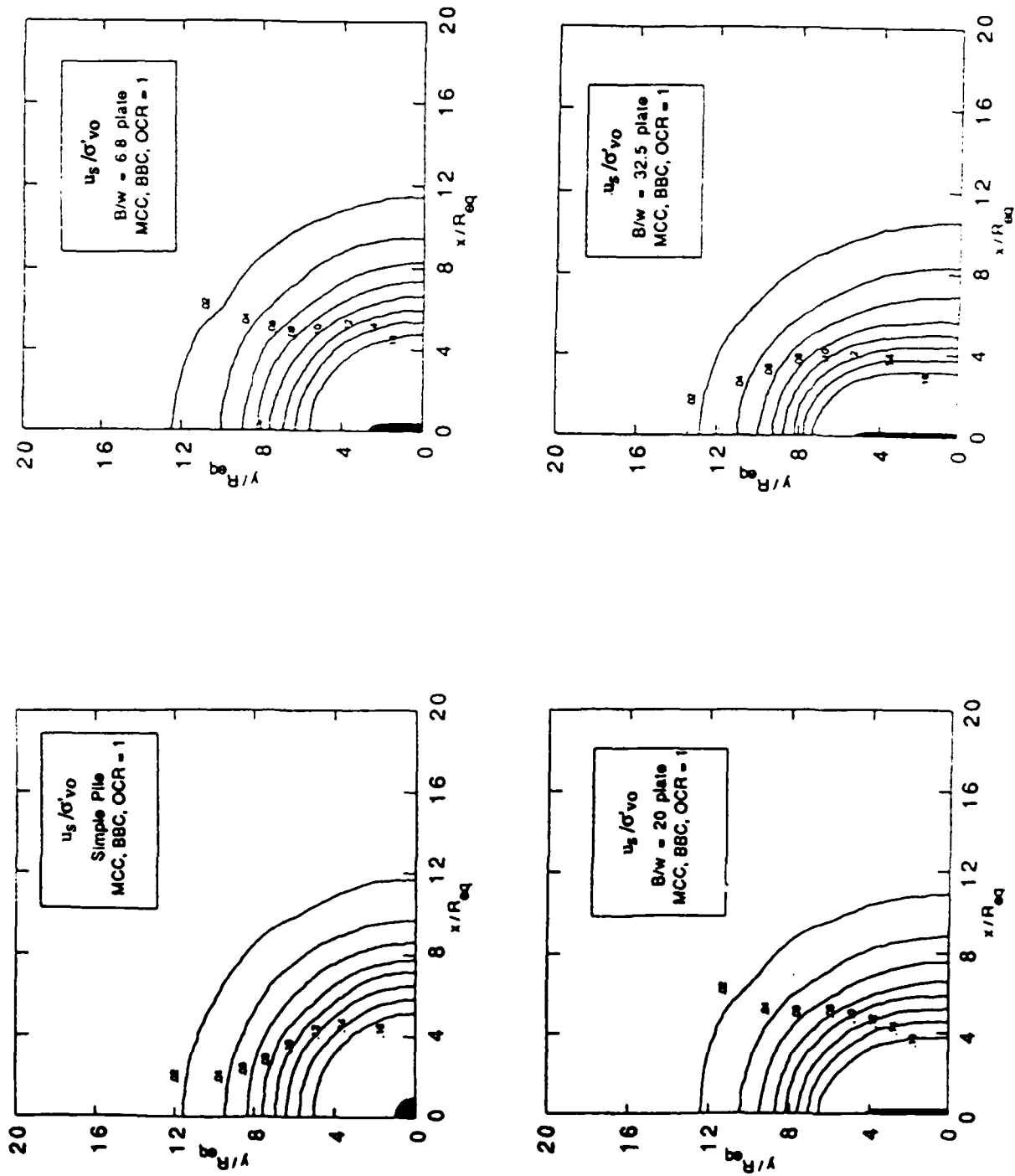
Figure 3.17. Effect of aspect ratio on predictions of shear induced pore pressures in the x-y plane around Simple Plates for base case analysis.
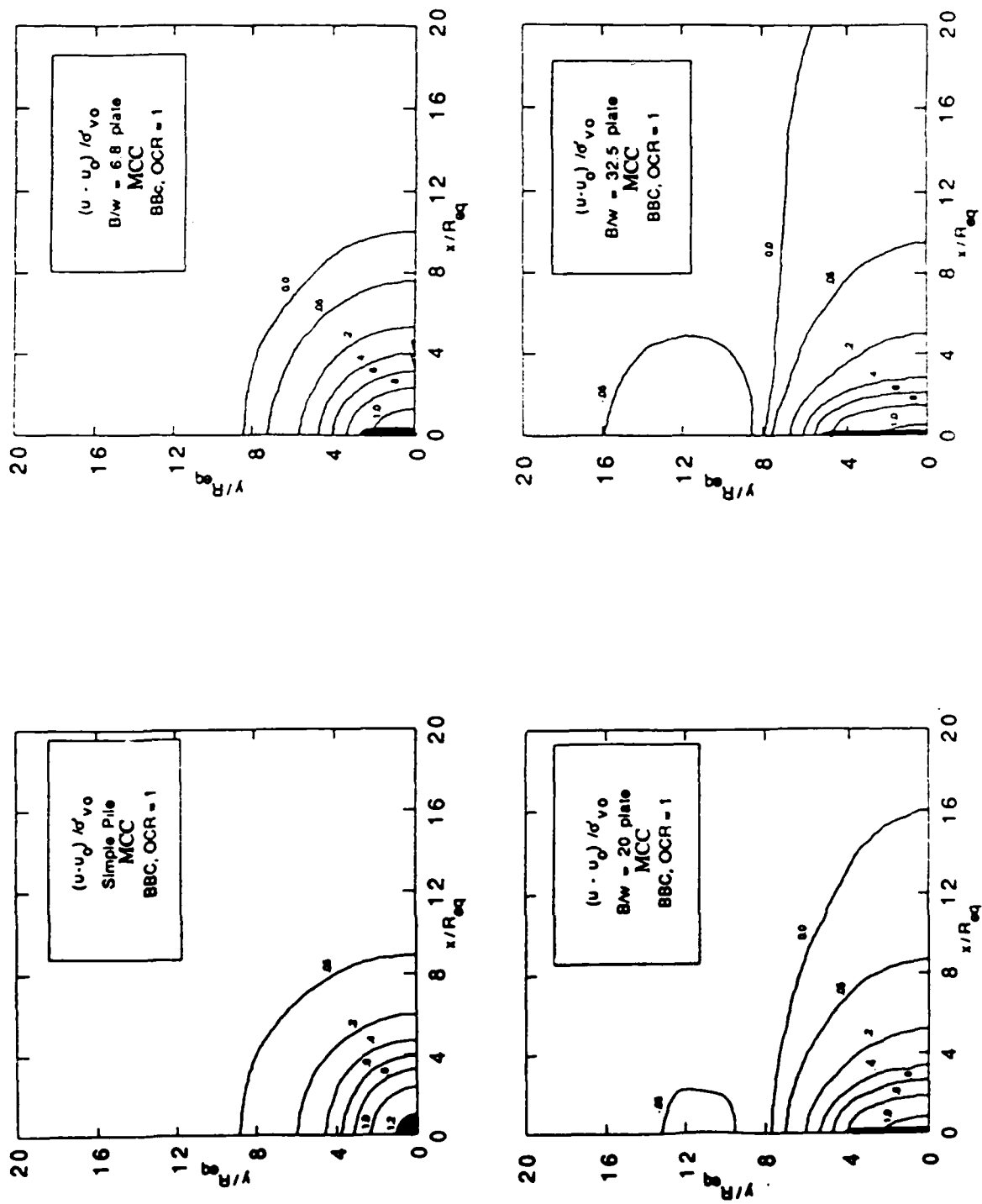
Figure 3.18. Effect of plate aspect ratio on predictions of excess pore pressures, $\Delta u/\sigma'_{vo}$, for base case analysis
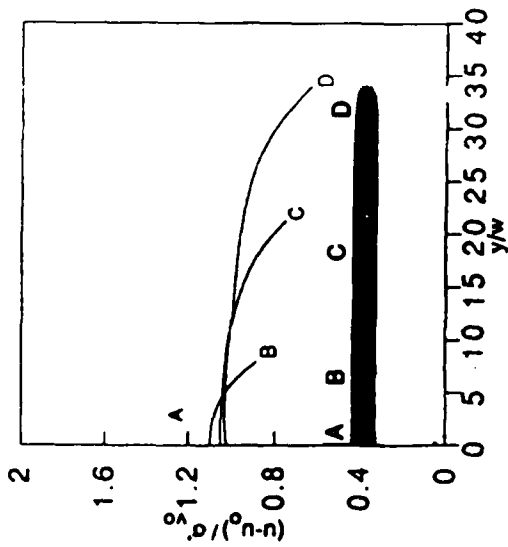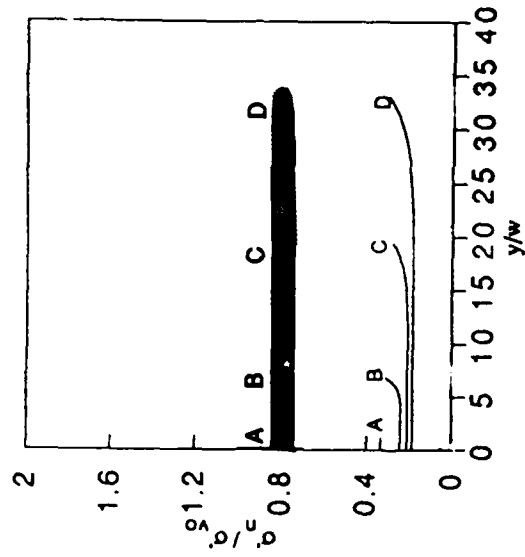
B/w	A Simple Pile	B 6.8	C 20.0	D 32.5
$(u - u_o)/\sigma'_{vo}$ on plate edge	1.2	0.88	0.75	0.60
$(u - u_o)/\sigma'_{vo}$ on plate center	1.2	1.10	1.05	1.03
σ'_n/σ'_{vo} on plate edge	0.35	0.39	0.43	0.49
σ'_n/σ'_{vo} on plate center	0.35	0.24	0.20	0.18
$(\sigma_n - u_o)/\sigma'_{vo}$ on plate edge	1.55	1.27	1.18	1.09
$(\sigma_n - u_o)/\sigma'_{vo}$ on plate center	1.55	1.34	1.25	1.21
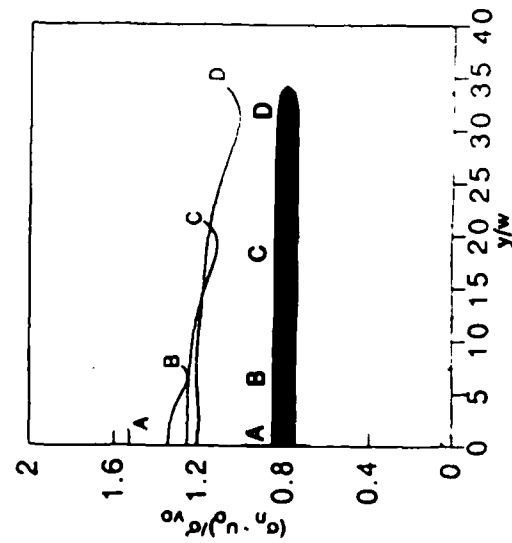
Figure 3.19. Effect of plate aspect ratio on the distribution of excess pore pressures, normal effective and total stresses along plate blade

80
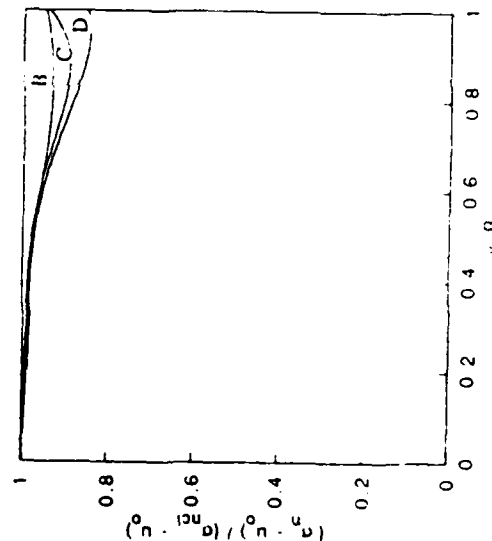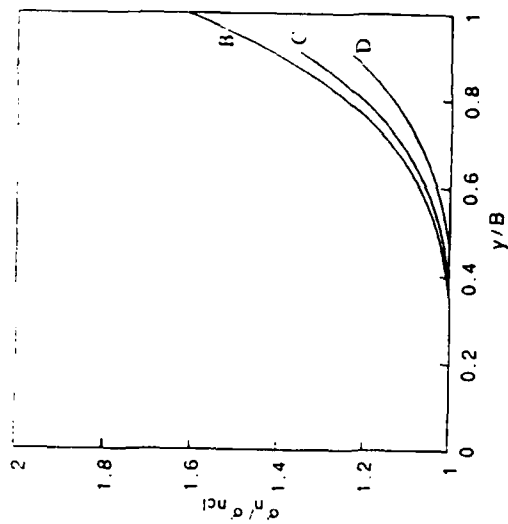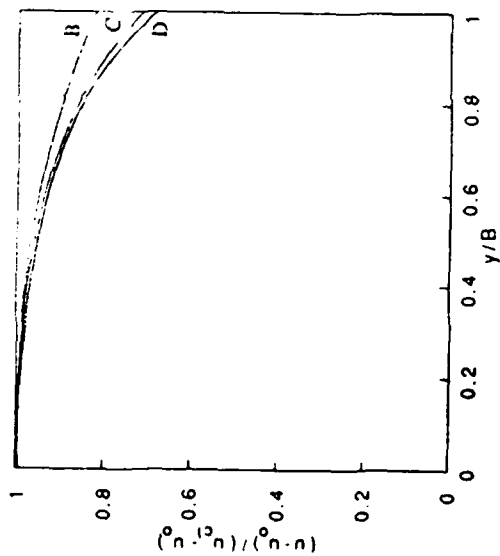
	B	C	D
B/w	6.8	20.0	32.5
$(u_{cl} - u_o)/\sigma'_{vo}$	1.10	1.05	1.03
$\sigma'_{ncl}/\sigma'_{vo}$	0.24	0.20	0.18
$(\sigma_{ncl} - u_o)/\sigma'_{vo}$	1.34	1.25	1.21

Figure 3.20.. Normalized excess pore pressures, normal effective and total stress distributions along plate blades
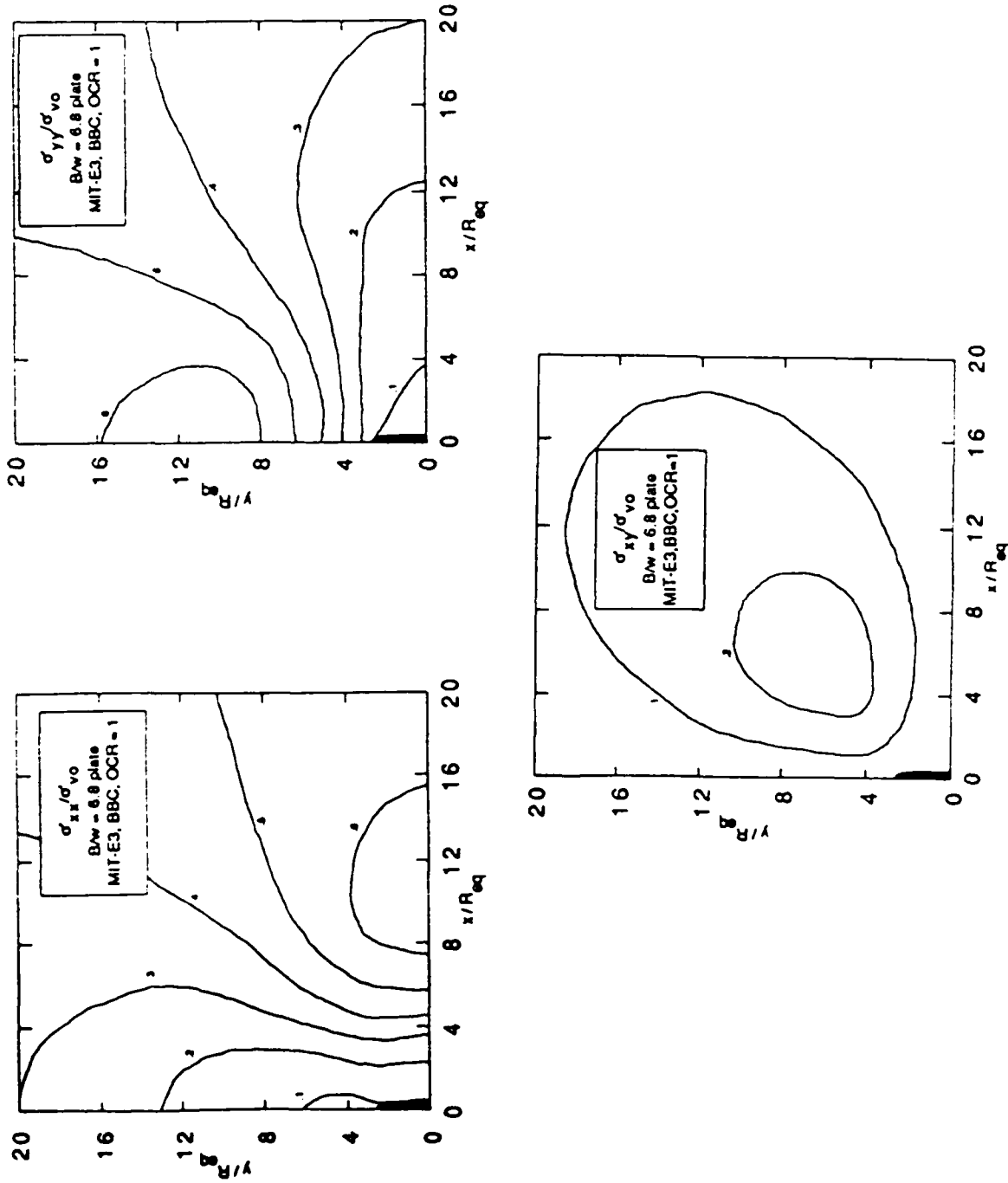
Figure 3.21. Distribution of effective stresses for K_0 - normally consolidated BBC around a Simple Plate, B/w=6.8, using the MIT-E3 model.
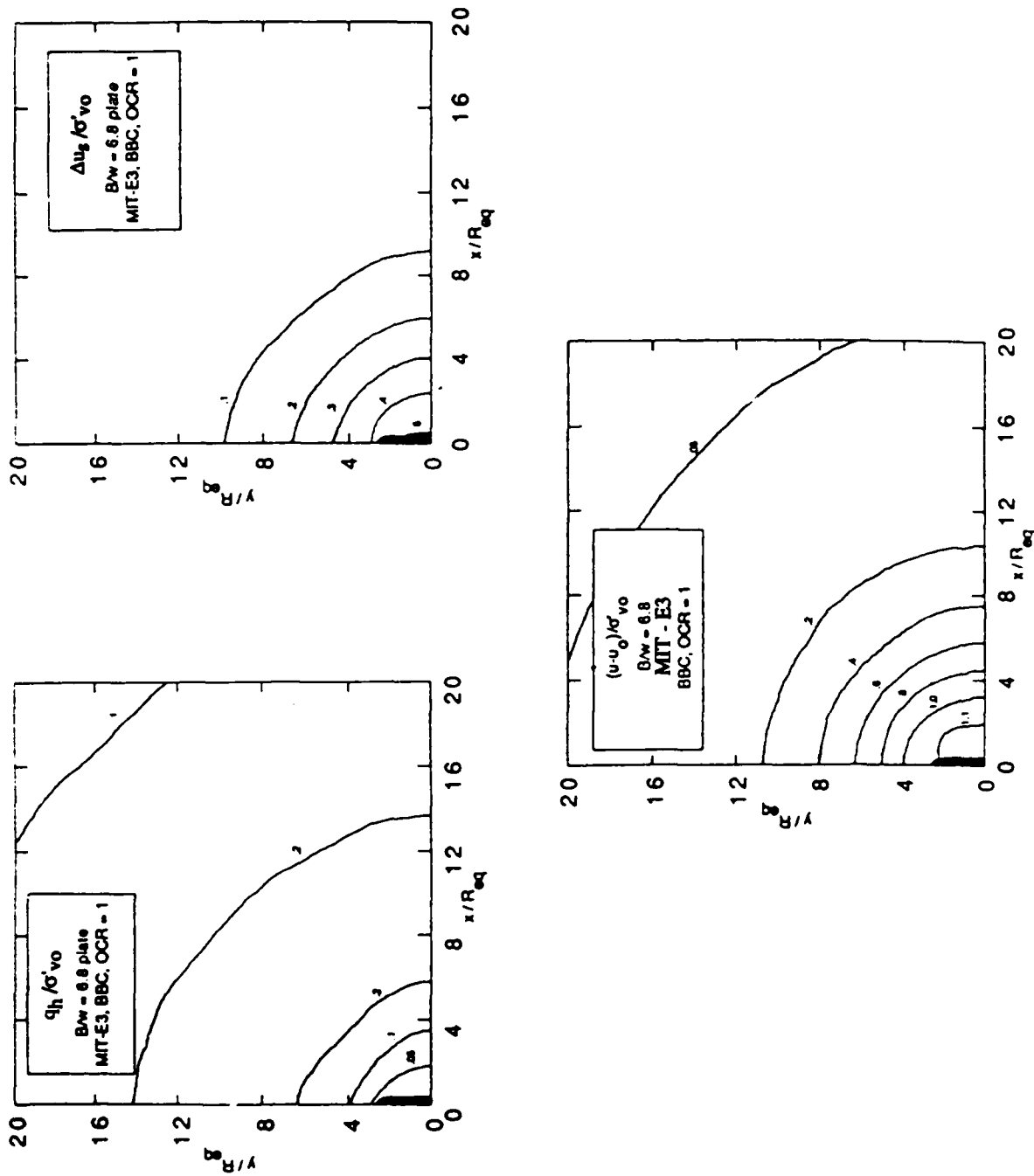
Figure 3.22. Distribution of shear stresses and excess pore pressures for K_0 - normally consolidated BBC around a Simple Plate, B/w=6.8, using the MIT-E3 model.
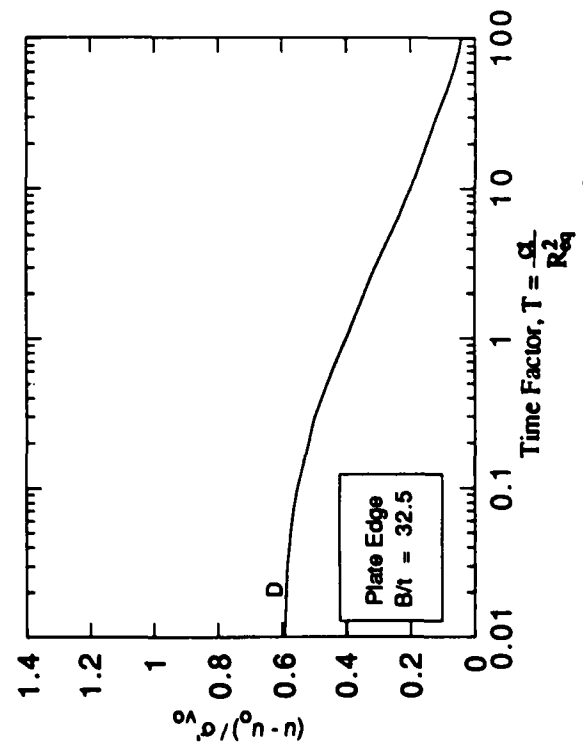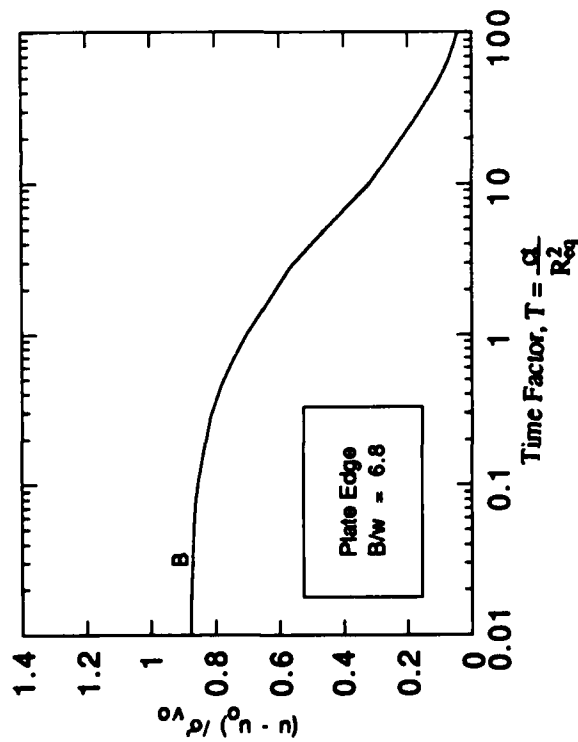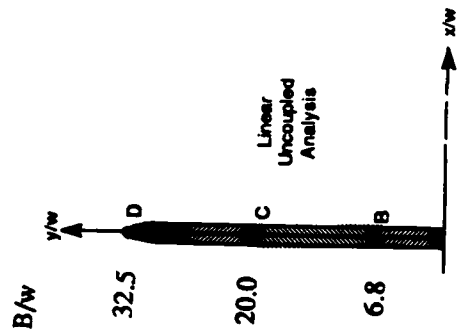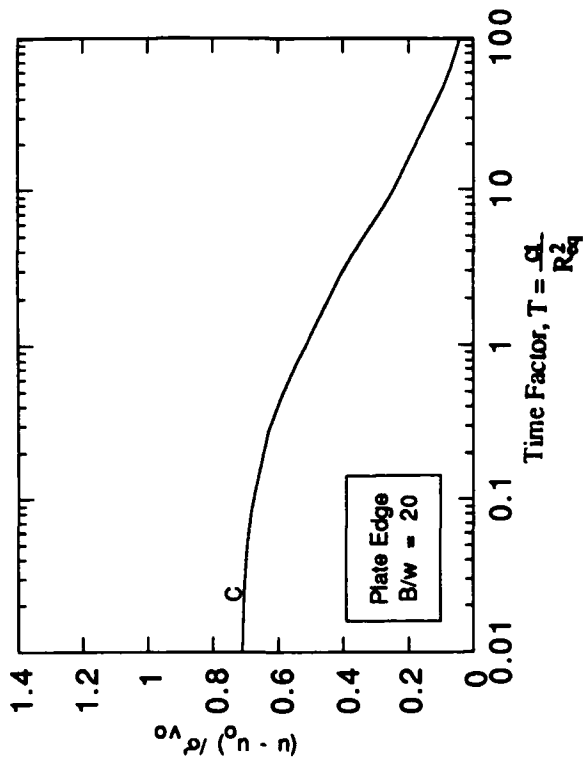
Figure 3.23. Effect of plate aspect ratio on dissipation of excess pore pressures at plate edge, base case analysis
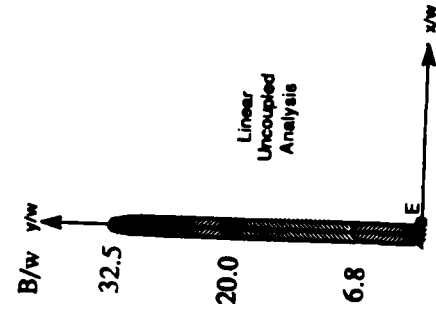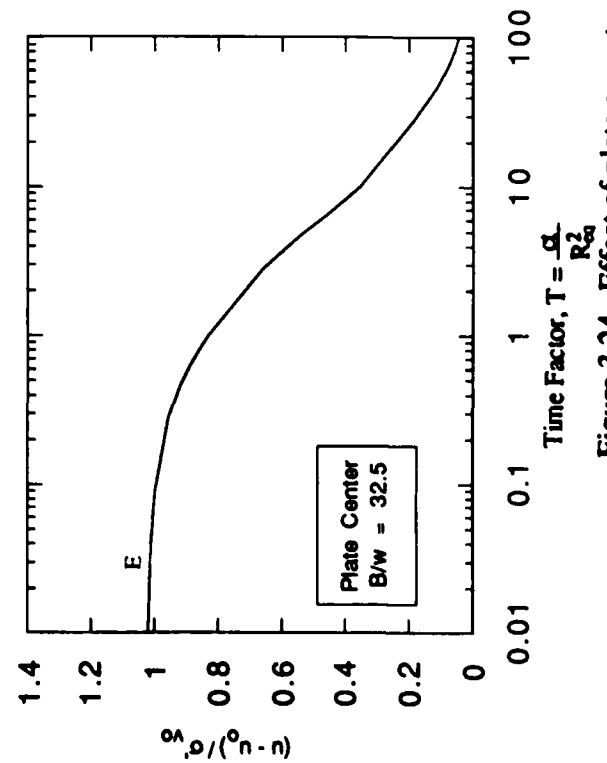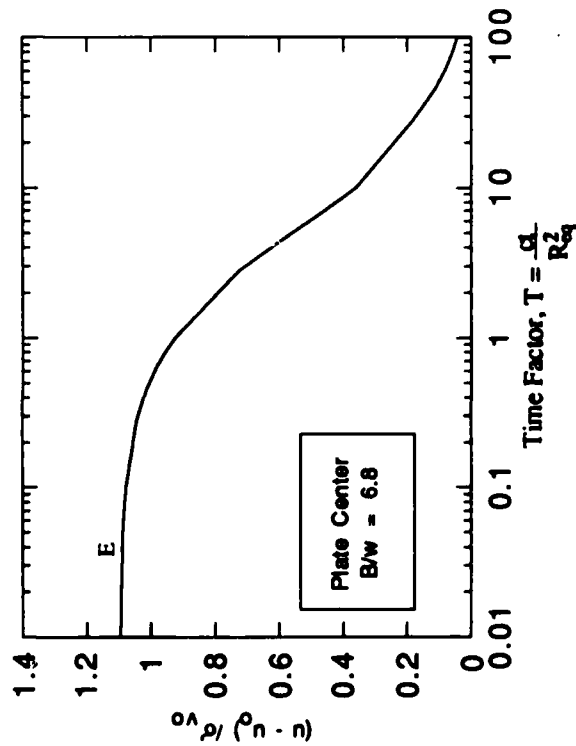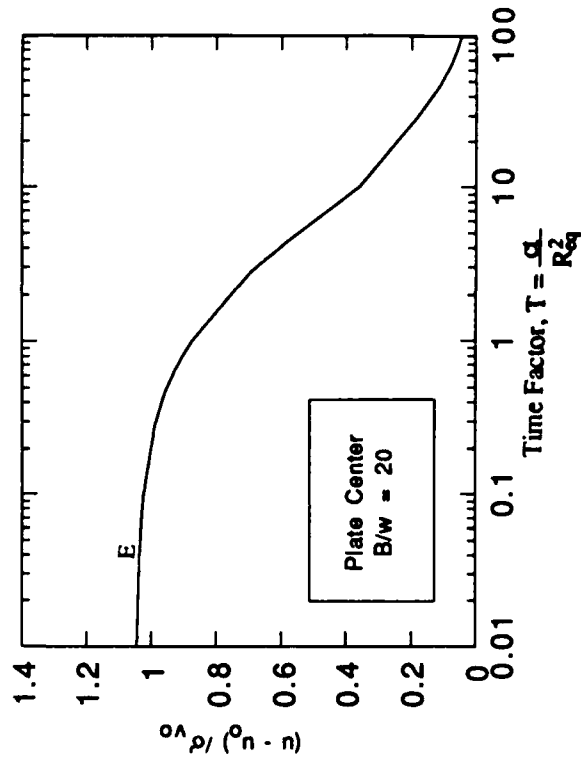
Figure 3.24. Effect of plate aspect ratio on dissipation of excess pore pressures at plate center, base case analysis
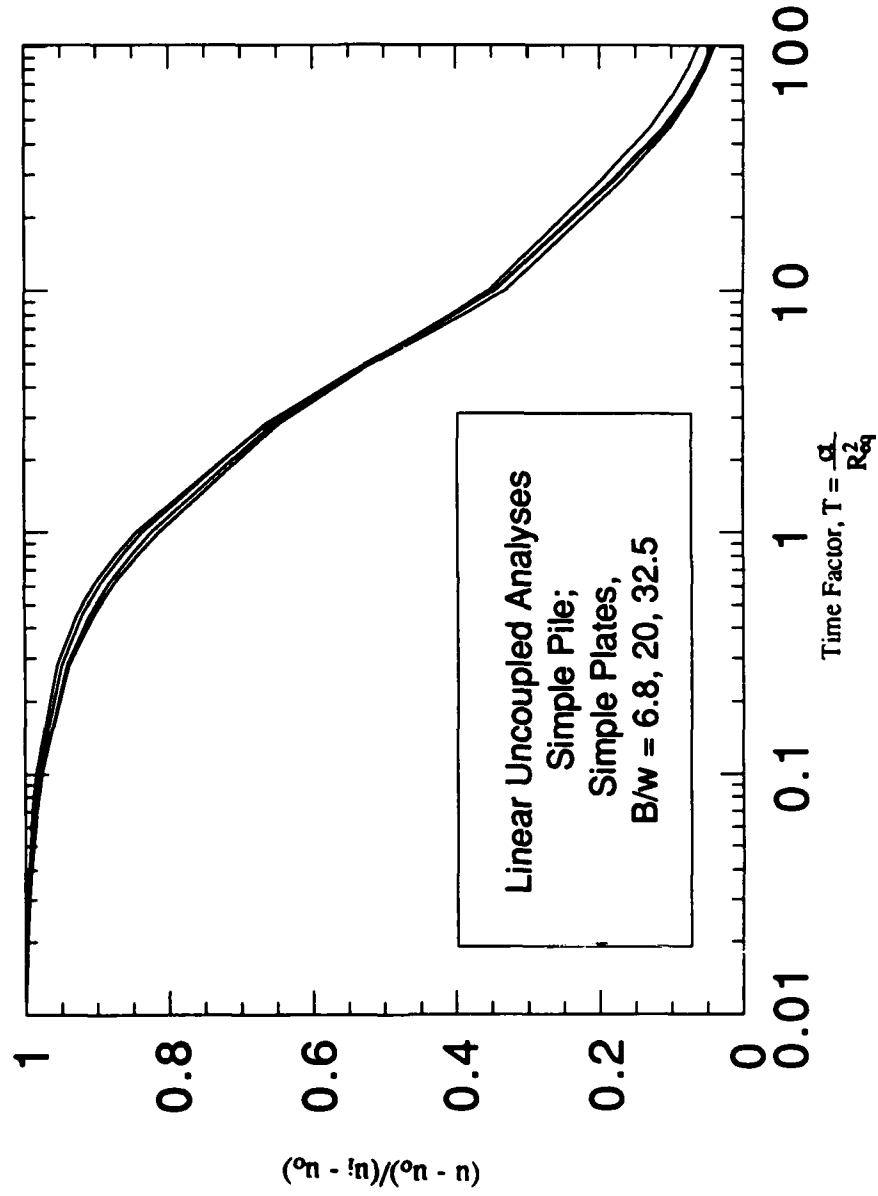
Figure 3.25. Effect of plate aspect ratio on normalized dissipation of excess pore pressure at center of plate, base case analysis

4. THE PIEZOCONE

4.1 INTRODUCTION

The piezocone penetrometer (CPTU; Janbu & Senneset, 1974; Baligh et al., 1981; DeRuiter, 1981) combines the measuring capabilities of: a) the electrical cone penetrometer (CPT; DeRuiter, 1971 Fig. 4.1a), which provides continuous measurement of tip resistance, q_c, and local skin friction, f_s, (acting along a friction sleeve); and b) the pore pressure probe (PPP, Fig. 4.1b), which measures pore pressures, u, both during penetration and in subsequent dissipation tests (Wissa, 1975; Torstensson, 1975). The simultaneous measurement of pore pressure and tip resistance gives the piezocone unique capabilities for estimating soil stratification and spatial variability (Baligh et al., 1980; Jones et al., 1981; Senneset & Janbu, 1984; Campanella & Robertson, 1988). The test is also widely used to estimate engineering properties using various empirical correlations. In clays, measurements of tip resistance and pore pressures during penetration are correlated with undrained shear strength and stress history; while pore pressure dissipation data are used to estimate consolidation and permeability properties. This chapter focuses on the prediction and interpretation of engineering properties during cone penetration.

In previous studies, the Strain Path Method (SPM; Baligh & Levadoux, 1980; Baligh, 1985a, b) has provided a rational framework for predicting piezocone penetration in clays, and hence establishing a basis for interpretation of the measured data. The previous studies have included the following:

1. Baligh and Levadoux (1980) presented predictions of the stresses and pore pressures around 60^0 and 18^0 cone penetrometers: Shear stresses in the soil were obtained using a total stress, multi-surface plasticity model (MIT-T1), with input parameters selected for K_0-normally consolidated Boston Blue Clay. Changes in mean total stress were estimated from radial equilibrium (c.f. Chapter 2 of this report), while a separate model was introduced for shear induced pore pressures.

2. Baligh (1985a) obtained upper bound, closed form expressions for the penetration resistance of 'simple pile' geometry, q_{sp}, based on the energy required to achieve steady penetration. These studies showed that the undrained point resistance at a particular depth depends on a) the level of total confining stress (σ_0, in-situ), b) the undrained shear strength of the clay, c) the shear strain at yield, and d) the shear

stiffness at small strain levels. Preliminary comparisons of the predicted point resistance indicated reasonable agreement with typical cone measurements; however, the analysis does not consider important aspects of soil behavior in the plastic region around the penetrometer and hence cannot be used for more detailed, site specific evaluations (Whittle et al., 1989).

3. Baligh (1986b) and Elghaib (1989)[1] have presented predictions of stress conditions at the tip of a 'simple pile' penetrometer[2] based on the strain history of soil elements along the centerline (ahead of the advancing penetrometer). For these assumptions, a simplified 'centerline analysis' was developed in order to predict the tip resistance and tip pore pressures during steady penetration, based on known soil properties. From these analyses, Elghaib (1989) has shown that the undrained shear strength, c_{uTC} (in triaxial compression) can be interpreted from measurements of either the tip resistance or tip pore pressures. The proposed interpretation method was shown to predict c_{uTC} to within ±25% using data from nine well documented sites.

In this chapter, comprehensive strain path predictions of effective stresses and pore pressures are presented for piezocone penetration in normally and lightly overconsolidated clays (OCR≤4). In the current work, distributions of effective stresses are obtained from generalized soil models[3] (MCC and MIT-E3); while excess pore pressures are found using the finite element solutions of the (modified) Poisson equation (described in Chapter 2). A detailed interpretation of the predictions then provides a basis for establishing possible correlations between piezocone measurements and soil properties. The predictions are also compared directly with measured data from well documented sites in order to establish the capabilities and limitations of the strain path analyses.

4.2 BACKGROUND

4.2.1 Cone Design and Testing Procedures

The basic geometry of the standard electrical cone (Fig. 4.1) comprises a

---

[1] This work has been summarized in Whittle et al. (1989).

[2] In this case the tip resistance, $q_c = (\sigma_{zz})_{tip}$.

[3] These same effective stress soil models will also be used in subsequent analysis of pore pressure dissipation and membrane expansion procedures (e.g. pressuremeter, etc.).

penetrometer with 10 cm^2 base area (i.e., shaft radius, R $\approx$ 1.78 cm) and apex angle, δ = 60°. The friction sleeve is located immediately behind the cone and has a surface area A_s=150 cm^2. The cone is installed at a standardized penetration rate, u$\approx$2 cm/sec. Baligh (1986c) has presented preliminary analyses which show that for the standard cone test penetrated at a velocity of 2cm/sec (i.e., u/R=1.1 sec^{-1}):

1. In low permeability clays (k<10^{-7} cm/sec), there is effectively no migration of excess pore water pressure during steady cone penetration (i.e., undrained).

2. In clean sands (<10% by weight smaller than ASTM sieve no.200) with permeability, 10^{-4} $\leq$ k $\leq$ 10^{-1} cm/sec, there is no measureable excess pore pressure during penetration due to the free migration of pore fluid (i.e., fully drained).

3. For intermediate classes of soils such as silt and 'dirty sands'[4] (with 10^{-7} $\leq$ k$\leq$ 10^{-4} cm/sec) partial dissipation of excess pore pressures will occur during penetration.

Continuous penetration of the cone is generally possible over 1m intervals, separated by short delays (Δt=15 to 90 sec) during which the next push rod is assembled. These delays introduce small discontinuities in the tip and pore pressure profiles due to partial dissipation of pore pressures.

There is currently no standardized design for either the dimensions or location of the porous filter elements used to measure penetration pore pressures (Fig. 4.2). However, most piezocones used in practice have a single porous element located either at the base or on the face of the cone (Fig. 4.3). Baligh and Levadoux (1980) have shown both experimentally and theoretically (based on strain path analyses) that there are large spatial variations in the excess pore pressures which develop around the cone during steady penetration. Thus, variations in the location of porous elements have provided a major source of confusion in the interpretation of engineering properties using piezocone pore pressures. The debate over optimal filter location is still unresolved.

Baligh (1986c) concludes that pore pressure measurements at the cone tip are reliable and repeatable, and provide the most sensitive indicators of soil stratification. Based on strain path analyses, the tip pore pressures are primarily controlled by a small number of soil properties (from centerline analyses; Elghaib, 1989; Whittle et al., 1989) and can be used to interpret undrained shear strength in clays. There are two main disadvantages of the tip location: a) the porous element is vulnerable to damage and abrasion; and b) the

---

[4]i.e., high proportion of fine materials.

measured pore pressure response can be significantly affected by the compressibility of the filter element (Battaglio et al. 1986). Many authors now support the view that mid-cone filter locations offer almost as reliable a profiling capability, but are less vulnerable to damage.

Tavenas et al. (1982), and Robertson and Campanella (1984) advocate the filter located at the base of the cone (especially for soil profiling). This location is very convenient for making essential corrections to the measured tip resistance (as discussed below). However, previous experimental and theoretical results have shown that there are large pore pressure gradients acting around the base of the cone[5]. Thus, the repeatability of base pore pressures is an important consideration in the piezocone design.

Wroth (1984) postulated that pore pressures measured at z/R=5-6 above the base of the cone provide the best indicator of stress history. This recommendation was based on the assumption that shear induced pore pressures contribute a significant percentage of the measured pore pressure around the shaft. In contrast, strain path analyses (Baligh, 1986b; Whittle, 1987) show that predictions of shaft pore pressures are strongly influenced by more complex aspects of soil behavior. Thus it is difficult to establish how measured pore pressures are related to soil properties.

In addition to the problems created by non-standardization of piezocone geometry, there are also a number of hardware design issues which have an important influence on the measured/reported data.

1. Load cell resolution:

   Almost all electrical cones are instrumented with a single load cell which can measure penetration resistance in soils ranging from very soft clays to very dense sands (i.e. $100 \leq q_c \leq 30{,}000$ kPa). Thus, it is clear that measurements in soft clays suffer from low resolution of the load cell readings which can have a very significant influence on the reliability of reported tip resistance. More sophisticated designs using two load cells with different ranges have been described by Ridgen et al. (1982) but are not common in practice.

2. Correction of tip resistance:

   When a piezocone is subjected to hydrostatic pressure, a shift occurs in the zero reading

---

[5]Particularly erratic measurements are obtained for highly overconsolidated clays; e.g. Powell & Uglow (1988).

of the load cell (and hence the implied tip resistance[6], DeRuiter, 1981, 1982; Campanella et al., 1982). This is due to unequal areas on which the pore water pressure is acting around the cone (Fig. 4.4a). Therefore the measured tip resistance, q_c, and the sleeve friction, f_s, do not measure the actual resistance offered by the surrounding soil. Correction of the tip resistance is difficult to achieve due to the non-uniformity of pore pressures acting around the cone in soil. Current correction procedures involve: a) estimating the 'apparent' area correction, $a = A_N / A_T$ (Fig. 4.4a) for a given cone design, and b) adjusting the cone resistance reading form test data, q_c, using the penetration pore pressure measured at the base of the cone, u_b, (Fig. 4.4a). Hence the corrected tip resistance is generally reported as:

$$q_T = q_c + (1-a) u_b \qquad (4.1)$$

If pore pressures are not measured at the base of the cone, further empirical modification factors are required[7]. The correction factor can increase the reported tip resistance by up to 20-30% in soft clays.

It is important to note that the apparent area factor is also subject to potential errors. For example, Nyirenda and Sills (1989) have correctly demonstrated that $a \neq A_N / A_T$, but is controlled by the equilibration of forces acting on the cone as shown in figure 4.4b. This figure indicates that the design of the friction sleeve and its O-ring seal can significantly affect the calculation of the correction factor. Thus the most reliable method for correcting tip resistance is to calibrate the cone in a pressurized water chamber.[8]

3. Response of the porous elements

The reliability (accuracy and response rate) of the monitored pore pressures depends largely on the rigidity of the measuring system. In practice, this can be achieved by using a small volume for the measuring 'fluid' and by ensuring that the filter is fully de-aired. Filter materials should contain small pores ($\sim 2\mu m$ in diameter; Smits, 1982) to ensure that the filter can sustain external tension forces (i.e., due to negative pore pressures in the soil). Battaglio et al. (1986) have also shown that the compressibility of the filter element located at the tip of the cone can lead to erroneous pore pressures, especially in stiff clays. This problem can be circumvented by re-locating the filter onto

---

[6]This also occurs in the load cell for the friction sleeve.

[7]For example, Baligh et al. (1980) assume that $0.3 \, u_{tip} \approx (1-a)u_b$.

[8]Even this process may not account for compression of the friction sleeve which occurs in the soil.

the face of the cone.

4.2.2 Interpretation of Engineering Properties of Clays

There are numerous empirical correlations reported in the literature in which piezocone penetration measurements (or ratios of measurements) are correlated with undrained shear strength and/or stress history of cohesive soils. The following paragraphs provide a brief summary of these existing correlations.

4.2.2.1 Undrained Shear Strength

The undrained shear strength, c_u, is commonly estimated from the cone resistance, q_c, (or corrected cone resistance q_T, equation 4.1) using the following equation[9]:

$$c_u = \frac{q_c - \sigma_{v0}}{N_k} \qquad \text{or} \qquad c_u = \frac{q_T - \sigma_{v0}}{N_{kT}} \qquad (4.2)$$

where σ_{v0} is the total overburden pressure, and N_k, N_{kT} are empirical cone factors.

The magnitudes of N_{kT} (or N_k) are backfigured by comparing cone resistance measurements (q_T or q_c) with some reference profile of undrained shear strength. For example, Baligh et al. (1980) report N_k=10-20 (Fig. 4.5a) for uncorrected tip resistance, q_c, correlated with field vane strengths, μc_{uFV} (where μ is a 'standard' correction factor introduced by Bjerrum (1972) based on plasticity index, I_p). Aas et al. (1986) report similar ranges for N_{kT} correlated with c_{uDSS} (i.e. undrained shear strength from laboratory direct simple shear tests[10]) based on data from five sites in Norway, with $1 \leq OCR \leq 8$. However, the same authors report much higher values of N_{kT} (up to 40) for overconsolidated clay when the net cone resistance ($q_T - \sigma_{v0}$) is normalized with the field vane strength (in this case the field vane strength has been corrected using a factor to account for anisotropy, μ_A; Fig. 4.5c). This discrepancy is loosely attributed to 'strain rate affects'. Other researchers (Kjekstad et al., 1978; Lunne et al., 1981, 1985; Thornburn et al., 1981; Rad & Lunne, 1988) report N_{kT}=5-20 using undrained triaxial compression

---

[9]In principle, the corrected tip resistance is preferred. However, due to the uncertainties in the reported correction factors, it may be just as satisfactory to use q_c and accept the intrinsic bias that then exists in the measured data.

[10]From recompression type tests.

data.

Undrained shear strength is also estimated from measured pore pressures using an empirical pore pressure factor, $N_{\Delta u}$:

$$c_u = \frac{u - u_0}{N_{\Delta u}} \qquad (4.3)$$

where u is the pore pressure measured at some (fixed) reference location on the cone. Lunne et al. (1985) report values $4 \leq N_{\Delta u} \leq 12$ from tests on North Sea clays with pore pressures measured at the base of the cone and undrained shear strength, c_{uTC} (from CAUC tests). Robertson et al. (1988) have reported $0 \leq N_{\Delta u} \leq 20$ from test data in the Vancouver area. However, the authors do not specificy the source/type of their reference c_u profile. Their results (Fig. 4.6) also produce similar ranges of N_{kT} ($5 \leq N_{kT} \leq 17$) as reported previously by Baligh et al. (1980).

A third dimensionless cone factor, N_{ke}, was introduced by Senesset et al. (1982) using both tip resistance and pore pressure measurements:

$$c_u = \frac{q_T - u}{N_{ke}} \qquad (4.4)$$

where u is the pore pressure measured at the base of the cone. The authors report values of $N_{ke} = 9 \pm 3$.

In concept, the difference ($q_T - u$) represents some measure of the effective stress acting in the soil close to the cone. In practice, calculated values of N_{ke} are likely to exhibit significant scatter especially in soft clays where $q_T \approx u$, and where there are potentially large errors in the reported magnitude of q_T. Mayne et al. (1990) have recently compiled data from 83 sites in which they show that (for non-fissured clays), $u = 0.53 q_T$ to $0.73 q_T$ (for intact clays; Figs. 4.7a,b), where u is measured either on the face or at the base of the cone. These results suggest that ($q_T - u$) = $0.27 q_T$ to $0.47 q_T$, and hence imply that c_u is proportional to the measured cone resistance q_T!

4.2.2.2 Stress History

The most widely used correlation for OCR is based on the ratio of excess pore pressure to net tip resistance, B_q, proposed by Senneset et al. (1982), and Jones and Rust (1982):

$$B_q = \frac{u - u_0}{q_T - \sigma_{v0}} \qquad (4.5)$$

In the standard definition of B_q, u is measured at the base of the cone, while q_T is the corrected tip resistance. Wroth (1984) attempts to rationalize the use of B_q by making the analogy between the shearing of the soil due to cone penetration and the failure of soil in laboratory shear tests using the following reasoning:

1. OCR is well correlated with the invariant pore pressure parameter, a_f measured at failure in laboratory undrained shear tests (Henkel, 1960)[11], where:

$$a_f = (\Delta u - \Delta \sigma)/\Delta \tau = \Delta u_s/\Delta \tau \qquad (4.6)$$

Δu_s is the shear induced pore pressure, $\Delta \sigma$ is the change in mean total stress, and $\Delta \tau$ is the change in octahedral shear stress.

2. For cone penetration, Wroth asserts that the maximum shear stress should be specified as a difference of two total stresses and hence advocates $(q_T - \sigma_{v0})$ to estimate undrained shear strength. He also speculates that $\Delta u_s/\Delta u$ reaches a maximum value at locations above the base of the cone.

3. The parameter B_q is then presented as a 'best available' ratio which is conceptually similar to a_f.

These arguments are, however, misleading for two main reasons: a) at low OCR ($\leq$4-8), Δu_s is only a small proportion of the total excess pore pressure ($\Delta u_s/\Delta u \approx$20-30%; Baligh, 1986b); while b) $(q_T - \sigma_{v0})$ is controlled by the shear stress at failure (τ_f) and not by the change in shear stress ($\Delta \tau$).

Based on these arguments, there is not a strong fundamental basis for correlating B_q to OCR, and the published correlations should be regarded as purely empirical. Jamiolkowski et al. (1985) and Robertson et al. (1986, 1988) have evaluated B_q correlations from a number of sites (e.g. Fig. 4.8[12]) and concluded that the value of B_q reflects changes of OCR within a soil deposit (e.g. Fig. 4.8a). However, due to differences in sensitivity, and pre-consolidation mechanism, there is no unique relationship between B_q and changes in OCR.

Mayne (1986, 1987) has presented direct correlations for OCR using: a) net normalized tip resistance, $(q_c - \sigma_{v0})/\sigma'_{v0}$ (uncorrected tip resistance; Fig. 4.9a); and b) normalized excess pore pressures, $(u-u_0)/\sigma'_{v0}$ (Fig. 4.9b). Assuming that natural soils exhibit

---

[11]a_f is a generalized version of the A parameter introduced by Skempton (1954) for triaxial shear tests.

[12]The data in figure 4.8b show that $0.3 \leq B_q \leq 1.0$. However, the same authors (fig. 4.6) report much higher B_q values (up to 1.6) in other published work from the same sites. Thus there appear to be discrepancies in the measured data reported in the literature.

normalized shear strength properties[13] (as used in SHANSEP analysis, Ladd & Foott, 1974); or critical state soil mechanics, Schofield & Wroth, 1968), then:

$$\frac{q_T - \sigma_{v0}}{\sigma'_{v0}} = a_1(OCR)^m \qquad (4.7a)$$

or

$$\frac{u - u_0}{\sigma'_{v0}} = a_2(OCR)^m \qquad (4.7b)$$

where a_1, a_2 are empirical coefficients backfigured from test data and m=0.8±0.05 (Ladd, 1989).

However, Mayne (1987) implicitly assumes m=1[14] and reports $\kappa = 1/a_1 = 0.2$ to 0.6 (Fig. 4.9a). These results are consistent with previous correlations for undrained strength (i.e. using N_{kt}=5 to 15, and $S=(c_{uTC}/\sigma'_{vc})_{NC}=0.3$).

A third type of correlation proposed for OCR uses pore pressures measured concurrently at two locations on the cone. For example, Robertson et al. (1986) sketch 'conceptual' pore pressure distributions around the cone based on comparisons of data from two highly overconsolidated clays (London clay and Taranto clay) with typical results for a 'normally consolidated clay' (Fig. 4.10a). These results prompted Sully et al. (1987) to correlate $(u_t - u_b)/u_0$ with OCR with surprising apparent success at low OCR[15] (Fig. 4.10b) and huge scatter at high OCR (Fig. 4.10c), while Robertson et al. (1989) have adopted u_t/u_b (Fig. 4.11a) whose true scatter is revealed by Mayne et al. (1990) (Fig. 4.11b).

Finally, Konrad and Law (1987) have presented a semi-empirical interpretation of tip resistance and tip pore pressures, (based on similar concepts to the centerline analysis described by Whittle et al, 1989). Konrad and Law estimate that the vertical effective stress at yield, σ'_{yc} (i.e. the vertical stress at the elasto-plastic boundary) is identical to the vertical effective stress at the tip of the cone, $(\sigma'_v)_{tip}$ (Fig. 4.12a). However, in order to use base pore pressures, u_b, to estimate σ'_{yc}, they introduce additional correction factors to account for cone geometry and interface friction:

---

[13]i.e. For normalized soil behaviour: $a_1 = SN_{kt}$ and $a_2 = SN_{\Delta u}$, where $S=(c_u/s'_{vc})_{NC}$ is the undrained strength ratio of the normally consolidated clay.

[14]Absolute values of m are masked by the scatter in the empirical factors a_1, a_2.

[15]The source of the reported OCR values is not given.

$$\sigma'_{yc} = \frac{q_T - \alpha u_b}{1 + M \tan\phi' \cot\frac{\delta}{2}} \qquad (4.8)$$

where ϕ' is the friction angle for shearing of normally consolidated clay at large strain levels, $\delta/2$ is the half apex angle, M is an interface friction factor and α is used to correct the base pore pressures (the authors propose M=0.5 to 1.0 and α=1.0 to 1.33; but actually use M=1.0, α=1.0). Finally, σ'_{yc} is correlated directly with σ'_p obtained from laboratory oedometer tests on five sensitive Canadian clays (Fig. 4.12b). The results of the study (Fig. 4.12c) show $0.8 \leq \sigma'_{yc}/\sigma'_p \leq 1.2$, for $1 \leq OCR \leq 5$. For a given site, the OCR can be estimated by iteration using the results from Fig. 4.12b. Preliminary assessment of equation 4.8 by Jamiolkowski et al. (1989) has been generally positive. However, the success of the method depends on the reliability of the measured values of q_T and u_b.

4.3. ANALYTICAL PREDICTIONS

4.3.1 Introduction

The previous sections have shown that there are currently a multiplicity of correlations to estimate undrained shear strength and stress history from piezocone measurements. The authors believe that these divergent correlations and the resulting confusion reflect two problems. One arises due to the lack of standardization of the piezocone design and testing techniques. This problem contributes to excessive scatter in reported tip resistance (i.e., measured versus corrected for unequal area effects) and penetration pore pressures (i.e., location and size of porous filters and their response times). The second problem arises due to lack of understanding of the fundamentals affecting piezocone data, even during fully undrained penetration. That is, which soil properties are most relevant and how should the response vary with tip geometry and location of the porous filter?

In previous analyses (using the Strain Path Method), Baligh (1986b), Elghaib (1989), and Whittle et al. (1989) have proposed that tip resistance and tip pore pressures can be used to estimate the undrained shear strength of clays. In this section, the analyses are extended to include detailed predictions of the stress and pore pressure distributions around a piezocone penetrometer as a function of overconsolidation ratio and of the soil model used to represent clay behavior. The aims of the analysis are: a) to provide insight into

possible relationships (and interrelationships) between piezocone measurements and soil properties (c_u, OCR); and, b) to evaluate more fully the assumptions used in previous centerline solutions. Predictions of effective stresses around the piezocone are achieved using two generalized effective stress soil models:

1. The Modified Cam Clay model (MCC; Roscoe & Burland, 1968) is used as a 'base case' against which the results of a more complex model (MIT-E3) can be compared. Table 4.1 summarizes the input parameters used by MCC and gives specific values (Whittle, 1987, 1990) to describe the behavior of K_0-consolidated Boston Blue Clay.

2. The MIT-E3 model (Whittle, 1987, 1990) was developed to describe more realistically the behavior of K_0-normally and moderately overconsolidated (OCR $\leq$ 8) clays observed in laboratory tests. The MIT-E3 model describes a) strain-softening of clays in undrained shearing, b) anisotropic stress-strain-strength, and c) small strain non-linearity for overconsolidated clays. Table 4.2 summarizes the input parameters used by the model together with selected values for Boston Blue Clay. Detailed evaluations of model predictions have been shown elsewhere (Whittle, 1990b,c).

Finite element solutions of the modified Poisson formulation (Section 2.5) are used to obtain predictions of excess pore pressures around the penetrometers.

4.3.2 Effect of Tip Shape

The tip geometry of the standard piezocone has an apex angle, $2\delta=60^0$. This geometry was adopted to be consistent with earlier standards for the electrical cone (DeRuiter, 1971). However, apart from the early work at MIT (Baligh et al., 1980; Vivatrat, 1978), there have been no detailed studies to evaluate the effects of tip geometry on piezocone predictions.

In recent analytical work (Baligh, 1985, 1986a,b; Elghaib, 1989) it has been assumed that the simple pile geometry can provide a good approximation for the standard 60^0 cone. A major advantage of this assumption is that the soil strains can be obtained in closed form (Baligh, 1985; Teh & Houlsby, 1989). Thus, numerical approximations[16] can be avoided and higher accuracy achieved in the predictions of effective stresses and pore pressures.

Figures 4.13a to d compare strain path predictions of effective stresses and excess pore

---

[16] These include the method of 'sources and sinks' (Baligh and Levadoux, 1980), boundary element/panel methods (Williamson, 1989) or finite differences (Teh, 1987).

pressures for; a) simple pile, b) (standard) 60^0 cone, and c) the 18^0 cone[17]. The solutions are presented for a 'base case analysis' using the MCC model with input parameters corresponding to K_0-normally consolidated BBC ($K_0 = 0.48$). The figures show the following:

1. Predictions of radial effective stress $\sigma'_{rr}/\sigma'_{v0}$ Fig. 4.13a) show similar patterns for all three tip geometries. There are large gradients of $\sigma'_{rr}/\sigma'_{v0}$ in the immediate vicinity of the tip ($\sigma'_{rr}/\sigma'_{v0} \approx 0.2$ at the tip for all three shapes) and immediately above the base of the cone. The radial effective stress reaches a maximum value, $\sigma'_{rr}/\sigma'_{v0} = 0.8$, and is almost constant along the upper face of the cone. Along the shaft, $\sigma'_{rr}/\sigma'_{v0} \approx 0.2\text{-}0.3$ for all three tip shapes[18], and are significantly less than $K_0 = 0.48$ which exists far from the penetrometer.

2. For the selected base case analysis, changes in the mean effective stress[19], σ'/σ'_{v0}, (Fig. 4.13b) are controlled exclusively by the magnitude of the octahedral shear strain, due to the isotropic yield behavior of the MCC model[20]. As a result, there are no changes in the shear induced pore pressures predicted around the surface of the penetrometer for the three geometries considered.

3. The cavity shear stress $(\sigma'_{rr} - \sigma'_{\theta\theta})/2\sigma'_{v0}$ (i.e. q_h, the maximum shear stress acting in a horizontal (r, θ) plane) (Fig. 4.13c) reaches a maximum value ($q_h/\sigma'_{v0} \approx 0.3$) close to the base of the 60^0 cone and simple pile tip. However, for the 18^0 cone, maximum cavity shearing occurs over the full face of the cone. At locations above the base, $q_h/\sigma'_{v0} \approx 0$ for the simple pile, while $q_h/\sigma'_{v0} < 0$ for the 18^0 and 60^0 cones. These reductions in q_h around the shaft can be attributed to details of the strain paths (see Section 3.2)[21].

4. Figure 4.13d shows that large excess pore pressures $(u-u_0)/\sigma'_{v0} > 2\text{-}3$ are predicted close to the tips of the penetrometers for all three geometries. For locations around the shaft (e.g. $z/R \approx 15\text{-}20$) the magnitude ($\Delta u/\sigma'_{v0} \approx 1.2$ at the shaft) and distribution of excess pore pressures are very similar and are not affected by tip geometry. For

---

[17]The 18^0 cone was used extensively in field tests presented by Baligh et al. (1980). The standard dilatometer (Chapter 5) also has an apex angle $\delta \approx 18\text{-}20^0$.

[18]At locations close to the shaft, small differences in effective stresses (Fig. 4.13a) may be due to numerical errors associated with the 18^0 and 60^0 cones.

[19]The shear induced pore pressure, $\Delta u_s \approx -\Delta\sigma'$.

[20]For the base case analysis, $\sigma'/\sigma'_{v0} = 0.653$ at K_0 conditions and 0.475 at critical state conditions.

locations closer to the tip, there are very high gradients of excess pore pressures which make interpretation of the contours very difficult. However, it can be seen from the shape of the contours that the excess pore pressures are approximately constant between the tip of the penetrometer and the base of the cones. The distribution of excess pore pressures are very similar at all locations for the simple pile and 60^0 cones. For the 18^0 cone, however, the distribution of excess pore pressures is significantly different. These results imply that the simple pile solutions cannot be used to simulate conditions around the tip of a sharp cone.

Figure 4.14 compares in more detail the excess pore pressures predicted for the three geometries for three different overconsolidation ratios of the soil (OCR = 1, 2, and 4). The excess pore pressures are reported at locations a) along the centerline (ahead of the tip) and surface of the three penetrometer geometries, and b) radially around the shaft of the penetrometers at steady state conditions (far above the tip of the penetrometer):

1. Distributions of excess pore pressure, predicted for the simple pile and 60^0 cone geometries, are very similar at all locations[22]: the maximum excess pore pressures occur at the tip of the penetrometers and match to within 1% at all OCR's. These results show that prediction of standard piezocone tip pore pressures can be reliably estimated from simple pile solutions, and confirms the hypothesis used in the centerline analyses presented by Elghaib (1989).

2. There are small variations in excess pore pressures ($10\pm$ %) at locations around the face of the 60^0 cones and simple pile. Thus, the pore pressures measured by a filter located on the face of the standard piezocone should measure very similar pore pressures to one located exactly at the tip.

3. For the 60^0 cone, there are severe gradients of excess pore pressures predicted close to the base of the cone (z/R $\approx$ 1.7). These effects become more pronounced as OCR increases. In contrast, for the simple pile, there is a more gradual decrease in excess pore pressures in this same region. This result indicates that pore pressures measured at or close to the base of a 60^0 cone can exhibit significant scatter depending on the exact location and size of the porous filter.

4. For the 18^0 cone, excess pore pressures are approximately constant over the face of the cone for z/R $\geq$ 1.5 ($\Delta u_{max}/ \sigma'_{v0}$ occurs close to the base of the cone, z/R $\approx$ 6.3) and are

---

[22]Differences up to 15% reported around the shaft may be due, in part, to numerical errors for the 60^0 cone.

similar in magnitude to the maximum pore pressures predicted by the 60^0 cone and simple pile geometry. There are large gradients of excess pore pressures very close to the tip of the 18^0 cone ($0 \leq z/R \leq 1.5$). Thus, tip pore pressures (at $z/R = 0$) for the 18^0 cone will be less reliable than those measured on the face of the cone.

The results in figures 4.13 and 4.14 have shown the similarity of effective stresses and excess pore pressures for the simple pile and 60^0 cone geometries. Based on these predictions, it can be expected that the tip resistance[23], q_c, will be similar for the two geometries:

$$q_c = \frac{1}{\pi R^2} \int (p_n \sin \alpha + p_t \cos \alpha) \, dA \qquad (4.9)$$

where p_n, p_t are the normal and tangential (total) interface tractions acting around the penetrometer face; α is the cone half-angle; and A is the surface area of the face.

The distributions of interface tractions are computed from the predicted effective stresses and pore pressures (e.g., Fig. 4.13 for OCR = 1 case). Table 4.3 summarizes the normalized net cone resistance (q_c - σ_{v0})/ σ'_{v0} for: a) the simple pile, b) the 60^0 cone penetrometer, and c) the centerline analyses, $q_c = (\sigma_{zz})_{tip}$, used by Elghaib (1989) (for a simple pile geometry). The results show that the tip resistance of the simple pile is typically 5 - 10 % larger than the tip resistance of the 60^0 cone. For the base case analyses, centerline solutions compute a tip resistance which is approximately the average of the simple pile and 60^0 cone values. These results show that the much simpler centerline approximation can be used to provide reasonable estimates of tip resistance. However, this conclusion from analyses using the MCC soil model needs to be checked for a more realistic soil model (such as MIT-E3).

Based on the above comparisons, the simple pile geometry can be used reliably to estimate the performance of a standard piezocone with 60^0 apex angle. Hence, the simple pile geometry is used throughout the remainder of this chapter.

4.3.3 Effect of Stress History

Figures 4.15a to d show predictions of the effective stresses and pore pressures around

---

[23]Note: $q_c \approx q_T$ in analytical predictions.

the simple pile for the base case analysis (MCC model, K_0-consolidated BBC) at OCR's = 1, 2 and 4. The results show the following:

1. Excess pore pressures, $\Delta u/\sigma'_{v0}$ (Fig. 4.15d) increase very significantly with OCR. At the tip of the simple pile, excess pore pressures increase from $\Delta u/\sigma'_{v0} = 2.7$ at OCR = 1, to 6.2 at OCR = 4^{24}. More modest changes occur at locations around the pile shaft ($\Delta u/\sigma'_{v0} = 1.2$ at OCR = 1, to 2.3 at OCR = 4)[25]. These results show clearly that filter locations on the tip or face of the piezocone should be more sensitive to changes in OCR in a particular deposit than filters located on the shaft. More detailed study of the predictions in figure 4.15d shows that as OCR increases the zone of disturbance (i.e. of excess pore pressures) decreases. This result can be attributed, in large part, to linear pre-yield behavior of the MCC model[26].

2. Contours of radial effective stress, $\sigma'_{rr}/\sigma'_{v0}$ (Fig. 4.15a) show spatial variations that are qualitatively similar for all OCR's. Maximum values of $\sigma'_{rr}/\sigma'_{v0}$ occur on the penetrometer at $z/R \approx 0$ to 0.5. For locations around the shaft (at $z/R > 10$), the radial effective stress is lower than K_0 at OCR=1 (i.e. $\sigma'_{rr}/\sigma'_{v0} = 0.3$ vs. $K_0 = 0.48$), but is higher than K_0 at OCR = 4 (i.e. $\sigma'_{rr}/\sigma'_{v0} = 1.1$ vs. $K_0 = 0.75$). It is also important to note that there are large variations in radial effective stresses in the region $0 \leq z/R \leq 7.5$ where the friction sleeve is located in standard cone designs. These results may account for some of the scatter observed in measurements of f_s.

3. Changes in mean effective stress (i.e. shear induced pore pressures) are related to the critical state conditions described by the MCC model. The magnitude of σ'/σ'_{v0} increases substantially with OCR, but is approximately constant at all locations around the simple pile as the large strains produce critical state conditions. Similarly, contours of cavity shear stress, q_h/σ'_{v0} (Fig. 4.15c) are qualitatively similar for all OCR's.

4.3.4 Effect of Soil Model

Whittle (1987, 1990b) has shown that more realistic predictions of the behavior of K_0-consolidated BBC (with $1 \leq$ OCR ≤ 8) measured in laboratory tests can be achieved using the MIT-E3 soil model. Figures 4.16a to d show predictions of the effective stresses and

---

[24]There are also large increases in tip resistance as shown in Table 4.3.

[25]Similar results are also obtained for 18^0 and 60^0 cones in Fig. 4.14.

[26]i.e. for $E < E_y$, the yield strain, MCC predicts no excess pore pressures in the soil.

excess pore pressures around the simple pile for OCR's = 1, 2 and 4. When compared with the predictions for the MCC model (Fig. 4.15) the following effects of soil model can be observed:

1. At a given OCR, the MIT-E3 model predicts much lower values of radial effective stress, $\sigma'_{rr}/\sigma'_{v0}$ (Fig. 4.16a) acting on the penetrometer than MCC. At OCR's = 1 and 2, $\sigma'_{rr}/\sigma'_{v0} \leq 0.3$ at all locations around the simple pile. At OCR = 4, the pattern of radial effective stress contours is similar for both MIT-E3 and MCC soil models. These results are due primarily to strain-softening described by MIT-E3.

2. For MIT-E3, the mean effective stress, σ'/σ'_{v0} (Fig. 4.16b) decreases from a maximum value at the tip of the pile, to a minimum value on the pile shaft. Hence, the maximum shear-induced pore pressures are along the pile shaft. These results reflect anisotropic behavior of the MIT-E3 model[27]. These predictions are significantly more complex than results from the MCC model for which 'critical state' conditions are uniquely defined (at a given OCR).

3. Distributions of cavity shear stress, q_h/σ'_{v0} (Fig. 4.16c) predicted by MIT-E3 are qualitatively similar to results for the MCC model and reflect the strain history for the simple pile geometry. Differences in magnitudes of q_h/σ'_{v0} reflect anisotropic shear strength of MIT-E3 (i.e. for shearing in the r-θ plane). Along the shaft ($z/R \geq 5$), $q_h/\sigma'_{v0} => 0$ for both soil models and $1 \leq OCR \leq 4$.

4. For OCR's = 1 and 2, the MIT-E3 model predicts that maximum excess pore pressures (Fig. 4.16d) occur at locations along the face of the cone (excess pore pressures on the face are up to 20% larger than tip pore pressures). These results are shown more clearly in figure 4.17. The excess pore pressures around the face ($-0.5 \leq z/R \leq 1.7$) are up to 40% lower for the MIT-E3 model as compared to MCC results. These differences are due primarily to strain softening and anisotropic behavior of MIT-E3, as described above[28]. At locations far above the tip, however, the two soil models give very similar predictions of excess pore pressures acting on the shaft of the penetrometer. The MIT-E3 model also predicts a much larger zone of disturbance (excess pore pressure) around the penetrometer, due primarily to small strain non-

---

[27]In this case, σ'/σ'_{v0} is no longer uniquely defined at critical state conditions. Similar results were also presented by Baligh and Levadoux (1980) for the anisotropic MIT-T1 total stress soil model.
[28]The predictions shown in Fig. 4.16d also imply limitations in the centerline analyses which require further investigation.

linearity. At OCR = 4, the maximum excess pore pressures predicted by MIT-E3 are only 10% lower than those for the MCC model. In this case, strain softening effects are minimized and inelastic behavior occurs much closer to the pile, hence differences between the two soil models become less significant.

4.3.5 Summary

The analytical predictions described in the previous sections provide a basis for evaluating which engineering properties of cohesive soils can be estimated from piezocone measurements and what interpretation techniques are best suited for making these estimates. Table 4.4 summarizes the analytical predictions of net tip resistance and excess pore pressures for K_0-consolidated BBC using the two effective stress soil models (MCC and MIT-E3) at OCR's 1, 2 and 4. The assumptions used to construct this table are as follows:

1. The simple pile geometry can be used to simulate stresses and pore pressure distributions around a 60^0 cone penetrometer (Fig. 4.18). Partial predictions for the 60^0 cone are included for comparison.

2. The (net) tip resistance is estimated by integrating the surface tractions from equation 4.9.

3. Four representative locations of pore pressure filter are considered (u_1, u_2, u_3, u_4; Fig. 4.18). It is assumed that the pore pressures measured at the tip or on the face of the cone are very similar in magnitude (u_1) and are equal to the maximum pore pressures predicted analytically.

4. The pore pressure, u_2, is measured at $z/R = 1.73$ for both the simple pile and 60^0 cones. Table 4.4 compares simple pile and 60^0 cone predictions for $(u_2-u_0)/\sigma'_{v0}$ using the MCC model. For the 60^0 cone, a range of values must be specified due to the severe gradients of excess pore pressures in this region (Fig. 4.14).

5. Pore pressure measurements u_3 and u_4 correspond to positions approximately at the top of the standard friction sleeve and at steady state conditions around the shaft, respectively.

Table 4.4 also summarizes ratios of the predicted measurements which have been used previously in empirical correlations (see section 4.2.3).

4.4 INTERPRETATION OF ENGINEERING PROPERTIES FROM PREDICTIONS

In this section, the correlations between undrained shear strength and OCR are compared systematically with (predicted) piezocone measurements.

Correlations can be classified according to: a) the functional relationship between the measurement and soil property of interest; and, b) the range of applicability of the correlation (range of measurements, soil properties and soil types). For an 'ideal' correlation, the measurement is directly proportional to the engineering property of interest and the correlation is universally applicable. Correlations of this type can be evaluated directly from the predictions in table 4.4. However, the existence of more complex functional relationships between the measurement and the soil property can only be evaluated by comparing predictions directly with field data from well-documented sites, as discussed in Section 4.5.

It is important to emphasize that the interpretations described in this section are based on the predictions in table 4.4 and contain certain limitations: a) the analyses have been performed for one particular type of soil (BBC), with $1 \leq OCR \leq 4$; and b) predictions of pore pressures around the piezocone using strain path analyses are obtained by approximate methods (Chapter 2). Differences in predictions from the two soil models can be attributed to complex aspects of soil behavior (e.g., strain softening, anisotropy, etc)[29], and provide initial insight into the effects of soil type on piezocone measurements[30].

4.4.1 Undrained Shear Strength

From the results shown in table 4.4, it can be seen that changes in the undrained strength ratio, c_{uTC}/σ'_{v0} correlate most closely with the net tip resistance, $(q_t - \sigma_{v0})/\sigma'_{v0}$, and tip pore pressures, $(u_1 - u_0)/\sigma'_{v0}$. Excess pore pressures measured at other locations around the cone (u_2, u_3, u_4) are much less sensitive to changes in undrained shear strength. Table 4.5 summarizes the predicted ratios[31], $(q_t - \sigma_{v0})/c_{uTC} = N_k$; $(u_1 - u_0)/c_{uTC} = N^1_{\Delta u}$; and $(u_2 - u_0)/c_{uTC} = N^2_{\Delta u}$. For an ideal correlation, N_k (or $N^i_{\Delta u}$) should be constant for all

---

[29]However, both MCC and MIT-E3 assume normalized clay behavior and neither describes rate effects (creep or strain rate dependent properties).

[30]Further studies are currently in progress to generate solutions for different types of soil, having stress-strain characteristics quite different from BBC.

[31] The notation N_k , $N^i_{\Delta u}$ (i = 1, 2, ...) is consistent with previous empirical correlations, see section 4.2.

OCR's and for both soil models. The results show the following:

1. For the MCC model, $N_k = 7.75 \pm 0.25$, which is within the lower range of values quoted previously from empirical correlations (e.g. Rad & Lunne, 1988) and from the centerline analyses (Elghaib, 1989). The MIT-E3 model predicts much lower tip resistance factors; $N_k = 4.9 \pm 0.5$. Differences between MCC and MIT-E3 are due, in large part, to the strain softening (sensitive) clay behavior modeled by MIT-E3. These results are consistent with field data reported by Ladanyi and Eden (1969)[32] and others, and also with centerline analyses of Elghaib (1989) (also discussed by Whittle et al., 1989). Overall, the predictions in table 4.5 suggest that undrained shear strength can be correlated directly with the net tip resistance ($q_t - \sigma_{v0}$) for a given soil. Thus, tip resistance measurements can be used to estimate <u>variations</u> in undrained shear strength within a particular soil deposit. However, the analytical predictions imply that the magnitudes of the undrained shear strength can be affected significantly by soil sensitivity.

2. The predicted tip pore pressure factors, $N_{\Delta u}^1$ (Tab. 4.5), are similar in magnitude for both MCC and MIT-E3 models[33] ($N_{\Delta u}^1 = 7.2 \pm 1.2$ for MCC, $N_{\Delta u}^1 = 5.0 \pm 0.6$ for MIT-E3). This result confirms earlier observations (Baligh, 1986b) that shear induced pore pressures represent a small fraction of the excess pore pressures at the tip of the penetrometer; hence, the ratio ($u_1 - u_0$)/($q_t - \sigma_{v0}$) (Tab. 4.4) varies over a very small range (1.29 to 0.77).

3. Excess pore pressures measured at the base of the cone ($u_2 - u_0$) are 10 to 40% smaller than tip pore pressures (Tab. 4.4). Direct correlations with undrained shear strength are significantly less reliable (e.g. $N_{\Delta u}^2 = 5.0 \pm 1.3$ for MCC model) than those predicted for tip pore pressures or net tip resistance.

Further direct correlations can be considered from differences in the measured tip resistance and pore pressures; ($q_t - u^i$)/$c_{uTC} = N_{ke}^i$ (following the notation of Senesset at al., 1982). In this case, results from the MCC model (Tab. 4.5) suggest that c_{uTC} can be estimated from either $N_{ke}^1 = 2.55 \pm 0.05$ or $N_{ke}^2 = 4.9 \pm 0.1$. However, these predictions

---

[32]For sensitive Canadian clays

[33]The predictions actually show more scatter in the $N_{\Delta u}^i$ values than in N_k. In practice, however, errors in correcting the tip resistance ($q_c \Rightarrow q_T$) may make u_1 a more reliable measurement.

can be directly linked to assumptions of critical state behavior in the MCC model. For MIT-E3, values of N_{ke}^i are more variable due to the anisotropic properties described in section 4.3.4. However, N_{ke}^2 values have the same variation as $N_{\Delta u}^1$. Thus, if base pore pressures are measured, $(q_t - u_2)$ provides a somewhat better correlation for undrained shear strength than $(u_2 - u_0)$ according to the MIT-E3 predictions.

4.4.2 Stress History

Using similar reasoning to the previous section, ideal correlations would show that piezocone measurements are proportional to the preconsolidation pressure, σ'_p. In table 4.6, the (predicted) piezocone measurements are normalized by σ'_p to form a set of dimensionless ratios (M_x^i, comparable to N_x^i developed in Tab. 4.5 for c_{uTC}). Inspection of these results shows the following:

1. Qualitatively, the results presented in tables 4.5 and 4.6 are very similar. Hence, $(q_t - \sigma_{v0})$ and $(u_1 - u_0)$ are the most reliable measurements to estimate σ'_p.

2. For a given piezocone measurement (e.g. tip pore pressures, u_1), there is a greater scatter in the corresponding dimensionless ratio for σ'_p than for c_{uTC} (i.e. there is more scatter in $M_{\Delta u}^i$ than in $N_{\Delta u}^i$). Thus, for a given soil deposit, the piezocone is a more sensitive indicator of changes in undrained shear strength, c_{uTC}, than of changes in preconsolidation pressure, σ'_p. However, the use of ratios such as B_q, to estimate OCR, can only be considered by comparison with measured data, as discussed in the next section.

4.5 COMPARISON WITH MEASURED DATA

In this section, the analytical predictions of piezocone measurements (Tab. 4.4) are compared directly with field data for Boston Blue Clay from two separate sites. These comparisons: a) illustrate capabilities and limitations of the strain path analyses for predicting the tip resistance and pore pressure measured by a piezocone; and b) enable the correlations proposed in the previous section to be evaluated.

Piezocone data have been obtained at two test sites containing deep layers of relatively uniform BBC:

1. Station 246 of the I-95 test embankment in Saugus, Massachusetts. This site has been

extensively studied in conjunction with the development of in-situ test devices (e.g. Baligh et al., 1978; Vivatrat, 1978; Morrison, 1984). Extensive field and laboratory testing has been carried out at the site to establish stratigraphy and engineering properties[34] of the site. Figure 4.19a shows the soil profile, index properties and stress history at the site. In-situ overconsolidation ratios range from OCR = 7 at depth d = 30 ft. to OCR = 1.23 at d = 120 ft. However, soil conditions are most uniform from d = 75 to 120 ft. in which the in-situ OCR ranges from 1.2 to 1.35 (Morrison, 1984). Piezocone data at the site, reported by Vivatrat (1978), Baligh et al. (1980), include a) the uncorrected tip resistance, q_c, and b) the tip pore pressures, u_1. Baligh et al. (1981) subsequently corrected the tip resistance using the tip pore pressures:

$$q_T = q_c + 0.3\,u_1 \qquad\qquad (4.11)$$

The corrected tip resistance is presented in this section. Baligh et al. (1980) also report pore pressures at four filter locations around an 18^0 cone penetrometer. These data have been discussed by Whittle and Aubeny (1990) (Appendix B) and are not considered further in this section.

2. South Boston Special Test Program for the Central Artery/Third Harbor Tunnel (CA/T) project[35]. This site, located in South Boston immediately adjacent to the proposed route of a thrird harbour tunnel has been extensively studied by Haley and Aldrich, Inc. and by on-going research at MIT[36]. Figure 4.19b summarizes the index properties and stress history at the test site obtained from extensive oedometer and continuous loading consolidation tests[37]. In-situ OCR's at the site range from OCR $\approx$ 5 at elevation[38] El. = 65 ft. to OCR = 1.1 at El. = -20 ft. The soil is significantly more sensitive below elevation, El. = 20 ft. Piezocone data were obtained at two locations and include: a) corrected tip resistance; and b) pore pressures at the base of the cone, u_2.

Figures 4.20a, b compare analytical predictions of the net tip resistance with the measured data, $(q_T - \sigma_{v0})/ \sigma'_{v0}$ at the two sites:

1. The reported measurements are average values recorded over 5 ft. intervals from the

---

[34]Unfortunately, there are no data for c_uTC at this site.

[35]For the South Boston site, both the piezocone data and the OCR profile are based on preliminary analyses that are currently being refined and show less scatter than indicated in Fig. 4.19b. These data should not be used or reproduced by other persons.

[36]This project is supported by a contract with Haley & Aldrich, Inc., Cambridge, MA.

[37]Laboratory shear strength tests are currently in progress.

[38]Elevations in the figure are quoted with respect to Boston City Base (BCB).

original penetration records. Error bars represent maximum and minimum measured data (over the same interval). Scatter in the overconsolidation ratio is based on the laboratory test data shown in figure 4.19.

2. The analytical predictions are directly from table 4.4. Input parameters for the MCC and MIT-E3 models (Tabs. 4.1 and 4.2, respectively) are based primarily on laboratory test data on resedimented BBC.

3. The most noticeable observation from figure 4.20 is that the test data from the two sites are not consistent. The net tip resistance (at a given OCR) is significantly (30 - 50%) higher at the Saugus site than at South Boston. The source of these differences may be partly attributed to uncertainties in the 'true' tip resistance at the Saugus site. Further investigation is required to establish other possible causes of this discrepancy.

4. The analytical predictions using the MCC model match the measured data very consistently at the Saugus site, while MIT-E3 underpredicts the net tip resistance. At South Boston, good agreement is found using the MIT-E3 model, while MCC overpredicts the measured data. If both sets of measurements are reliable, then these trends suggest significant differences in soil properties at the two sites (either sensitivity or stiffness). In both cases, the net tip resistance increases significantly with OCR as predicted from the strain path analyses.

Figures 4.21a and b compare the analytical predictions with the measured excess pore pressures at the two sites. At the Saugus site the MCC model gives excellent agreement with tip pore pressures $(u_1 - u_0)/\sigma'_{v0}$, while MIT-E3 underpredicts the measurements by up to 50% for OCR $\leq$ 2. The measured data confirm the sensitivity of the tip pore pressures to changes in overconsolidation ratio, as predicted by the strain path analyses. At South Boston, the base pore pressures show very little variation with OCR and hence confirm previous assessments that preconsolidation pressures cannot be reliably estimated from the $(u_2 - u_0)$ data. Analytical predictions for both soil models underpredict the measured data at OCR $\leq$ 4.

The differences in tip resistance and piezocone pore pressures (i.e. $(q_T - u_1)/\sigma'_{v0}$ from Saugus and $(q_T - u_2)/\sigma'_{v0}$ from South Boston; Fig. 4.22) both show well defined trends with OCR. Analytical predictions from the MCC model are in excellent agreement with the data at Saugus, but significantly overpredict the behavior measured at South Boston. In contrast, MIT-E3 gives better matching with South Boston data and does not describe correctly the trends measured at Saugus.

Finally, the ratios of excess pore pressure to net tip resistance are considered in figures 4.23a and b. The data from the Saugus site (B_q^1 ; using tip pore pressures) show a consistent decrease with OCR and range from $B_q^1 \approx$ 1.1 at OCR$\approx$1.2 to 0.8 at OCR = 4. Predictions using the MCC model again show excellent agreement with these data, while MIT-E3 gives a consistently higher value of B_q^1. At South Boston, the B_q^2 ratio (this is the more common ratio presented in empirical correlations after Senneset et al., 1982) shows much larger changes with OCR, ranging from B_q^2 = 1.7 at OCR = 1.1, to 0.6 at OCR $\approx$ 5. In this case both the MCC and MIT-E3 models significantly underpredicts the measured ratio at OCR < 2. However, MIT-E3 predicts higher values of B_q^2 and is more consistent with the trends in the measured data.

Overall, the results in figure 4.23 are consistent with earlier observations that BBC at the South Boston site may exhibit significantly different properties to the material underlying the Saugus site. In particular, the clay at South Boston appears to be more sensitive at low OCR and is therefore better described by the MIT-E3 analyses. More definitive results are expected as further test data become available.

Test Type	Parameter/ Symbol	Physical contribution/ meaning	Boston Blue Clay
Oedometer or CRS	e_0	Void ratio at reference stress on virgin consolidation line	1.12
	λ	Compressibility of virgin normally consolidated clay	0.184
	κ	Compressibility of overconsolidated clay	0.034
Undrained Triaxial (OCR=1; CK_0UC)	ϕ'_{TC}	Critical state friction angles in triaxial compression	33.4^0
K_0-oedometer or K_0-triaxial	2G/K	Ratio of elastic shear to bulk modulus (Poisson's ratio for intial unload)	1.05

Table 4.1 Input Material Properties used by the MCC Model

Test Type	Parameter/ Symbol	Physical contribution/ meaning	Boston Blue Clay	Empire Clay
Oedometer or CRS	e_0	Void ratio at reference stress on virgin consolidation line	1.12	1.26
	λ	Compressibility of virgin normally consolidated clay	0.184	0.274
	C	Non-linear volumetric swelling behaviour	22.0	24.0
	n		1.6	1.75
	h	Irrecoverable plastic strain	0.2	0.2
K_0-oedometer or	K_{0nc}	K_0 for virgin normally consolidated clay	0.48	0.62
K_0-triaxial	2G/K	Ratio of elastic shear to bulk modulus (Poisson's ratio for initial unload)	1.05	0.86
Undrained Triaxial	ϕ'_{TC}	Critical state friction angles in triaxial compression and	33.4^0	23.6^0
Shear Tests:	ϕ'_{TE}	extension (large strain failure criterion)	45.9^0*	21.6^0
OCR=1; CK_0UC	c	Undrained shear strength (geometry of bounding surface)	0.86	0.75
OCR=1; CK_0UE	s_t	Amount of post-peak strain softening in undrained triaxial compression	4.5	3.0
OCR=2; CK_0UC	ω	Non-linearity at small strains in undrained shear	0.07	0.2
	γ	Shear induced pore pressure for OC clay	0.5	0.5
Resonant Column	κ_0	Small strain compressibility at load reversal**	0.001	0.0035
Drained Triaxial	ψ_0	Rate of evolution of anisotropy (rotation of bounding surface)	100.0	100.0

Table 4.2 Input Material Properties used by the MIT-E3 Model

---

* Value is based on data from Ladd & Varallyay (1965). More recent data suggest $\phi'_{TE} \approx 40^0$

** Alternatively use field shear wave velocity test data

Predictions of Net Tip Resistance, $\dfrac{q_t - \sigma_{v0}}{\sigma'_{v0}}$			
OCR	Simple Pile	60^0 Cone	Centerline Analysis
1.0	2.65	2.50	2.61
2.0	4.77	4.44	4.66
4.0	8.43	7.71	8.07

* Effective stresses from MCC model for K_0-consolidated BBC
Pore pressures from modified Poisson formulation

Table 4.3 Comparison of tip resistance predictions using the Strain Path Method

Model	OCR	K_0	Analytical Predictions of Piezocone Measurements					Predicted Ratios of Measurements		
			$\dfrac{q_t - \sigma_{v0}}{\sigma'_{v0}}$	$\dfrac{u_1 - u_0}{\sigma'_{v0}}$	$\dfrac{u_2 - u_0}{\sigma'_{v0}}$	$\dfrac{u_3 - u_0}{\sigma'_{v0}}$	$\dfrac{u_4 - u_0}{\sigma'_{v0}}$	$B_q^1 = \dfrac{u_1 - u_0}{q_t - \sigma_{v0}}$	$B_q^2 = \dfrac{u_2 - u_0}{q_t - \sigma_{v0}}$	$\beta = \dfrac{u_2 - u_0}{u_1 - u_0}$
MCC	1.0	0.48	2.5 - 2.6	2.7	2.0 (2.0 - 2.5)	1.4	1.3	1.04 - 1.08	0.77 - 0.80 (0.8 - 1.0)	0.74 (0.7 - 0.9)
	2.0	0.57	4.4 - 4.7	4.1	2.7 (2.8 - 3.6)	1.8	1.7	0.88 - 0.93	0.58 - 0.61 (0.6 - 0.8)	0.66 (0.7 - 0.9)
	4.0	0.75	7.7 - 8.1	6.2	3.9 (3.9 - 5.3)	2.4	2.3	0.77 - 0.81	0.48 - 0.51 (0.5 - 0.7)	0.62 (0.6 - 0.9)
MIT-E3	1.0	0.48	1.4 - 1.6	1.8	1.6	1.3	1.2	1.12 - 1.29	1.03 - 1.17	0.91
	2.0	0.57	2.3 - 2.5	2.5	2.1	1.6	1.5	1.0 - 1.08	0.85 - 0.93	0.85
	4.0	0.75	5.4 - 6.1	5.9	3.4	2.2	2.0	0.96 - 1.09	0.55 - 0.63	0.58

( ) Predicted values for 60^0 cone tip geometry
* See figure 4.18 for locations of porous filter elements

Table 4.4 Predictions of piezocone measurements for K_0-consolidated BBC

Model	OCR	$\dfrac{c_{uTC}}{\sigma'_{vc}}$	K_0	$N_k = \dfrac{q_t - \sigma_{v0}}{c_{uTC}}$	$N^1_{\Delta u} = \dfrac{u_1 - u_0}{c_{uTC}}$	$N^2_{\Delta u} = \dfrac{u_2 - u_0}{c_{uTC}}$	$N^1_{ke} = \dfrac{q_t - u_1}{c_{uTC}}$	$N^2_{ke} = \dfrac{q_t - u_2}{c_{uTC}}$
MCC	1.0	0.32	0.48	8.0	8.4	6.3	2.6	4.8
	2.0	0.57	0.57	7.8	7.1	4.6	2.5	5.0
	4.0	1.05	0.75	7.5	5.9	3.7	2.6	4.8
Variation*				3%	17%	26%	2%	2%
MIT-E3	1.0	0.33	0.48	4.5	5.5	4.8	2.1	2.7
	2.0	0.54	0.57	4.4	4.4	3.7	1.7	2.4
	4.0	1.05	0.75	5.4	5.6	3.3	0.8	3.1
Variation*				10%	12%	19%	45%	13%

* Variation $= \dfrac{\Delta x}{2\hat{x}} \cdot 100\%$; where $\Delta x = x_{max} - x_{min}$ and $\hat{x} = \dfrac{x_{Min} + x_{Max}}{2}$

Table 4.5 Dimensionless ratios for predicting undrained shear strength

Model	OCR	$\dfrac{c_{uTC}}{\sigma'_{vc}}$	K_0	$M_k = \dfrac{q_t - \sigma_{v0}}{c_{uTC}}$	$M^1_{\Delta u} = \dfrac{u_1 - u_0}{c_{uTC}}$	$M^2_{\Delta u} = \dfrac{u_2 - u_0}{c_{uTC}}$	$M^1_{ke} = \dfrac{q_t - u_1}{c_{uTC}}$	$M^2_{ke} = \dfrac{q_t - u_2}{c_{uTC}}$
MCC	1.0	0.32	0.48	2.6	2.7	2.0	0.9'	1.6
	2.0	0.57	0.57	2.3	2.1	1.4	0.7	1.4
	4.0	1.05	0.75	2.0	1.6	1.0	0.7	1.3
Variation*				13%	26%	33%	13%	10%
MIT-E3	1.0	0.33	0.48	1.5	1.8	1.6	0.7	0.9
	2.0	0.54	0.57	1.2	1.3	1.1	0.5	0.7
	4.0	1.05	0.75	1.4	1.5	0.9	0.2	0.8
Variation*				11%	16%	28%	56%	13%

* Variation $= \dfrac{\Delta x}{2\hat{x}} \cdot 100\%$; where $\Delta x = x_{max} - x_{min}$ and $\hat{x} = \dfrac{x_{Min} + x_{Max}}{2}$

Table 4.6 Dimensionless ratios for predicting pre-consolidation pressure
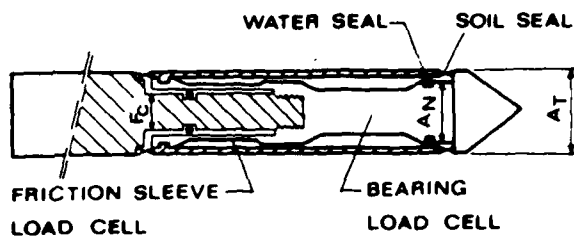
Figure 4.1a. Typical Electrical Cone (Schaap and Zuidberg, 1982)
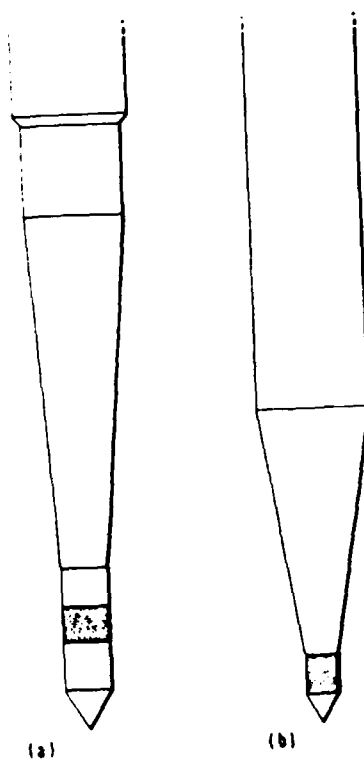
Figure 4.1b. Pore pressure probes (Torstensson, 1975; Wissa et al., 1975)
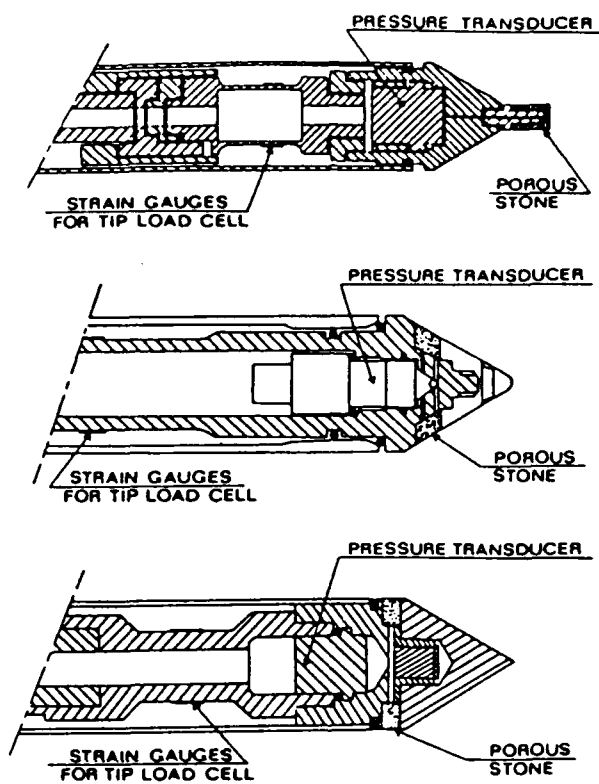
Figure 4.2   Examples of piezocones

Filter Location	Filter Material	Filter Thickness (mm)	Reference
	Stainless Steel	12.8	Wissa (1975)
	Stone	7.0	Wissa (1975)
	Ceramic / Stone	6.5 / 7.0	Zuidberg et al. (1982) / McClelland (1985)
	Stainless Steel / Polyethylene / Stainless Steel	2.5 / 5.0 / 4.0	Torstensson (1982) / Campanella et al. (1982) / v.d. Berg (1982)
	Sintered Bronze	-	McClelland (1985)

Figure 4.3   Pore pressure filter designs for piezocones
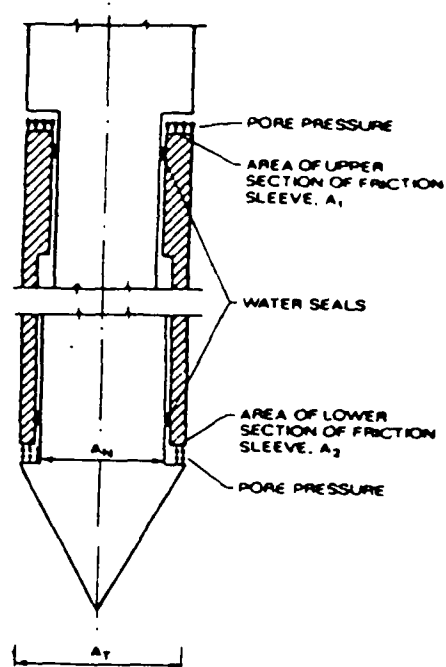
Figure 4.4a. Unequal surface areas of cones (Battaglio and Maniscaldo, 1983)
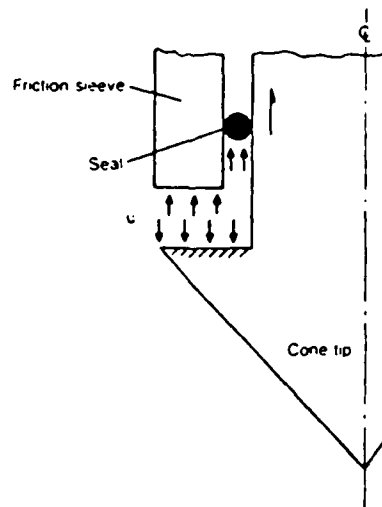
Figure 4.4b   Unequal surface areas of cones (Sills et al., 1989)
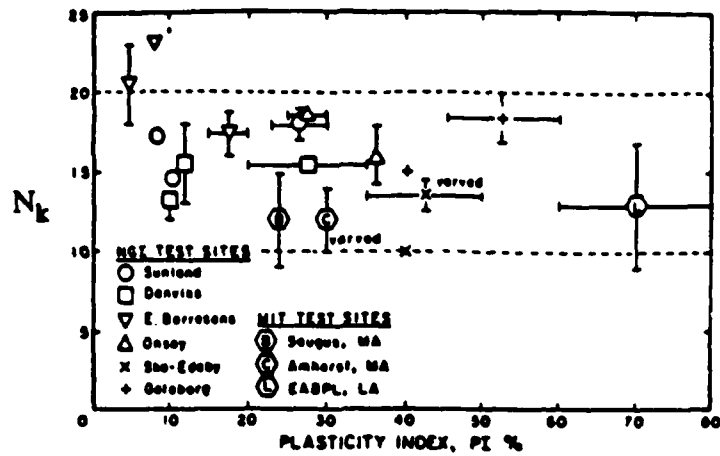
a) $s_u = \mu s_u$ (FV) (From Baligh et al., 1980)
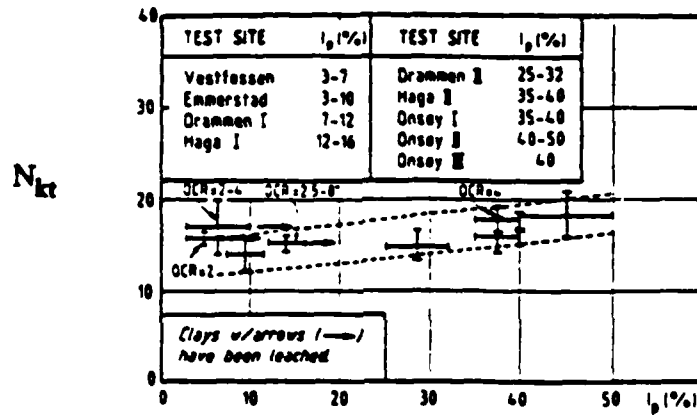
b) $s_u = s_u(LAB) = s_u(DSS)$ (From Aas et al., 1986)
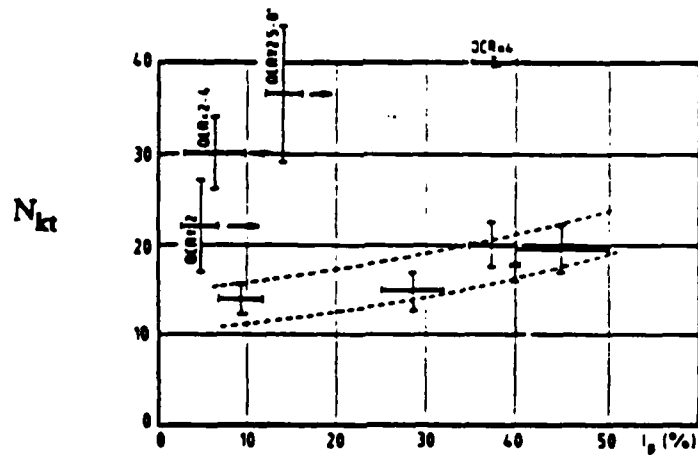
c) $s_u = \mu_A\, s_u(FV)$ (From Aas et al., 1986)

Figure 4.5   Cone resistance factor, N_k
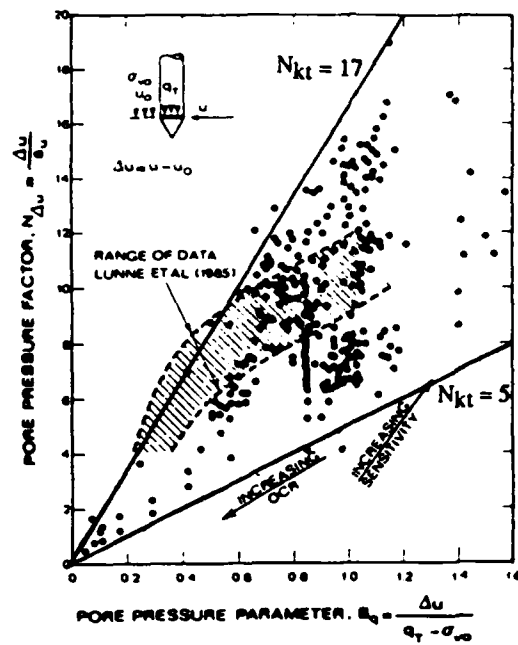
$N_{\Delta u}$ versus B_q (From Campanella and Robertson, 1988)

Figure 4.6   Pore pressure factor, $N_{\Delta u}$ (Robertson et al., 1986)
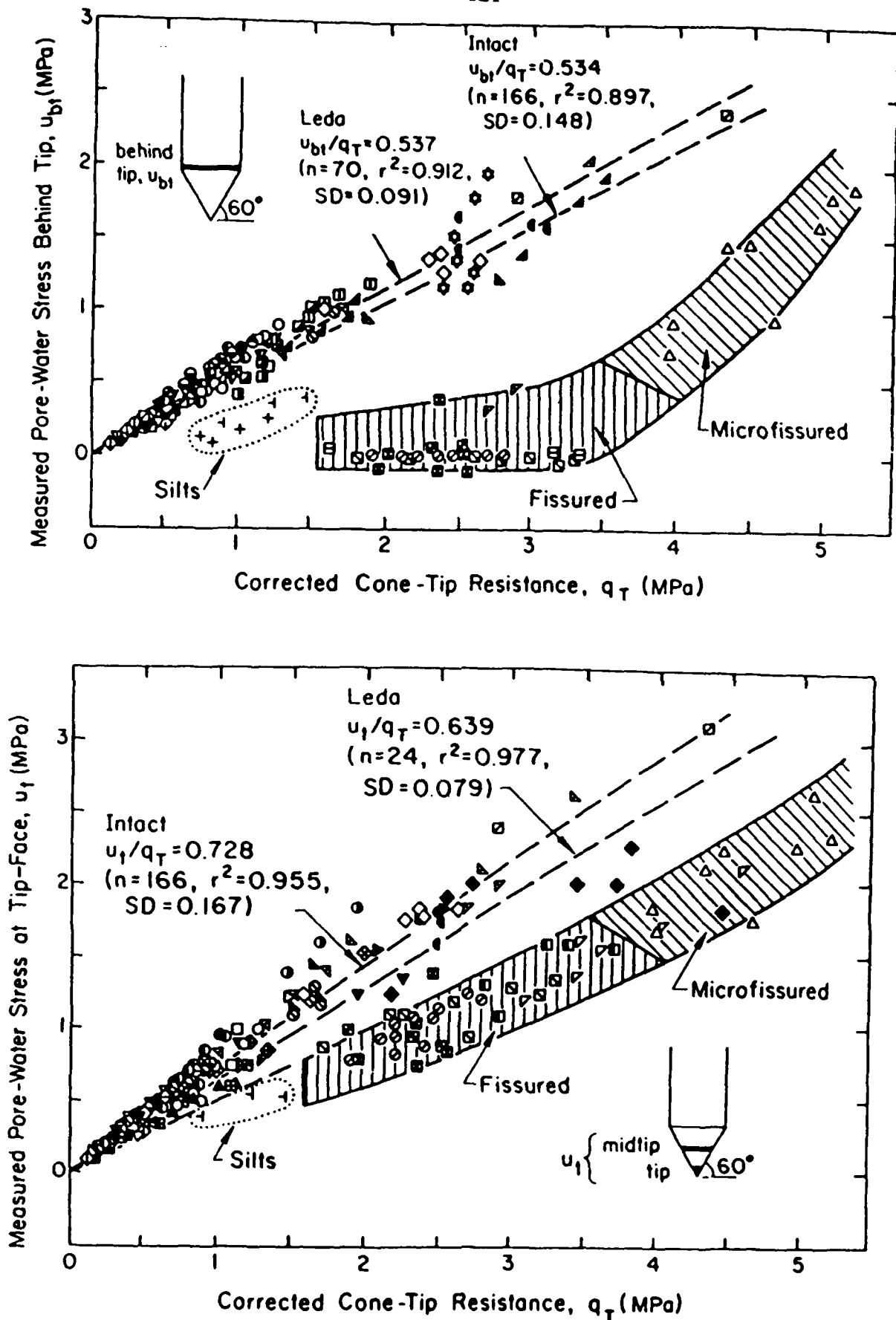
Figure 4.7   Relationships between tip resistance, q_T and measured pore pressures (Mayne et al., 1990)

OVERCONSOLIDATION RATIO OCR   PORE PRESSURE COEFFICIENT Bq

$$Bq = \frac{u_{max} - u_o}{q_t - \sigma_{vo}}$$

- $60°$ STANDARD TIP
- u_{max} MEASURED AT CONE TIP
- $q_t = q_c + 0.2 u_{max}$

z (m)   z (m)

a) BBC site

OVERCONSOLIDATION RATIO OCR   PORE PRESSURE COEFFICIENT Bq

WEATHERED CRUST

OCR CONSTANT ≈ 1.2

$$Bq = \frac{u_{max} - u_o^{(*)}}{q_t - \sigma_{vo}}$$

$60°$

FILTER STONE

z (m)   z (m)
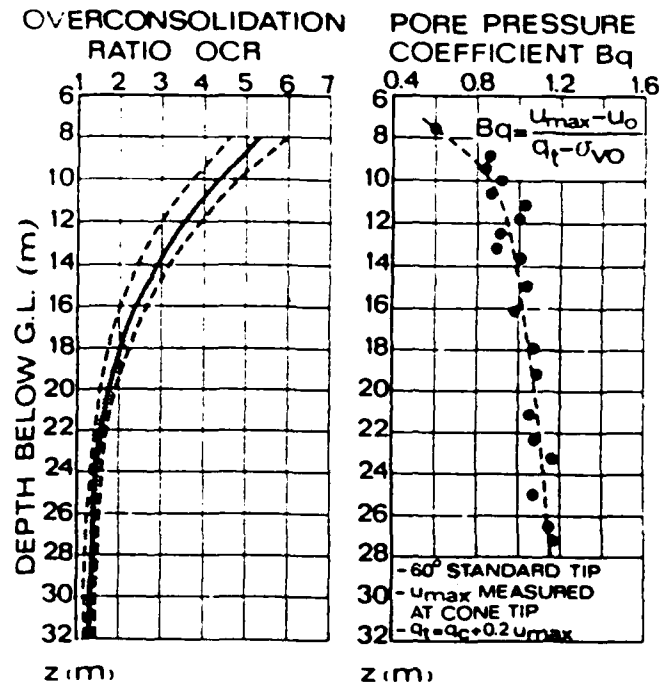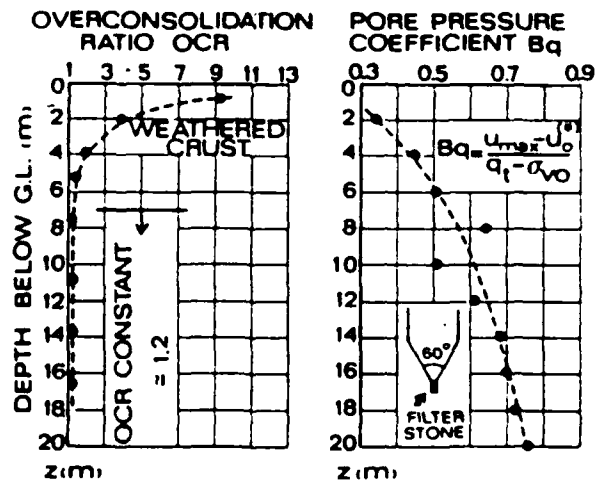
(*) THE WRITERS ARE NOT AWARE IF q_c USED HAS ALREADY BEEN CORRECTED FOR Δu EFFECT

b) Onsøy site

Figure 4.8a   Evaluation of B_q parameter with OCR (Jamiolkowski et al., 1985)
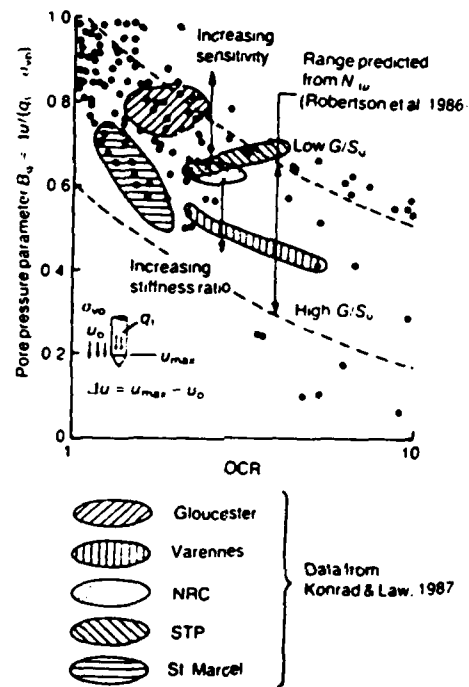
Figure 4.8b   Evaluation of B_q parameter with OCR (Robertson et al., 1989)
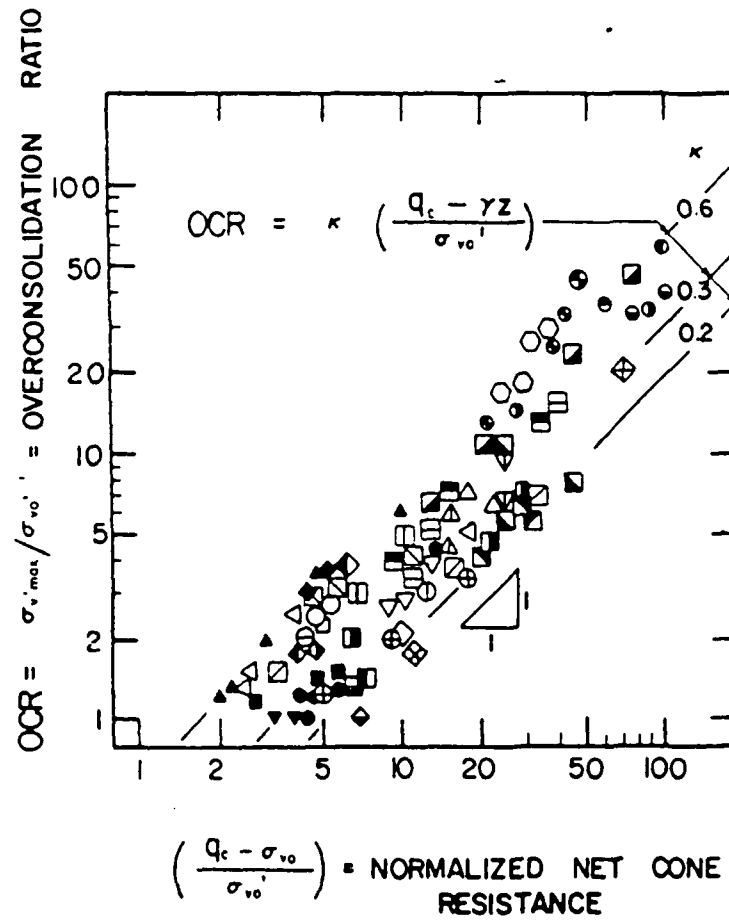
Figure 4.9a   Correlation between net tip resistance and OCR (Mayne, 1987)
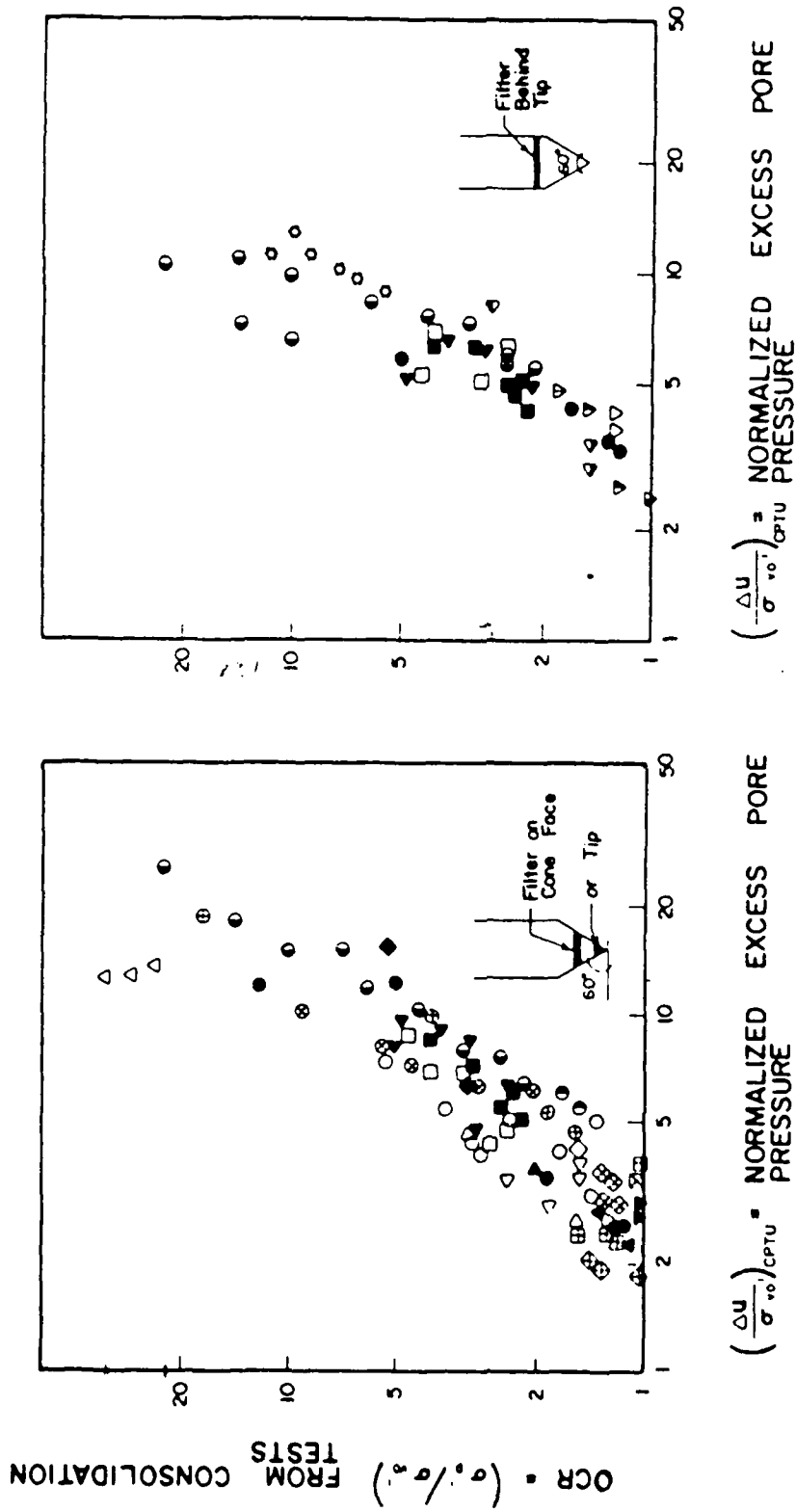
Figure 4.9b   Correlation between piezocone pore pressures and OCR (Mayne, 1986)
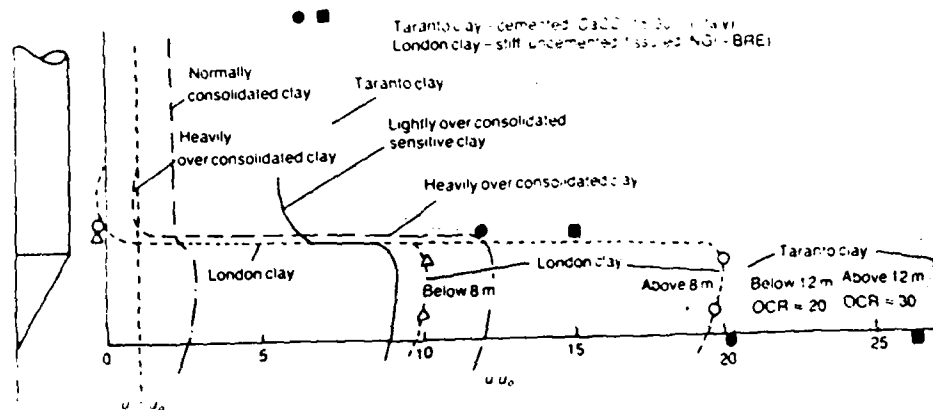
Figure 4.10a   Conceptual distribution of pore pressure around piezocone (Robertson et al., 1986)
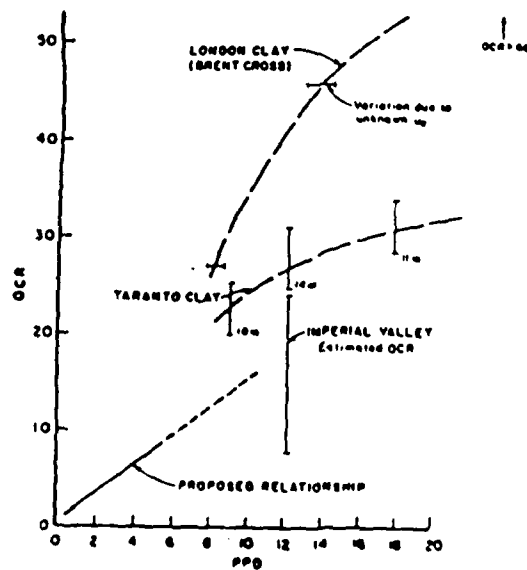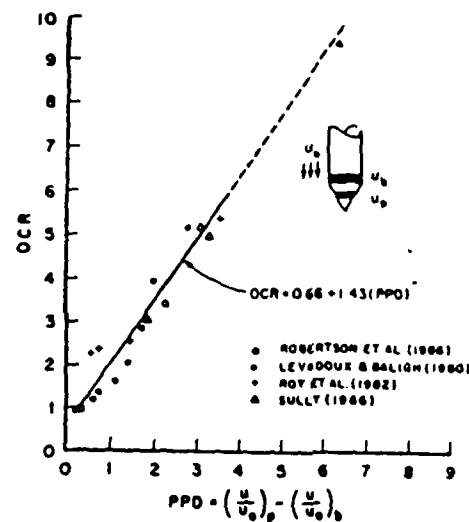
Figure 4.10b. Correlation of pore pressure difference with OCR (Sully et al., 1987)
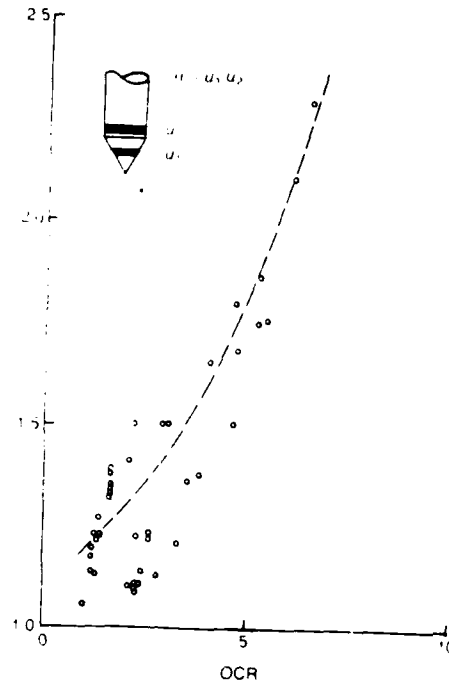
Figure 4.11a   Correlation of pore pressure ratio with OCR (Robertson et al., 1989)
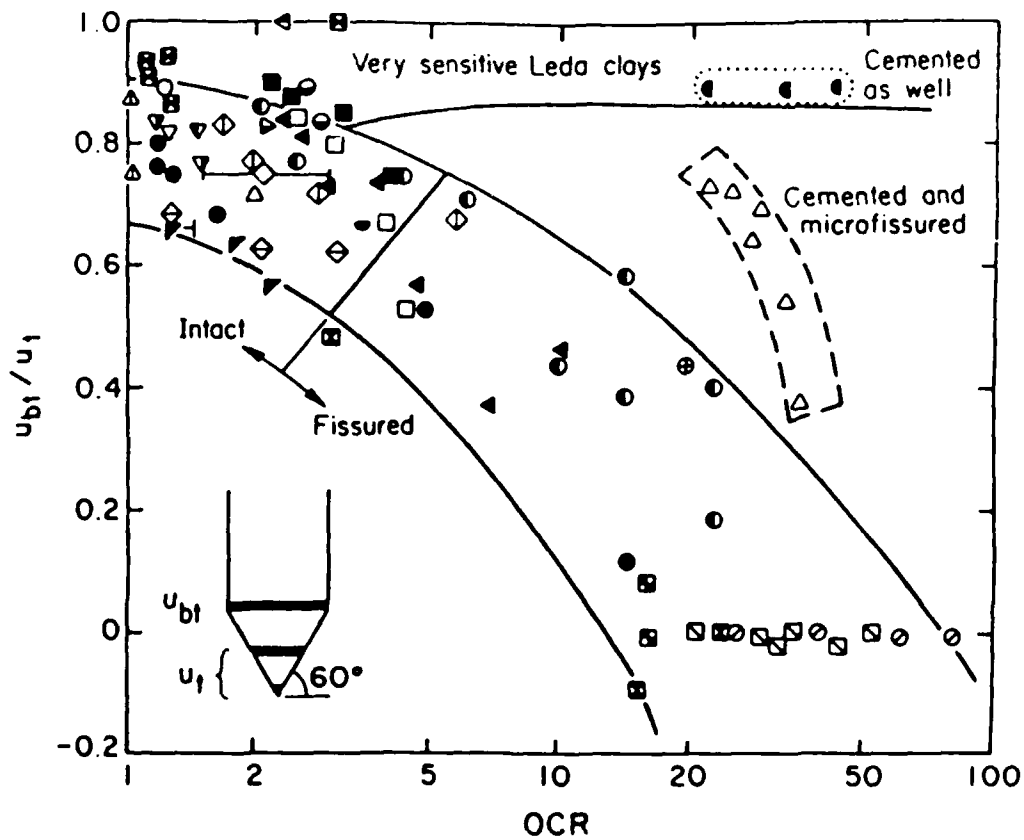
Figure 4.11b   Correlation of pore pressure ratio with OCR (Mayne et al., 1990)
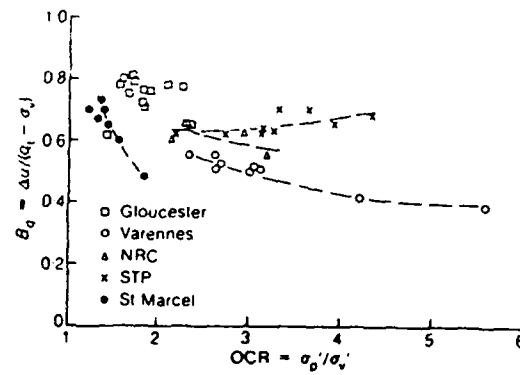
Figure 4.12b   OCR from vertical yield stress (Konrad and Law, 1987)
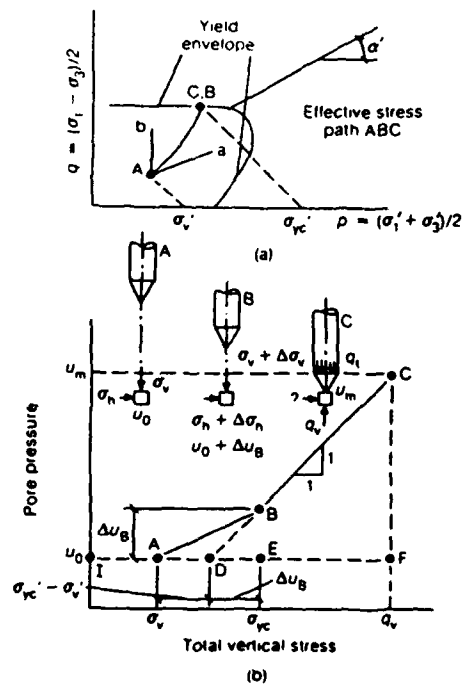
Figure 4.12a   Stress paths of idealized soil elements at cone tip (Konrad and Law, 1987)
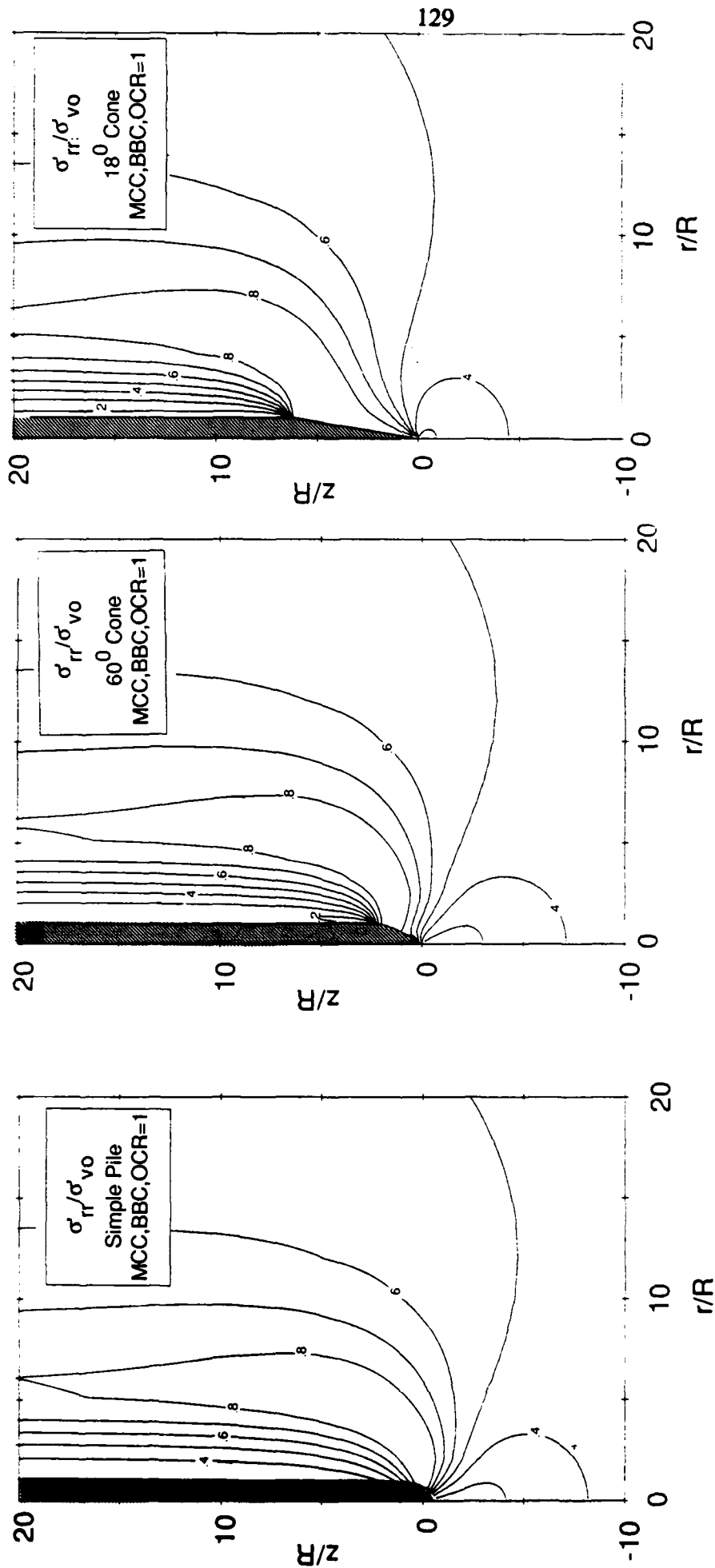
Figure 4.13   Effect of tip shape on predictions of effective stresses and pore pressures

a) $\sigma'_{rr}/\sigma'_{v0}$

130
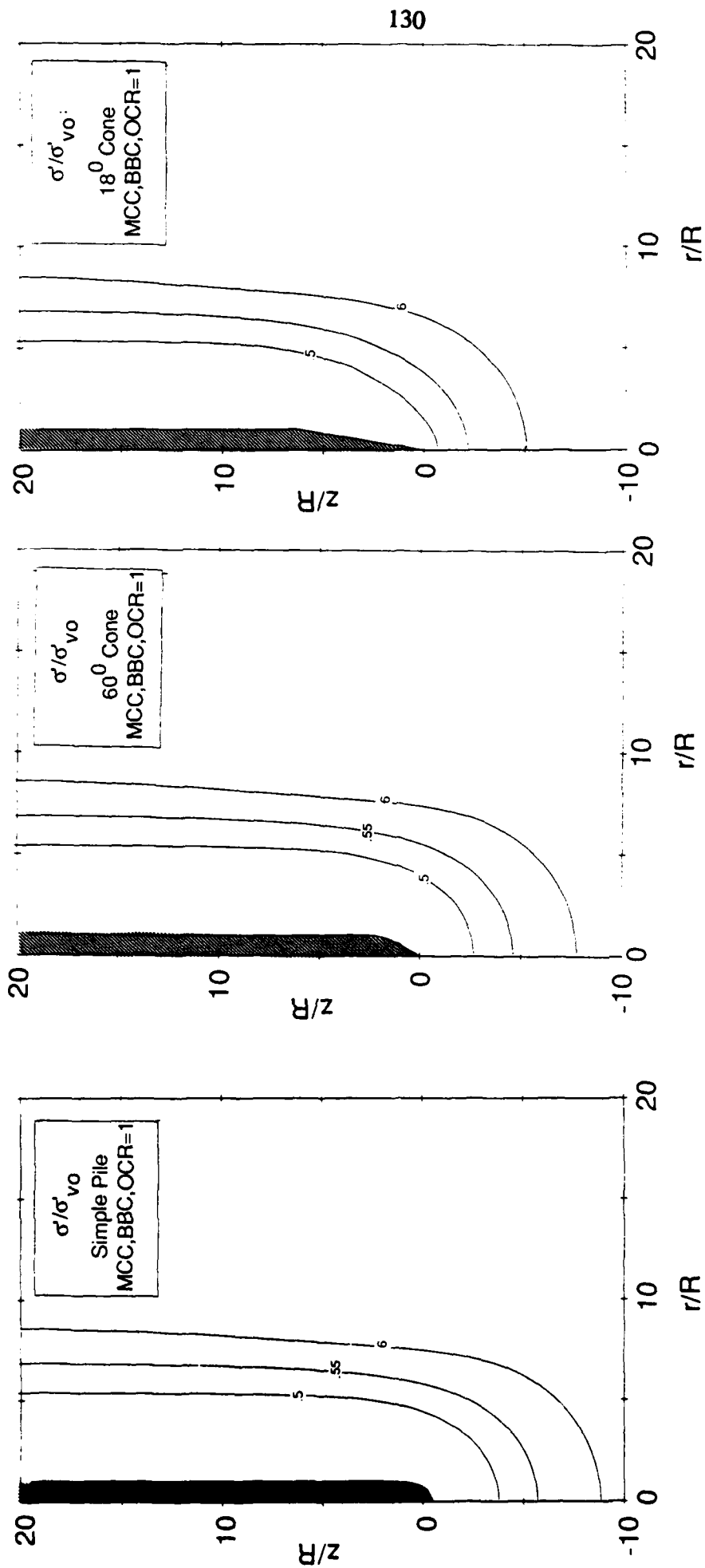
Figure 4.13   Effect of tip shape on predictions of effective stresses and pore pressures (Contd.) b) σ'/σ'_{v0}
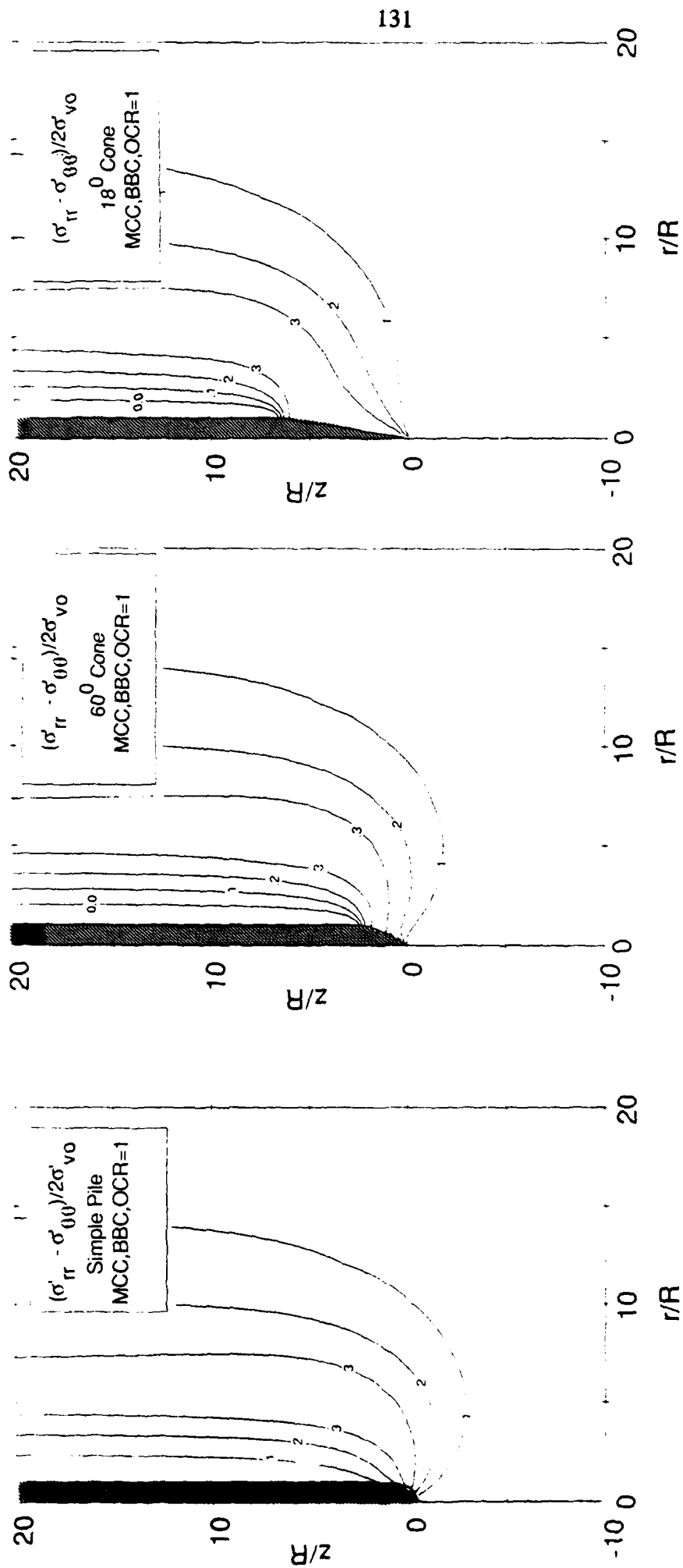
Figure 4.13   Effect of tip shape on predictions of effective stresses and pore pressures
(Contd.) c) $(\sigma'_{rr} - \sigma'_{\theta\theta})/2\sigma'_{v0}$
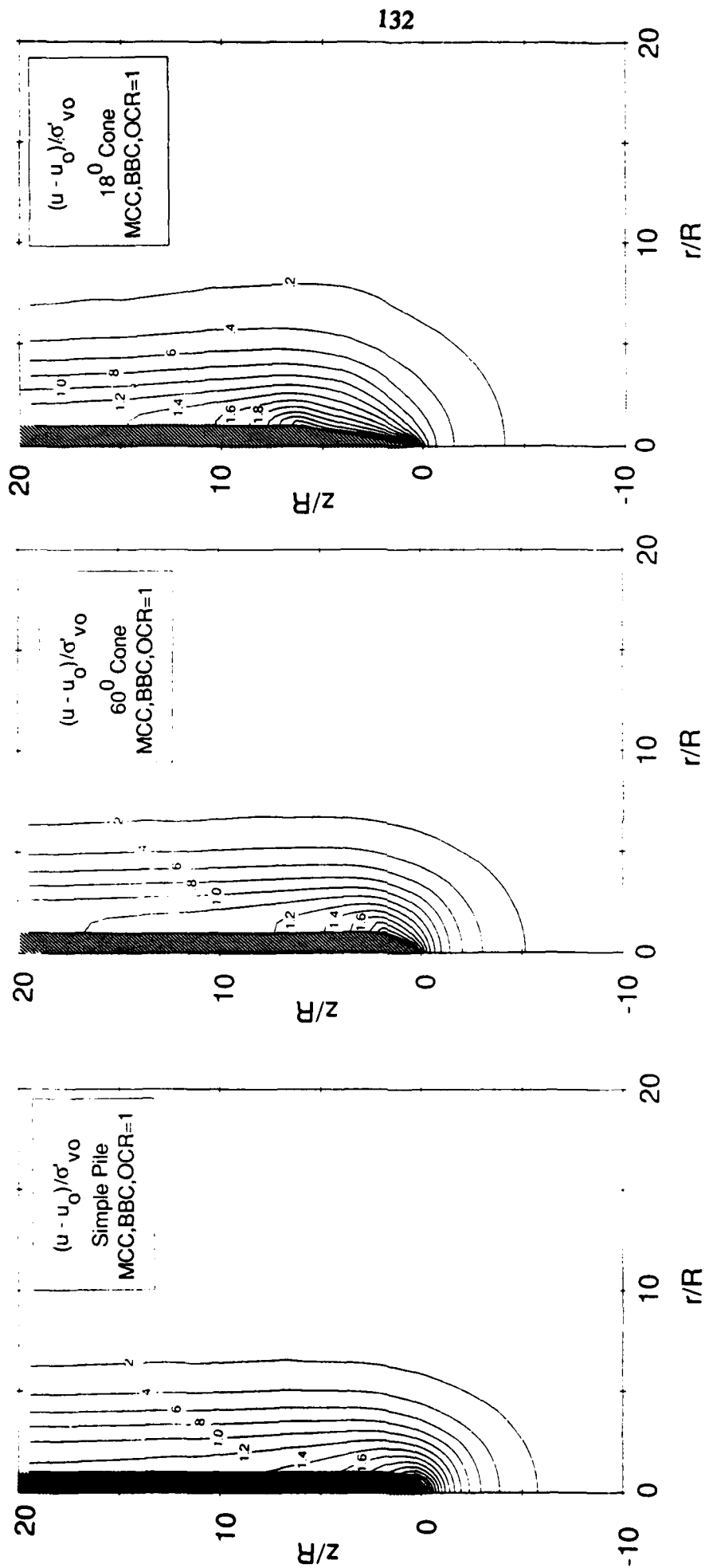
Figure 4.13   Effect of tip shape on predictions of effective stresses and pore pressures
(Contd.) d) $(u-u_0)/\sigma'_{vo}$
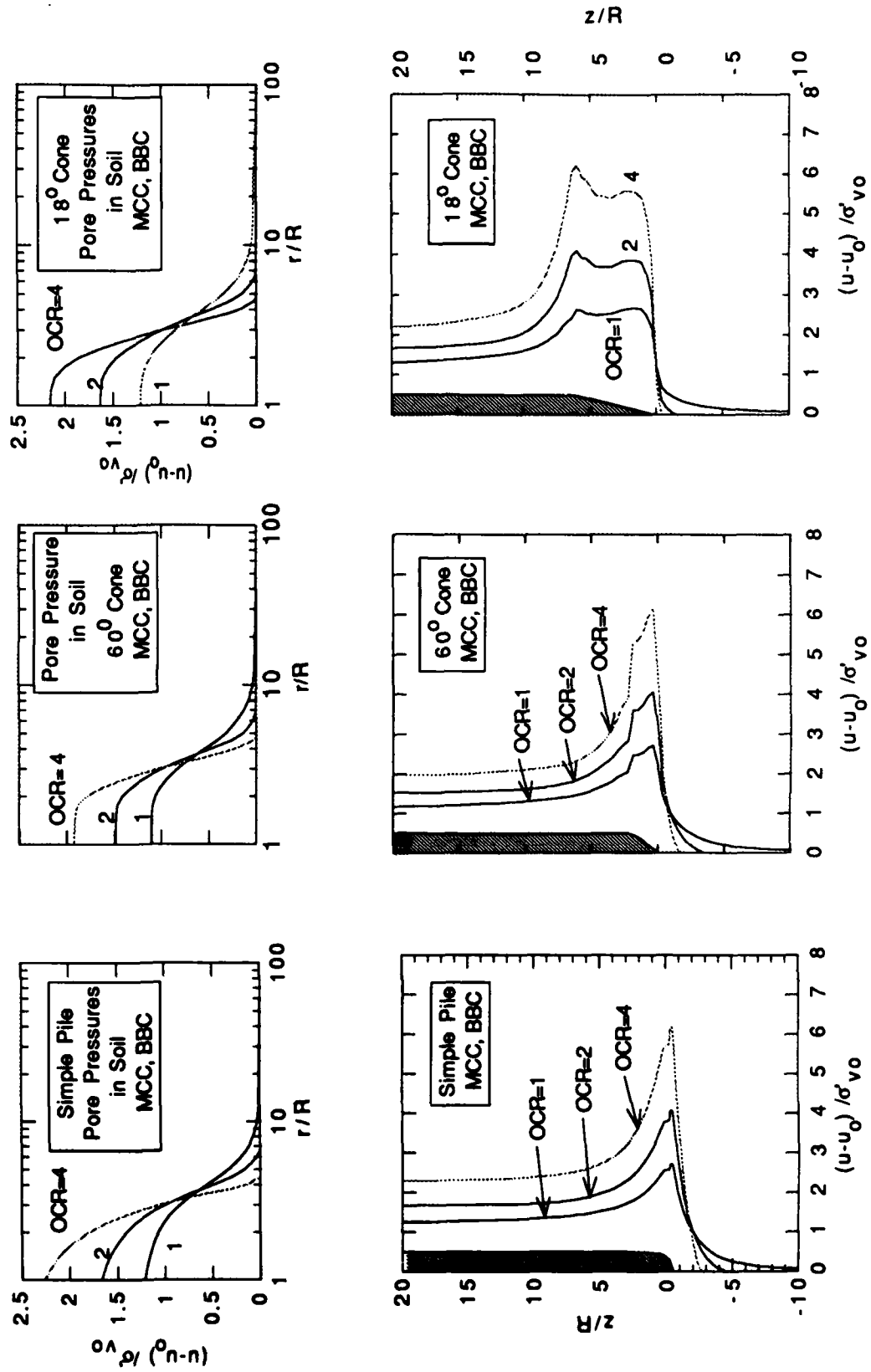
Figure 4.14   Summary of effect of tip shape on distributions of excess pore pressures
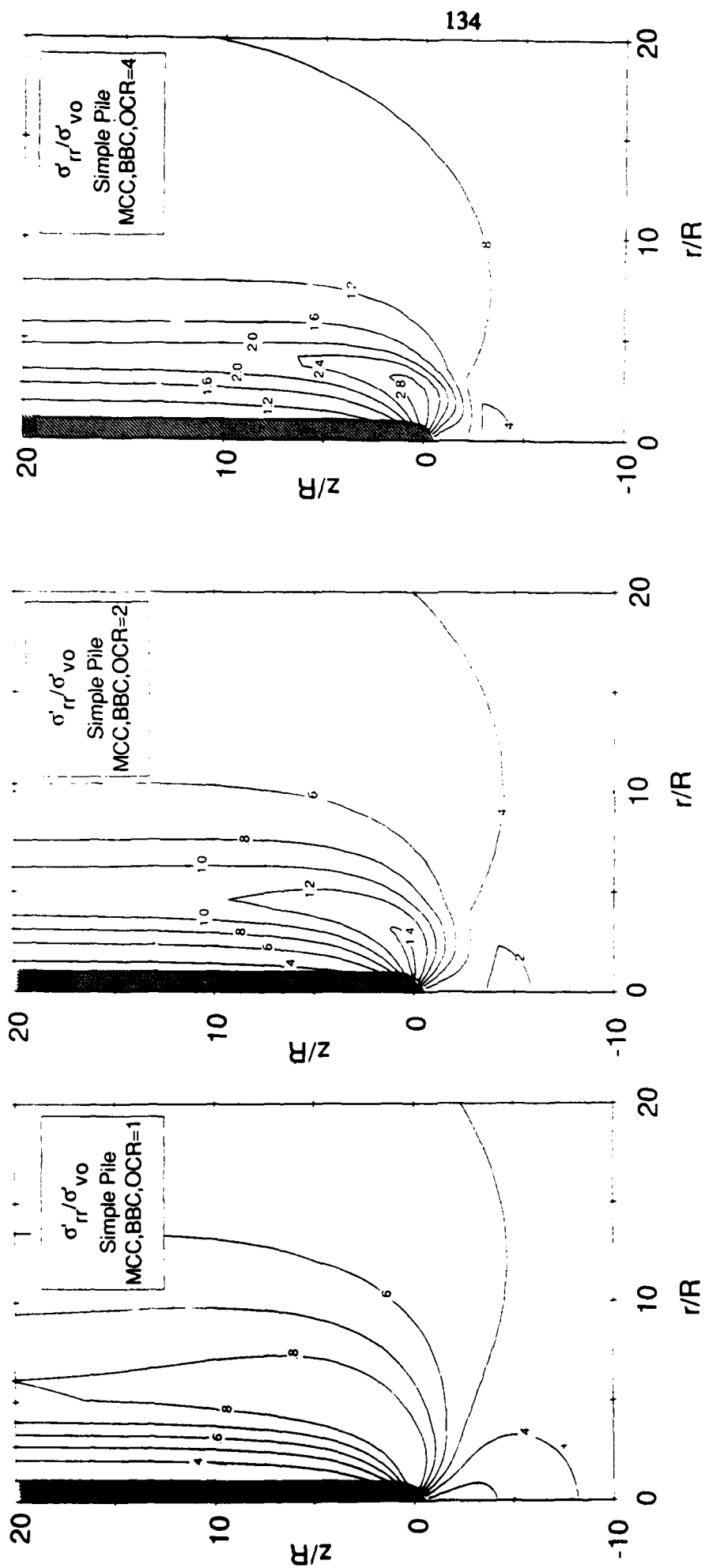
Figure 4.15   Effect of Overconsolidation ratio on predictions of effective stresses and pore pressures a) $\sigma'_{rr}/\sigma'_{v0}$
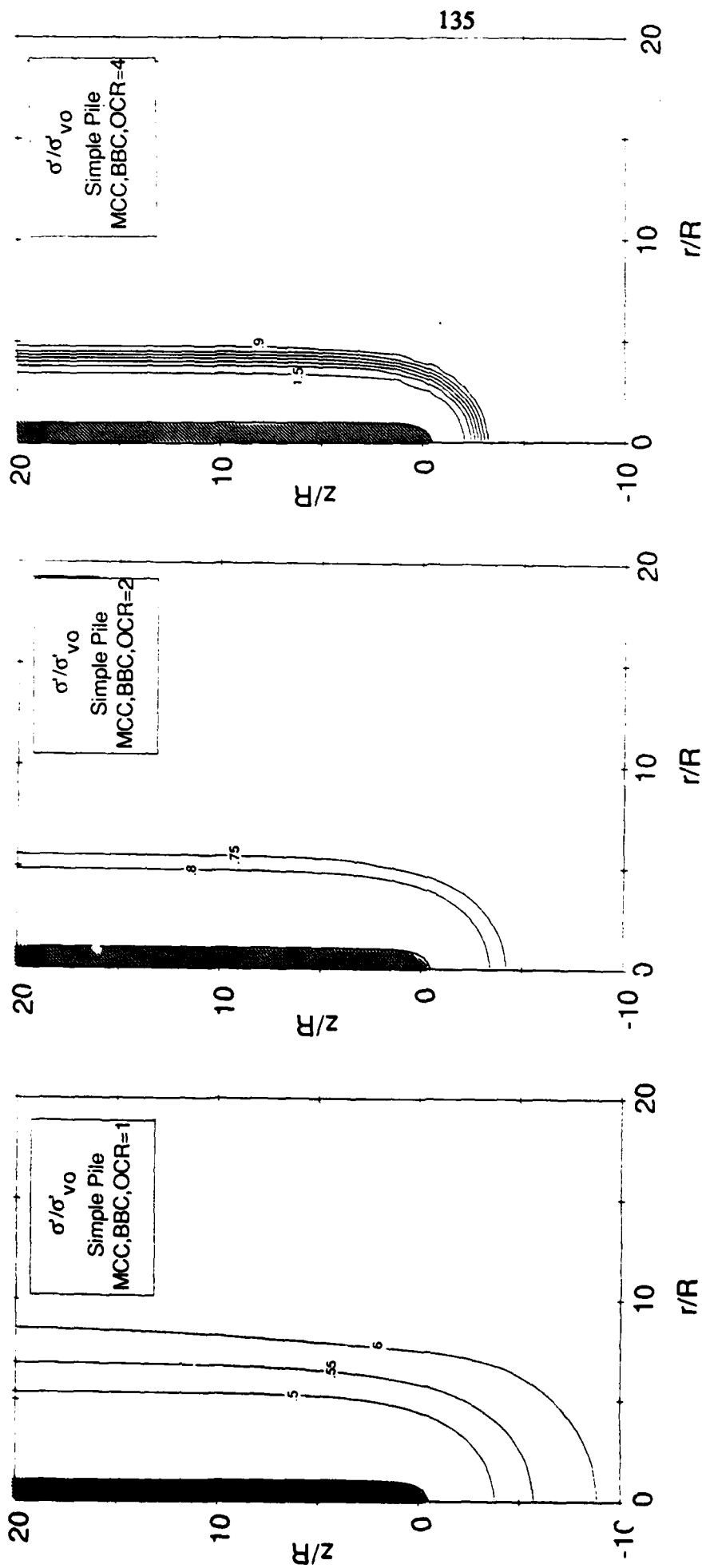
Figure 4.15   Effect of Overconsolidation ratio on predictions of effective stresses
and pore pressures (Contd.) b) σ'/σ'_{v0}
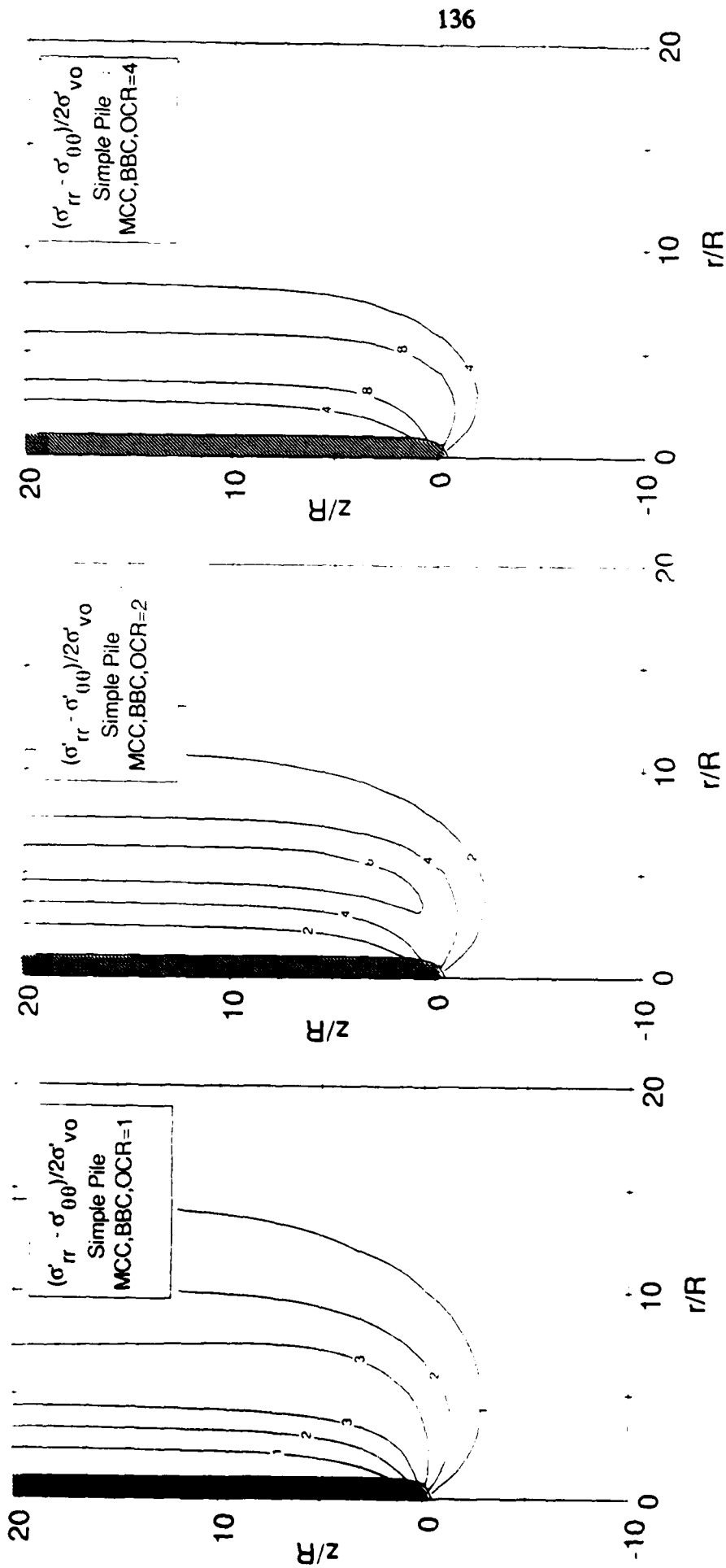
Figure 4.15   Effect of Overconsolidation ratio on predictions of effecive stresses and pore pressures (Contd.) c) $(\sigma'_{rr} - \sigma'_{\theta\theta})/2\sigma'_{v0}$
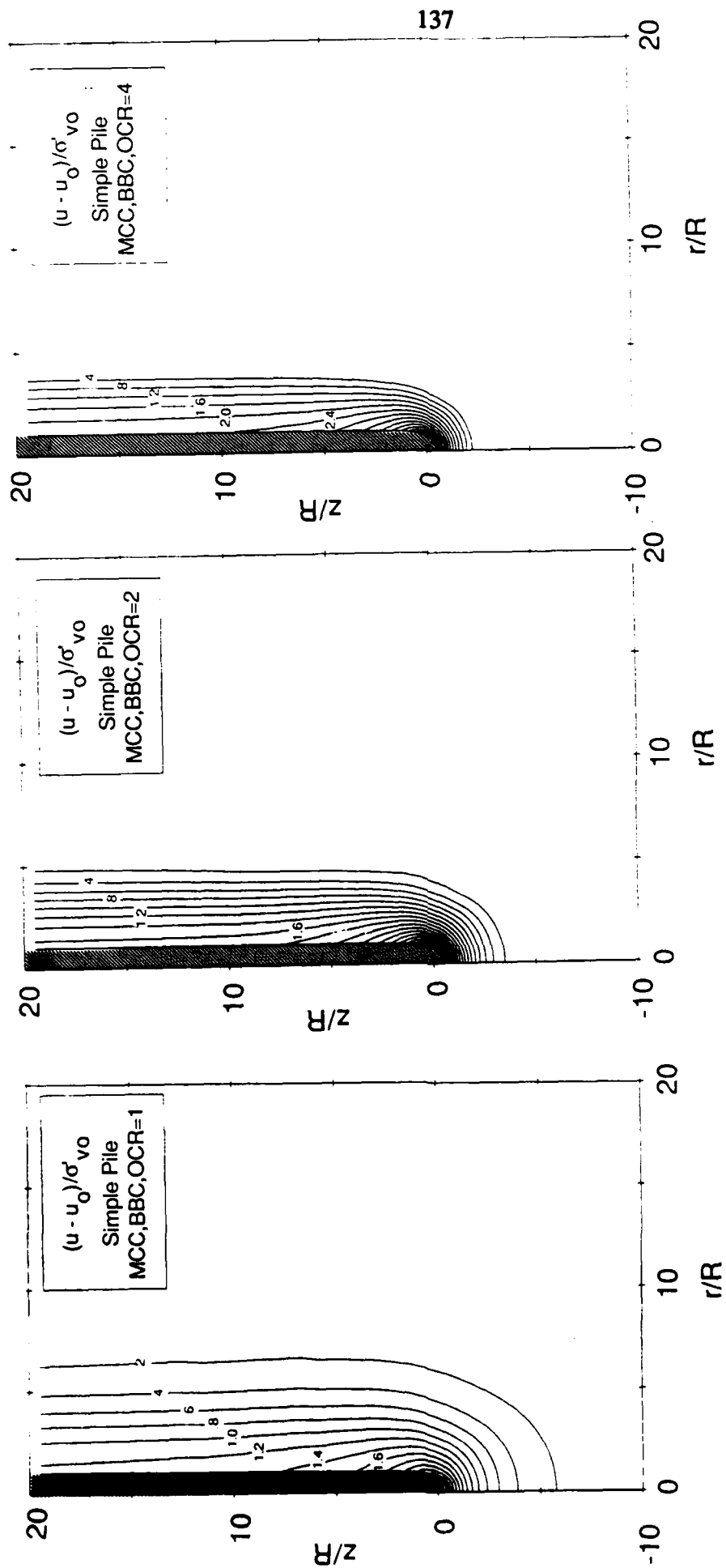
Figure 4.15   Effect of Overconsolidation ratio on predictions of effective stresses
and pore pressures (Contd.) d) $(u-u_0)/\sigma'_{v0}$
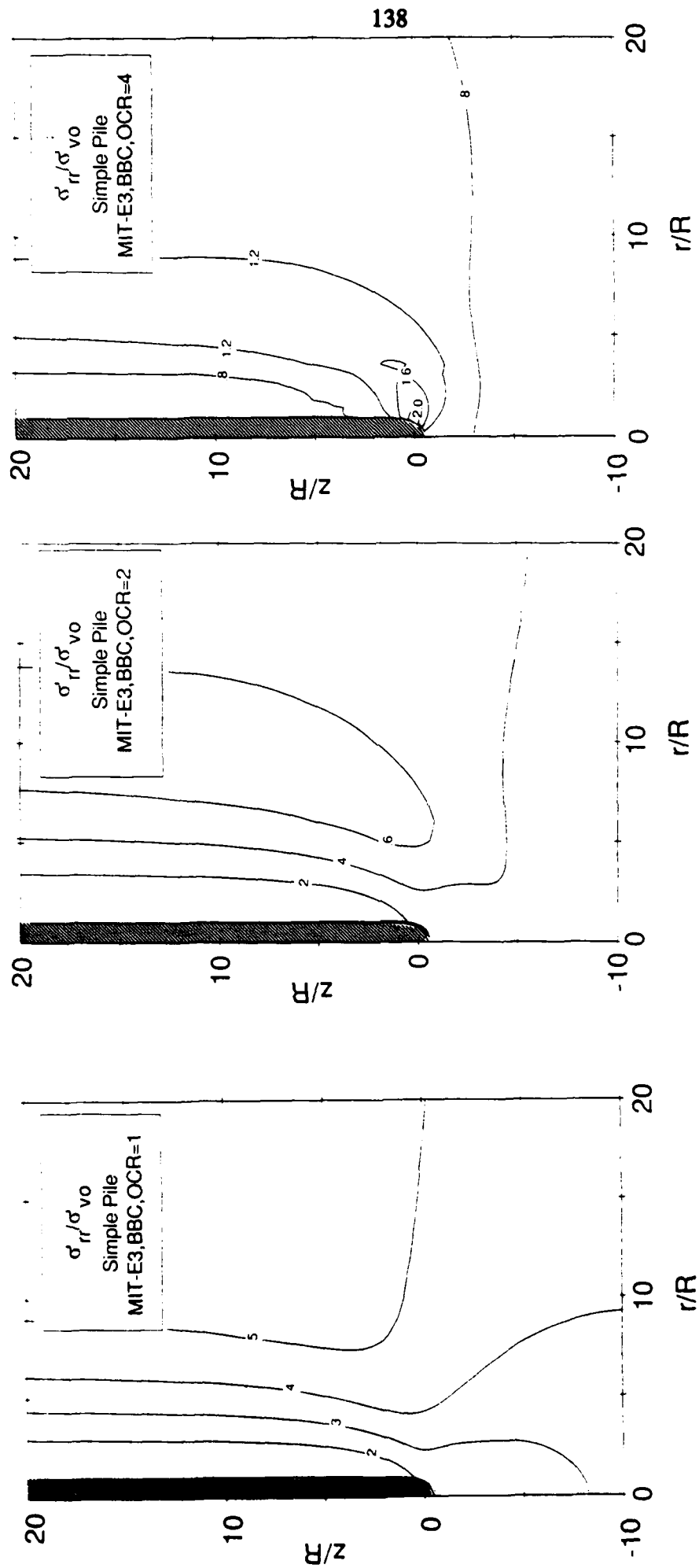
Figure 4.16   Predictions of effective stresses and pore pressures using
the MIT-E3 model a) $\sigma'_{rr}/\sigma'_{v0}$
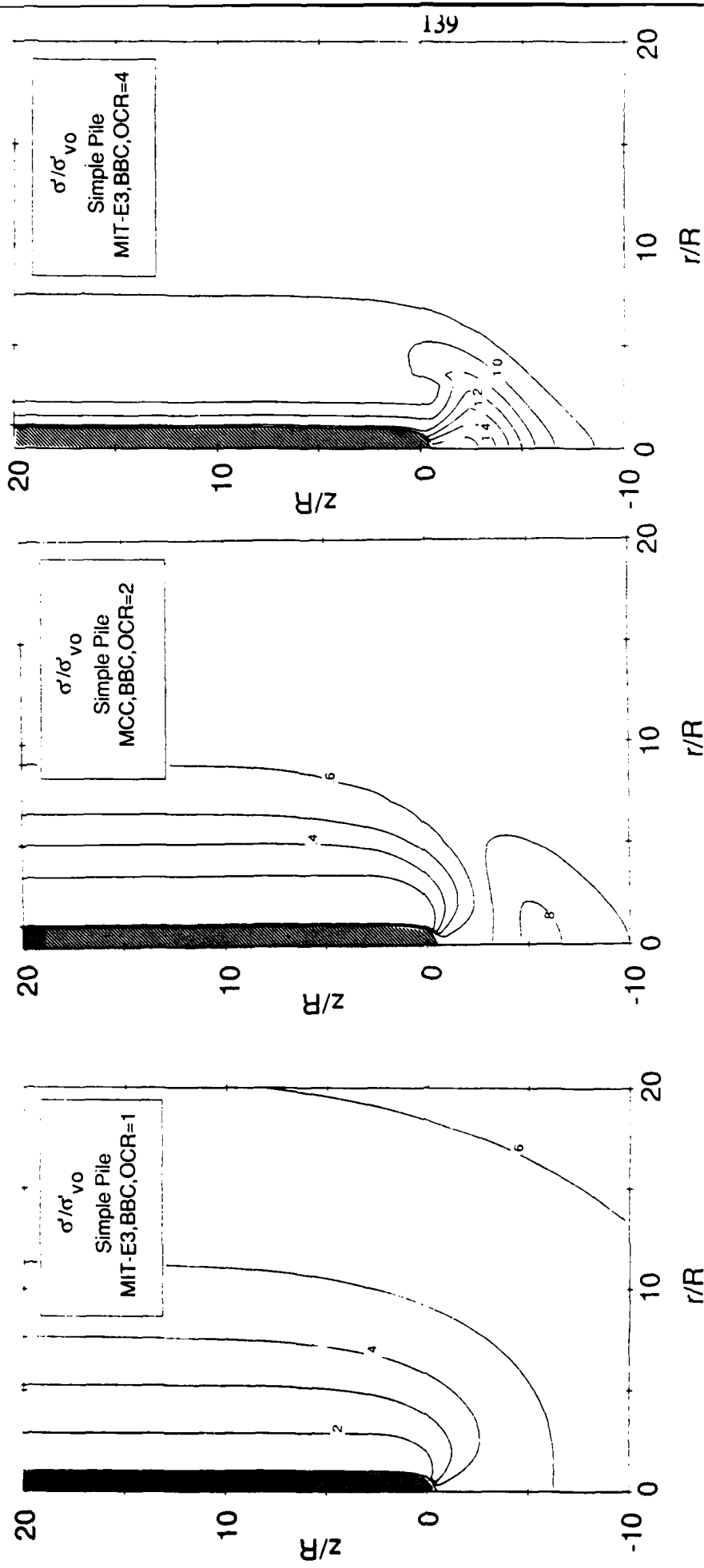
Figure 4.16   Predictions of effective stresses and pore pressures using the MIT-E3 model (Contd.) b) σ'/σ'_{v0}
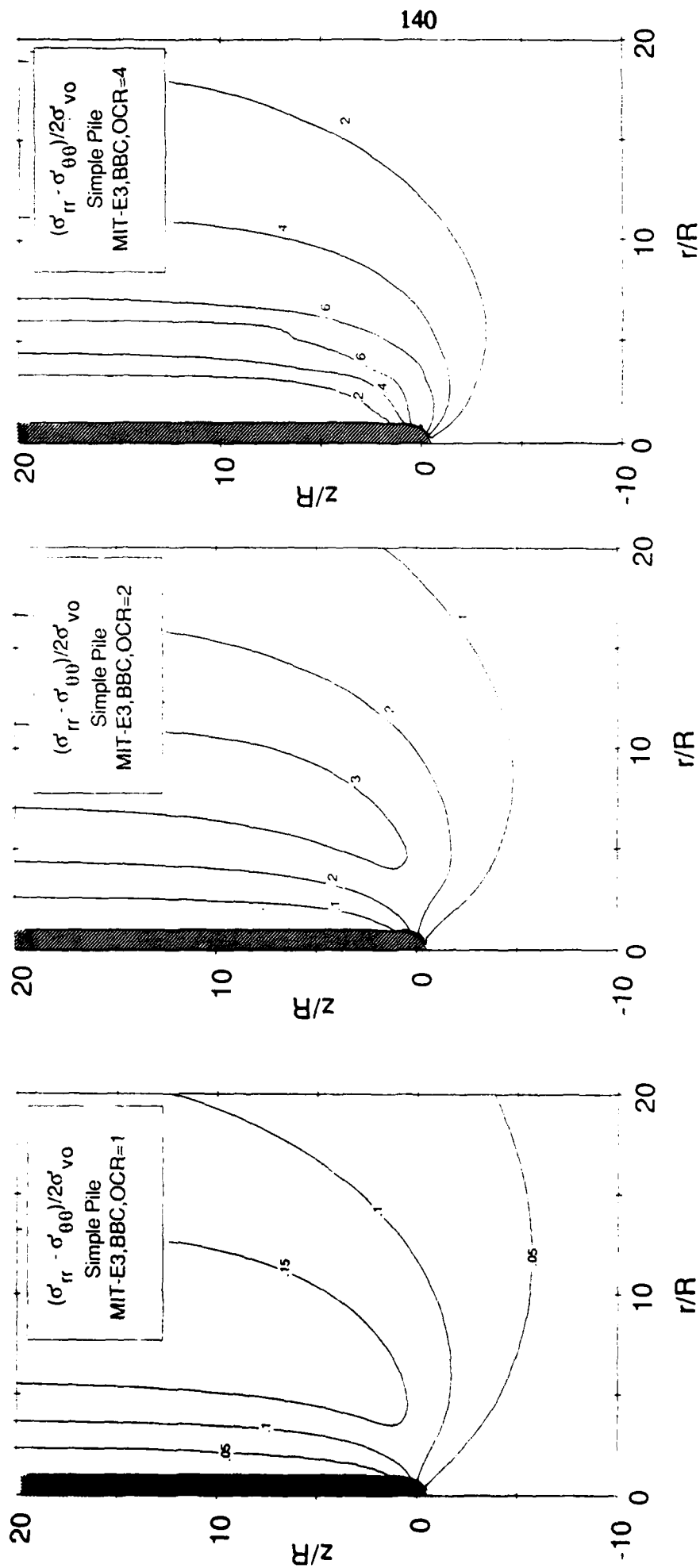
Figure 4.16   Predictions of effective stresses and pore pressures using
the MIT-E3 model (Contd.) c) $(\sigma'_{rr} - \sigma'_{\theta\theta})/2\sigma'_{v0}$
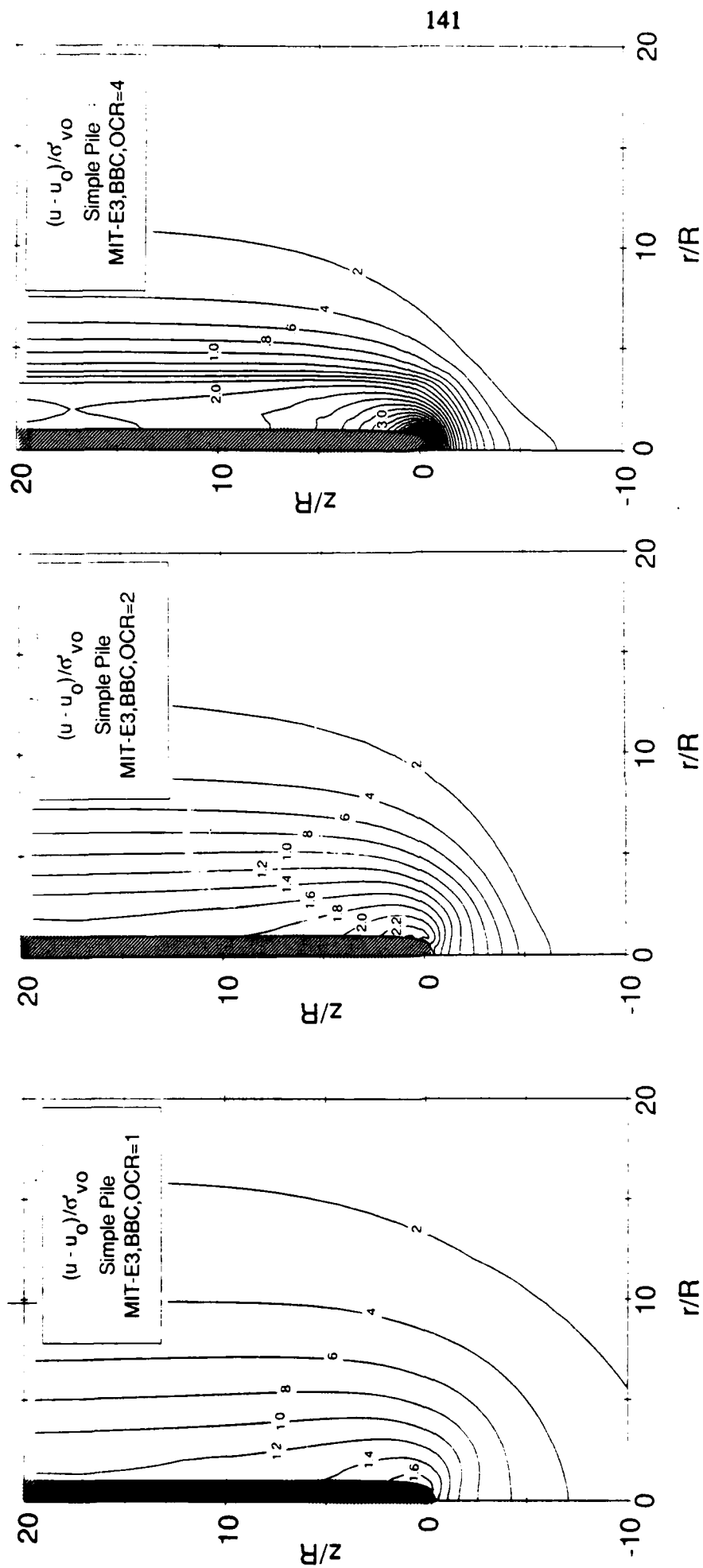
Figure 4.16   Predictions of effective stresses and pore pressures using
the MIT-E3 model (Contd.) d) $(u-u_0)/\sigma'_{v0}$
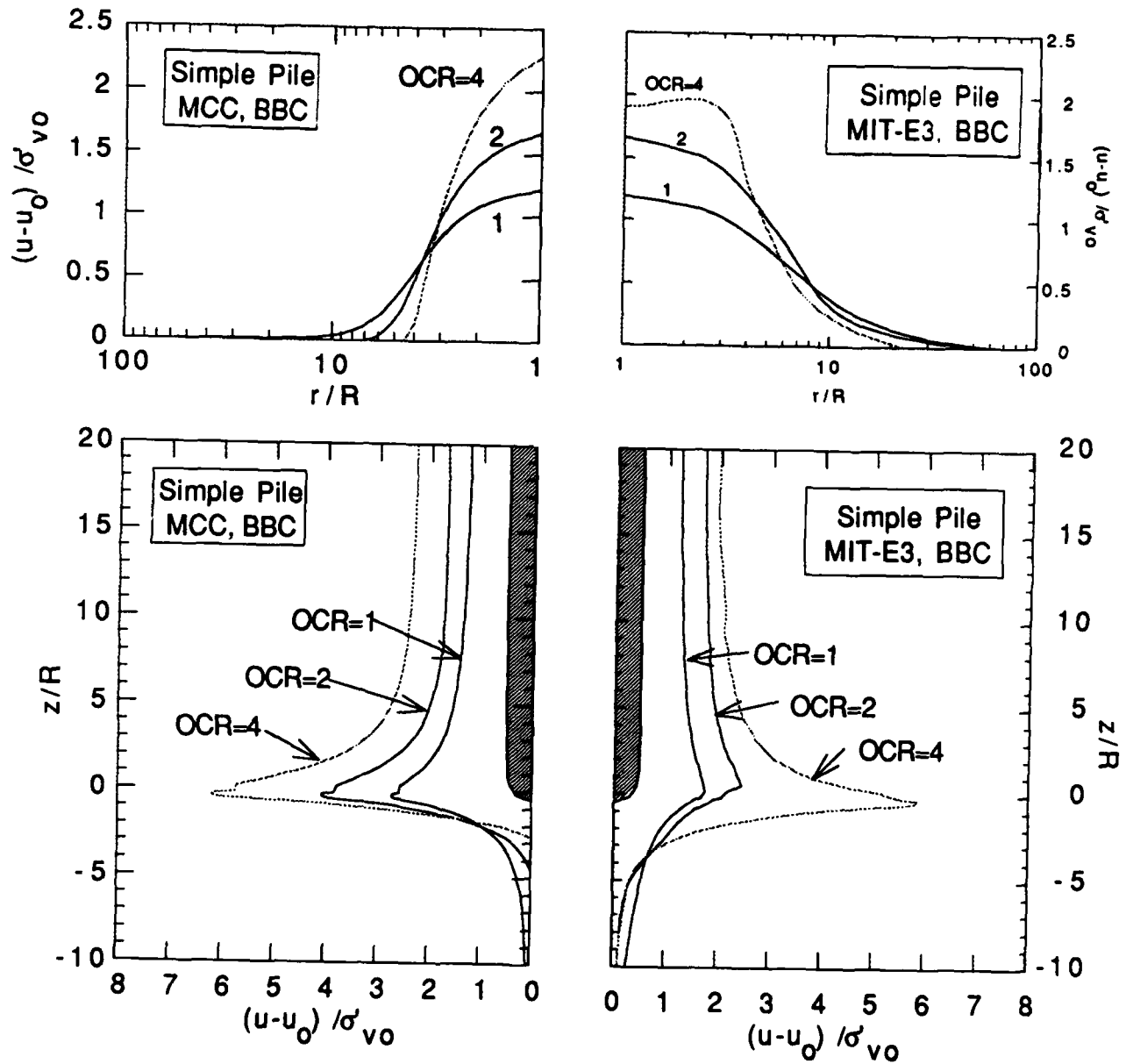
Figure 4.17   Effect of soil model on distributions of excess pore pressures
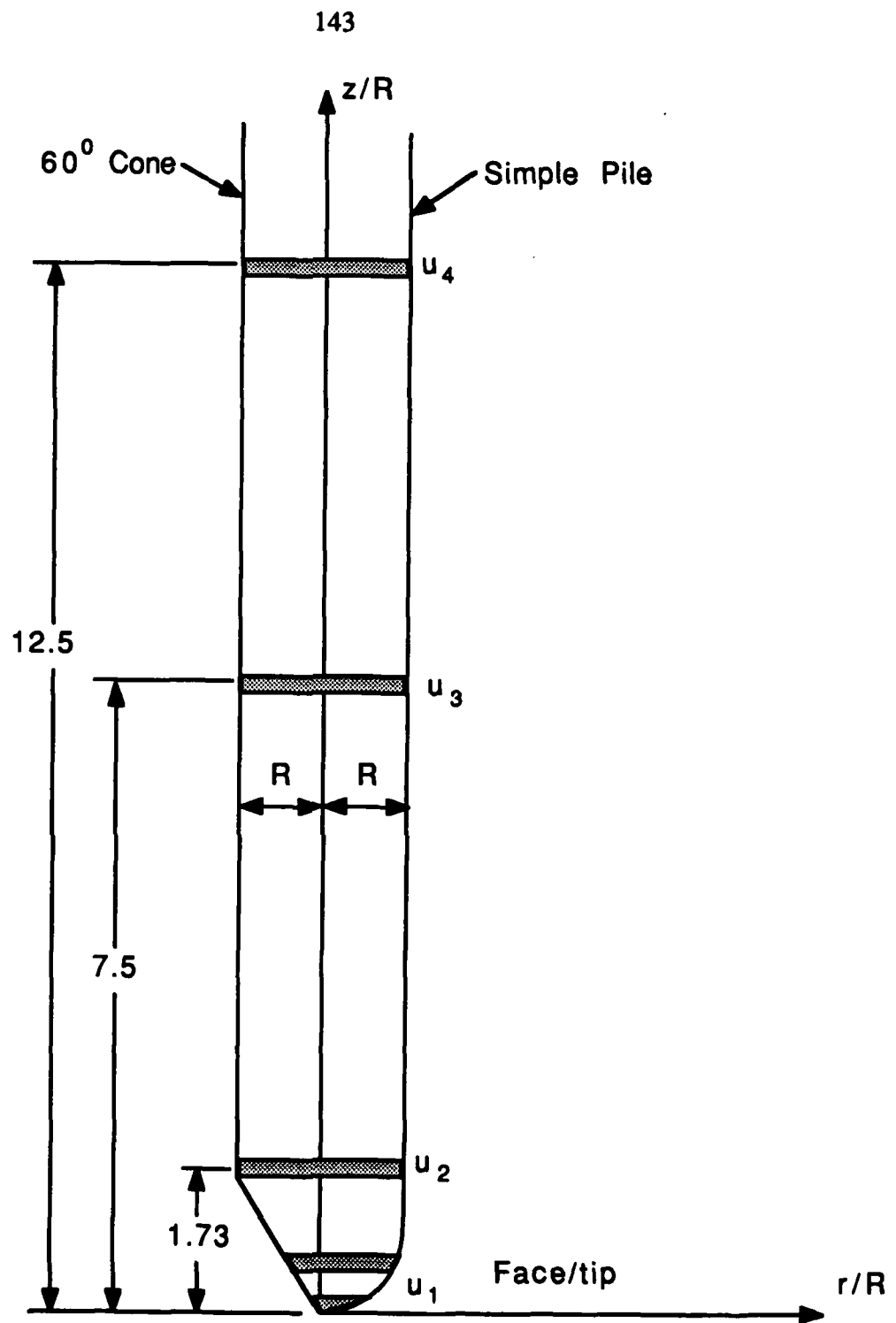
Figure 4.18   Definitions used to interpret predictions of piezocone pore pressures
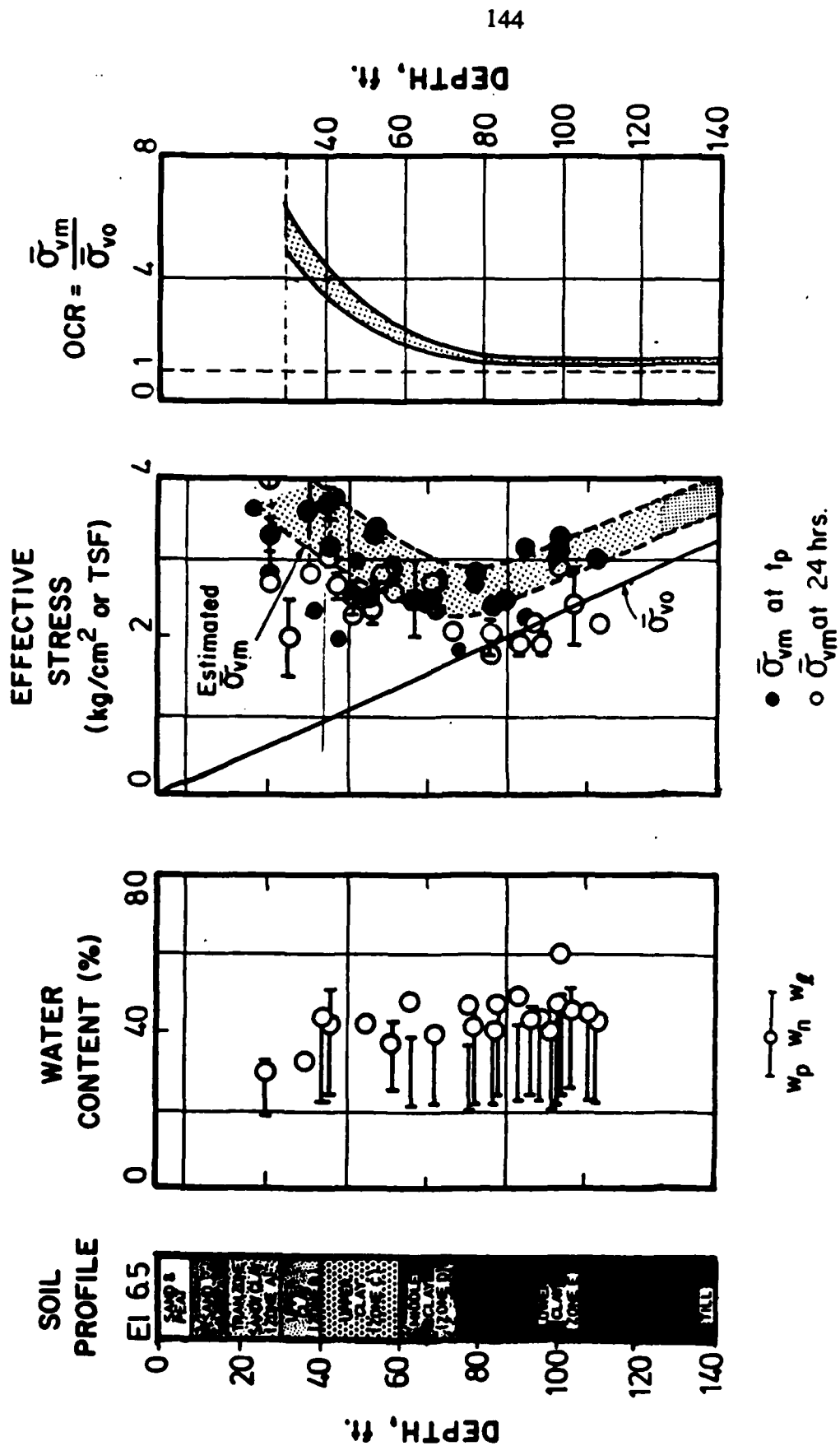
Figure 4.19a   Index properties and stress history, Saugus test site (Morrison, 1984)
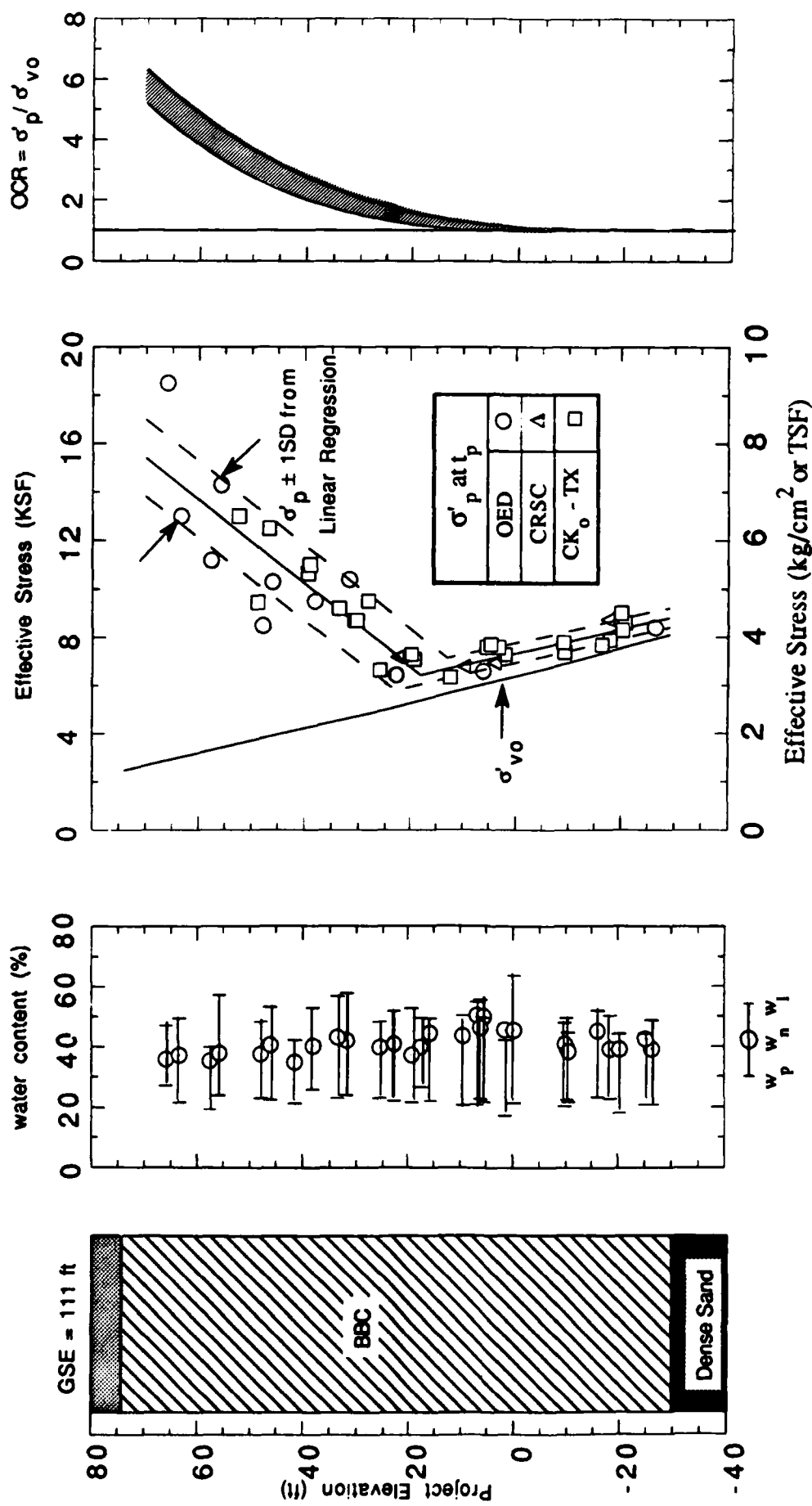
NOTE: Project Elevation = MSL + 100.0 ft.

4.19b Index properties and stress history, South Boston test site (Ladd, 1990)
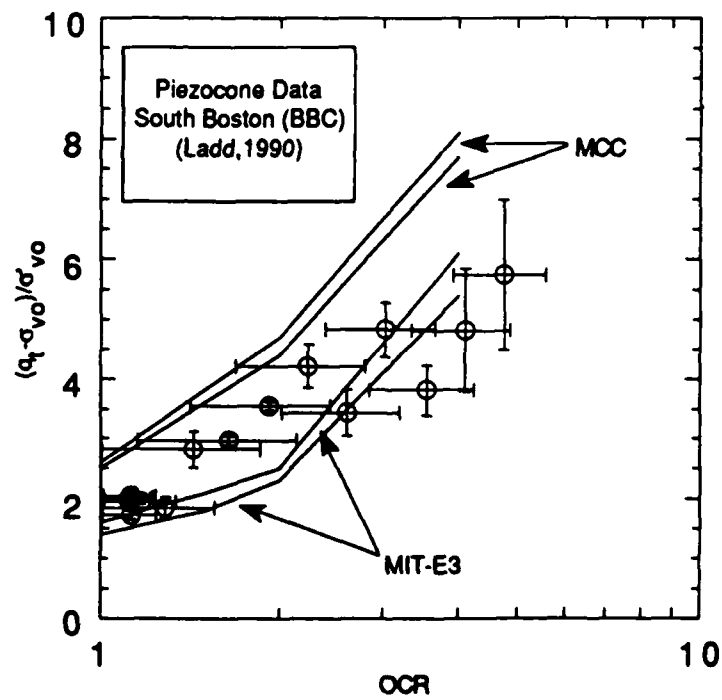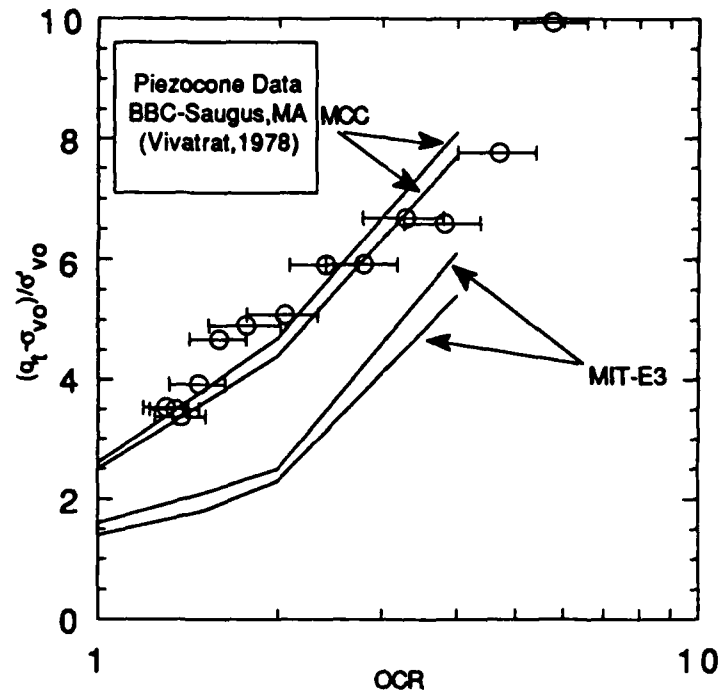
Figure 4.20   Comparison of predictions and measured data for net tip
resistance in BBC
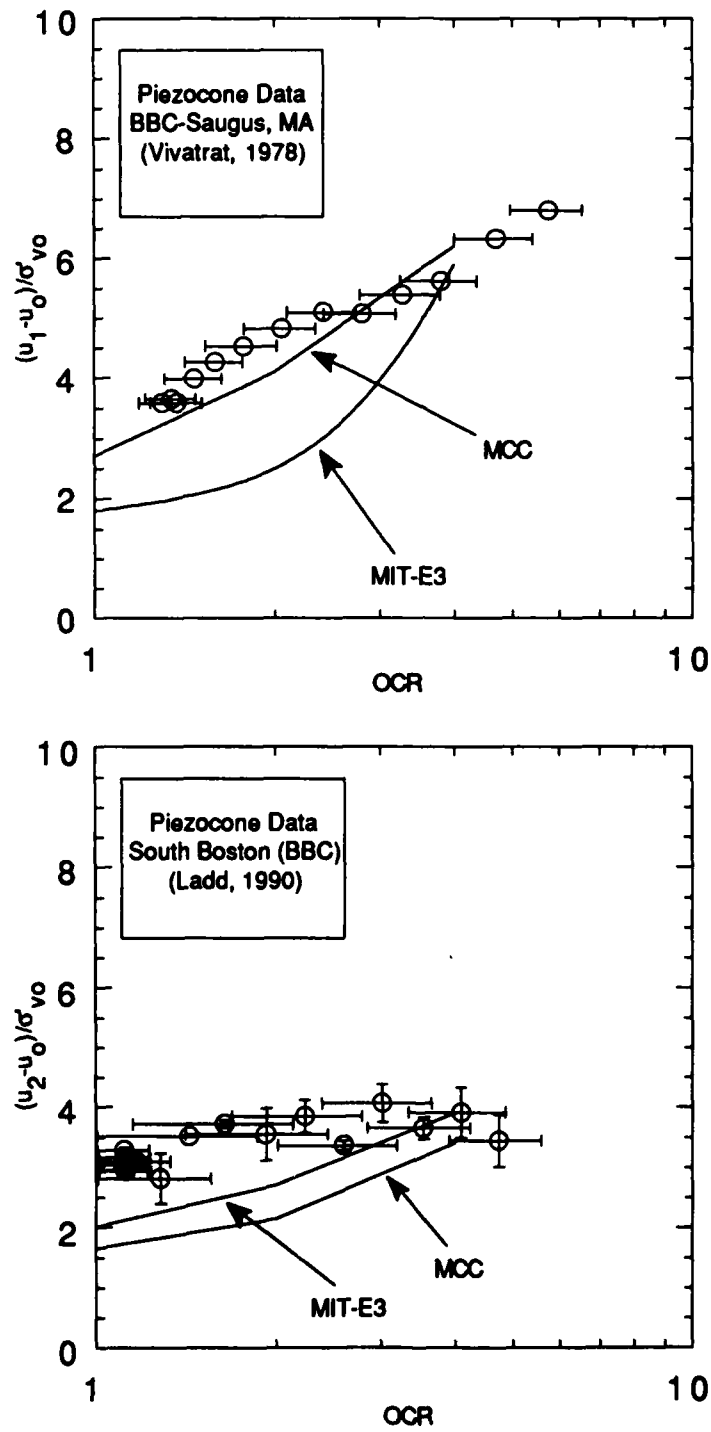
Figure 4.21   Comparison of predictions and measured data for excess pore
pressures in BBC
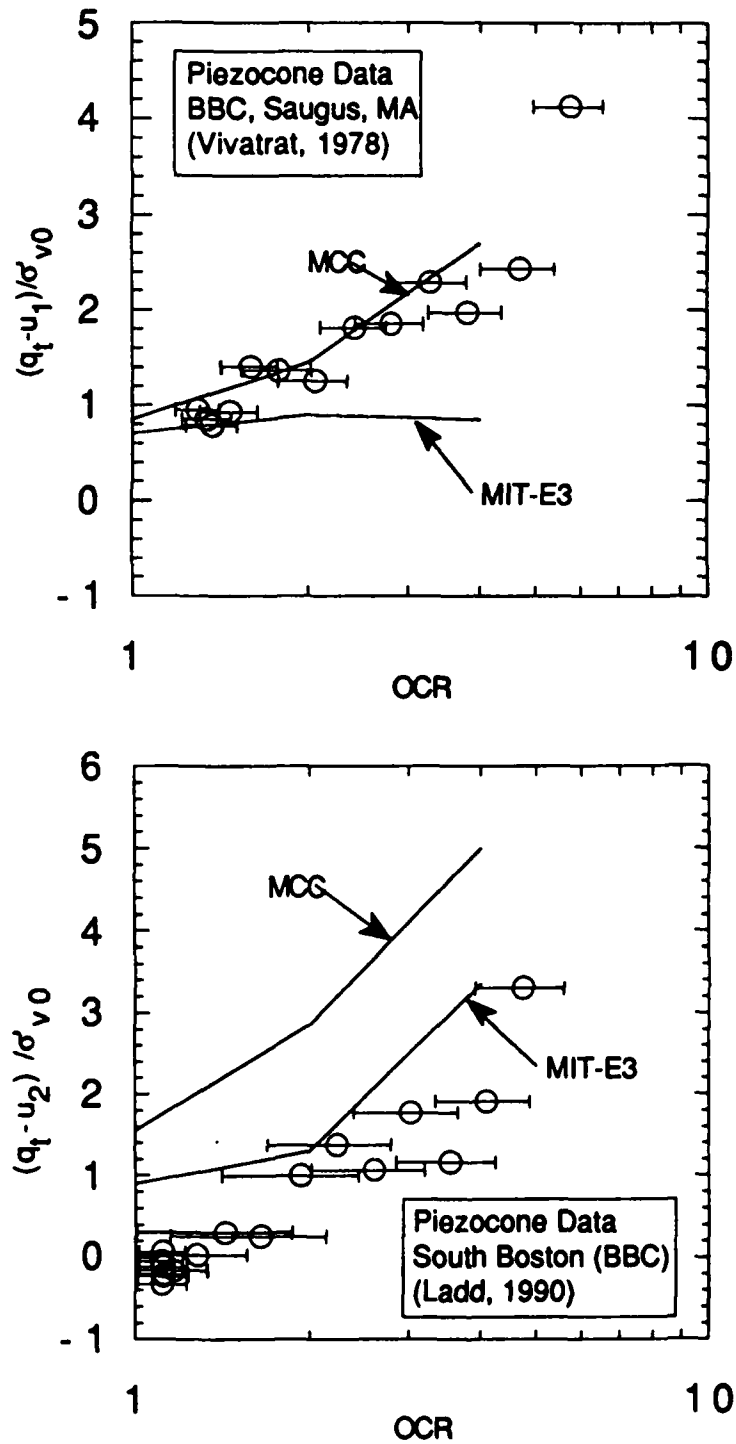
Figure 4.22 Comparison of predictions and measured data for the effective tip resistance in BBC
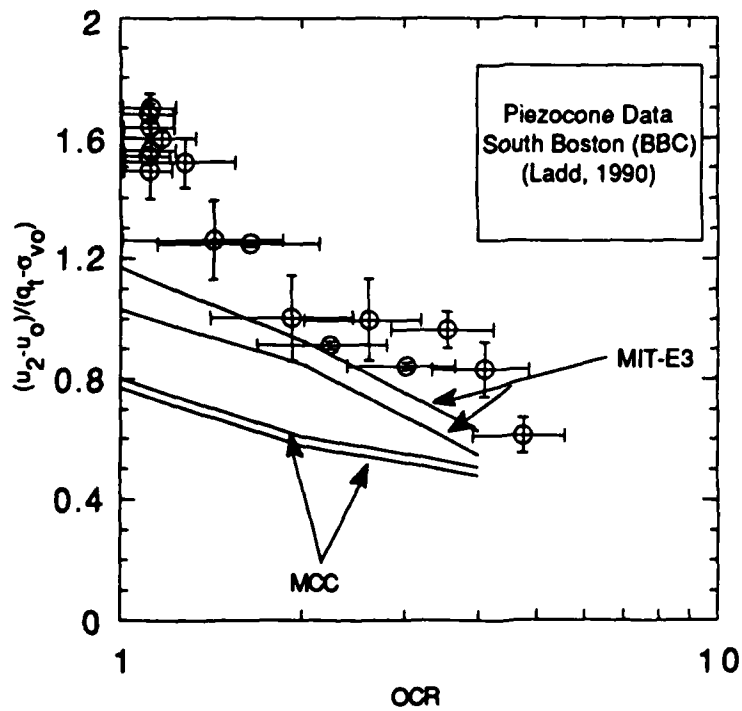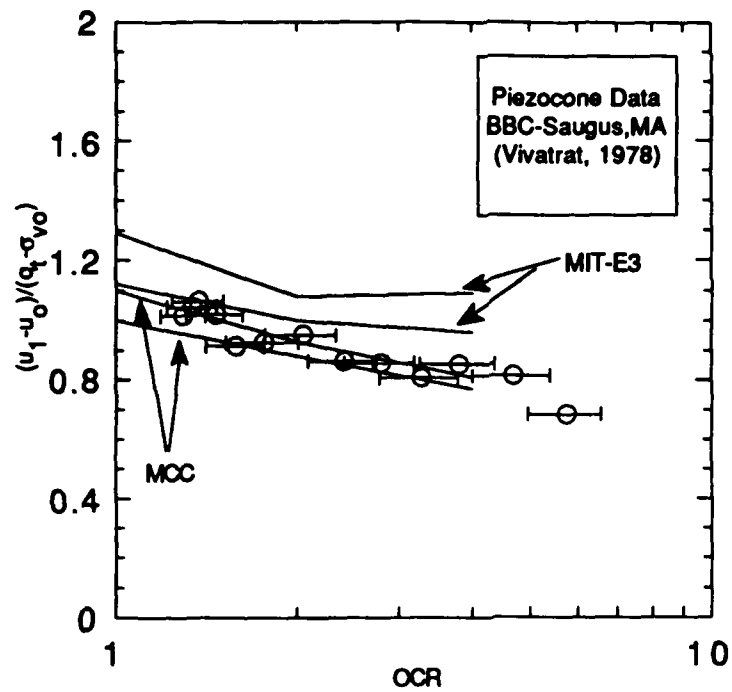
Figure 4.23   Comparison of predictions and measurements for the B_q ratio in BBC

5. THE MARCHETTI DILATOMETER

5.1 INTRODUCTION

The dilatometer (Fig. 5.1) was developed in Italy by Marchetti (1980) and introduced into the United States in 1982 (Schmertmann, 1982). It has gained considerable popularity due to its operational simplicity, repeatibility of measurements and low cost. The device consists of a flat blade with overall thickness, $2w=14mm$, aspect ratio $B/w=6.8$, and cutting edge with apex angle $2\delta=18^0$. The dilatometer is instrumented with a flexible circular steel diaphragm to measure the lateral pressure. The diaphragm has a total surface area, $A_D \approx 2800mm^2$. The standard dilatometer (DMT) procedure involves the following steps (Schmertmann, 1986):

1. The blade is jacked vertically into the ground (at a steady rate, $u \approx 1\text{-}2$ cm/sec) over a standard interval (10-20cm)

2. Immediately on interruption of jacking, the internal 'contact pressure', p_0, required to displace the membrane is measured.

3. The membrane is then inflated to a prescribed displacement ($\Delta=1mm$), at which the pressure p_1 is recorded.

4. Membrane pressure is released prior to subsequent jacking and a closure pressure, p_2, is obtained when the membrane recontacts the plane of the plate (Luttenegger and Kabir, 1988),.

More elaborate procedures have recently been proposed, including a) measurement of $p(t)$ from holding tests (Marchetti et al., 1986; Robertson et al., 1988), and b) measurement of pore pressures in conjunction with the lateral stress diaphragm, (Robertson et al., 1988, Boghrat, 1982).

In the original development of the dilatometer, Marchetti (1980) combined the measured pressures p_0 and p_1 with the known (estimated a priori) in-situ pore pressure, u_0, and effective overburden stress, σ'_{v0}, to form a set of three dimensionless indices:

$$I_D = \text{Material Index} = \frac{p_1 - p_0}{p_0 - u_0} \tag{5.1a}$$

$$K_D = \text{Horizontal Stress Index} = \frac{p_0 - u_0}{\sigma'_{v0}} \tag{5.1b}$$

$$E_D = \text{Dilatometer Modulus} = 34.7 \, (p_1 - p_0) \tag{5.1c}$$

Empirical correlations were then developed (Marchetti, 1980) to provide estimates of

the following characteristics and properties:

1. From I_D, a soil classification that is 'closely related' to the prevailing grain size fraction.

2. From K_D, the in-situ lateral pressure ratio, $K_0 = \sigma'_{h0}/\sigma'_{v0}$, and OCR $= \sigma'_p/\sigma'_{v0}$ (for both granular and cohesive soils.) The undrained shear strength of cohesive soils is then estimated using the SHANSEP procedure relating c_u/σ'_{v0} to OCR (Ladd and Foott, 1974).

3. From E_D, (together with I_D and K_D), the 1-D constrained modulus, $M = 1/m_v$, for both granular and cohesive soils.

It is apparent from the correlations that the contact pressure, p_0, (used in K_D) is most important in estimating engineering properties of cohesive soils (K_0, OCR, c_u.) In this chapter, the fundamental solutions for installation stresses and pore pressures described in chapters 2 and 3 are applied to the predictions of contact pressure, p_0, measured by the dilatometer. The analytical solutions provide a rational basis: a) for estimating the effects of membrane geometry (size and location) on the measurement of p_0, b) for comparing p_0 with lateral stress measurements for axisymmetric devices such as full-displacement pressuremeter tests, and c) for interpretation of test measurements.

Analytical predictions of effective stresses and excess pore pressures around the dilatometer are obtained using: a) strain paths for an equivalent simple plate geometry (chapter 3); b) generalized effective stress soil models (MCC and MIT-E3) with input parameters corresponding to K_0-consolidated Boston Blue Clay (BBC) with $1 \leq OCR \leq 4$ (Tables 4.1, 4.2); and c) finite element solutions of the Poisson equation (chapter 2). The predictions are evaluated by comparison with measured data from a test site in South Boston for which the preconsolidation history has been determined from an extensive laboratory test program (Ladd, 1990). Further comparisons with data from a number of well-documented test sites suggest severe limitations of the K_D index for estimating OCR in soft clays.

5.2 INTERPRETATION OF CONTACT PRESSURE, p_0

Although dilatometer tests in saturated cohesive soils provide (empirical) estimates of several engineering parameters, the discussion in this chapter is focused on the prediction of undrained shear strength and stress history. Predictions of stress history are particularly important as the actual in-situ OCR (or preconsolidation pressure, σ'_p) can be obtained quite reliably from laboratory oedometer or CRSC tests (if performed on high quality

samples)[1]. Hence, the analytical predictions of contact pressures can be evaluated by comparison with measurements from well documented sites.

Based on data from 9 test sites in Italy (Fig. 5.2a), Marchetti (1980) proposed the following corelation for OCR

$$OCR = a \, K_D^m \tag{5.2}$$

where a=0.34 and m=1.56.

Subsequent work by Lacasse and Lunne (1988) and Powell and Uglow (1988) based on data from well documented sites in Norway and the U.K., respectively, show that the correlation originally proposed by Marchetti can underpredict or overpredict the actual OCR by a factor of 3-4. Figure 5.2b shows the correlation reported by Lacasse and Lunne (1982) based on data from seven well documented marine clay sites. From these results, the authors propose revised correlations for OCR using equation 5.2 with m=1.35 to 1.67. However, more detailed investigation of the data for Onsøy (section 6.3, Whittle et al., 1989) has shown possible discrepancies in the reported correlations. Subsequently, Lunne et al. (1989) have presented separate correlations for 'young' and 'old' clays, figure 5.2c, following the suggestion of Powell and Uglow (1988). Even with this subdivision, it is clear that there is a wide scatter in predictions of OCR from the K_D index.

Figure 5.2d shows the correlations presented by Powell et al. (1988) from four sites in the U.K. In this case, the correlations between the different sites are radically different from one another and do not match the correlations developed by Marchetti (1980). In large part, these differences might be explained by the types of clay at these sites:

1. Brent Cross (London Clay) and Madingley (Gault Clay) are sites with ancient clays which have been heavily overconsolidated. Preconsolidation pressures, σ'_p, are very difficult to estimate from oedometer tests (e.g. Bond, 1990). For example, at Brent Cross, Jardine and Bond (1990) report OCR=20 to 70+ from oedometer tests, while geological history suggests OCR=10-20 (Burland, 1990).

2. For the Cowden till similar difficulties may be associated with the deposition of the clay at low water content as a 'lodgement till' (Hight, 1983).

3. Finally the Grangemouth clay is a recent low plasticity alluvial clay of moderate sensitivity (Powell and Uglow, 1988) and similar to a number of clays considered by Marchetti (1980).

---

[1]In comparison, reported values of undrained shear strength depend on the mode of shearing, consolidation procedure etc.

4. In addition, Section 6.3 of Whittle et al. (1989) pointed out large discrepancies between the c_u/σ'_{v0} values quoted by Powell et al. (1988) compared with the OCR values shown in figure 5.2c.

Finally, Mayne (1987) suggests a simple correlation between OCR and K_D based on data from the 29 sites shown in figure 5.2e:

$$\sigma'_p = \frac{p_0 - u_0}{\delta} \qquad (5.3a)$$

or

$$OCR = \frac{K_D}{\delta} \qquad (5.3b)$$

where $\delta = 1$ to 3.

More recently, Robertson et al. (1988) have shown that the 'closure pressure', p_2, is approximately equal to the penetration pore pressure[2]. Although this method has not been evaluated in detail, it is likely to give a large scatter in predicted OCR as the lateral effective stress is small compared to either p_0 or p_2 (i.e. it suffers the same limitations previously reported for the piezocone using (q_t-u) (see Chapter 4).

5.3 PREDICTIONS OF DISTURBANCE DUE TO DILATOMETER INSTALLATION

5.3.1 The Dilatometer Geometry

The standard (Marchetti) dilatometer (Fig. 5.1) has an approximate aspect ratio B/w=6.8 (95mm/14mm) and a tip apex angle, δ=18-20°. Lateral stresses are measured in a 60mm diameter flexible steel membrane centered at a vertical location z/w=13 (90mm/7mm) above the tip of the blade. Accurate modeling of the surface geometry of the dilatometer can be achieved by numerical boundary element methods (panel methods). This approach was first proposed by Huang (1989) and has been investigated in detail by Williamson (1989) and Whittle et al. (1989). This study has shown that although the panel method can be used to model accurately the surface geometry, numerical accuracy of the strain paths is very difficult to achieve. Thus the results of panel method computations require careful evaluation in order to establish their reliability and accuracy for a given discretization of the surface. This imposes severe restrictions on the practical use of the

---

[2]Thus the difference, $(p_0-p_2) \approx \sigma'_{xx}$, the lateral effective stress.

panel method for estimating stresses and pore pressures around the dilatometer.

In this work, the dilatometer geometry is approximated using a simple plate of the same overall aspect ratio (B/w=6.8) as described in Chapter 3. Figure 5.3 shows the simple plate geometry. Differences in geometry between the simple plate and the dilatometer include:

1. The simple plate has a 'blunt' tip geometry as compared to the sharp apex angle ($\delta \approx 18$-20^0) of the dilatometer.

2. The simple plate has smooth curved edges in the horizontal plane, while the dilatometer is square cut.

3. The dilatometer extends to a finite vertical elevation z/w=34, while the simple plate is infinite in vertical extent.

The approximations of tip geometry have been studied in detail for axisymmetric cone penetrometers in Chapter 3. These results have shown that the stresses and pore pressures above the base of the conical tip are very similar for the simple pile, 18^0 and 60^0 cones and good matching of the solutions can then be achieved by adjusting the reference vertical location of the simple pile with respect to the location of tip of the 18^0 cone. Figure 5.4 shows that if a point source is located at the elevation of the base of the cone (i.e., at z/R$\approx$6.5 as shown in figure 5.4) the corresponding simple pile solution matches closely the 18^0 cone solution for all locations above the base of the cone. This result suggests that reliable predictions of the stresses and pore pressures on the dilatometer membrane can be achieved using the simple plate solution (B/w=6.8) with the source at the elevation of the base of the 20^0 dilatometer tip (z/w=5.7). In this case the center of the membrane on a standard dilatometer will be located at z/w=7.2. Note that the dilatometer has an equivalent radius ($R_{eq}=\sqrt{4Bw/\pi}$) of 20.5mm; therefore, the normalized equivalent diameter of the DMT membrane shown in figure 5.4 is 60/20.5$\approx$2.9.

5.3.2 Effective Stresses and Pore Pressures

Figure 5.5 (a,b,c,d) presents a complete picture of the stresses (σ'_{rr}, σ', $q_h{}^3$) and excess pore pressures (Δu) generated around the simple plate dilatometer during installation. The results correspond to the 'base case' analysis (presented in previous

---

[3]The cavity shear stress is defined as the maximum shear stress acting in a horizontal plane; i.e.

$q_h = \sqrt{(\sigma_{xx} - \sigma_{yy})^2 - \sigma_{xy}^2}$; Dilatometer

$q_h = (\sigma_{rr} - \sigma_{\theta\theta})/2$; Cone

chapters) using the Modified Cam Clay model with input parameters selected to characterize K_0-normally consolidated Boston Blue Clay. The figures show contours of stresses in two planes; a) the vertical center plane through the dilatometer membrane (y=0 plane), and b) the horizontal plane corresponding to the steady state stress field far above the tip of the penetrometer (z/w=200 plane). Excess pore pressures ($\Delta u/\sigma'_{v0}$, Fig. 5.5d) are obtained from finite element solutions of the modified Poisson equation, as described in Chapter 2. All dimensions are normalized by the equivalent radius of the dilatometer, R_{eq} (=$\sqrt{4Bw/\pi} \approx 2.94$, Chapter 3), in order to compare with predictions for an axisymmetric penetrometer (simple pile). The normalized dimensions of the B/w=6.8 plate therefore become:

Normalized half-thickness of plate=w/R_{eq}=1/2.94=0.34
Normalized half-width of plate=B/R_{eq}=2.3

The location of an equivalent membrane (i.e., of same diameter and center) is also marked on the axisymmetric penetrometer in figures 5.5a to d[4].

Overall, it can be seen that the magnitudes and distributions of the effective stresses and excess pore pressures are very similar for both penetrometer geometries and have the following characteristics:

1. Excess pore pressures (Fig. 5.5d) achieve maximum values at or close to the penetrometer tip ($\Delta u_{tip}/\sigma'_{v0} \approx 3$). At locations far above the tip of the penetrometer, the excess pore pressures are $\Delta u/\sigma'_{v0} \approx 1.0$ to 1.2 or about 0.3 to 0.4 times the tip pore pressures. The region of excess pore pressures extends to lateral distances $x/R_{eq} \approx 10$-20 and is controlled by the elastic shear modulus (G/σ'_{v0}; Baligh, 1986a, Whittle, 1987) used in the MCC model.

2. Above $z/R_{eq} \approx 5$ the lateral effective stress $\sigma'_{xx}/\sigma'_{v0}$ ($\sigma'_{rr}/\sigma'_{v0}$; for the axisymmetric case) is approximately constant and equal to 0.2 to 0.3 (Fig. 5.5a). The lateral stress acting on the interface is smaller than the free field (K_0) stress condition due to principal stress rotations described the strain path method (Whittle and Baligh, 1990).

3. Cavity shear stresses q_h/σ'_{v0} (Fig. 5.5c) are zero in the far field (since $\sigma'_{xx}=\sigma'_{yy}=\sigma'_{h0}$), increase to a maximum slightly above 0.3 at $R_{eq} \approx 5$, and then decrease to less than 0.05 at the indenter interface.

4. Changes in the mean effective stress (Fig. 5.5b) are small and reflect the description of

---

[4] By coincidence, this membrane is at an elevation comparable to the friction sleeve on standard piezocones (Chapter 4)

'critical state' conditions (σ'/σ'_{v0} is uniquely defined at large strains for all modes of shearing) used in the MCC model.

Apart from the overall similarities, a more detailed comparison of the stresses in the vicinity of the dilatometer membrane shows:

1. Excess pore pressures acting at the dilatometer boundary vary by up to 30% along the membrane ($\Delta u/\sigma'_{v0} \approx 1.8$-$2.4$; also shown in Fig. 5.5d). Similar magnitudes and variations are predicted at the same locations on the axisymmetric penetrometer.

2. The lateral effective stresses acting at the center of the dilatometer membrane, $\sigma'_{xx}/\sigma'_{v0}=0.21$, is significantly smaller than that for the equivalent axisymmetric membrane ($\sigma'_{rr}/\sigma'_{v0}=\sigma'_{xx}/\sigma'_{v0}=0.6$ at the membrane center $z/R_{eq}=2.45$).

3. The effective stresses, $\sigma'_{xx}/\sigma'_{v0}=0.21$ (see also Fig. 5.6), are much smaller than the excess pore pressures at all locations around the membrane. Thus measurements of total lateral pressures obtained using the standard dilatometer are controlled by excess pore pressures, as observed by Luttenegger (1988) and Robertson et al.(1988).

5.3.3 Evaluation of Contact Pressure from Analytical Solutions

In general, the net contact pressure, p_0-u_0, measured by the dilatometer can be equated with the net average total normal stress acting on the membrane:

$$(p_0 - u_0) \ = \ (\sigma_{xx} - u_0)_{avg} \ = \ \frac{\int (\sigma_{xx} - u_0) \, dA}{A} \tag{5.4}$$

In principle, predictions of p_0-u_0 require a complete knowledge of the three-dimensional effective stress fields around the dilatometer to estimate pore pressures from equilibrium. Figure 5.6 shows the distributions of lateral stresses and excess pore pressures acting at the surface of the simple plate dilatometer: a) along the vertical centerline of the device (y/w=0 plane); and b) in a horizontal steady state plane (z/w=200)[5]:

1. The lateral pressures are almost constant across the width of the ('equivalent') membrane (Fig. 5.6b), with variations in horizontal effective stresses and pore pressures being less than 5%.

2. In the vertical plane (Fig. 5.6a), there in a fairly significant (25%) decrease in net total lateral stress (σ_{xx}-u_0) moving from the bottom to the top of the membrane. Horizontal

---

[5]In this case, it is assumed that the steady state plane can be used to assess the lateral variations in stresses and pore pressures across the membrane.

effective stresses are very nearly constant with respect to the vertical coordinate. The fact that pore pressure, and hence total stress, vary significantly along the membrane is a potential source of scatter in DMT correlations.

Based on the results in figure 5.6, the dilatometer contact pressure can be calculated assuming no variation in σ_{xx} in the y-direction (at any given z) as follows:

$$(p_0 - u_0) = \frac{\int_{z_1}^{z_2} (\sigma_{xx} - u_0)\, 2\, \sqrt{r_m^2 - (z-z_c)^2}\ dz}{\pi\, r_m^2} \qquad (5.5)$$

where r_m is the membrane radius and z_c is the elevation of the membrane center.

Application of Equation 5.5 to the results in figure 5.6 gives $K_D=(p_0-u_0)/\sigma'_{v0}=2.23$, which is essentially equal to the lateral stress acting at the center of the membrane is $(p_0-u_0)/\sigma'_{v0}=2.21$. This result suggests that the contact pressure can be reliably estimated for the purposes of analysis from the total lateral stress acting at the center of the membrane; however, further analyses based on more realistic soil models at varying OCR's are required to verify this tentative conclusion.

5.3.4 Analytical Predictions of Dilatometer Membrane Conditions

This section presents predictions of total lateral stress and pore pressure conditions at the center of a dilatometer membrane immediately following undrained penetration. Assuming that the total lateral stress at the center of the DMT membrane closely approximates the contact pressure, p_0, measured in the standard dilatometer test (section 5.3.3). While not a standard DMT measurement, predictions of pore pressures at the center of the membrane are also considered in this section to assess whether installation pore pressures can be used to improve the interpretion of dilatometer test results. Such pore pressure measurements could be obtained directly from a filter located at the center of the membrane as described by Robertson et al. (1988). Based on the assumptions described in previous sections, table 5.1 presents a summary of analytical predictions for plate dilatometer contact pressures. The table shows results for two soil models (MCC and MIT-E3) with input parameters selected for Boston Blue Clay with initial OCR's of 1, 2, and 4.

The aim of these predictions is to address the following questions regarding interpretation of DMT measurements in cohesive soils:

1. Which soil parameter(s) is being measured, i.e. which soil parameter provides the most suitable basis for correlation with DMT results? While many soil parameters will undoubtedly affect a DMT measurement, the aim is to identify one which has a dominating role to be used as a basis for correlations. Soil parameters which will be considered in this section are a) OCR (σ'_p/σ'_{v0}) because it controls the undrained behavior of cohesive soils, and b) undrained shear strength c_u because it has been shown to provide a reliable basis for correlation in other penetration tests (e.g. the correlation between ($q_c-\sigma_{v0}$) and c_u in the piezocone test; chapter 4). Since c_u is dependent upon shearing mode, correlations should use a consistent reference shear strength (TC, DSS, or TE). In this section c_{uTC} will be used as the reference shear strength.

2. Which DMT measurement provides the most reliable basis for estimating soil properties? Consideration will first be given to the K_D parameter measured in the standard DMT, defined by equation 5.1b; $K_D = (p_0 - u_0)/\sigma'_{v0}$. If pore pressures are measured at the center of the membrane, a number of additional parameters may be considered as a means for estimating soil properties, which can include:

$$\frac{u - u_0}{\sigma'_{v0}} = \text{Normalized excess pore pressure}$$

$$\frac{p_0 - u}{\sigma'_{v0}} \cong \text{Normalized effective lateral stress}$$

$$\frac{u - u_0}{p_0 - u_0} \cong \text{Ratio of excess pore pressure to total lateral stress}$$

Finally, the normalized net change in horizontal total lateral stress; $(p_0-\sigma_{h0})/\sigma'_{v0}$ at the membrane will be considered. Although this parameter would be of limited practical value, as σ_{h0} is generally unknown, it will be considered for the purpose of understanding the mechanics of plate penetration (i.e., do soil properties relate to total stresses or to net stresses acting on the penetrometer?).

3. How do DMT measurements vary with soil properties? The first type of relationship linking soil parameter (OCR, c_{uTC}) to DMT measurement (K_D, etc.) that will be considered is that of a direct proportion between soil parameter and DMT measurement:

$$(\text{soil parameter}) = a \times (\text{DMT measurement}) \qquad 5.6$$

where 'a' is a constant. This type of relationship is desirable as it clearly relates soil

parameter to measurement in a way that can be readily interpreted. Using MCC and MIT-E3 model predictions, a number of DMT measurements (K_D, pore pressure, etc.) will be used evaluated to determine whether they can be directly related (approximately) to either OCR or c_u.

If no direct relationships relating soil property to measurement can be identified, then more complex functions, such as a power function of the form proposed by Marchetti (1980) (see also equation 5.2):

$$(\text{Soil Property}) = a \times (\text{DMT measurement})^m \qquad (5.7)$$

(where 'a' and 'm' are constants) must be considered. While such relationships tend to be highly empirical and difficult to understand, they may prove necessary if no simple relationship can be identified relating DMT measurements to soil properties.

4. What is the range of applicability of a correlation? This question can be considered in two parts: a) can meaningful site-specific correlations be developed (i.e., over what range of OCR and for what conditions of soil variability will a correlation be valid at a specific site?) and b) can such correlations be extrapolated to other sites, i.e., are reliable universal correlations possible for a wide range of soils? These questions can be addressed by comparing model predictons of DMT measurements for a series of differing soil types (with respect to sensitivity, plasticity, etc.) to assess the influence of variations in soil type. As of this writing, these predictons are not complete; however, some tentative conclusions on this issue are possible by comparing MCC (insensitive soil, i.e., no strain softening) predictions to MIT-E3 (moderate sensitivity) predictions for BBC.

5.3.4.1 Correlation with Undrained Shear Strength, c_{uTC}

Table 5.2a shows predictions of DMT membrane pore pressures and stresses normalized membrane stresses and pore pressures normalized by the undrained shear strength, c_{uTC}. This table indicates:

1. Predictions of $(u-u_0)/c_{uTC}$, $(p_0-u_0)/c_{uTC}$, and $(p_0-\sigma_{h0})/c_{uTC}$ based on both the MCC and MIT-E3 models all vary substantially (30-50%) as the OCR increases from 1 to 4; i.e. these ratios cannot be considered to be even approximately constant over the range of OCR considered. This result implies that $(u-u_0)$, (p_0-u_0), and $(p_0-\sigma_{h0})$ cannot be directly correlated to undrained shear strength, c_{uTC}, in a manner described by equation 5.6.

2. The normalized effective lateral stresses acting on the membrane, σ'_{xx}/c_{uTC}, predicted

from the MCC model are approximately constant with OCR; however, the MIT-E3 model shows this ratio to vary substantially with OCR (by a factor of over 3). The different trends predicted from the two models can be attributed to the strain-softening behavior in the MIT-E3 model. In any event, this result implies that under realistic conditions involving strain softening, effective lateral stresses, σ'_{xx}, cannot be reliably correlated the undrained shear strength, c_{uTC} in a manner described by equation 5.6.

The fact that DMT membrane measurements can not be linearly correlated to undrained shear strength suggests that it is not worthwhile to pursue simple correlations between DMT measurements and undrained shear strength. While some authors (Lacasse and Lunne, 1988; Marchetti, 1980) propose more complex K_D-c_u correlations of the type described by equation 5.7, it appears preferrable to correlate DMT measurements to OCR, because a) stress history profiles (from oedometer tests) can be more reliably defined than shear strength profiles, and b) shear strength is dependent upon shearing mode, which complicates correlations.

5.3.4.2 Correlations with Stress History, OCR

Table 5.2b shows MCC and MIT-E3 predictions of DMT membrane pore pressures and stresses normalized by preconsolidation pressure σ'_p. Again it can be seen that $(u-u_0)/\sigma'_p$, $(p_0-u_0)/\sigma'_p$, and $(p_0-\sigma_{h0})/\sigma'_p$, all vary substantially (by up to a factor of 2) with OCR. This implies that direct correlation (of the type defined by equation 5.6) between DMT membrane measurements and preconsolidation pressure cannot be considered even as an approximation.

The ratio of excess pore pressure to total stress, $(u-u_0)/(p_0-u_0)$, merits discussion, since similar correlations to predict OCR have been proposed (e.g. B_q, Senneset et al., 1982) in the piezocone test. The results in Table 5.1 show that both the MCC and the MIT-E3 models predict very little variation in this ratio with OCR, i.e. a slight decrease of only 5 to 10% as OCR increases from 1 to 4. The analyses therefore indicate that DMT measurements of $(u-u_0)/(p_0-u_0)$ cannot provide a reliable basis for correlations with OCR, especially given the likely scatter in actual DMT test data.

The above observations imply:

1. Simple linear correlations between DMT measurements and OCR do not appear feasible; therefore, there is no alternative to the empirical power function relationships (equations 5.2 and 5.7) proposed by Marchetti (1980).

2. Membrane pore pressure measurements will not simplify the interpretation of the dilatometer test; therefore, no compelling reason exists for abandoning the K_D parameter in favor of pore pressure or effective stress measurements. However, pore

pressure data might be useful for other purposes, such as for soil classification or for estimation of consolidation behavior.

Table 5.1 presents MCC and MIT-E3 model predictions of K_D versus OCR. These predictions suggest that, for a given set of soil parameters, a unique relationship exists between OCR and K_D; therefore, a correlation of the type proposed equation by 5.2 is possible. Second, recalling that the MCC predictions represent an insensitive soil while the MIT-E3 predictions[6] represent a moderately sensitive soil, it can be seen that the location and slope of the K_D-OCR curve in log(K_D)-log(OCR) space is sensitive to variations in soil sensitivity. This second conclusion should be considered tentative until model predicitons with soil input parameters for a wider range of soil types are completed. The implications of these observations on practical use of the DMT are:

1. Site specific log(K_D)-log(OCR) correlations can probably be developed from DMT test in soils exhibiting a) normalized behavior (no cementation, etc.) and b) minimal variation in soil type. This conclusion is based on the model predictons showing that for a given set of (normalized) soil properties a unique K_D-OCR relation can be established.

2. It is unlikely that a general, universal, correlation between DMT K_D and OCR can be established. This conclusion is based on the apparent sensitivity of the location and trend of the K_D-OCR curve to variations in soil type. A corollary to this conclusion is that, at sites exhibiting substantial variations in soil type, even site specific correlations cannot be reliably established.

5.3.5 Comparisons with Axisymmetric Penetrometers

The full displacement pressuremeter test (FDPMT) combines a cone penetrometer with a pressuremeter. Devices described by Baguelin and Jezequel (1983), Withers et al. (1986), and Briaud and Shields (1979) are shown in figure 5.7. For the device described by Withers et al., the center of the expandible membrane is located a normalized vertical distance $z/R \approx 43$ above the cone tip, and has a length $L/R \approx 21$. As discussed in chapter 2, a steady state condition occurs above $z/R \approx 15-20$ during cone penetration; therefore, the entire membrane can be considered to be located in the steady state zone. The initial total stress, p_i, measured in this test corresponds to the average total lateral stress acting on the membrane and is therefore analgous to the contact pressure, p_0, measured in the dilatometer test. Since the membrane is located entirely in the steady state zone, p_i can be taken to be

---

[6]With input parameters describing K_0-consolidated BBC

equal to the steady state total lateral stress.

MCC and MIT-E3 predictions of p_i ($=\sigma_{rr}-u_0$) are shown in Table 5.3. Comparison of these predictions with the dilatometer predictions in Table 5.1 indicate that MCC predictions of total lateral stress at the FDPMT membrane are 15-30% less than the DMT predictions. This can be largely attributed to the fact that the FDPMT membrane is locate in the steady state zone, while the DMT membrane is located nearer to the tip. MIT-E3 predictions indicate the FDPMT p_i to be roughly 10-20% less than the corresponding DMT predictions. Comparisons by Luttenegger and Blanchard (1990) of the measured FDPMT p_i and DMT p_0 at eight sites generally confirm the MIT-E3 predicted trends.

5.4 COMPARISONS WITH MEASURED DATA

In this section the model predictions presented in section 5.3 are compared with measured data in order to determine:

1. The capabilities and limitations of the analytical predictions for describing a) the magnitude of K_D, and b) variations in K_D with stress history.

2. The validity of the preliminary conclusions drawn in the previous section: a) K_D cannot linked to OCR by a simple direct proportion; b) that well-defined trends can be established between K_D and OCR at sites exhibiting normalized behavior (no cementation, etc.) and minimal variability in soil type; c) a universal correlation relating K_D to OCR for all soils is not feasible; and d) at sites showing extensive soil variability or non-normalized behavior, even site-specific cannot be reliably obtained.

In this section, seven well-documented sites are reviewed to assess the relationship between DMT K_D and OCR. The OCR profiles are based on either oedometer or constant rate of strain consolidaton (CRSC) tests. A description of the geotechnical characteristics of each of the seven sites is described below:

1. South Boston test site (associated with the Central Artery/Third harbour tunnel project; CA/T). This site (index properties and stress history are shown in figure 4.19b; Ladd, 1990) includes a deep stratum of Boston Blue Clay between elevations[7] 74ft and -29ft, with in-situ OCR's ranging from OCR $\approx$ 5 at elevation z = 65 ft. to OCR = 1.1 at z = -20 ft. The soil is significantly more sensitive below elevation z = 20 ft.

2. Potomac River Alluvium. This site (Mayne, 1987) consists of organic silty clay having

---

[7]Elevations in the figure are quoted with respect to Boston City Base (BCB); elevation +100ft is mean sea level.

an average liquid limit, $w_L \approx 83\%$ and an average plasticity index, $I_p \approx 37\%$. Below a depth of 11 m the liquidity index generally ranges, $I_L = 0.5$ to 0.8. Above 11m, the liquidity index is highly variable, $I_L = 0.4$ to 1.6. Below 12m depth the soil has a relatively constant OCR in the range of approximately 1.2 to 1.7. Above 12m OCR's decrease from approximately 3 to 1.5.

3. Porto Tolle. This site located on the delta of the Po River is described by Ghionna et al (1981) and Jamiolkowski et al. (1982). The stratum of interest for the dilatometer evaluation is the soft silty clay between depths of 10 to 28m. This stratum contains frequent seams and lenses of fine silty sand, which never exceed a few centimeters thickness. The liquid limit within the stratum, $w_L = 52.3 \pm 2.2$, and the mean plasticity index, $I_p = 30.5 \pm 1.6\%$. The sensitivity measured from field vane tests ranges from 2 to 3. The entire statum has a slight, uniform OCR ranging from 1.2 to 1.3.

4. Drammen. The Drammen site (Lacasse and Lunne, 1982) is a marine deposit consisting of sand and clay (0-5m) overlying a 5m layer of plastic clay (5-10m) and 35m of lean clay (10-45m). In the plastic layer (5-10m) the liquid limit ranges, $w_L = 50\text{-}70\%$ and plasticity index ranges, $I_p = 25\text{-}30\%$; while in the lean clay layer (below 10m), $I_p = 10\text{-}15\%$. The sensitivity (based on field vane data) ranges from 6-8 in the plastic clay layer and from 4-7 in the lean clay layer. The OCR is relatively uniform in both layers, with an OCR from 1.3-1.5 in the plastic layer and from 1.1-1.2 in the lean clay layer.

5. Onsøy. The Onsøy site (Lacasse and Lunne, 1982) is a soft to medium marine clay deposit extending to 45m depth. Liquid limit and plasticity indices range from 55-75% and 20-35%, respectively. In the upper 2-6m the OCR decreases from 15 to 1.3. Below 6m the OCR is essentially constant at 1.3, and the sensitivity based on field vane data ranges from 5-6.

6. Florence Lake. This deposit is an oxbow lake of the nearby Missouri River, consisting of plastic alluvial clay (Whittle et al., 1989.) The plasticity index increases with depth to approximately 60% at a depth of 20ft, and then decreases with depth to a value of about 25% at a depth of 40 ft. The liquidity index, $I_L = 0.6\text{-}0.9$ throughout the deposit, with no observable trend with depth. The oedometer data indicate an OCR profile with three zones: a) a normally consolidated zone below 20ft, b) a nearly constant preconsolidation pressure from 10-20ft, and c) a crust below the surface with scattered OCR's ranging from approximately 1.5-10. Sensitivity measured from field vane tests ranges from 3-4 at depths greater than 10ft.

7. New Jersey Varved Clay. This site is described in detail by Whittle et al. (1989). Preconsolidaton pressure data indicate a desiccation crust within the top 15-20ft and then a constant amount of preconsolidation ($\sigma'_p - \sigma'_{v0}$) within the lower 40ft.

For the purpose of establishing whether the model predictions realistically portray actual DMT behavior, MCC and MIT-E3 predictions of K_D for BBC are compared to DMT measurements taken from the South Boston test site (BBC), as presented in figure 5.8. The solid lines show the predictions at the center of the membrane, while the dashed lines show the predicted lateral stresses at the top and bottom of the membrane. This comparison shows:

1. For OCR>2 and for low OCR, the MCC and MIT-E3 predictions compare well to measured data. For $1.2 \leq OCR \leq 2$, the predictions do not match measurements with respect to either magnitudes or trend with varying OCR. However, application of Marchetti's (1980) technique to obtain OCR's from the measured K_D values predict a more or less constant preconsolidation pressure within the upper 65 ft of clay, which contradicts the actual σ'_p profile. Other interpretation techniques could not remove this serious discrepancy. Moreover, preliminary data indicate that the clay at this site does not exhibit normalized behavior (Ladd, 1990). Such behavior cannot be modelled by either the MIT-E3 or MCC models, which may further contribute to the discrepancy between model predictions and measured K_D.

2. The width of the scatter band is comparable to the width of the band defined by the predicted total lateral stresses at the top and bottom of the membrane. This suggests that the data scatter may be related to the variability of total stresses and pore pressure along the DMT membrane.

Plots of K_D versus OCR on a log-log scale for the remaining six sites are shown in figure 5.9. From these plots it can be seen that:

1. At three sites, Onsøy, Potomac, and Florence Lake, the data show a clearly defined K_D-OCR (site-specific) relationship. In all three cases, the data show that for a given OCR, the scatter in K_D is less than 25%. Such trends are consistent with model predictions indicating that reliable site-specific trends are possible in deposits exhibiting minimal heterogeneity and (presumably) normalized behavior.

2. The Drammen data indicate a much wider scatter band (factor of 2 variation in K_D at a given OCR). This could be linked to the heterogeneity of the deposit and supports the suggestion that the relationship of K_D versus OCR is heavily influenced by variations in soil properties.

3. The New Jersey varved clay data shows K_D to be virtually independent of OCR for OCR>2. This could be a consequence of the unique behavior of varved clays. Evaluation of these data in light of model predictions is not feasible, as neither model is capable of realistically simulating a varved clay. However, as discussed in Section 6.5.3 of Whittle et al. (1989), the DMT data completely "missed" the high

preconsolidaton within the upper desiccated crust of the deposit for reasons that still remain unknown.

4. All data sets indicate that a complex relationship exists between K_D and OCR; that is, K_D cannot be correlated (even approximately) to OCR by a simple direct proportion (note that a 1:1 slope on a log-log plot implies that a directly proportional relationship exists). This further reinforces the notion that K_D is related to OCR in a very complex manner that can only be treated within an empirical framework.

Finally all seven data sets are superimposed in figure 5.10. The wide scatter band demonstrates that a universal K_D-OCR relationship cannot be established. This suggests that extrapolation of site-specific relatonships to new sites cannot be considered a reliable procedure.

Soil Model	OCR	K_0	$\dfrac{c_{uTC}}{\sigma'_{v0}}$	$\dfrac{(u-u_0)}{\sigma'_{v0}}$	$\dfrac{\sigma'_{xx}}{\sigma'_{v0}}$	$\dfrac{p_0-u_0}{\sigma'_{v0}}*$	$\dfrac{u-u_0}{p_0-u_0}$	$\dfrac{p_0-\sigma_{h0}}{\sigma'_{v0}}$
MCC	1.0	0.48	0.32	2.0	0.2	2.2	0.9	1.7
	2.0	0.57	0.58	2.3	0.4	2.7	0.9	2.1
	4.0	0.75	1.05	3.3	0.7	3.9	0.8	3.2
MIT-E3	1.0	0.48	0.33	1.4	0.05	1.5	1.0	1.0
	2.0	0.57	0.54	2.2	0.1	2.3	1.0	1.8
	4.0	0.75	1.05	2.8	0.5	3.4	0.9	2.0

* K_D

Note: All predictions based on stresses at center of membrane; $p_0 = \sigma_{xx}$

Table 5.1 Predictions at center of dilatometer membrane for K_0-consolidated Boston Blue Clay

Soil Model	OCR	K_0	$\dfrac{c_{uTC}}{\sigma'_{v0}}$	$\dfrac{(u-u_0)}{c_{uTC}}$	$\dfrac{\sigma'_{xx}}{c_{uTC}}$	$\dfrac{p_0-u_0}{c_{uTC}}$	$\dfrac{p_0-\sigma_{h0}}{c_{uTC}}$
MCC	1.0	0.48	0.32	6.3	0.7	6.9	5.4
	2.0	0.57	0.58	4.0	0.6	4.7	3.7
	4.0	0.75	1.05	3.1	0.6	3.7	3.0
MIT-E3	1.0	0.48	0.33	4.3	0.2	4.5	3.0
	2.0	0.57	0.54	4.0	0.2	4.2	3.2
	4.0	0.75	1.05	2.7	0.5	3.2	1.9

Table 5.2a Prediction of DMT membrane stresses normalized by c_{uTC}
for K_0-consolidated BBC

Soil Model	OCR	K_0	$\dfrac{c_{uTC}}{\sigma'_{v0}}$	$\dfrac{(u-u_0)}{\sigma'_p}$	$\dfrac{\sigma'_{xx}}{\sigma'_p}$	$\dfrac{p_0-u_0}{\sigma'_p}$	$\dfrac{p_0-\sigma_{h0}}{\sigma'_p}$
MCC	1.0	0.48	0.32	2.0	0.2	2.2	1.7
	2.0	0.57	0.58	1.2	0.2	1.4	1.1
	4.0	0.75	1.05	0.8	0.2	1.0	0.8
MIT-E3	1.0	0.48	0.33	1.4	0.05	1.5	1.0
	2.0	0.57	0.54	1.1	0.06	1.2	0.9
	4.0	0.75	1.05	0.7	0.3	0.8	0.5

Table 5.2b Prediction of DMT membrane stresses normalized by σ'_p
for K_0-consolidated BBC

Soil Model	OCR	K_0^+	$\dfrac{c_u^{TC}}{\sigma'_{v0}}$	$\dfrac{(u-u_0)}{\sigma'_{v0}}$	$\dfrac{\sigma'_{rr}}{\sigma'_{v0}}$	$\dfrac{\sigma_{rr}-u_0}{\sigma'_{v0}}$*	$\dfrac{u-u_0}{\sigma_{rr}-u_0}$	$\dfrac{\sigma_{rr}-\sigma_{r0}}{\sigma'_{v0}}$
MCC	1.0	0.48	0.32	1.3	0.3	1.5	0.8	1.1
	2.0	0.57	0.58	1.7	0.5	2.2	0.8	1.6
	4.0	0.75	1.05	2.3	1.0	3.2	0.7	2.5
MIT-E3	1.0	0.48	0.33	1.2	0.1	1.4	0.9	0.9
	2.0	0.57	0.54	1.7	0.2	1.9	0.9	1.4
	4.0	0.75	1.05	2.0	0.7	2.7	0.7	1.9

+ $K_0 = \sigma'_{r0}/\sigma'_{v0}$

* i.e. Lift-off pressure, $p_i = \sigma_{rr}$

Table 5.3 Predictions at center of membrane of full displacement pressuremeter in BBC at z/R=20
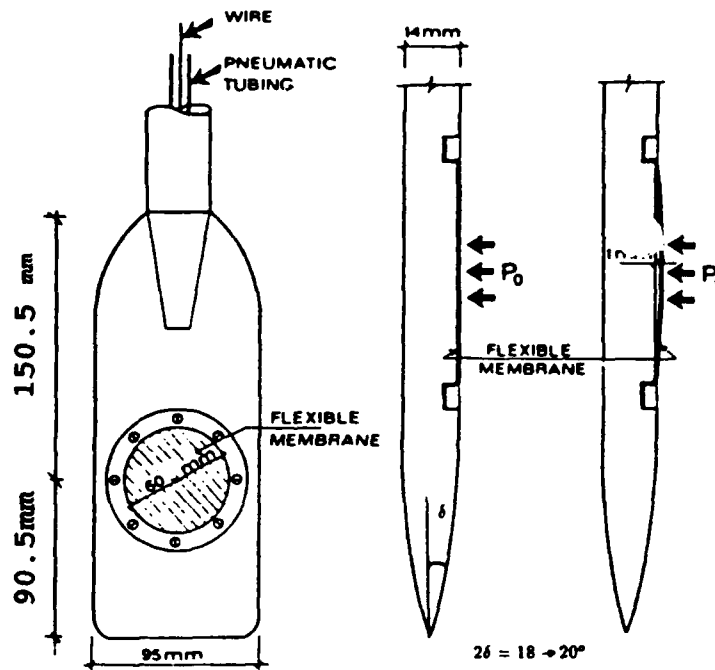
Figure 5-1: Geometry of the Marchetti Dilatometer
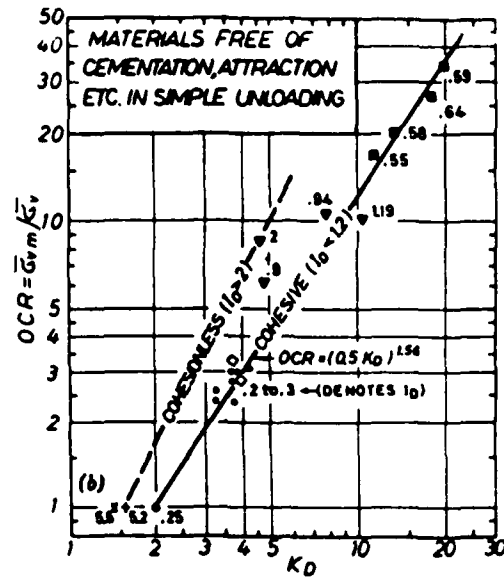
a) Marchetti (1980)
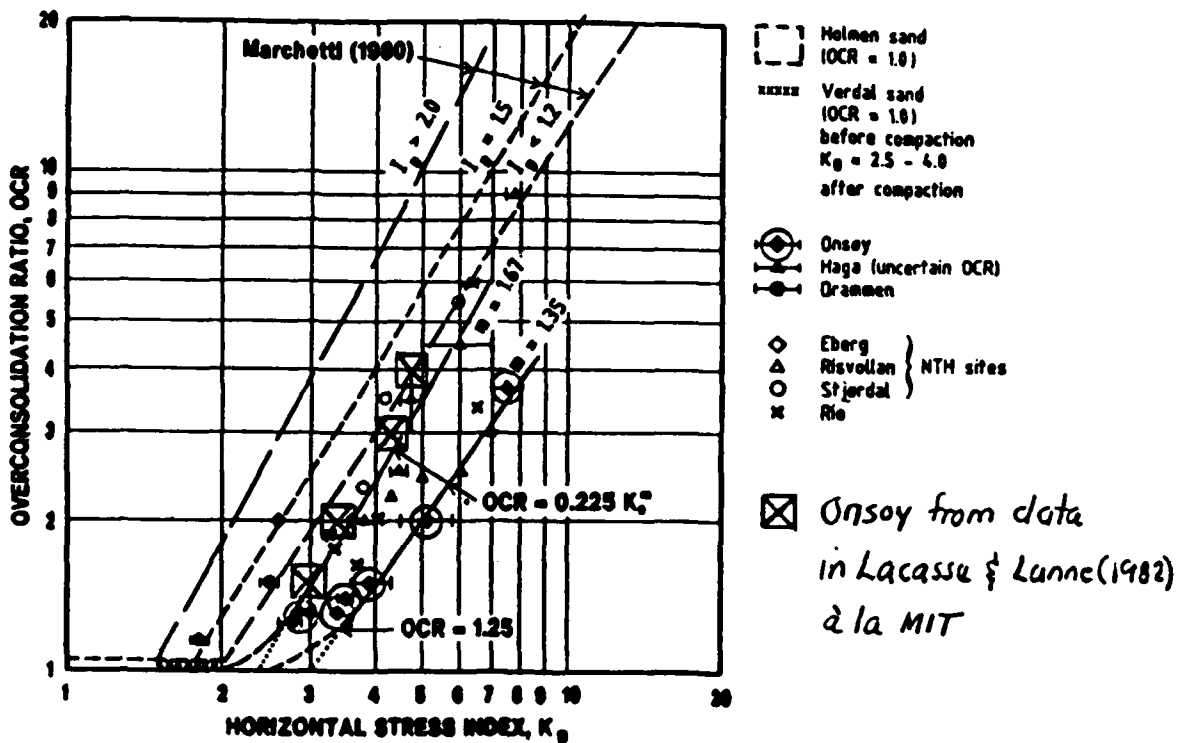
b) Lacasse and Lunne (1982)

Figure 5.2. Empirical correlations between overconsolidation ratio and dilatometer contact
pressure,p_0: a) Marchetti (1980); b) Lacasse and Lunne (1982); c) Lunne et
al. (1989); d) Powell and Uglow (1988); e) Mayne (1986)
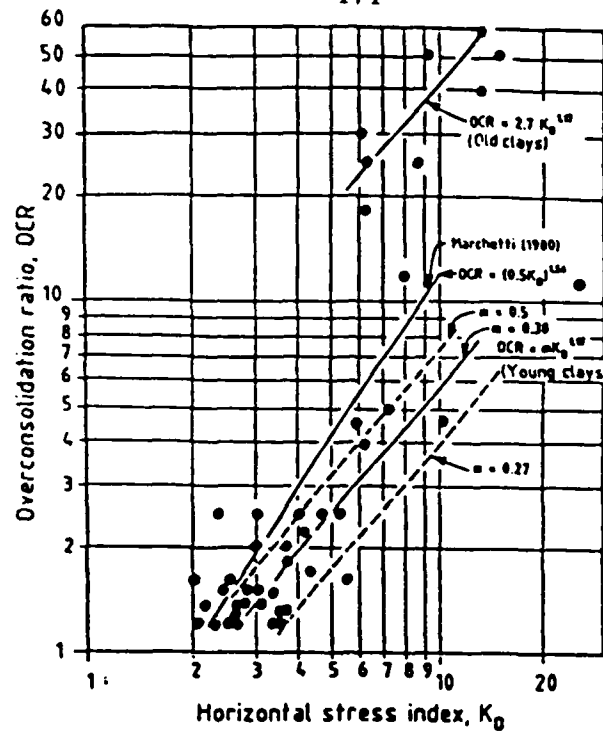
Fig. 34 Revised OCR correlation for dilatometer test (Lunne et al., 1989)

c) Lunne et al. (1989)
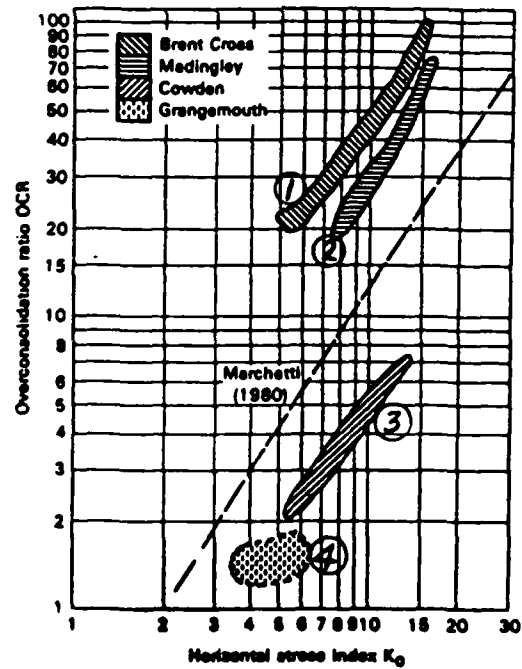
d) Powell and Uglow (1988)
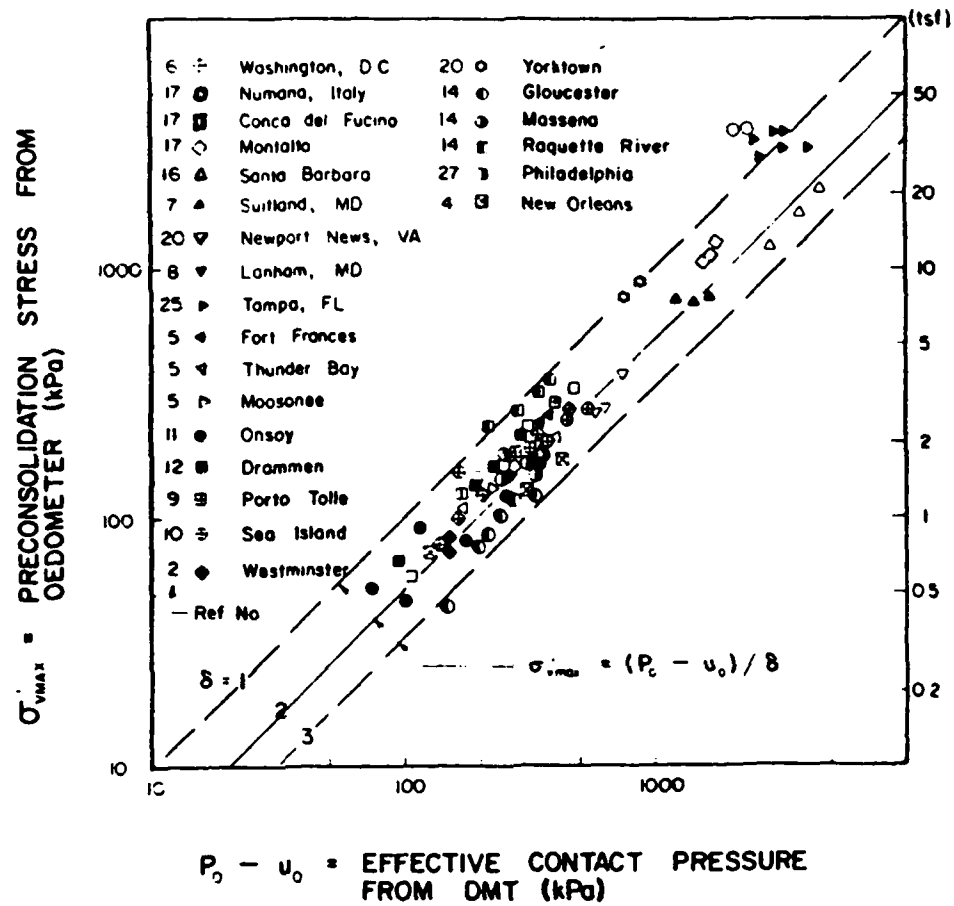
Figure 5-2 (cont.)

e) Mayne (1986)

Figure 5-2 (cont.)

z/w

Dilatometer Membrane

Simple Plate, B/w=6.8

x/w

y/w
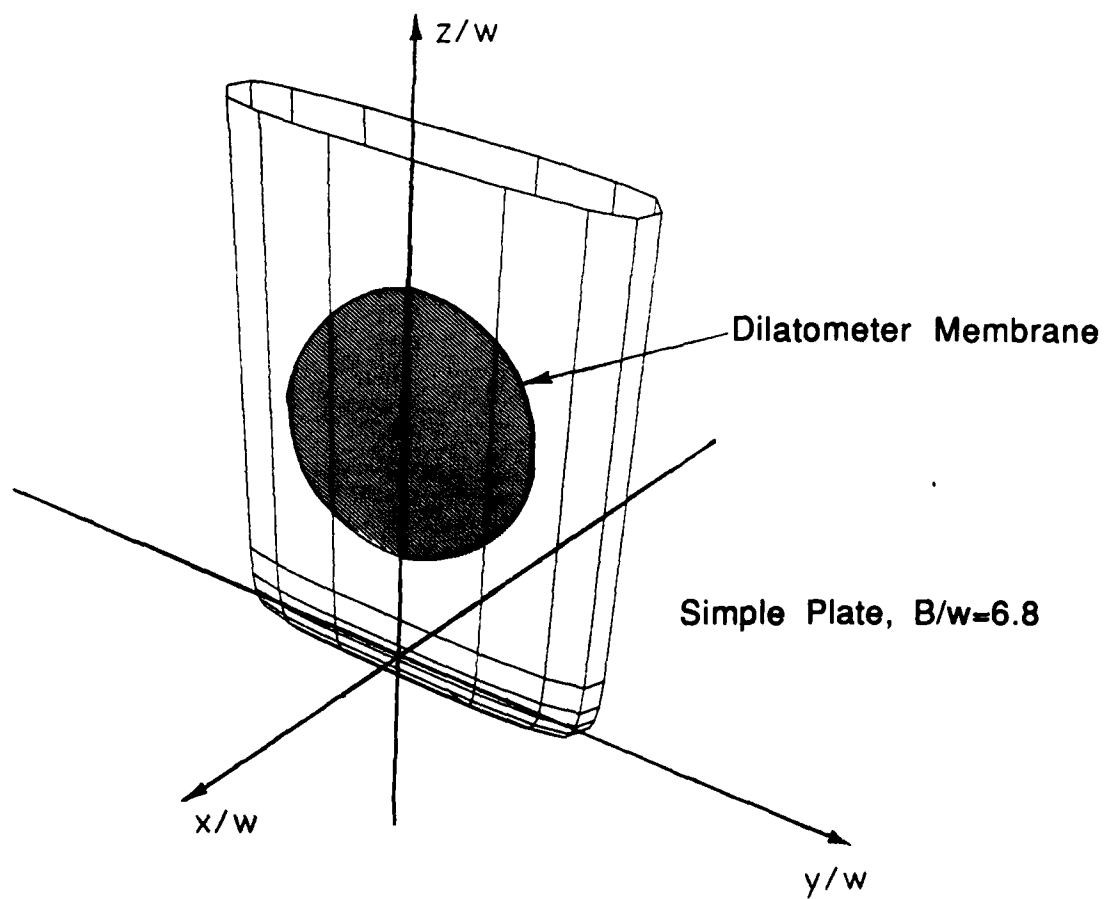
Figure 5-3 Geometry of Simple Plate Used to Simulate Dilatometer
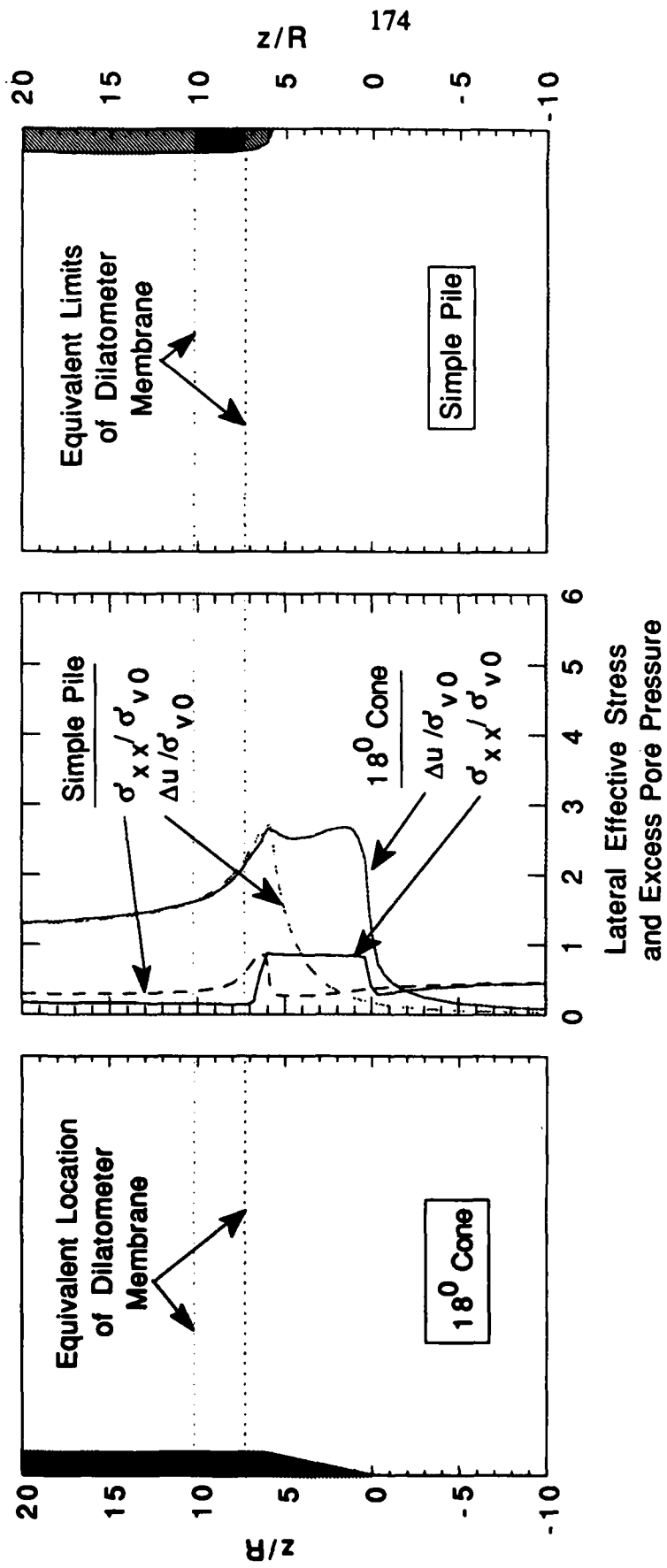
Figure 5-4 Comparisons of Simple Pile Solution to 18⁰ Cone Solution
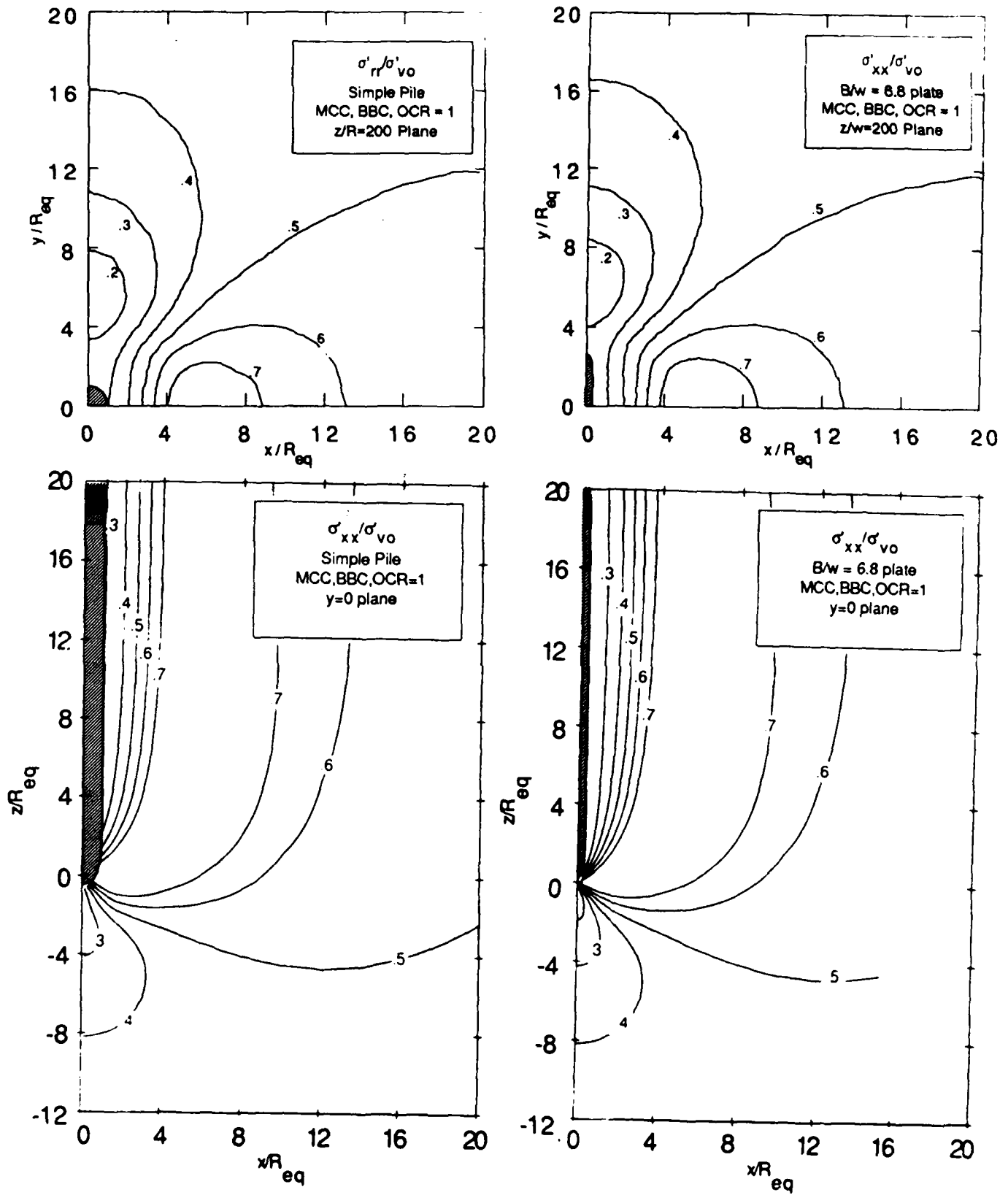
a) Lateral Stresses

Figure 5-5 Simple Pile and Simple Plate Stress and Pore Pressure Contours
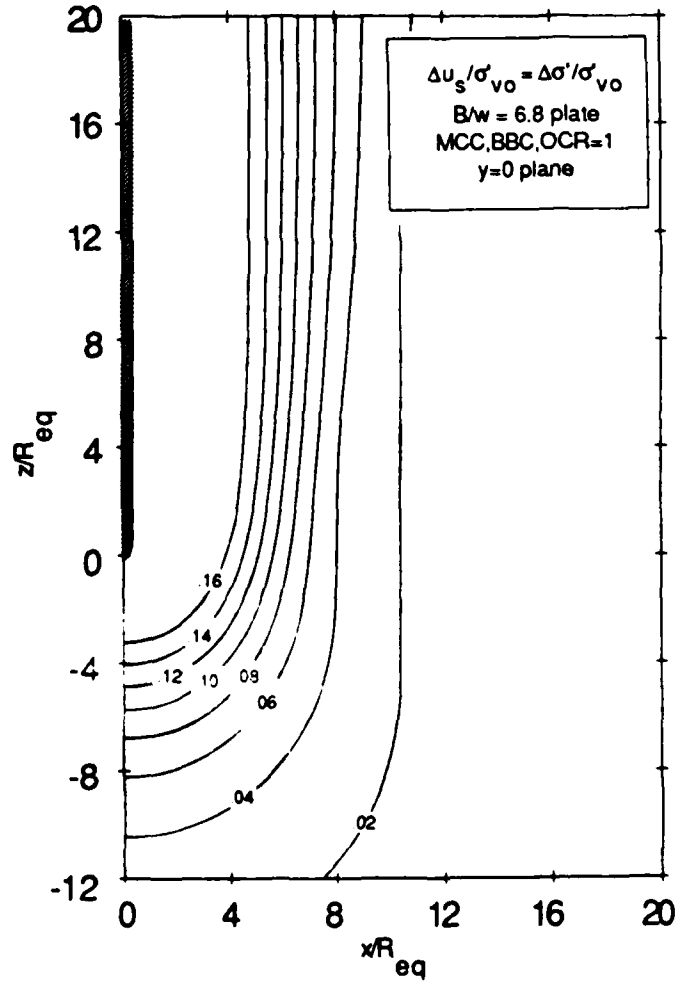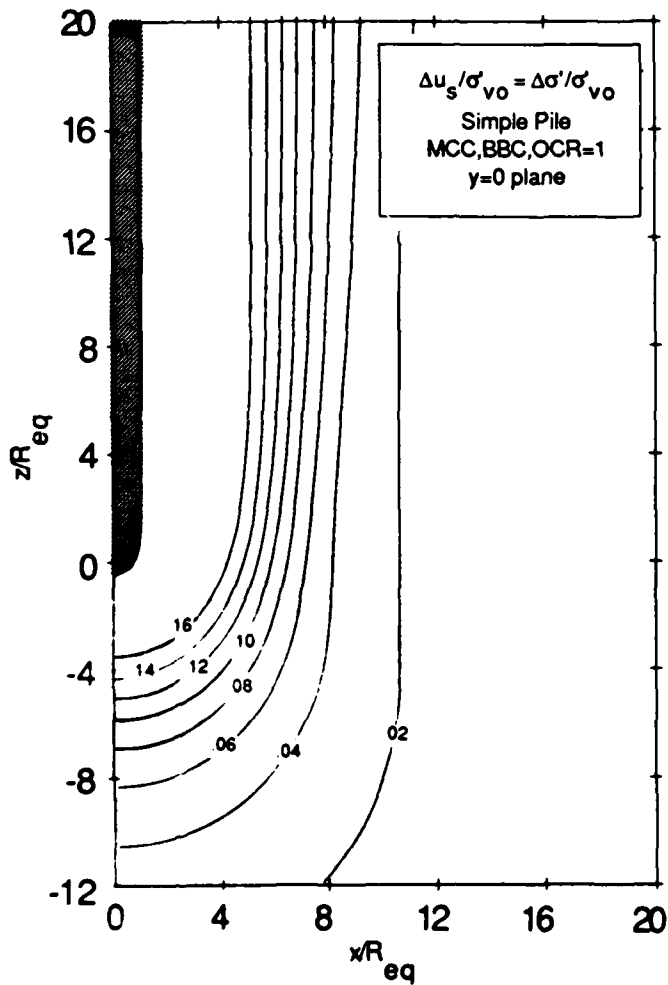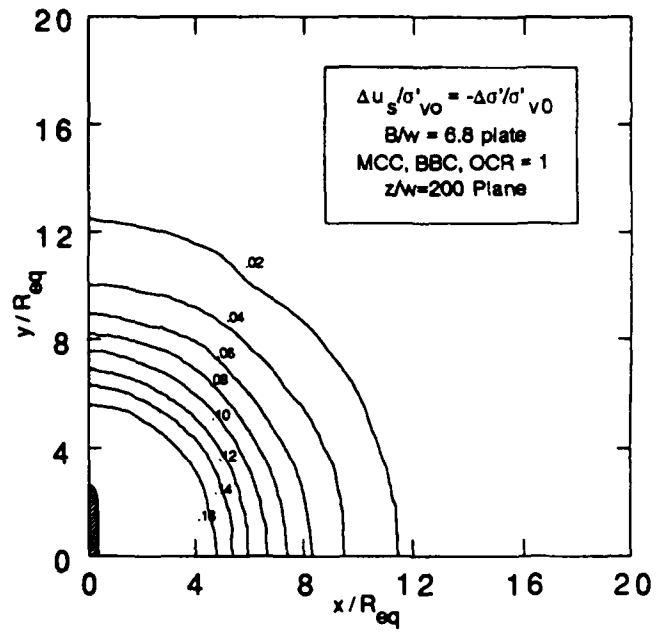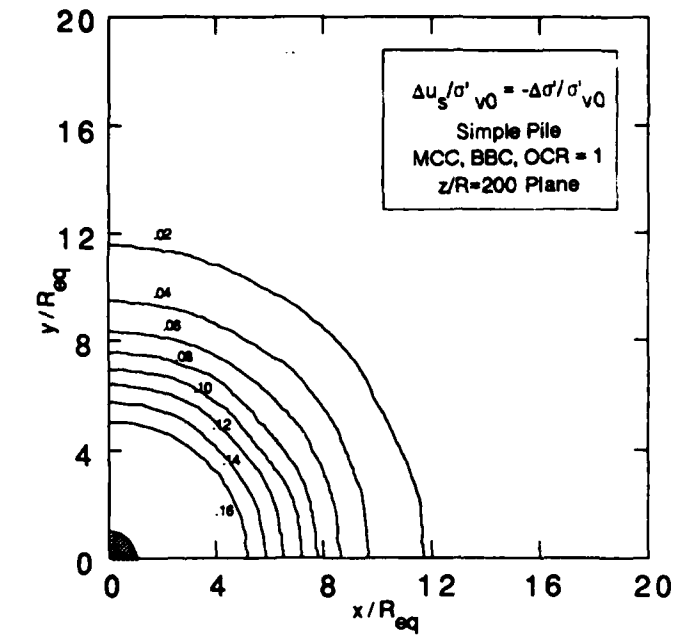
Figure 5-5 (cont.) b) Shear-Induced Pore Presures
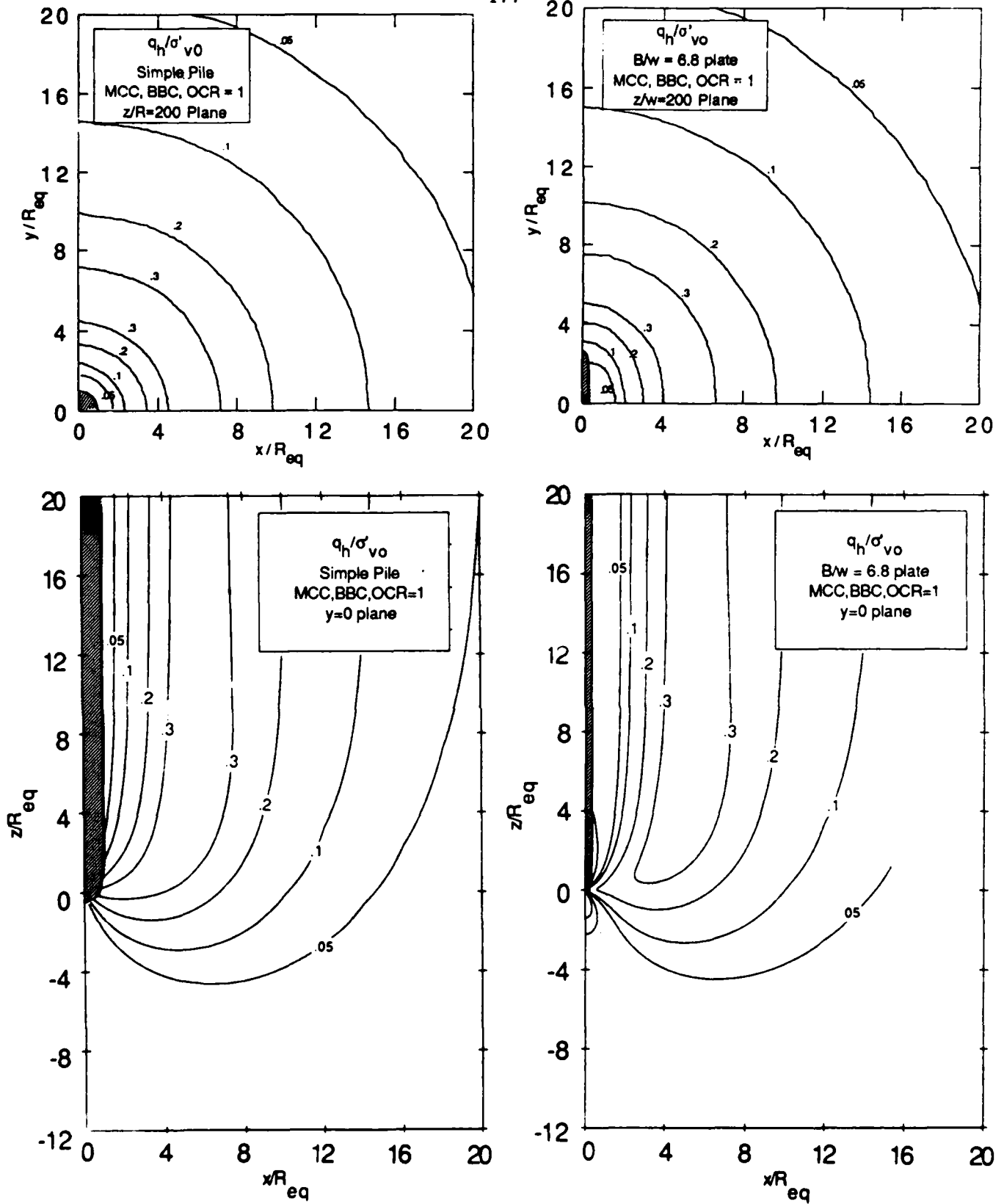
Figure 5-5 (cont.) c) Cavity Shear Stresses
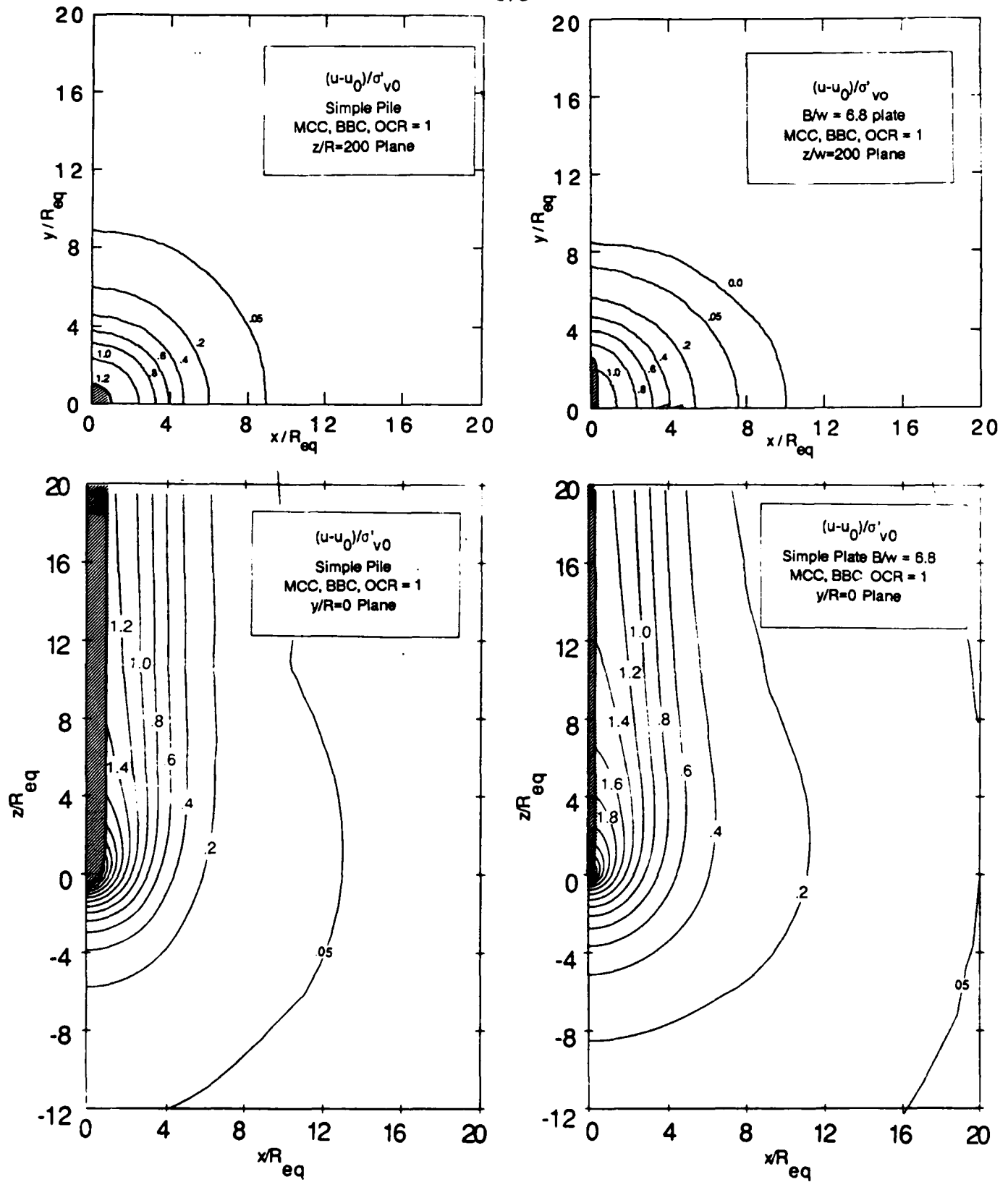
Figure 5-5 (cont.) d) Excess Pore Pressures
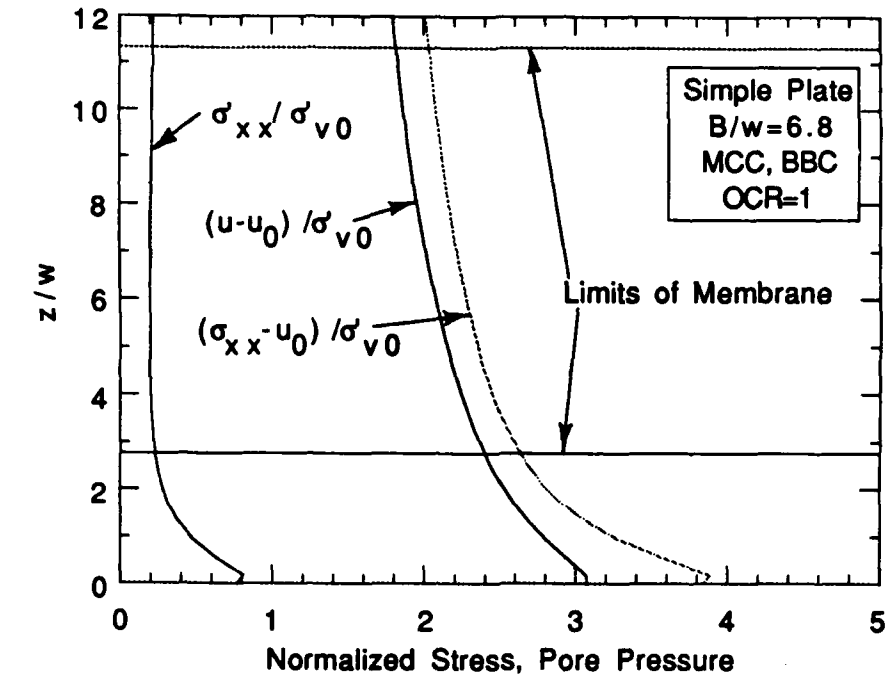
a) y=0 Plane
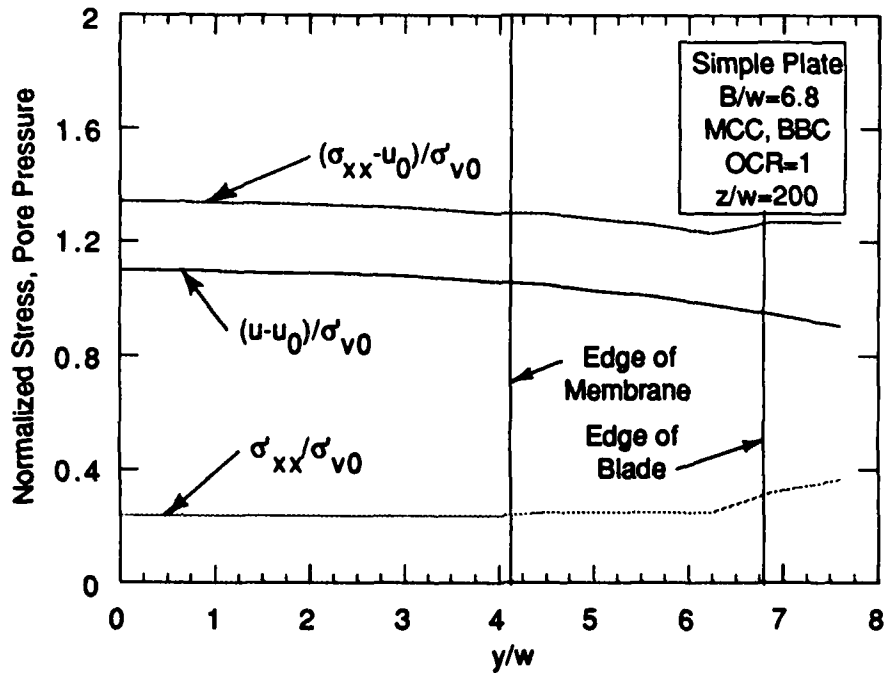
b) z/w=200 Plane

Figure 5-6 Stress and Pore Pressure Distribution Along Dilatometer Membrane
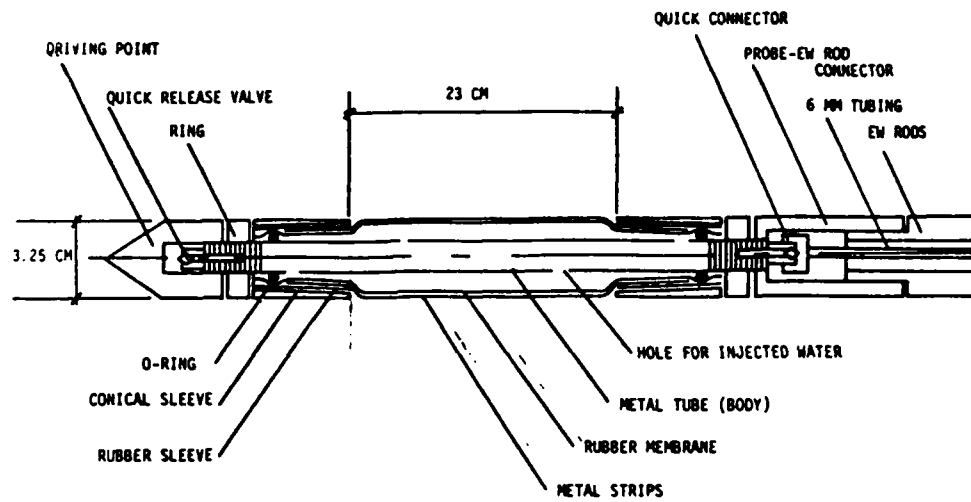
a) Briaud and Shields (1979)
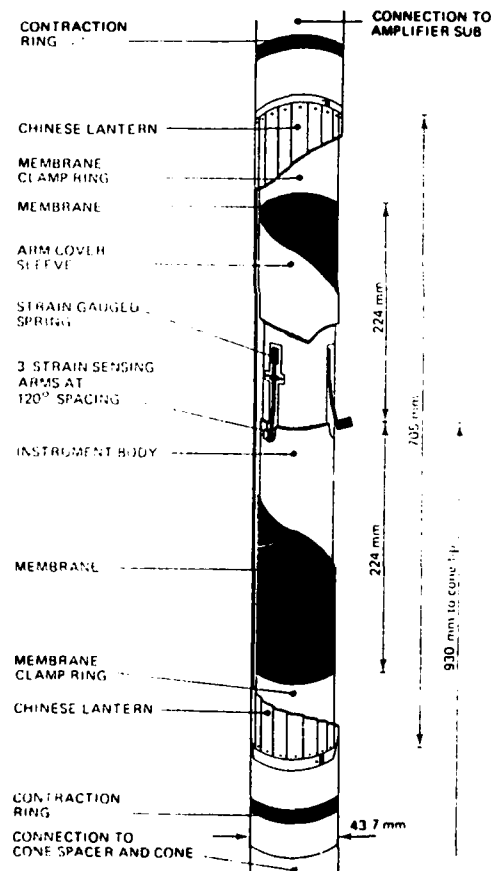
b) Withers et al. (1986)

Figure 5-7 Full Displacement Pressuremeters
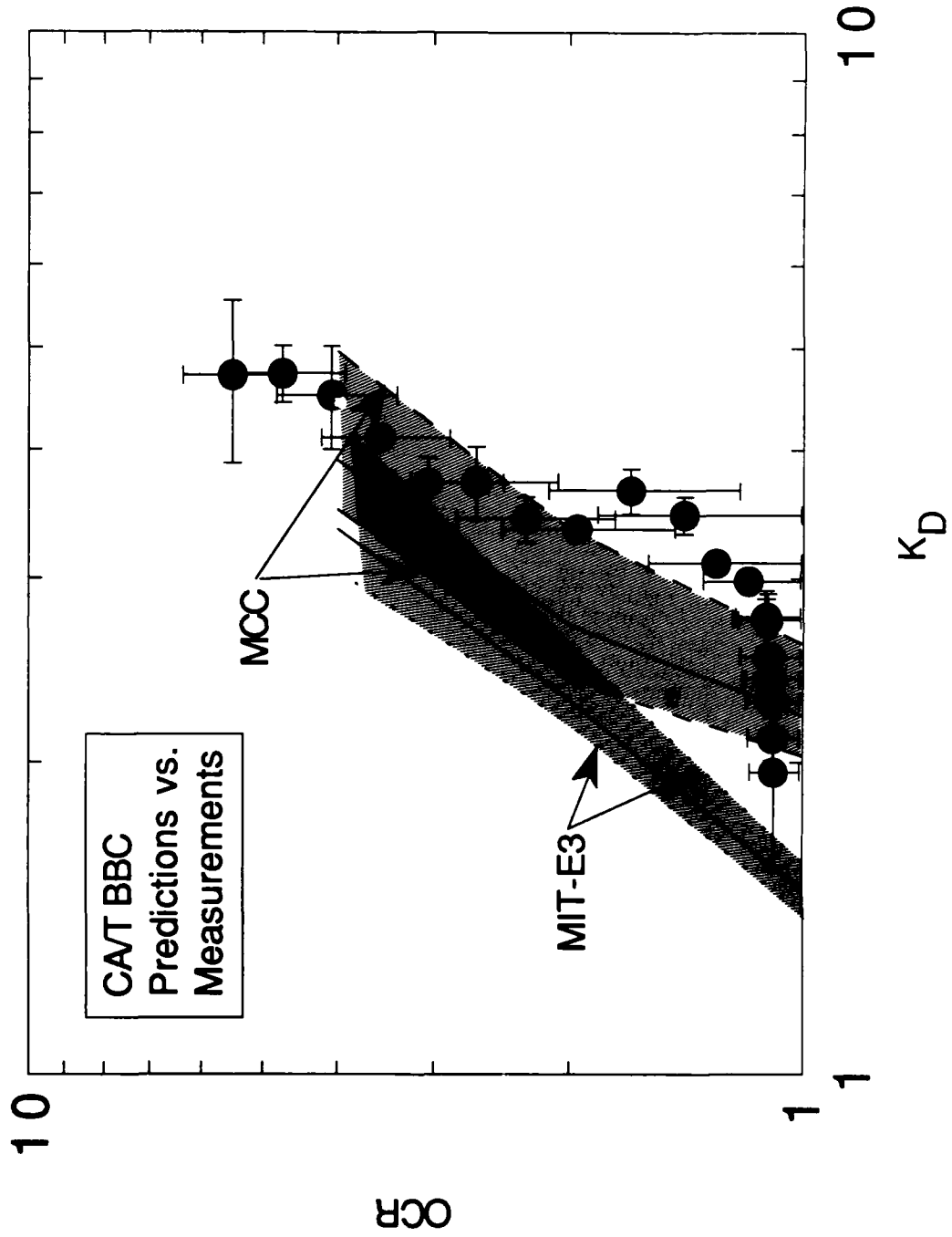
Figure 5-8 Comparison of Predictions to CA/T Data
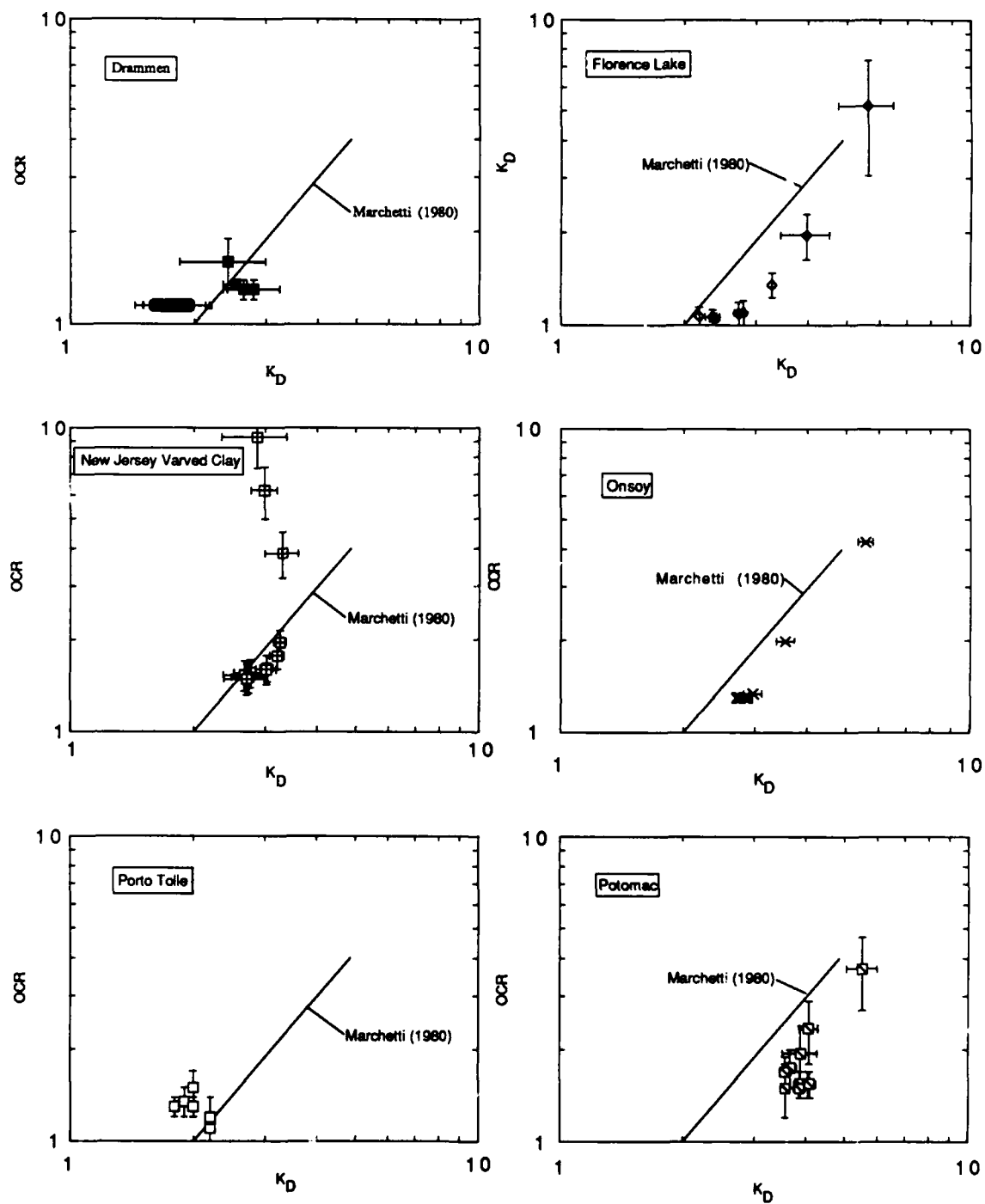
Figure 5-9 Correlation of Dilatometer Index, K_D, with OCR for Six Well-Documented Sites

$$K_D = (p_0 - u_0) / \sigma'_{v0}$$
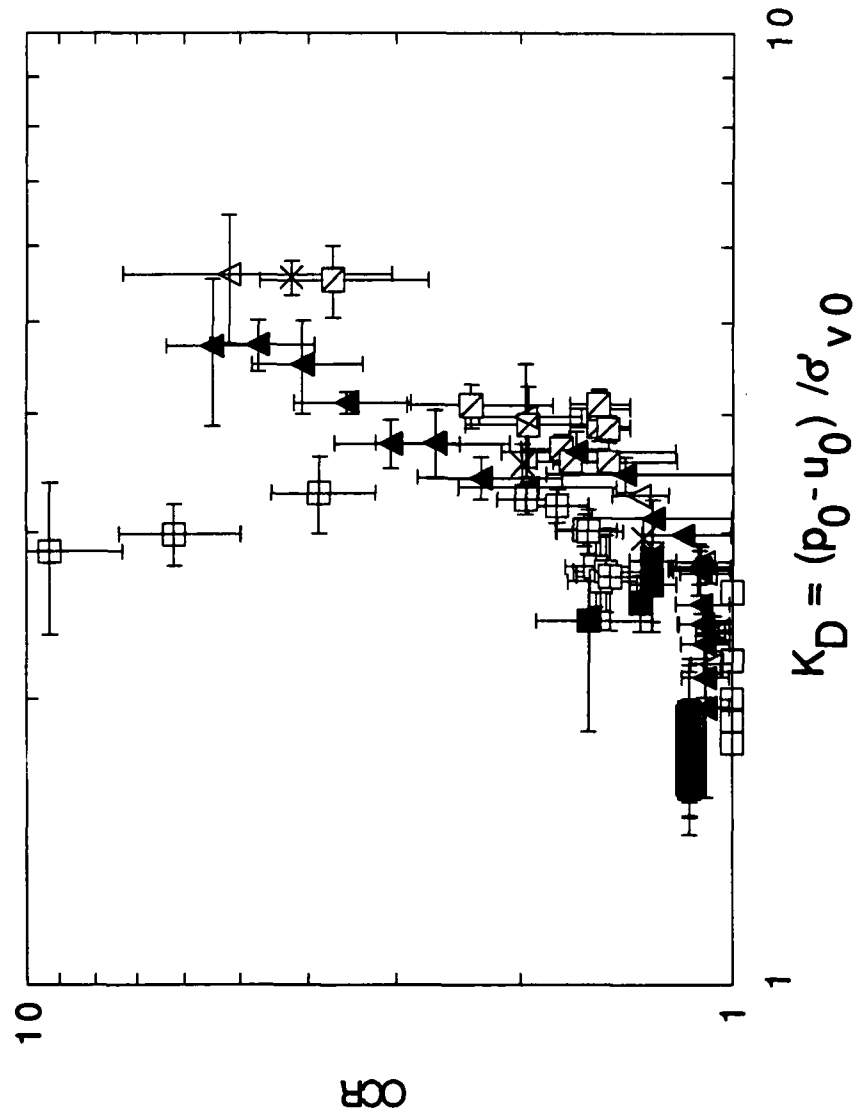
Figure 5-10 Correlation of Dilatometer Index, K_D, with OCR, Summary

6. THE FIELD VANE TEST

6.1 INTRODUCTION

The field vane test (FVT) is the most widely used test for estimating the in-situ undrained shear strength (c_u) of cohesive deposits. The test has many advantages, including, relative simplicity, inexpensive testing procedure and a large empirical data base. The field vane first gained extensive worldwide use in the late 1940's (Carlson, 1948; Cadling and Odenstad, 1948) and has been widely correlated with shear strength measured in laboratory shear tests (Chandler, 1988). The undrained shear strength (c_{uFV}) is usually determined directly from the maximum torque, M, measured during rotation, and empirical "correction factors" are widely used to modify the reported strength. For example, Bjerrum (1973) introduced a correction factor based on plasticity index in order to achieve a better correlation between undrained strength measured from a field vane (c_{uFV}) and undrained strength back calculated from embankment failures. Other factors have been proposed to account for a) anisotropy (Wroth, 1984); b) rotation rate (Torstensson, 1977); and c) time delay between vane insertion and rotation (Roy & Leblanc, 1988).

In this chapter the analytical procedures developed for flat plate penetration (chapter 3) are applied to the geometry of the field vane. These results provide *quantitative guidance* on the disturbance caused by field vane insertion, and provide initial distributions of stresses and pore pressures to be used in subsequent analyses of vane rotation.

6.2 THE STANDARD FIELD VANE TEST

6.2.1 Test Procedure

Figure 6.1 shows examples of typical field vane geometries, with either a rectangular or tapered end. Typical dimensions are given by Chandler (1988) and are summarized in the figure. The standard procedure for performing a field vane test (ASTM D 2573, 1972) consists of the following steps:

1. The vane is advanced from the bottom of the bore hole, or to the depth at which the test is to be conducted.

2. The vane is rotated by applying a torque at a rate, $\dot{\theta} \leq 0.1°$ /sec. The maximum torque, M is recorded. Typically, there is a short delay ($\Delta t \approx 5$ minutes) between insertion and rotation.

3. The vane is then rotated through a minimum of 10 revolutions in order to estimate the remoulded strength of the soil.

6.2.2 Test Interpretation

The conventional method of field vane interpretation relates the undrained shear strength of the soil (c_u) to the peak torque (M) via the equation (Chandler, 1988):

$$c_{uFV} = \frac{xM}{\pi D^3} \qquad (6.1)$$

where x is typically taken as x=0.86. This conventional interpretation assumes that: a) the shear stress distribution is uniform on both the vertical and horizontal surfaces that define the cylindrical surface traced out by a rotating vane (Fig. 6.2), and b) the soil is isotropic with respect to undrained shear strength.

Donald et al. (1977) present a three dimensional elastic finite element study of the stress distributions along the potential field vane failure surface. Their results showed that the shear stress distribution is far from uniform along the top and bottom failure surfaces (Fig. 6.2). This result is consistent with laboratory measurements presented by Menzies and Merrifield (1980). By fitting a polynomial approximation to the elastic shear stress distribution, Wroth (1984) suggests that the conventional interpretation for undrained strength is conservative and proposes that x = 0.94 provides a more realistic estimate for c_{uFV}. Since the factor x is the ratio of the total torque acting on the vertical failure surface to the total applied torque, this result suggests that the shearing resistance of the soil acting on the vertical section of the failure surface will dominate the strength result.

6.2.3 Effects of Vane Insertion

It has long been recognized that insertion of the field vane causes disturbance in clays and that this distribution affects the measured field vane strength (Chandler, 1988). Based on visual observations, Cadling and Odenstad (1948) interpret a zone of disturbance around the blades of the field vane as shown in figure 6.3a. The effect of disturbance is then quantified using a perimeter ratio ($\alpha \approx 8w/2\pi B$), which implies that the proportion of the failure surface affected by disturbance is controlled by the thickness of the blades. La Rochelle et al. (1973) conducted a systematic study to evaluate the effects of vane thickness on the measured strength. Their work includes: a) photographic techniques that confirm a

similar pattern of disturbance to that reported by Cadling and Odenstad (Fig. 6.3b), and b) measurements of c_{uFV} from laboratory tests as a function of vane thickness (perimeter ratio) (Fig. 6.3c). Their results showed that the undrained shear strength decreases as the vane thickness increases from 1.6 to 4.7 mm.

Vane insertion also generates excess pore pressures in the soil. There are no direct field measurements of the magnitudes of these pore pressures. However, significant increases in undrained shear strength (up to 50%) have been observed when the rest period (prior to vane rotation) is increased and have been attributed to dissipation of installation pore pressures (a process of 'set up' similar to that observed for driven piles in clay). For example, figure 6.4 shows measured data for c_{uFV} as a function of time after vane insertion for two sensitive Scandinavian clays (Torstensson, 1977). It can be seen that most of the strength increase occurs in the first four hours after vane insertion. Data reported in the literature suggest that the strength increase is most pronounced for highly sensitive clays.

6.3 PREDICTION OF DISTURBANCE DUE TO FIELD VANE INSERTION

The geometry of a standard rectangular field vane can be simulated by superimposing simple plate solutions (Fig. 6.5). This section describes analytical predictions of strain, effective stresses, and excess pore pressures due to the installation of a standard field vane. The aspect ratio for each blade of the vane is taken as B/w = 32.5 (refer to Fig. 3.1). The stress and pore pressure predictions are only considered in a 'steady state' horizontal x-y plane. This corresponds to a plane far above the cutting edge of the vane. These solutions can be considered representative of disturbance effects acting around the potential vertical failure surface.

6.3.1 Strains and Deformations

Figure 6.6 shows the magnitude of the octahedral shear strain (E) versus lateral distance normalized to the equivalent radius (R_{eq}) for a vane, where:

$$R_{eq} = \sqrt{\frac{8Bw}{\pi}} \qquad (6.3)$$

Along two planes of symmetry (x=y plane, x=0 plane), the results are compared with solutions presented previously for the simple pile and B/w = 32.5 plate. This figure shows the following:

1. Far from the blade, strain levels in the soil are not affected by the shape of the penetrometer, but are controlled by the volume of soil displaced (i.e., by R_{eq}).

2. Near the indenter, the magnitude of E_{oct} is smaller for the field vane than for a B/w = 32.5 plate on the x=0 plane.

3. Along the x=y plane, a local region of minimum E occurs at a radial distance ranging from about 1-2. This suggests that a small region of soil elements sandwiched between the two blades of the vane will experience less shearing than surrounding soil elements.

Contours of final retardation are shown in figure 6.7. Comparison of this result with the observations shown in figure 6.3 reveal striking similarities, and suggest that what is really being shown in figure 6.3 are retardation, or drawdown contours for soil elements initially located on a horizontal plane. The visually observed region is where soil elements have undergone detectable amounts of net vertical motion during installation.

6.3.2 Effective Stresses and Pore Pressures

Predictions of effective stresses and pore pressures around the field vane are obtained using the procedures described in previous chapters. Figures 6.8 a, b and c illustrate typical predictions of effective stresses using the MCC model with input parameters corresponding to K_0-normally consolidated BBC, while figure 6.8d shows the excess pore pressures from finite element solutions of the Poisson equation. The lateral dimensions in the figures are normalized by the equivalent radius (R_{eq} = 9 mm for a standard field vane) to enable direct comparison with predictions for other geometries (e.g. simple plate solutions presented in chapter 3). It should also be noted that the results are presented for one quadrant of the field vane, although the geometry imposes additional symmetry around the x=y plane. The figures show the following:

1. The lateral effective stress (σ'_{xx}) is almost uniform along the surface of the field vane ($\sigma'_{xx}/\sigma'_{v0} \approx 0.2$ on OB in Fig. 6.8a) and is significantly lower than the free field stress ratio, $K_0 = 0.48$, but is identical to the stress predicted previously for a simple plate of similar aspect ratio (B/w = 32.5, Fig 3.16d).

2. The in plane shear stress, $\sigma'_{xy}/\sigma'_{v0}$ (Fig. 6.8b) is symmetric about the x=y plane, and the predicted magnitudes are similar to those predicted previously for the simple plate.

3. The maximum horizontal shear stress, q_h/σ'_{v0}, gives an indication of the shear stresses that exist around the field vane prior to vane rotation. Maximum shear stresses occur at locations $r/R_{eq} \approx 5-7$, outside the zone of interest for vane rotation. Along the potential failure surface (AB), $q_h/\sigma'_{v0} \approx 0.1$.

4. Excess pore pressures (Fig. 6.4d) achieve maximum values, $(u-u_0)/\sigma'_{v0} \approx 1.1$ at

locations close to the stem of the field vane (point O). These pore pressures are comparable in magnitude to those predicted previously for the simple pile and simple plate geometries (Fig. 3.19). The zone of significant excess pore pressures extends to radial distances, $r/R_{eq} \approx 8$ (i.e. measurable pore pressures can be expected up to lateral distances greater than one blade length beyond the edge of the vane). There are significant radial gradients of pore pressures at all locations along the blades (OA,OB), and the potential failure surface (AB). Average excess pore pressures along AB range from $(u-u_0)/\sigma'_{v0} \approx 0.6\text{-}0.8$.

In order to illustrate the effects of soil model on the predictions of disturbance due to vane insertion, figure 6.9 shows a parallel set of predictions obtained using the MIT-E3 model (Whittle, 1987) with the same input parameters of K_0-normally consolidated BBC. For these soil properties, the MIT-E3 model captures more realistically the anisotropic, strain softening properties observed in laboratory tests on BBC. The results show the following:

1. The effective stress acting over the surface of the blade ($\sigma'_{xx}/\sigma'_{v0} \approx 0.08$ on OB in Fig. 6.9a) is substantially smaller than the values predicted by the MCC model (Fig. 6.8a), but similar to predictions presented in section 3.4.4 for a simple plate (with B/w=6.8). Low values of effective lateral stresses obtained using the MIT-E3 model can be attributed, in large part, to strain softening behavior described by the model during undrained shear.

2. The maximum shear stress contours (q_h/σ'_{v0}, Fig. 6.9c) are similar in forn to results presented by the MCC model (Fig. 6.8c). However, the magnitudes of q_h/σ'_{v0} are 50-70% less using the MIT-E3 model.

3. Maximum values of excess pore pressure, $(u-u_0)/\sigma'_{v0}$, (Fig. 6.9d) are predicted on the x=y plane at a radial distance $r/R_{eq} \approx 1$ from the stem of the vane[1]. The zone of excess pore pressure generation extends to much greater radial distances than predicted by the MCC model. This result reflects the small strain non-linearity described by the MIT-E3 model.

Figure 6.10a compares the magnitudes of excess pore pressures acting along the potential failure surface (AB) predicted by the MCC and MIT-E3 models. The MIT-E3 prediction is 14-34% higher than the MCC resultg along AB. Also note that the pore pressure distribution is fairly uniform for the MIT-E3 prediction, whereas, the MCC model predicts a pore pressure variation of about 30%.

---

[1]This peak is roughly in the same location as where the octahedral shear strain was reported to be a minimum (figure 6.4).

Figure 6.10b compares the radial effective stresses ($\sigma'_{rr}/\sigma'_{v0}$) acting normal to the potential failure surface (AB) for the MCC and MIT-E3 predictions. These results are of critical interest in subsequent predictions of undrained shear strength from vane rotation. The results show:

1. For the MCC model, $\sigma'_{rr}/\sigma'_{v0}$ values range from 0.45 to 0.55 and hence are similar in magnitude to the initial $K_0=0.48$ condition. These predictions support earlier assumptions of Aas et al. (1986) and Wroth (1984) that vane insertion does not affect the lateral effective stress acting on the potential failure surface.

2. For the MIT-E3 model, $\sigma'_{rr}/\sigma'_{v0}= 0.2$ to 0.25, which represents a significant reduction in effective stress due to vane insertion. This result can be attributed, in large part, to strain softening (sensitive) behavior described by the model.

6.4 PORE PRESSURE DISSIPATION

Using initial conditions generated from the 'base case' analysis, linear, uncoupled consolidation analyses were performed in order to provide preliminary estimates of the effects of partial drainage in standard field vane test procedures. Figure 6.11 shows the dissipation of excess pore pressure where, u is the current pore pressure, u_i is the initial pore pressure after insertion, and u_0 is the in-situ pore pressure prior to installation. The results are reported for a dimensionless time factor defined by:

$$T = \frac{c_h t}{R_{eq}^2} \tag{6.4}$$

The dissipation curves are presented for two points: "O", located near the stem of the vane blade, and "C" located on the x=y plane at a radial distance of $r/w = 34^2$. The results show the following:

1. At the stem of the vane (O) dissipation is initially slow, because the initial gradient of excess pore pressure is small (Fig. 6.8d).

2. At C the excess pore water pressure initially rises, leading to a delay in pore water pressure decay. The normalized pore water pressure dissipation ($\Delta u/\Delta u_i$, Fig. 6.9b) shows that 50% dissipation will occur at a time factor, $T \approx 6$, at the vane stem (O), but will not occur until $T \approx 15$ on the failure surface at point C. Thus, more than twice the time is required to achieve 50% consolidation on the failure surface.

In order to interpret the practical importance of the results presented in figure 6.9, the

---

[2] i.e. on the potential cylindrical failure surface A-B.

dissipation times must be scaled using a) the dimensions of a standard field vane ($R_{eq} \approx 9$ mm, and b) typical values of the horizontal coefficient of consolidation (c_h). Baligh and Levadoux (1986) report values of c_h for Boston Blue Clay ranging from; $c_h = 0.01 - 0.04$ cm^2/sec.

Using this information along with figure 6.11, dissipation times may be calculated, and are reported in table 6.1. These results show the following:

1. The typical rest period ($\Delta t \approx 5$ minutes) between insertion and rotation allows less than 20% consolidation on the potential failure surface. Even slower consolidation can be expected for sensitive clays, based on initial pore pressure fields presented for MIT-E3. Hence, partial drainage is not expected to be a significant factor using standard field vane test procedures in low permeability clays.

2. For points on the potential failure surface (e.g C; Tab. 6.1), 50% consolidation occurs for 'rest periods' between 0.6 and 1.5 hours. These results suggest that significant drainage of excess pore pressures will occur in the time frame of 1-10hours and provides preliminary evidence to explain the increases in undrained shear strength reported by Torstensson (1977) (Fig. 6.4).

6.5 DISCUSSION

The results presented in this chapter represent the first quantitative explanation of disturbance that occurs during field vane installation, and have shown the following:

1. The visually observed region of disturbance (Fig. 6.3) corresponds to areas of soil deformation (retardation), but does not provide a measure of the extent of excess pore water pressure development.

2. Vane installation can lead to significant reductions in the effective normal stress acting along the potential failure surface, especially for strain softening (sensitive) soils.

3. Very little drainage (less than 20%) occurs during the typical 5 minute rest period between vane insertion and rotation.

   The next step in the field vane research will use the installation conditions presented in this chapter as initial conditions in the analysis of field vane rotation.

O. Near the center of the vane blade:

Excess Pore Pressure Ratio: $\bar{u} = (u - u_0)/(u_i - u_0)$	Time, t (minutes) $c_h = 0.01$ cm^2/sec	Time, t (minutes) $c_h = 0.04$ cm^2/sec
80%	2.0	8.0
60%	5.4	21.6
40%	12.2	48.8
20%	40.5	162

C. On the potential failure surface:

Excess Pore Pressure Ratio: $\bar{u} = (u - u_0)/(u_i - u_0)$	Time, t (minutes) $c_h = 0.01$ cm^2/sec	Time, t (minutes) $c_h = 0.04$ cm^2/sec
80%	5.4	21.6
60%	11.5	46.0
40%	27.0	108.0
20%	74.3	297.2

Table 6.1. Pore pressure dissipation following vane installation; linear uncoupled analysis

RECTANGULAR VANE   TAPERED VANE

D = 65 mm
H = 130 mm
t = 2 mm
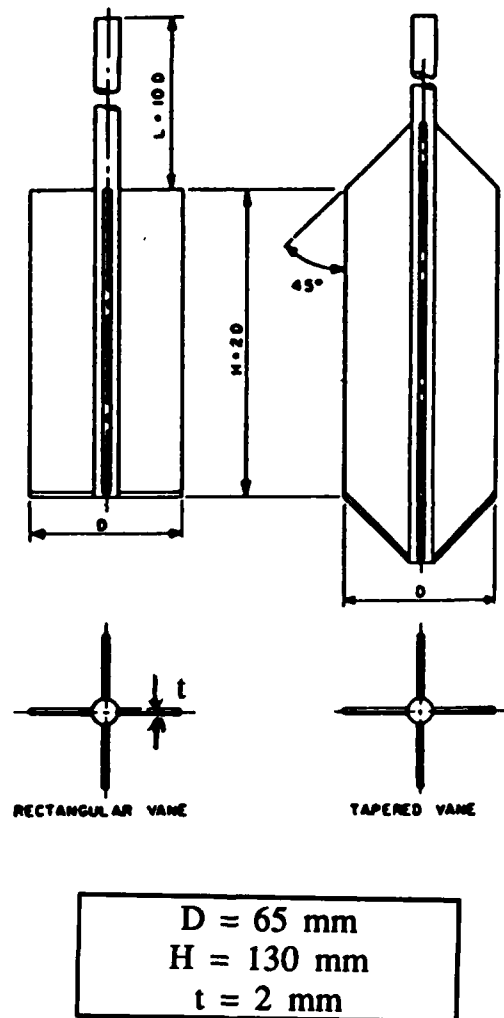
Figure 6.1. Typical Field Vane geometries
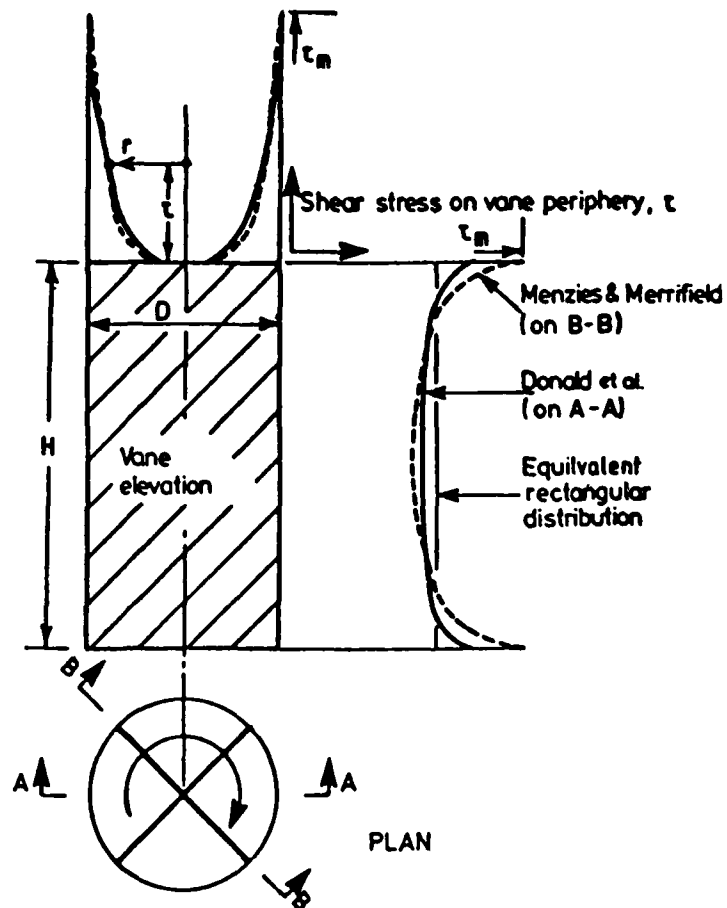
Figure 6.2. Distribution of shear stresses along potential Field Vane failure surface

194

Perimeter ratio.

$$\alpha = 4e/_{\pi D}$$
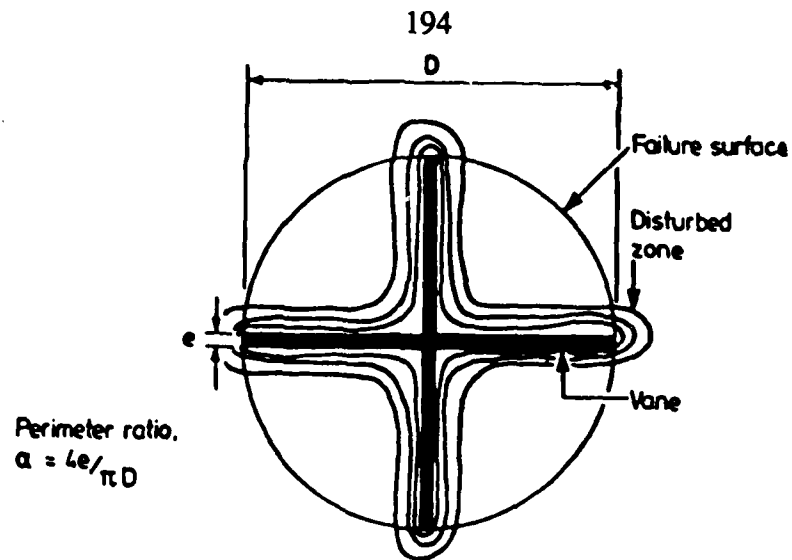
Figure 6.3a. Cadling and Odenstad (1948) model of disturbance due to vane insertion
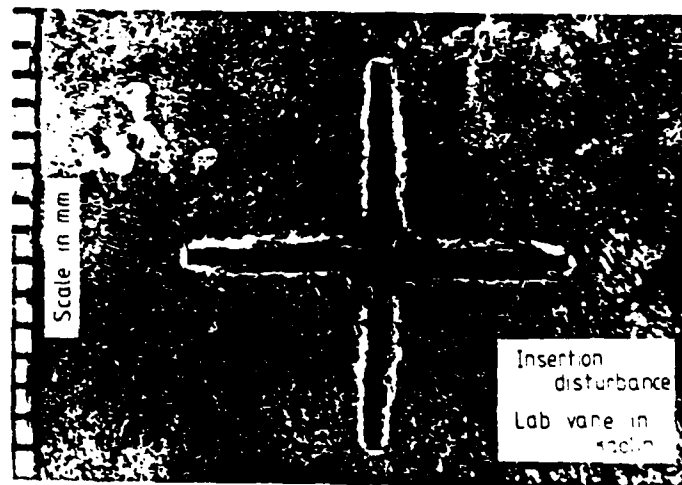
Figure 6.3b. Observation of disturbance due to vane insertion (LaRochelle et al., 1973)
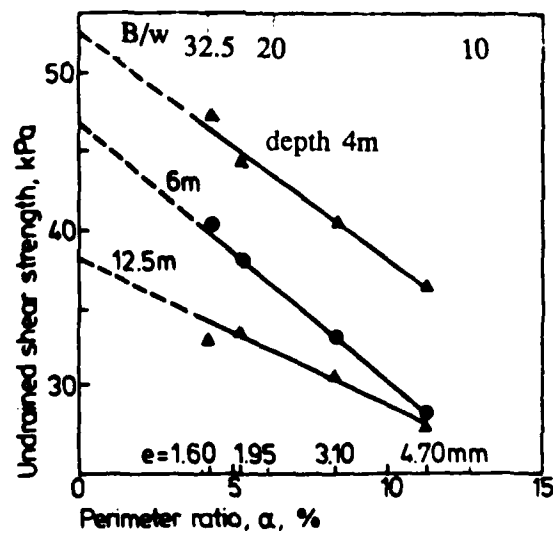
Figure 6.3. Measured undrained shear strength as a function of Field Vane aspect ratio
(La Rochelle et al. 1973)
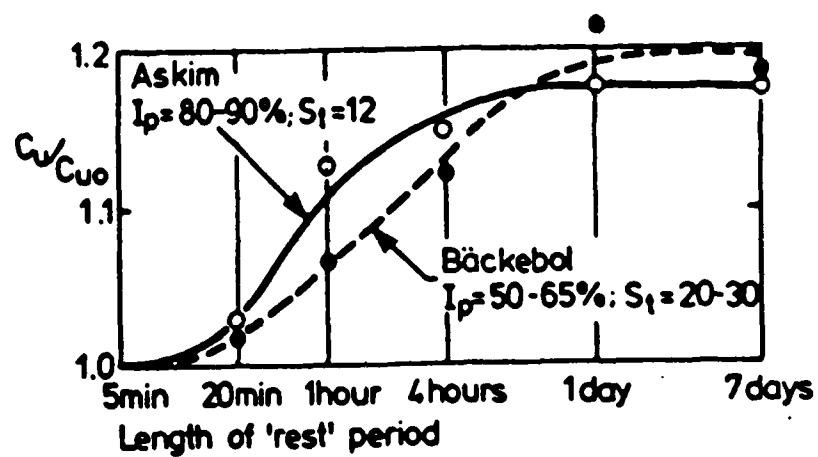
Figure 6.4. Increase in undrained shear strength due to time delay after vane insertion (Torstensson, 1977)
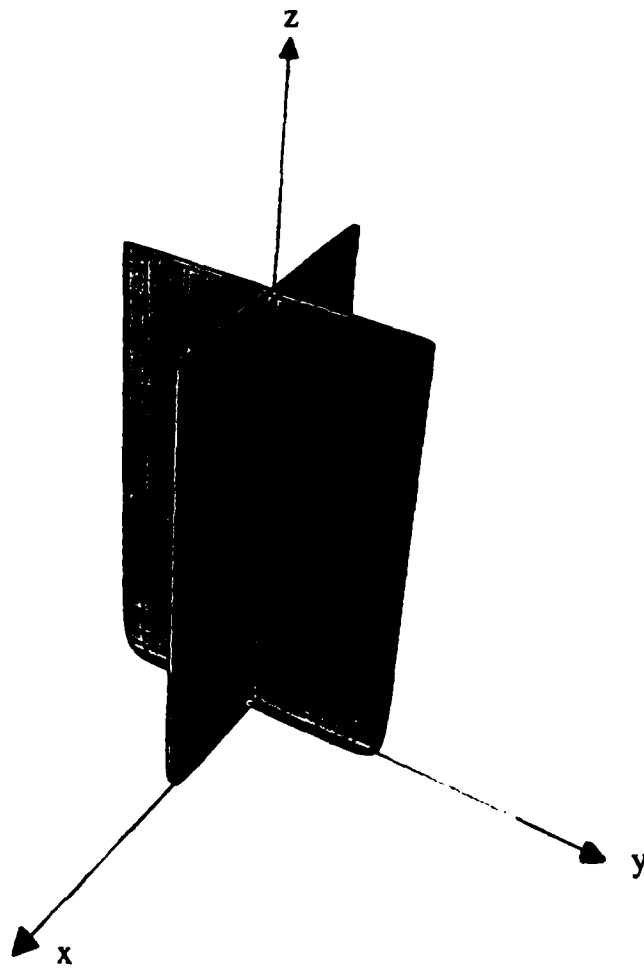
Figure 6.5. Simulation of Field Vane geometry using Simple Plate solutions
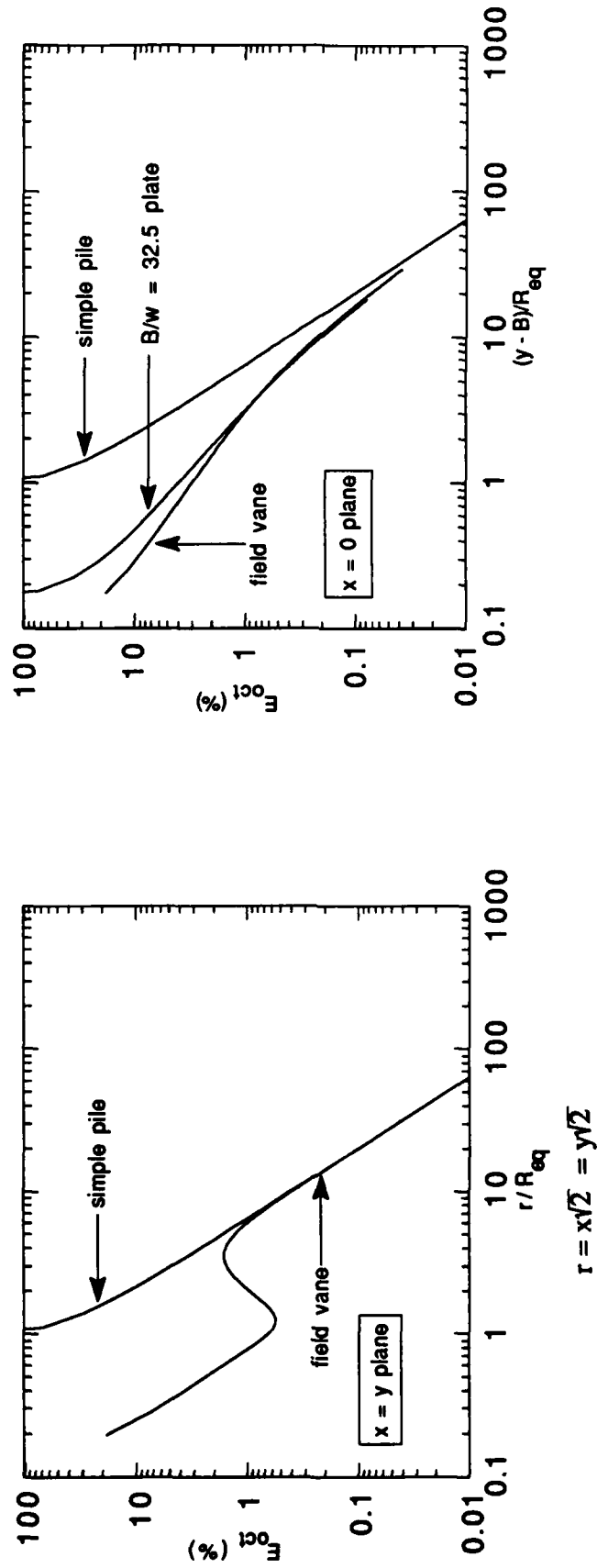
Figure 6.6. Octahedral shear strains caused by Field Vane installation
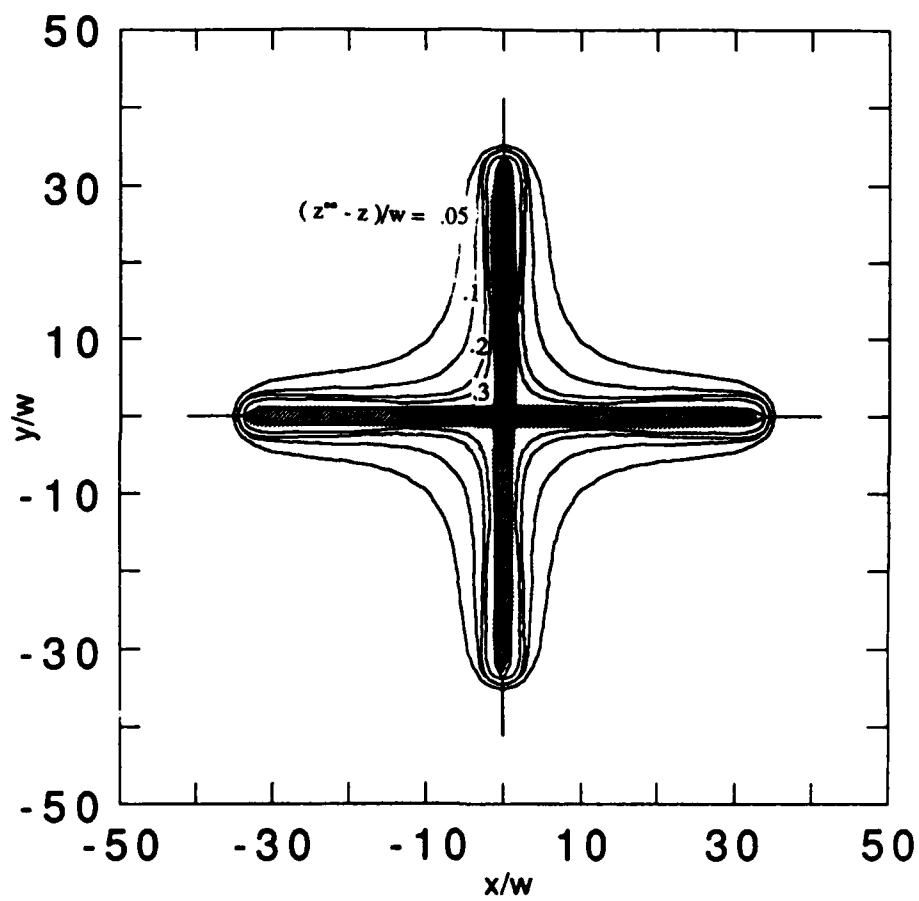
Figure 6.7. Vertical retardations of soil elements predicted around Field Vane
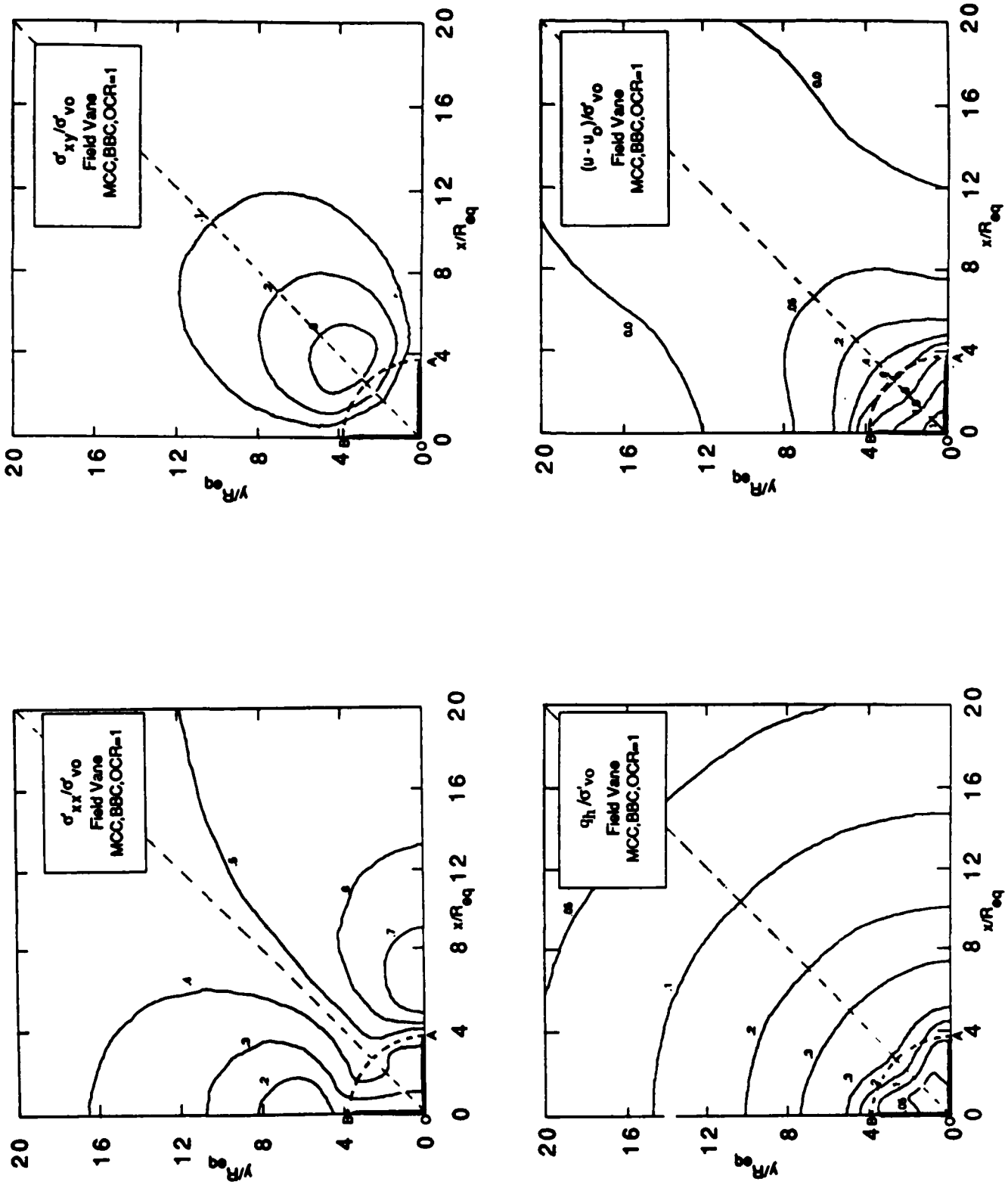
Figure 6.8. Effective stresses and excess pore pressures predicted around the Field Vane for K_o
-normally consolidated BBC, using the MCC model
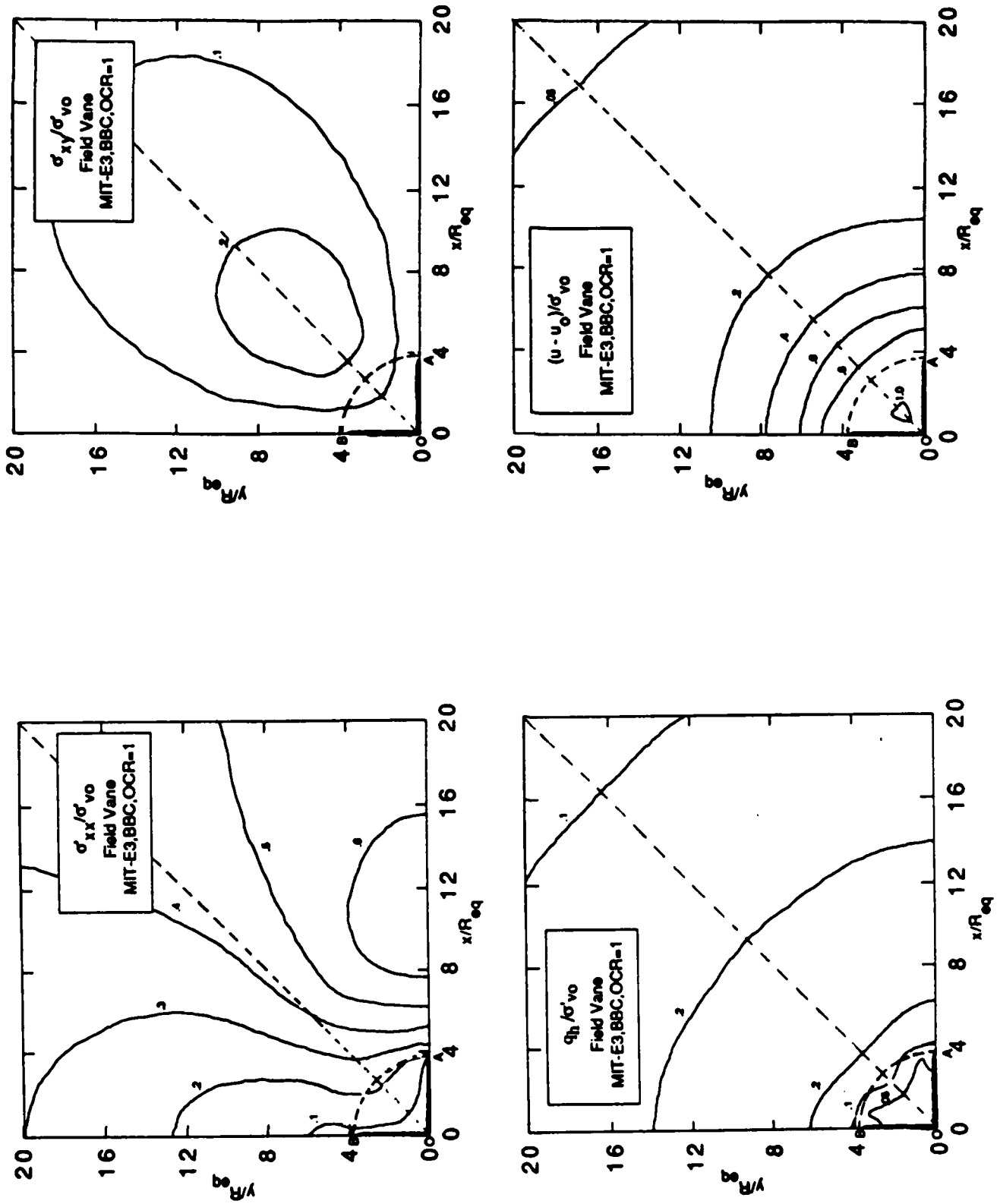
Figure 6.9. Effective stresses and excess pore pressures predicted around the Field Vane for K_o
-normally consolidated BBC, using the MIT-E3 model
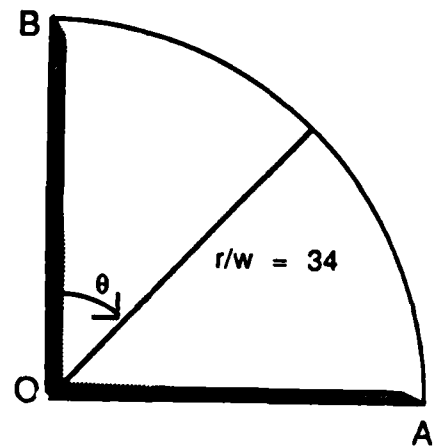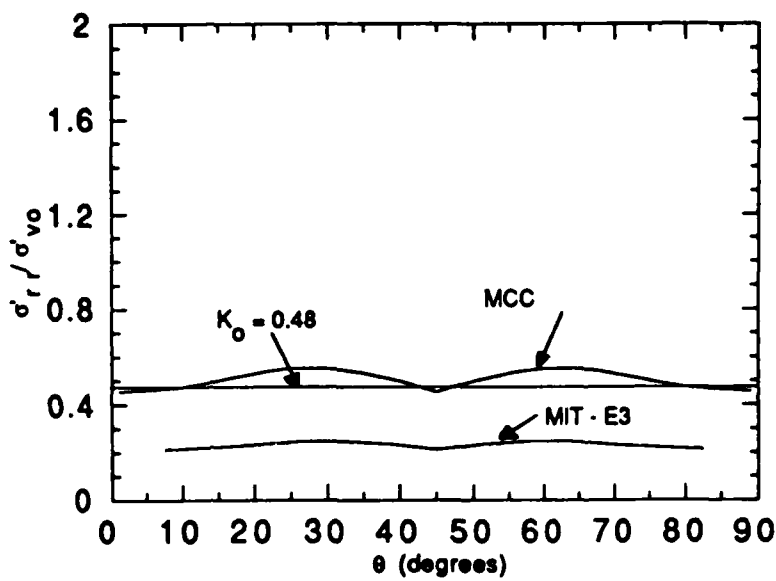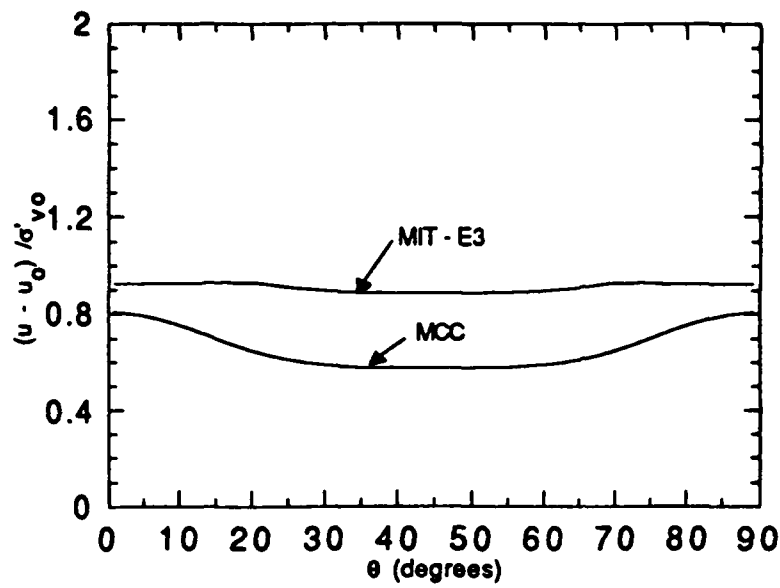
Figure 6.10. Excess pore pressure and radial effective stress acting on potential failure surface
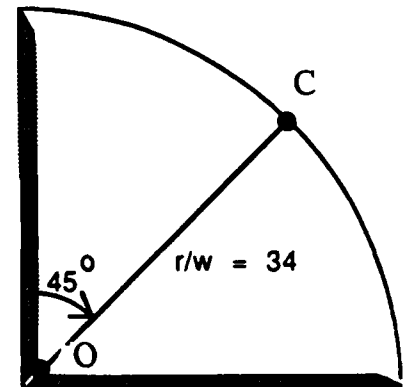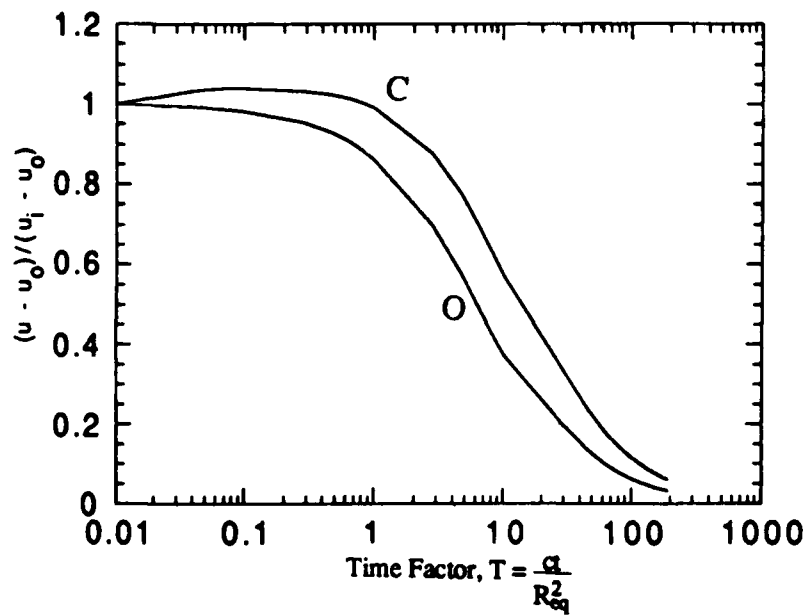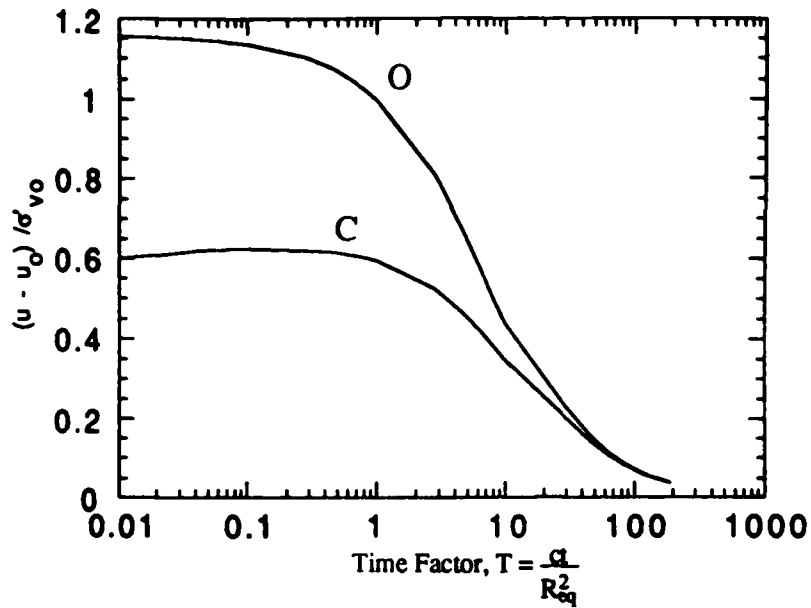
Figure 6.11. Dissipation of excess pore pressures around the Field Vane, linear uncoupled analysis

7. SUMMARY

The research achievements during the second year of the project have included the following:

1. The development and evaluation of reliable numerical methods for estimating pore pressure distributions around penetrometers from the Strain Path Method. In the proposed method, equilibrium conditions are satisfied by numerical solution of a Poisson equation. This formulation avoids arbitrary assumptions regarding the path of integration and is particularly suitable for more complex penetrometer geometries. An important modification of the Poisson formulation is introduced to enforce vertical equilibrium conditions ahead of the tip of the penetrometer. The proposed formulation has been used to estimate distributions of excess pore pressures for piezocone penetrometers (section 4), the Marchetti dilatometer (section 5) and the field vane (section 6).

2. The mechanics of flat plate penetration have been clarified using the fundamental analytical solutions for a simple plate geometry. It has been shown that plate geometry can be understood in terms of two parameters: a) the aspect ratio, B/w, (i.e., the ratio of the length to width of the plate), and b) the equivalent radius, R_{eq}, which is a measure of the volume of soil displaced by the penetrometer. The equivalent radius controls the lateral extent of disturbance caused by the plate installation (e.g., at locations far from the surface of the penetrometer, soil strains and displacements depend only on the volume of soil displaced). The aspect ratio controls the distribution of stresses and pore pressures in the soil around the penetrometer. The magnitudes of effective stresses and excess pore pressures acting at the center of the plate are similar to predictions presented previously for axisymmetric penetrometers and are not significantly affected by the aspect ratio of the plate (for the aspect ratios considered in this study; $6.8 \leq B/w \leq 32.5$) Excess pore pressures acting at the edge of the plate are typically 20-25% smaller than at the center of the plate. Dissipation of excess pore pressures measured at the center of plate penetrometers are controlled by the equivalent radius of the penetrometer.

3. Comprehensive strain path analyses have been used to predict the stresses and pore pressures acting around a piezocone penetrometer in normally and lightly overconsolidated clays ($OCR \leq 4$). The analyses have demonstrated the effects of tip geometry, soil modeling and stress history of the soil on piezocone measurements

during steady penetration:

The results have confirmed that net tip resistance and tip pore presssures (measured either at the tip of the 60^0 cone or on the face of the cone) are the measurements which correlate most closely with undrained shear strength (or preconsolidation pressure) of the soil[1]. However, interpretation of undrained shear strength using either of these measurements contains a number of uncertainties which have yet to be resolved: 1) The predicted tip resistance factor is affected by other soil properties such as strain softening, which have yet to be investigated in detail; 2) the measured tip resistance is often not reliable due to the difficulty in correcting for unequal area effects; 3) the analytical solutions generally underpredict the measured pore pressures. This result is probably due to strain rate dependent behavior of the clay which is not described by the existing soil models.

The predictions show that pore pressures measured at the base of the cone are difficult to interpret due to the large gradients of the excess pore pressures in the soil. Pore presssures measured at the base or at locations along the shaft of the piezocone are also much less sensitive to changes in undrained shear strength or preconsolidation pressure than those obtained on the face of the cone.

Comparisons of analytical predictions with field data from piezocone tests in Boston Blue Clay at two sites have shown that the analytical predictions can describe accurately trends in the measured data. However, consistent differences in the data at the two sites suggests differences in the soil properties at the two sites which require further investigation.

4. Using the analytical developments described in sections 2 and 3, strain path analyses of the Dilatometer contact pressure, p_0, have been presented for normally and lightly overconsolidated clays (OCR≤4). The analyses show that the stresses acting on the dilatometer membrane are not uniform due to the proximity of the membrane to the tip of the penetrometer. A systematic study of the predicted contact pressure has found that there are no simple linear correlations between the p_0 and the undrained shear strength or preconsolidation pressure of the soil. Furthermore, the predictions show that even when pore pressures are measured on the dilatometer membrane (as proposed by a number of authors) there is still no simple interpretation of engineering properties from contact conditions. Thus, the analyses imply serious limitations of the dilatometer for estimating

---

[1]These results support the use of the centerline analyses presented by Whittle et al. (1989).

engineering properties of clays. A direct comparsion of analytical predictions with measured data in Boston Blue Clay confirms that stress history cannot be reliably estimated from the contact pressure. Further studies of data from seven well documented test sites has shown that dilatometer contact pressures exhibit significant scatter and that site specific correlations for estimating the preconsolidation pressure vary significantly for different types of clay.

5. Based on the results in section 6, the disturbance caused by field vane installation has been clarified: In contrast to existing hypotheses, the analyses show that disturbance of the stress and pore pressures fields is not limited to the soil immediately adjacent to the blades of the vane. Large excess pore pressures are predicted at points along the potential failure surface ($\Delta u/\sigma'_{v0}=0.8$ to 1.0; for K_0-normally consolidated BBC), while significant reductions in effective stresses occur for sensitive clays (less than K_0 conditions). Preliminary calculations of pore pressure dissipation show that there there is little dissipation of the installation pore pressures during a typical rest period (prior to vane rotation), however, almost complete dissipation occurs within 1 to 5 hours after vane insertion.

8. REFERENCES

Aas, G., Lacasse, S., Lunne, T. & Hoeg, K. (1986) "Use of in-situ tests for foundation design on clay," Proc. ASCE Specialty Conference on Use on In Situ Tests in Geotechnical Engineering (in-Situ '86), Blacksburg, VA., pp 1-30.

ASTM (1972) "Standard Test Method for Field Vane Shear Test in Cohesive Soil" ASTM Standard D 2573-72

Azzouz, A.S., Baligh, M.M. & Ladd, C.C. (1982), "Cone penetration and engineering properties of soft Orinoco clay," MIT Sea Grant Report, MITSG-82-11, 53p.

Azzouz, A.S. & Baligh, M.M. (1984) "Behavior of friction piles in plastic Empire clays," Research Report R84-14, Dept. of Civil Engineering, MIT, Cambridge, MA., 619p.

Azzouz, A.S. & Lutz, D.G. (1986) "Shaft behavior of a model pile in plastic Empire clays," ASCE. Journal of Geotechnical Engineering, Vol. 112, No. GT4, pp. 389-406.

Baguelin, F.J. & Jezequel, J.F. (1983) "The LPC pressiopenetrometer," Proc. ASCE Conf. on Geotechnical Practice in Offshore Engineering, Austin, TX, pp. 203-219.

Baligh, M.M. (1975), "Cavity expansion in sands with curved envelopes," ASCE. Journal of Geotechnical Engineering, Vol. 102, GT11, pp. 1131-1146.

Baligh, M.M. (1985a), "Strain Path Method," ASCE. Journal of Geotechnical Engineering, Vol. 111, No. GT9, pp. 1108-1136.

Baligh, M.M. (1985b), "Fundamentals of deep penetration, I: Shear stresses," MIT Report R85-9, Order No. 776, 64p.

Baligh, M.M. (1985c), "Fundamentals of deep penetration, II: Pore pressures," MIT Report R85-10, Order No. 777, 78p.

Baligh, M.M. (1986a) "Undrained deep penetration: 1. Shear stresses," Géotechnique, Vol. 36, No. 4, pp. 471-485.

Baligh, M.M. (1986b) "Undrained deep penetration: II. Pore pressures," Géotechnique, Vol. 36, No. 4, pp. 487-501.

Baligh, M.M. (1986c) "Dervation and development of piezocone penetrometer data interpretation methods," Report submitted to the US Bureau of Mines, 3 Vols.

Baligh, M.M. & Levadoux, J-N. (1980), "Pore pressure dissipation after cone penetration," MIT Report No. 80-11, Order No. 662, Dept. of Civil Engrg., MIT, Cambridge, MA.

Baligh, M.M. & Levadoux, J-N (1986), "Consolidation after undrained piezocone penetration II: Interpretation," ASCE Journal of Geotechnical Engineering, Vol.

112, No. GT7, pp. 727-745.

Baligh, M.M., Vivatrat, V. & Ladd, C.C. (1980) "Cone penetration in soil profiling," ASCE Journal of Geotechnical Engineering, Vol. 106, GT4, pp. 447-461.

Baligh, M.M., Azzouz, A.S., Wissa, A.E.Z., Martin, R.T. & Morrison, M.J. (1981) "The Piezocone Penetrometer," Proc. Symposium on Cone Penetration Testing and Experience, ASCE Natl. Convention, St. Louis, MO., pp. 247-263.

Bathe, K.J. (1982), Finite Element Procedures in Engineering Analysis, Prentice-Hall, N.J.

Bathe, K.J. (1987) A Finite Element Program for Automatic Dynamic Incremental Nonlinear Analysis of Temperatures, Report ARD 87-2, ADINA R&D, Inc., Watertown,MA.

Battaglio, M. & Maniscaldo, R. (1983) "Il piezocono: Esecuzione ed interpretazione," Report No. 607, Politecnico di Torino.

Battaglio, M., Bruzzi, D., Jamiolkowski, M. & Lancellotta, R. (1986) "Interpretation of CPT's and CPTU's," Proc. 4th Intl. Geotechnical Seminar on Field Instrumentation and in Situ Measurements, Singapore.

Berg, A.P.v.d. (1982)"Latest development in static cone penetrometers ans other soil testing equipment," Proc., 2nd European Symposium on Penetration Testing, Amsterdam, Vol. 2, pp. 447-455.

Bjerrum, L. (1972) "Embankments on soft ground," Proc. ASCE Spec. Conf. on Performance of Earth and Earth Supported Structures, Lafayette, Ind., Vol. 2, pp. 1-54.

Boghrat, A. (1982) "The design and construction of a piezoblade and evaluation of the Marchetti dilatometer in some Florida soils," PhD Thesis, Univ. of Florida, Gainsville, FL.

Bond, A.J. (1990) "Behaviour of displacement piles in overconsolidated London Clay," PhD Thesis, University of London, 725p.

Briaud, J.L. & Shields, D. (1979) " A special pressuremeter and pressuremeter test for pavement evaluation and design," ASTM Geotechnical Testing Journal, Vol. 2, No. 3, pp. 143-151.

Burland, J.B. (1990) "On the compressibility and shear strength of natural clays," Géotechnique, Vol. 40, No.3, pp 329-378.

Butterfield, R. & Bannerjee, P.K., (1970), "The effect of pore water pressure on the ultimate bearing capacity of driven piles," Proceedings, 2nd S.E. Asia Conf. on Soil Engineering, Singapore, pp 385-394.

Cadling, L. & Odenstad, S. (1948) "The Vane Borer," Proc Royal Swedish Geotechnical

Institute, No. 2.

Campanella, R.G. & Robertson, P.K. (1988) "Current status of the piezocone test", Proc. ISOPT-1, Orlando, FL., Vol. 1, pp. 93-117.

Campanella, R.G., Gillespie, D. & Robertson, P.K. (1982), "Pore pressure during cone penetration," Proc. ESOPT-II, Amsterdam, Vol. 2, pp. 507-512.

Carlson, L. (1948) "Determination in situ of the shear strength of undisturbed clay by means of a rotating auger," Proc. 2nd Intl. Conf. on Soil Mechs. & Fdn. Engrg., Rotterdam, Vol. 1, pp 265-270.

Chandler, R.J. (1988) "The in-situ measurement of the undrained shear strength of clays using the field vane", Vane Shear Testing in Soils: Field and Lab. Studies, ASTM STP 1014, pp. 13-44.

Chin, C.T & Whittle, A.J. (1984) "The use of ADINAT to solve a Poisson equation: The solution of the octahedral stress field caused by penetration of a 2-D axisymmetric indenter," Unpublished Project, MIT, Cambridge, MA.

Chin, C.T. (1986), "Open-ended pile penetration in saturated clays," PhD Thesis, MIT, Cambridge, MA, 296p.

Cleveland, W.S. (1979), "Robust locally weighted regresion and smoothing scatterplots", Journal of the American Statistical Association, Vol. 74, No. 368, Theory and Methods Section, pp 829-836.

DeGroot, D.J. (1989) "The Multi-Directional Simple Shear Apparatus with application to the design of offshore Arctic structures," PhD Thesis, MIT, Cambridge, MA.

de Ruiter J. (1971) "Electrical penetrometer for site investigation", ASCE Journal for Soil Mechs. & Fdn. Engrg., Vol 97, No. SM2, pp. 457-472.

de Ruiter J. (1981) "Current Penetrometer Practice", Proc. Symposium on Cone Penetration Testing and Experience, ASCE Natl. Convention, St. Louis, MO., pp. 1-48.

de Ruiter J. (1982) "The static cone penetration test State-of the-Art Report", Proc. ESOPT-II, Vol. 2, Amsterdam, pp 389-405.

Donald, I.B., Jordan, D.O., Parker, R.J. & Toh, C.T. (1977) "The Vane Test- A critical appraisal," Proc. 9th Intl. Conf. on Soil Mechs. & Fdn. Engrg., Tokyo, Vol. 1, pp 81-88.

Draper, N., & Smith H. (1981), Applied Regression Analysis, John Wiley & Sons, New York.

Elghaib, M.K. (1989), "Prediction and interpretation of piezocone tests in clays, sands and silts," PhD Thesis, MIT, Cambridge, MA, 404p.

Germaine, J.T. (1980) "Evaluation of self-boring pressuremeter tests in soft cohesive

soils," SM Thesis, MIT, Cambridge, MA.

Handy, R.L., Remmes, B., Moldt, S. & Lutenegger, A.J. (1982) "In-situ stress determination by Iowa stepped blade," ASCE Journal of Geotechnical Engineering, Vol. 108, No. GT11, pp. 1405-1422.

Henkel, D.J. (1960) "The relationships between the effective stresses and water content in saturated clays," Géotechnique, Vol. 10, pp. 41-54.

Hess, J.L. & Smith, A.M.O. (1962), "Calculation of non-lifting potential flow about arbitrary three dimensional bodies," Douglas Aircraft Company Report No. ES-40622.

Hess, J.L. & Smith, A.M.O. (1964), "Calculation of non-lifting potential flow about arbitrary three dimensional bodies, Journal of Ship Research, Vol. 8, No. 2, pp. 22-44.

Hight, D.W., Gens, A., & Symes, M.J. (1983) "The development of a new hollow cylinder apparatus for investigating the effects of principle stress rotation in soils," Géotechnique, Vol. 33 No. 4, pp. 385-396.

Huang, A-B. (1989), "Strain path analyses for arbitrary 3-D penetrometers", Intl J. for Anal. & Num. Meth. in Geomech., Vol. 13, No. 5, pp. 551-564

Jamiolkowski, M., Ladd, C.C., Germaine, J.T. & Lancellotta, R. (1985) "New developments in field and laboratory testing of soils, Theme Lecture 2," Proc. 11th Intl. Conf. on Soil Mechs. & Fdn. Engrg., San Fransisco, Vol. 1, pp. 57-153.

Jamiolkowski, M., Battaglio, M. & Bruzzi, D. (1989) "Discussion, Session 3," Proc. Conf. on Penetration Testing in the UK, Birmingham, pp. 180-183.

Janbu, N. & Senneset, K. (1974) "Effective stress interpretation of in-situ static penetration tests," Proc. ESOPT-I, Stockholm, Vol. 2.2, pp. 181-193.

Jardine, R.J. & Bond, A.J. (1989) "Behaviour of displacement piles in heavily overconsolidated clay," Proc. 12th Intl. Conf. on Soil Mechs. & Fdn. Engrg., Rio de Janiero, Vol. 2, pp. 1147-1152.

Jones, G.A. & Rust, E. (1982) "Piezometer penetration testing," Proc. ESOPT-II, Amsterdam, Vol. 2, pp. 607-613.

Jones, G. A., Van Zyl, D. & Rust, E. (1981) "Mine tailings characterization by piezometer cone", Proc. Symposium on Cone Penetration Testing and Experience, ASCE Natl. Convention, St. Louis, MO., pp. 303-324.

Karlsrud, K. & Haugen, T. (1985) "Axial statsic capacity of steel model piles in overconsolidated clay," Proc. 11th Intl. Conf. on Soil Mechs. & Fdn. Engrg.,San Fransisco, Vol. 3, pp. 1401-1406.

Kjekstad, O., Lunne, T., and Clausen, C.J.F. (1978) "Comparison between in-situ cone

resistance and laboratory strength for overconsolidated North Sea Clays", Marine Geotechnology , Vol. 3, No. 1, pp. 23-36.

Konrad, J.M. & Law, K.T. (1987) "Preconsolidation pressure from piezocone tests in marine clays," Géotechnique, Vol. 37, No. 2, pp. 177-190.

Lacasse, S. (1979) "Effect of load duration on undrained behaviour of clay and sand," NGI Internal Report, No. 40007-2.

Lacasse, S. & Lunne, T. (1982) "Dilatometer tests in two soft marine clays," Proc. Conf. on Updating Subsurface Sampling of Soils and Rocks and their In-situ Testing, Santa Barbara, CA., 8p. (also NGI Report No. 146)

Lacasse, S. & Lunne, T. (1988) "Calibration of dilatometer correlations," Proc. ISOPT-1, Orlando, FL., Vol. 1, pp. 539-548.

Ladanyi, B. & Eden, W.J. (1969) "Use of the deep penetration test in sensitive clays," Proc. 7th Intl. Conf. on Soil Mechs. & Fdn. Engrg., Mexico City, Vol. 1, pp. 225-230.

Ladd, C.C. (1989) "Stability evaluation during staged construction," 22nd Terzaghi Lecture, to be published in ASCE Journal of Geotechnical Engineering.

Ladd, C.C. (1990) Unpublished report submitted to Haley & Aldrich, Cambridge, MA.

Ladd, C.C. & Foott, R. (1974) " New design procedure for stability of soft clays," ASCE, Journal of Geotechnical Engineering, Vol. 100, No. GT7, pp. 763-786.

Ladd, C.C. & Foott, R. (1977) "Foundation design of embankments constructed on varved clays," FHWA Report No.TS-77-214, US Dept of Transportation, 234p.

Ladd, C.C., Foott, R., Ishihara, K., Schlosser, F. & Poulos, H.G. (1977) "Stress-deformation and strength characteristics, State-of-the-Art Paper," Proc. 9th Intl. Conf. on Soil. Mechs. & Fdn. Engrg., Tokyo, Vol. 2, pp. 421-494.

LaRochelle, P., Roy, M. & Tavenas, F. (1973) "Field measurements of cohesion in Champlain clays," Proc. 8th Intl. Conf. on Soil Mechs. & Fdn. Engrg., Moscow , Vol. 1, pp. 229-236.

Levadoux, J-N. (1980) "Pore pressures in clays due to cone penetration," PhD Thesis, MIT, Cambridge, MA., 752p.

Levadoux, J-N. & Baligh, M.M. (1980), "Pore pressures in clays due to cone penetration," Research Report R80-15, Order No. 666, Dept. of Civil Engrg., MIT, Cambridge, MA.

Levadoux, J-N, Baligh, M.M. (1986), "Consolidation after undrained piezocone penetration. I: Prediction", ASCE, Journal of Geotechnical Engineering,Vol. 112, No. GT7, pp 707-726.

Lee, J.T. (1987) "A potential based panel method for the analysis of marine propellers in

steady flow," PhD Thesis, MIT, Cambridge, MA.

Lunne, T., Myrvoll, F., & Kjekstad, O. (1981) "Observed settlements of five North Sea gravity platforms, NGI Technical Report No. 52410/s-6.

Lunne, T., Christoffersen, H.P., & Tjelta, T.I. (1985) "Engineering use of the piezocone test in North Sea Clays," Proc. 11th Intl. Conf. on Soil Mechs. & Fdn. Engrg., San Fransisco, Vol. 2, pp. 907-912.

Lunne, T. , Lacasse, S., Rad, N.S. & Decourt, L. (1989) "SPT, CPT, Pressuremeter testing and recent developments on in-situ testing: General Report Session 2," Proc. 12th Intl. Conf. on Soil Mechs. & Fdn. Engrg., Rio de Janeiro, 65p.

Lutenegger, A.J. (1988) "Current status of the Marchetti dilatometer," Proc. ISOPT-1, Orlando, FL, Vol. 1, pp. 137-155.

Lutenegger, A.J. & Kabir, M.G. (1988) "Dilatometer C-reading to help determine stratigraphy," Proc. ISOPT-1, Orlando, FL., Vol. 1, pp. 549-554.

Luttenegger, A.J. & Blanchard, K.C. (1990) "A comparison between full displacement pressuremeter tests and dilatometer tests in clay," Proc. 3rd Intl. Conf. on Pressuremeter Testing, Oxford, pp. 309-320.

Lutenegger, A.J., Timian, D.A. (1986) "In-situ tests with K_0-Stepped Blade," Proc. ASCE Conf. on Use of In-situ Tests in Geotechnical Engineering. (In-situ '86), Blacksburg, VA, pp 730-751.

Marchetti, S. (1980) "In-situ tests by flat dilatometer," ASCE, Journal of Geotechnical Engineering, Vol. 106, No. GT3, pp. 299-321.

Marchetti, S., Totani, G., Campanella, R.G. & Robertson, P.K. (1986) "The DMT σ_{HC} method for piles driven in clay," Proc., ASCE Conf. on Use of In-Situ Tests in Geotechnical Engineering. (In-situ '86), Blacksburg, VA., pp. 765-779.

Mayne, P.W. (1986), "CPT indexing of in-situ OCR in clays," Proc., ASCE Conf. on Use of In-Situ Tests in Geotechnical Engineering. (In-situ '86), Blacksburg, VA., pp. 780-793.

Mayne, P.W. (1987) "Determining preconsolidation stress and penetration pore pressures from DMT contact pressures," ASTM Geotechnical Testing Journal, Vol. 10, No. 3, pp. 146-150.

Mayne, P.W., Kulhawy, F.H. & Kay, J.N. (1990) "Observations on the development of pore-water stresses during piezocone penetration in clays," Canadian Geotechnical Journal, Vol. 27, pp. 418-428.

Menzies, B.K.& Merrifield, C.M. (1980) " Measurements of shear stress distribution on the edges of a shear vane blade" Géotechnique, Vol . 30, No. 2, pp. 314-318.

Morino, L. & Kuo, C-C. (1974), "Subsonic aerodynamics for complex configurations,"

AIAA Journal, Vol. 12, No. 2, pp. 191-197.

Morrison, M.J. (1984) " In situ measurements on a model pile in clay," PhD Thesis, MIT, Cambridge, MA., 700p.

Newman, J.N. (1986) "Distributions of sources and normal dipoles over a quadrilateral panel," Journal of Engineering Mathematics, Vol. 20, pp. 113-126.

Nyirenda, Z.M. & Sills, G.C. (1989) "Discussion, Session 3," Proc. Conf. on Penetration Testing in the UK, Birmingham, pp. 183-184.

Powell, J.J.M. & Uglow, I.M. (1988) "Marchetti dilatometer testing in UK soils," Proc. ISOPT-1, Orlando, FL., Vol. 1, pp. 555-562.

Powell, J.J.M., Quartermain, R.S.T. & Lunne, T. (1989) "Interpretation and use of the piezocone test in UK clays," Proc. Conf. on Penetration Testing in the UK, Birmingham, pp. 151-156.

Rad, N. S. & Lunne, T. (1988) "Direct correlations between piezocone test results and undrained shear strength of clay," Proc. ISOPT-1, Orlando, FL., Vol. 2, pp. 911-918.

Randolph, M.F., Carter, J.P. & Wroth, C.P. (1978), "Driven piles in clay: Effects of installation and subsequent consolidation," Géotechnique, Vol. 29, No. 4, pp. 361-393.

Ridgen, W.J., Thorburn, S., Marsland, A. & Quartermain, R.S.T. (1982) "A dual load range cone penetrometer," Proc. ESOPT-II, Amsterdam, Vol. 2, pp. 787-796.

Robertson, P.K. & Campanella, R.G. (1983), "Interpretation of cone penetration tests, II: Clays," Canadian Geotechnical Journal, Vol. 20, No. 4, pp. 734-745.

Robertson, P.K., & Campanells, R.G. (1984) "Guidelines for use and interpretation of the electronic cone penetration test", Soil Mechanics Series No.69, Dept. of C.E., The University of British Columbia, Vancouver.

Robertson, P.K., Campanella, R.G., Gillespie, D., & Greig, J. (1986) "Use of piezometer cone data" Proc. ASCE Conf. on Use of In-situ Tests in Geotechnical Engineering, (In-situ '86), Blacksburg, VA, pp. 1263-1280.

Robertson, P.K., Campanella, R.G., Gillespie, D. & By, T. (1988) "Excess pore pressures and the flat dilatometer test," Proc. ISOPT-1, Orlando, FL., Vol. 1, pp. 567-576.

Roscoe, K.H., Burland, J.B. (1968) "On the generalized stress-strain behaviour of 'Wet' clay", Engineering Plasticity , Ed. J. Heyman and F.A. Leckie, Cambridge University Press, pp. 535-609.

Rourk, T.L. (1961) "Model studies of a pile failure surface in a cohesive soil, " MS Thesis, Georgia Inst. of Tech., Atlanta.

Rouse, H. (1959) Advanced Mechanics of Fluids, Wiley & Sons, New York.

Roy, M & Leblanc, A. (1988) "Factors affecting the measurement and interpretation of the vane strength in soft sensitive clays," Vane Shear Testing in Soils: Field and Lab Studies, ASTM STP 1014, pp. 117-130.

Schaap, L.H.J. & Zuidberg, H.M. (1982) "Mechanical and electrical aspects of the electrical cone penetrometer tip," Proc. ESOPT-II, Amsterdam, Vol. 2, pp. 841-851.

Schmertmann, J.H. (1982) "A Method for determining the friction angle in sands from the Marchetti dilatometer test," Proc. 2nd European Symp. on Penetration Testing, (ESOPT 2), Amsterdam, Vol. 1, pp. 853-861.

Schmertmann, J. (1986) "Suggested method for performing the flat dilatometer test," ASTM Geotechnical Testing Journal, Vol. 9, No. 2, pp. 93-101.

Senneset, K., Janbu, N. & Svanø, G. (1982), "Strength and deformation parameters from cone penetration tests, " Proc., 2nd European Symposium on Penetration Testing, Amsterdam, Vol. 2, pp. 863-870.

Senneset, K. & Janbu, N. (1984), "Shear strength parameters obtained from static cone penetration tests, " ASTM STP No. 883, pp. 41-54.

Skempton, A.W. (1954) "The pore pressure coefficients A and B," Géotechnique, Vol. 4, No. 4, pp.143-152.

Smits, F.P. (1982) "Penetration pore pressure measured with piezometer cones", Proc. ESOPT-II, Amsterdam, Vol. 2, pp. 887-881.

Soderberg, L.O., "Consolidation theory applied to foundation pile time effects," Géotechnique, Vol. 12, pp. 217-225.

Sully, J.P., Campanella, R.G. & Robertson, P.K. (1987), "Overconsolidation ratio of clays from penetration pore pressures," ASCE Journal of Geotechnical Engineering, Vol. 114, No. GT2, pp. 209-216.

Tavenas, F., Blanchette, G., Leroueil, S., Roy, M. & LaRochelle, P. (1975) "Difficulties in the in-situ determination of K_0 in soft sensitive clays" (1975) Proceedings: In-Situ Measurement of Soil Properties, Raleigh, NC, pp. 450-476.

Tavenas, F., Leroueil, S., and Roy, M. (1982) "The piezocone test in clays: Use and limitations" Proc. ESOPT-II, Amsterdam, Vol. 2, pp. 889-894.

Tedd, P. & Charles, J.A. (1981) "In-situ measurement of horizontal stress in overconsolidated clay using push-in spade-shaped pressure cells," Géotechnique, Vol. 31, No. 4, pp. 554-558.

Teh, C-I (1987), "An analytical investigation of the cone penetration test," PhD Thesis, University of Oxford.

Teh, C-I; Houlsby, G.T. (1987), "Undrained deep penetration, I. Shear stresses; Discussion of Paper by M.M. Baligh," Géotechnique, Vol. 37, No. 4, pp. 525-527.

Teh, C-I & Houlsby, G.T. (1989) "An analytical study of the cone penetration test in clay," Oxford University Soil Mechanics Report, No. OUEL 1800/89.

Thornburn, S., Laird, C.L., & Reid, W.M., (1981) "The importance of stress histories of cohesive soils and the cone penetration test", The Structural Engineer, 59A, pp. 87-92.

Torstensson, B.A. (1975) "Pore pressure sounding instrument," Proc. ASCE Conf. on In-situ Measurement of Soil Properties, Rayleigh, NC, Vol. 1, pp. 48-54.

Torstensson, B.A. (1977) "Time-dependent effects in the field vane test," Intl. Symposium on Soft Clay, Bangkok, pp 387-397.

Torstensson, B.A. (1982) "A combined pore pressure and point resistance probe," Proc., ESOPT-II, Amsterdam, Vol. 2, pp. 903-908.

Tumay, M.T., Acar, Y.B., Cekirge, M. & Ramesh, N. (1985) "Flow field around cones in steady penetration," ASCE, Journal of Geotechnical Engineering, Vol. 111, No. GT2, pp. 325-342.

Vivatrat, V. (1978) "Cone penetration in clays," PhD Thesis, MIT, Cambridge, MA., 427p.

Weinstein, A. (1948) "On axially symmetric flows," Quarterly of Applied Mathematics, Vol. 5, No. 4, pp. 429-434.

Whittle, A.J. (1987) "A constitutive model for overconsolidated clays with application to the cyclic loading of friction piles," ScD Thesis, MIT, Cambridge, MA. 641p.

Whittle, A.J. (1989a), "A model for overconsolidated clays: I Formulation," submitted submitted for publication, December 1989

Whittle, A.J. (1989a), "A model for overconsolidated clays: II Evaluation," submitted for publication, December 1989.

Whittle, A.J. (1990), "A constitutive model for overconsolidated clays," MIT Sea Grant Report No. MITSG90-15.

Whittle, A.J., Ladd, C.C., Baligh, M.M. (1989) "Interpretation of in-situ testing of cohesive soils using rational methods", Annual Technical Report submitted to Air Force Office of Scientific Research Report, November.

Whittle, A.J. & Baligh, M.M. (1990), "Prediction and evaluation of pile shaft behaviour in lightly overconsolidated clays," submitted for publication.

Whittle, A.J. & Aubeny, C.P. (1991) "Pore pressure fields around piezocone penetrometers installed in clays," Proc. IACMAG'91, Cairns, Australia, May.

Williamson, A.E. (1989) "Use of a panel method to predict disturbance due to penetrometer installation in clays", SM Thesis, MIT, Cambridge, MA, 143p.

Wissa, A.E.Z., Martin, R.T. & Garlanger, J.E. (1975) "The Piezometer Probe," Proc. ASCE Conf. on In-situ Measurement of Soil Properties. Rayleigh , NC, Vol. 2, pp. 536-545.

Withers, N.J., Schapp, B.L., and Dalton C. (1986) "The development of the full displacement pressuremeter," The Pressuremeter and its Marine Applications. ASTM STP No. 950, pp. 38-56.

Woodward-Clyde Consultants (1989) "Analysis of instrumentation data, Arthur C. Storz Expressway, Omaha, Nebraska," Final Report to HDR Engrs. Inc., 2 Vols.

Wroth, C.P. (1984), "The interpretation of in-situ soil tests," Géotechnique, Vol. 34, No. 4, pp. 449-489.

Zuidberg, H.M., L.H.J.Schapp, and F.L. Beringen (1982) "A penetreometer for simultaneous measuring of cone resistance, sleeve friction, and dynamic pore pressure," Proc., 2nd European Symposium on Penetration Testing, Amsterdam, Vol. 2, pp. 963-970.

LIST OF THESES IN PROGRESS OR COMPLETED

PhD theses:

Majid K. Elghaib (1989) "Prediction and Interpretation of Piezocone Data during Undrained, Drained and Partially Drained Penetration" completed July 1989.

Charles P. Aubeny: thesis in progress, expected completion December 1991.
pore pressures due to penetrometer installation

Youssef Hashash: thesis in progress, expected completion September 1991
non-linear finite element modeling

Thomas C. Sheahan: Thesis in Progress
rate effects in soils

Masters Theses:

Anne E. Williamson (1989) "Use of a Panel Method to Predict Distrurbance due to Penetrometer Installation in Clays", completed August 1989.

Alexander Rafalovich "The Mechanics of Plate Penetration in Clays," expected completion date, February 1991.

LIST OF PAPERS SUBMITTED

A.J. Whittle "A Model for Predicting the Behaviour of Overconsolidated Clays: I Formulation, submitted to Géotechnique, December 1989

A.J. Whittle "A Model for Predicting the Behaviour of Overconsolidated Clays: I Evaluation, submitted to Géotechnique, December 1989

A.J. Whittle (1991a) "An interpretation of pile load tests at the Haga site," Proc. OMAE '91, Stavangar, Norway, June.

A.J. Whittle (1991b) "MIT-E3: A constitutive model for overconsolidated clays," Proc. IACMAG'91, Cairns, Australia, May.

A.J. Whittle & C.P. Aubeny (1991) "Pore pressure fields around piezocone penetrometers installed in clays," Proc. IACMAG'91, Cairns, Australia, May.

Appendix A

Isoparametric Interpolation Functions

List of Tables

List of Figures

i	h_i	$\dfrac{\partial h_i}{\partial s}$	$\dfrac{\partial h_i}{\partial t}$
1	$\dfrac{1}{4} st(1+s)(1+t)$	$\dfrac{1}{4} t(1+t)(1+2s)$	$\dfrac{1}{4} s(1+s)(1+2t)$
2	$-\dfrac{1}{4} st(1-s)(1+t)$	$-\dfrac{1}{4} t(1+t)(1-2s)$	$-\dfrac{1}{4} s(1-s)(1+2t)$
3	$\dfrac{1}{4} st(1-s)(1-t)$	$\dfrac{1}{4} t(1-t)(1-2s)$	$\dfrac{1}{4} s(1-s)(1-2t)$
4	$-\dfrac{1}{4} st(1+s)(1-t)$	$-\dfrac{1}{4} t(1-t)(1+2s)$	$-\dfrac{1}{4} s(1+s)(1-2t)$
5	$\dfrac{1}{2} t(1-s^2)(1+t)$	$- st(1+t)$	$\dfrac{1}{2} (1-s^2)(1+2t)$
6	$-\dfrac{1}{2} s(1-s)(1-t^2)$	$-\dfrac{1}{2} (1-t^2)(1-2s)$	$st(1-s)$
7	$-\dfrac{1}{2} t(1-s^2)(1-t)$	$st(1-t)$	$-\dfrac{1}{2} (1-s^2)(1-2t)$
8	$\dfrac{1}{2} s(1+s)(1-t^2)$	$\dfrac{1}{2} (1-t^2)(1+2s)$	$- st(1+s)$
9	$(1-s^2)(1-t^2)$	$- 2s(1-t^2)$	$- 2t(1-s^2)$

Table A.1 Isoparametric Interpolation Functions and Their Derivatives for 9-Node Isoparametric Element

Table A.2 Interpolation Functions and Their Derivatives for a Four-Node Isoparametric Element *

h_i	$\partial h_i/\partial s$	$\partial h_i/\partial t$
$(1+s)(1+t)/4$	$(1+t)/4$	$(1+s)/4$
$(1-s)(1+t)/4$	$-(1+t)/4$	$(1-s)/4$
$(1-s)(1-t)/4$	$-(1-t)/4$	$-(1-s)/4$
$(1+s)(1-t)/4$	$(1-t)/4$	$-(1+s)/4$

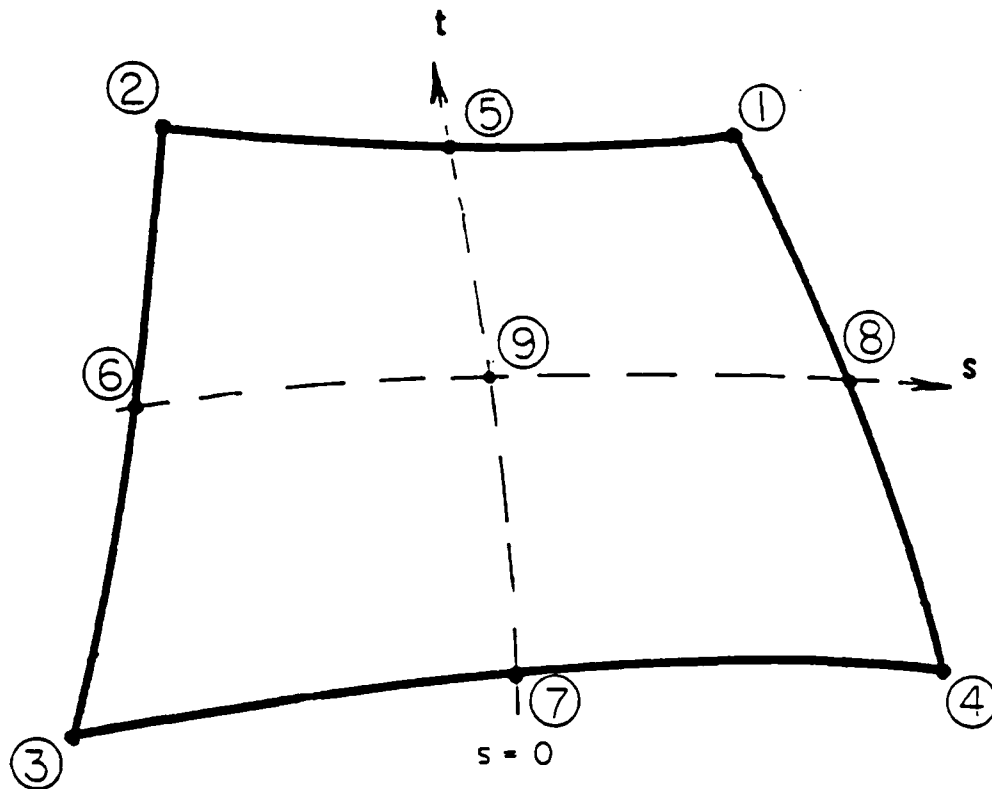*Nodal point locations are illustrated in Figure A.1.

Figure A.1 Isoparametric Element Definition Sketch

Appendix B

Publications Submitted

A.J. Whittle and C.P Aubeny, 'Pore pressure fields around piezocone penetrometers installed in clays', submitted to Seventh Conference of the International Association for Computer Methods and Advances in Geomechanics, Cairns, Australia, October, 1990.

Pore pressure fields around piezocone penetrometers installed in clays

Andrew J. Whittle & Charles P. Aubeny,
Massachusetts Institute of Technology

ABSTRACT: This paper describes a numerical method for estimating the pore pressures that are generated around a penetrometer during steady, deep, undrained penetration in a uniform deposit of low permeability clay. Using the Strain Path Method, the effective stresses around the penetrometer are first determined from the strain paths of soil elements using an appropriate soil model. The pore pressures are then obtained by integrating the equilibrium equations using the known fields of effective stresses. However, due to the approximate nature of the Strain Path Method, the equilibrium equations are not satisfied uniquely, such that the pore pressures are integration path dependent. In the proposed method, an approximate, 'averaged' pore pressure field is obtained by solving the complete set of equilibrium equations in the form of a Poisson equation. An accurate numerical procedure is presented to solve this equation.

The proposed method has two advantages: 1) it is rational and needs no subjective judgemer' to estimate the distributions of pore pressures; and 2) it can be used for penetrometers of general shape, and hence can be useu to unify the interpretation of installation disturbance for different types of in-situ test used in geotechnical practice. Examples illustrate the capabilities of the proposed method for pore pressure distributions around axisymmetric and flat plate penetrometers.

INTRODUCTION

The undrained penetration of intrusive test devices (e.g. piezocone, field vane, dilatometer etc.) in low permeability clay deposits leads to the development of excess pore pressures in the soil. For normally and moderately overconsolidated clays, these pore pressures are large and dominate other soil stresses and hence hold the key to the understanding of penetration mechanisms (Baligh, 1986b). Reliable analytical predictions of penetration pore pressures are essential if engineering properties of soils are to be interpreted rationally from in-situ measurements, both during penetration and in subsequent activities such as dissipation and holding tests, membrane expansion, vane rotation etc. The Strain Path Method (SPM; Baligh, 1985, 1986a, b) provides a general analytical framework for describing the mechanics of quasi-static, steady, undrained deep penetration in saturated clay. The method assumes that, due to the severe kinematic constraints in deep penetration problems, deformations and strains are essentially independent of the shearing resistance of the soil, and can be estimated with reasonable accuracy based only on kinematic considerations and boundary conditions. By considering the 2-dimensional deformations of soil elements, SPM analyses provide a more realistic framework for describing the mechanics of deep penetration problems than one-dimensional (cylindrical or spherical) cavity expansion methods, and can account properly for the effects of non-linear and inelastic soil behaviour. On the other hand, the assumptions of strain-controlled behaviour used in the strain path method greatly simplify the problem of steady deep penetration and avoid the complexity of large scale numerical (finite element) analyses.

Assuming that effective stresses control soil behavior, then the excess pore pressures during steady penetration are obtained from equilibrium considerations. However, due to the approximate nature of the analysis, the equilibrium equations are not satisfied exactly and hence predictions of excess pore pressures around the penetrometer are not unique. This paper shows that by combining the equilibrium equations, an 'average' field of pore pressures can be obtained from the solution of a Poisson type equation. This approach reduces the uncertainities in the predicted pore pressures and is especially useful for non-axisymmetric penetrometers.

EQUILIBRIUM IN THE STRAIN PATH METHOD

The analysis of steady deep penetration problems using the Strain Path Method (Baligh, 1985, 1986a, b) includes the following steps:

1. Soil deformations are considered in terms of the steady flow of soil around a static penetrometer. Approximate velocity fields are estimated from potential theory (i.e. treating the soil as an incompressible, inviscid and irrotational fluid) and are differentiated with respect to the spatial coordinates in order to obtain strain rates ($\dot{\varepsilon}_{ij}$). For simple geometries, these solutions can be obtained in closed form (Baligh, 1985; Tch & Houlsby, 1989), while numerical methods are required for more complex geometries (methods of sources and sinks, boundary element methods etc).

2. Integration of the strain rates along the streamlines defines the strain paths (histories) for individual soil elements around the penetrometer. Baligh (1986a) shows that soil

elements are subject to complex histories of straining involving reversals of individual strain components.

3. Effective stress fields around the penetrometer are estimated from the strain paths using a generalized effective stress soil model to characterize the constitutive behavior of the soil. Input parameters for the model include, initial stresses and pore pressures in the ground (σ_{ij}^0, u_0), together with (model specific) material properties. Previous studies (Baligh, 1986b; Whittle & Baligh, 1990) have shown that realistic predictions of effective stresses acting at the indenter-soil interface can be achieved using comprehensive soil models (Whittle, 1990) which incorporate strain softening, small strain non-linearity and anisotropic properties of clay.

4. Using the known field of effective stresses, pore pressures are obtained from equilibrium equations:

$$-\frac{\partial u}{\partial x_j} = \frac{\partial \sigma'_{ij}}{\partial x_j} = g_i \qquad (1)$$

where it is assumed that changes in stresses due to gravity forces are negligible (Baligh, 1985). For axisymmetric problems, the equations can be expressed in a cylindrical coordinate frame as:

$$-\frac{\partial u}{\partial r} = g_r = \frac{\partial \sigma'_{rr}}{\partial r} + \frac{\partial \sigma'_{rz}}{\partial z} + \frac{\sigma'_{rr} - \sigma'_{\theta\theta}}{r} \qquad (2a)$$

$$-\frac{\partial u}{\partial z} = g_z = \frac{\partial \sigma'_{zz}}{\partial z} + \frac{\partial \sigma'_{rz}}{\partial r} + \frac{\sigma'_{rz}}{r} \qquad (2b)$$

In principle, the pore pressures can be calculated by integrating in either the radial or vertical (z) direction (using the known distributions g_r, g_z respectively). If the stress fields are exact, the predicted pore pressure will be independent of the path of integration and the stress gradients will satisfy the relation:

$$\frac{\partial g_r}{\partial z} = \frac{\partial g_z}{\partial r} \qquad (3)$$

This condition is only satisfied if the strain paths are compatible with the model used to determine the stresses. However, from step 1, the strains are approximated using potential flow theory and are not compatible with the soil model used in step 3.

Figure 1 illustrates the potential differences in predictions of pore pressures that can arise by satisfying equilibrium in different directions. The figure shows the distribution of excess pore pressures, $(u-u_0)/\sigma'_{v0}$, at points along the surface of a 60^0 cone penetrometer and at vertical locations ahead of the penetrometer tip. The initial fields of effective stresses were predicted using the Modified Cam Clay soil model (MCC; Roscoe & Burland, 1968) with material properties selected to represent the behavior of K_0-normally consolidated Boston Blue Clay. The results show the following:

1. At the tip of the penetrometer, the excess pore pressures from vertical equilibrium (Δu^z) are approximately 50% higher than those from radial equilibrium (Δu^r). Ahead of

the tip, the distributions of excess pore pressures show similarly large variations due to integration path.

2. Differences between radial and vertical integration paths are especially significant as soil elements move past the level of the base of the cone. Vertical equilibrium pressures, Δu^z, decrease rapidly and become unbounded (i.e. continue to decrease with distance along the penetrometer), while Δu^r reach a steady state solution at a distance z/R=10-20 above the tip of the cone. Levadoux & Baligh (1980) attribute this behavior, in large part, to unrealistic predictions in σ'_{rz}, which contribute significantly to equilibrium in the vertical direction.

Figure 1. Pore pressures predicted around a 60^0 cone by different equilibrium equations
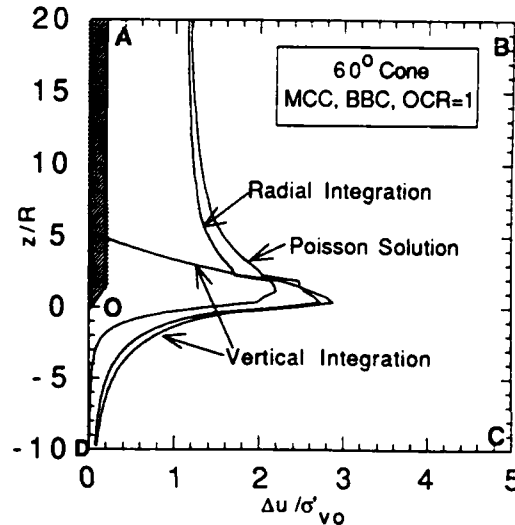
Subsequent studies have shown that:

1. In the region ahead of the cone tip, the soil is subject to triaxial compression modes of shearing only and hence vertical equilibrium can be used reliably to estimate pore pressures at the tip of a piezocone (Elghaib, 1989).

2. Far behind the penetrometer tip, predictions of excess pore pressures can be obtained from radial equilibrium. However, the magnitudes of the predicted pore pressures are strongly influenced by complex aspects of soil behavior (Whittle & Baligh, 1990).

For other locations around the cone, the path dependence in the predicted pore pressures represents a major source of uncertainty in the analysis. Iterative schemes for correcting the equilibrium imbalance have been proposed by a number of authors (Baligh, 1985; Teh, 1987). However, none of these has been successfully implemented to date. Another approach has been to include the strain path solutions as initial conditions in a finite element analysis (Teh & Houlsby, 1989). In this way, equilibrium imbalance can be directly removed from the solution by adjusting the out of balance body forces. Further computations of steady state conditions can then be achieved with appropriate assumptions regarding

indenter interface properties.

Table 1. Predictions of Excess Pore Pressures around a 60⁰ Cone Penetrometer

Location:	z/R	Equilibrium Condition		
		Vertical	Radial	Poisson
Tip	0	2.86	2.00	2.77
Mid-Cone	0.87	2.77	2.10	2.63
Cone Base	1.73	2.30	2.17	2.48
Mid-Friction Sleeve	7.5	-	1.28	1.40
Top Friction Sleeve	12.5	-	1.20	1.27
Shaft	>50	-	1.10	1.10

* using MCC soil model
properties for K_0-normally consolidated Boston Blue Clay

$\phi'_{TC}=33^0$, $\lambda=0.184$, $\kappa=0.034$,

$e_0=1.12$, $G/\sigma'_{v0}=22$, $K_{0NC}=0.48$

THE POISSON FORMULATION

An alternative approach, which can ameliorate the difficulties associated with path dependent pore pressures, is to solve both equlibrium equations by taking the divergence of eqn. 2:

$$\nabla^2 u = -\nabla \cdot g = -q \qquad (4)$$

In this case the scalar pore pressure field is determined as the solution of a Poisson equation using standard finite element techniques. In principle, the flux term, q, is calculated by numerical differentiation (first and second derivatives) of the stress components from the strain path method. However, accurate numerical evaluation of second derivatives is very difficult to achieve, especially in regions of high stress gradients. Considerable simplifications in computing can be achieved using the divergence theorem to estimate an average flux within a given finite element:

$$\int_v q\, dV = \int_A g \cdot n\ dS \qquad (5)$$

$$\bar{q}\, V = \sum_{i=1}^{n} (g \cdot n)_i\, \Delta S_i \qquad (6)$$

where; $\bar{q}$ = average q within element
V = volume of element
g = pore pressure gradient vector on side i
of the n-sided element
n = unit vector normal to side i of the element
S_i = Surface area of side i of the element

The numerical procedure for evaluating derivatives of stress components (g) is based on the construction of nine node isoparametric elements (Bathe, 1982).

Boundary conditions for the Poisson equation (locations A,B,C,D are shown schematically in fig. 1) include: 1)

$\partial u/\partial r=0$, due to symmetry along the centreline (OD); 2) u=0, along BCD (assuming soil behavior is linear far from the penetrometer); and 3) $\partial u/\partial z=0$, to satisfy steady state conditions along AB. The most difficult boundary condition is that at the penetrometer boundary (OA), which cannot be obtained by physical reasoning. This boundary is treated in an approximate manner by computing the gradients adjacent to the indenter interface (g_r and g_z) and imposing the condition:

$$g_n = g_r n_r + g_z n_z \qquad (7)$$

where n_r, n_z are the components of the unit vector normal to the interface. Detailed numerical studies have demonstrated the numerical accuracy and stability of the proposed Poisson equation solutions (Aubeny, 1990).

Figure 1 compares the pore pressures computed using the Poisson equation with those reported from radial and vertical equilibrium. Table 1 summarizes the numerical values at five locations where pore pressure have been measured in conjunction with penetrometer tests:

1. Ahead of the cone, pore pressures from the Poisson equation are similar in magnitude to those calculated from vertical equilibrium. This result confirms the importance of vertical equilibrium ahead of the penetrometer.
2. All three methods predict severe gradients of pore pressures around the base of the cone. This result implies that rational interpretation of soil properties using base pore pressures involves significant uncertainties.
3. For locations above the base of the cone, differences between Poisson and radial equilibrium pore pressures are less than 20%. Poisson solutions always satisfy the steady conditions far above the cone tip.

Overall, the results in figure 1 show that the excess pore pressures computed from the Poisson equation reflect: a) the dominant mode of vertical equilibrium ahead of the tip; b) recover the steady state from radial equilibrium along the shaft; and c) provide a rational basis for estimating the magnitude and distribution of pore pressures at intermediate locations around the cone.

EFFECT OF SOIL PROPERTIES & TIP SHAPE

Extensive studies have been conducted to evaluate the effects of soil properties and indenter geometries on the excess pore pressures during penetration using the Poisson formulation. Figures 2a, b illustrate the effects of tip geometry by comparing predictions for the 60⁰ cone with solutions for a blunt ended penetrometer referred to as a 'simple pile' (Baligh, 1985). The shape of the simple pile is generated by a point source in a uniform flow field such that closed form expressions are available for the strains around the penetrometer (Baligh, 1985; Teh & Houlsby, 1989). As a result, effective stresses and pore pressures can be computed with higher accuracy than is possible for geometries (such as the 60⁰ cone) in which the strain paths are evaluated numerically. The figures also report excess pore pressures corresponding to OCR's=1, 2 and 4 for K_0-consolidated Boston Blue Clay obtained using the MCC model.

The results show that the magnitudes and distributions of excess pore pressures are very similar for the simple pile and

Figure 2a. Excess pore pressures around a simple pile

Figure 2b. Excess pore pressures around a 60⁰ cone
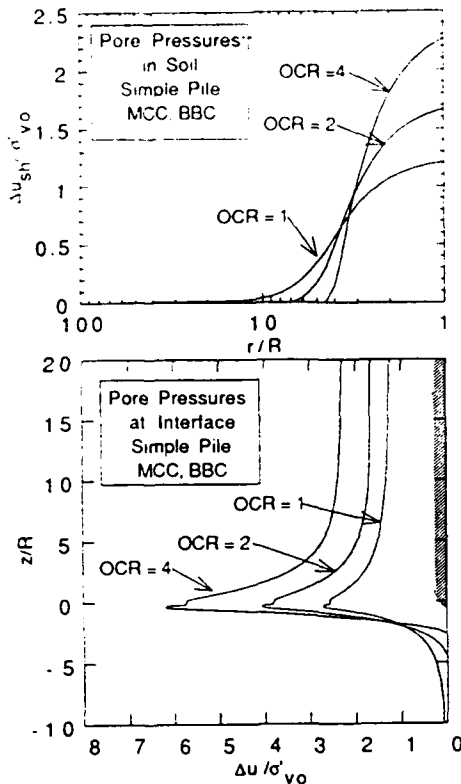
60^0 cone at all OCR's. The tip pore pressures ($\Delta u_{tip}/\sigma'_{v0}$) are practically identical in all cases (Table 2), while shaft pore pressures ($\Delta u_{shaft}/\sigma'_{v0}$) are 10-20% higher for the simple pile. Small changes in excess pore pressures are predicted for locations $z/R>15$ above the tip. Further comparisons between the two geometries can be made by computing the tip resistance, q_c, using the effective stresses from the strain path together with the pore pressures from figure 2:

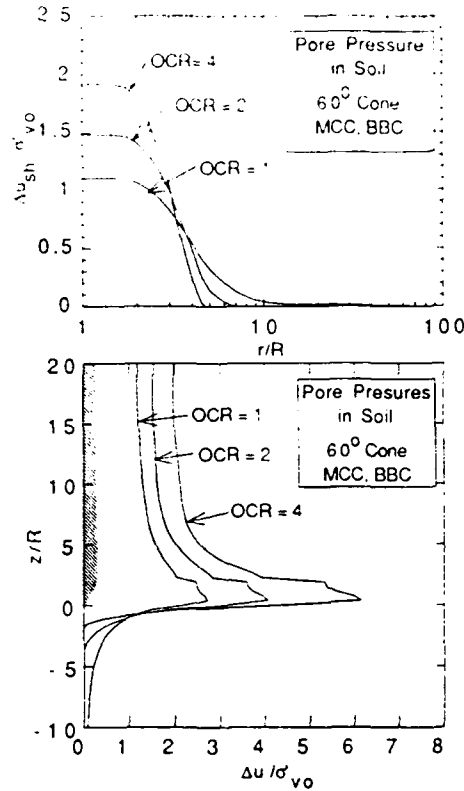$$q_c = \frac{1}{\pi R^2} \int \{p_n \sin\alpha + p_t \cos\alpha\}\, dA \qquad (8)$$

where p_n, p_t, are the total tractions normal and tangential to the indenter interface, respectively; α is the cone half-angle; and A is the surface area of the tip.

The normalized tip resistance factors, $N_{kt}=(q_c-\sigma_{v0})/c_{uTC}$, (where c_{uTC} is the undrained shear strength in triaxial compression) are then shown in table 2. Simple pile tip resistance factors are consistently 5-10% larger than those predicted for the 60^0 cone.

From these comparisons, it is clear that the simple pile geometry provides a very good approximation for more detailed studies of the performance of standard piezocones (with 60^0 cone angles) (Elghaib, 1989).

The results in figure 2 also illustrate some of the effects of

soil behavior on pore pressure measurements:

1. The largest excess pore pressures occur at (or very close to) the tip of the penetrometers. Tip pore pressures ($\Delta u_{tip}/\sigma'_{v0}$) also increase very significantly with OCR and are primarily controlled by the undrained shear strength of the soil (c_{uTC}, in triaxial compression, table 2).

Table 2. Predicted Excess Pore Pressures and Tip Resistance around Cone Penetrometers and Simple Pile

OCR	$\frac{c_{uTC}}{\sigma_{vc}'}$	E_y (%)	$\frac{\Delta u_{tip}}{\sigma_{v0}'}$	$\frac{\Delta u_{base}}{\sigma_{v0}'}$	$\frac{\Delta u_{shaft}}{\sigma_{v0}'}$	Cone Tip Factor, N_{kt}
1	0.32	0.01	2.71 (2.71)	2.49 (2.57)	1.10 (1.22)	7.81 (8.28)
2	0.58	0.84	4.05 (4.05)	3.60 (3.80)	1.49 (1.67)	7.65 (8.23)
4	1.05	1.75	6.15 (6.18)	5.34 (5.77)	1.92 (2.27)	7.34 (8.03)

( ) Simple Pile Geometry

E_y is the octahedral yield strain ($=1/\sqrt{2}\varepsilon_y$, measured in undrained triaxial shear test)

2. Pore pressures along the shaft of the penetrometers ($z/R>15$) are much smaller than at the tip ($\Delta u_{shaft}/\Delta u_{tip}=0.3$ to 0.4) and show much smaller changes with OCR. Hence pore pressure filters located in this region are less sensitive to changes in soil properties.

3. There are relatively small changes ($10\pm3\%$) in the pore pressures predicted for locations along the face of cone (or simple pile). This implies that pore pressures measured at the tip or on the face of the cone will not be greatly affected by variations in filter location or thickness.

EVALUATION WITH MEASURED DATA

Baligh et al. (1979) report measurements of excess pore pressures at six locations around an 18^0 cone penetrometer installed in Boston Blue Clay with in-situ OCR in the range $1.3\leq OCR\leq4$. Figure 3 compare these measured data (reported at 4ft intervals for four locations) with predictions of excess pore pressures, $(u-u_0)/\sigma'_{v0}$, using the effective stress fields from the MCC model (as above) together with the proposed Poisson formulation:

1. For position P1, on the face of the cone, the predicted pore pressures agree well with the measured data (within 10%) in the lower clay (below 60ft) where soil conditions are most uniform. Between 40 and 60ft, there is more scatter in the measured data (attributed to sand seams in the clay, Baligh et al., 1979), but the agreement is still reasonable.

2. At the base of the cone (P2) the predicted pore pressures match closely the measured data at depths greater than 60ft. However, in the uppper material predictions overestimate the measured pore pressures.

3. Along the shaft (P3 and P4), the predictions underestimate the measured data at all depths by up to 50%. This discrepancy is consistent with previous observations of pore pressures around model pile shafts (Azzouz & Morrison, 1988; Whittle & Baligh, 1990) and reflects the sensitivity of the predictions to complex aspects of soil behavior.

EFFECT OF PENETROMETER SHAPE

The path dependence of pore pressures predicted from the strain path method is also important for non-axisymmetric penetrometers such as dilatometers, spade cells, field vane etc. Figure 4 shows Poisson equation pore pressures at steady state conditions (i.e. far behind the penetrating tip, penetration is in the z-direction) around one quadrant of a thin plate penetrometer with aspect ratio, $B/t=32.5$. The predictions are presented for the case of K_0-normally consolidated BBC using the MCC soil model (as in fig. 1). Table 3 compares the magnitude of the pore pressures at the center (A) and edge (B) of the plate estimated by satisfying equilibrium in the x and y directions separately. The table shows that due to the inequilibrium of strain path solutions, the predicted pore pressures can vary by 30-50%, while Poisson pore pressures average out the effects of the path dependence..

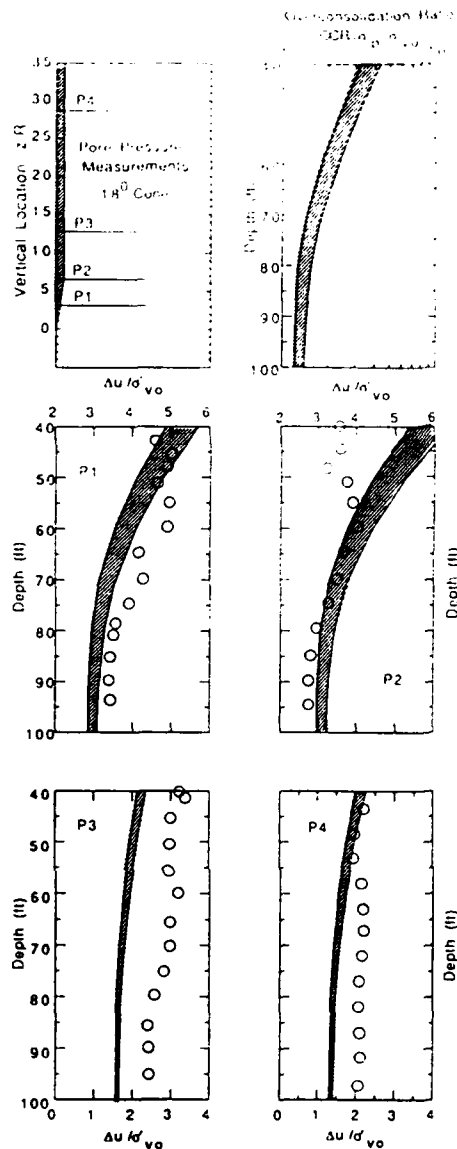Figure 3. Evaluation of predicted excess pore pressures around an 18^0 cone penetrometer in Boston Blue Clay

Table 3. Values of Excess Pore Pressure, $(u-u_0)/\sigma'_{v0}$, around Plate Penetrometer with B/t=32.5

PLATE; B/t=32.5	Equilibrium Direction		
	x	y	Poisson
A	0.84	1.14	1.02
B	0.50	0.76	0.59

The lengths in figure 3 are normalized by the radius of an equivalent simple pile, R_{eq} (where R_{eq} is obtained by matching the areas of the two sections; $R_{eq} = \sqrt{4Bt/\pi}$). The results show that :

1. The magnitudes of the pore pressures around the thin plate are 10-50% smaller than those predicted from the simple pile.
2. Around the face of the plate, the lateral extent of the excess pore pressures is similar for both the thin plate and the simple pile. This implies that the zone of distrubance in front of the plate is controlled primarily by the volume of soil displaced during penetration. Around the edge of the plate, the zone of excess pore pressures is significantly reduced.

Figure 4. Comparison of excess pore pressures around a thin plate and a simple pile shaft
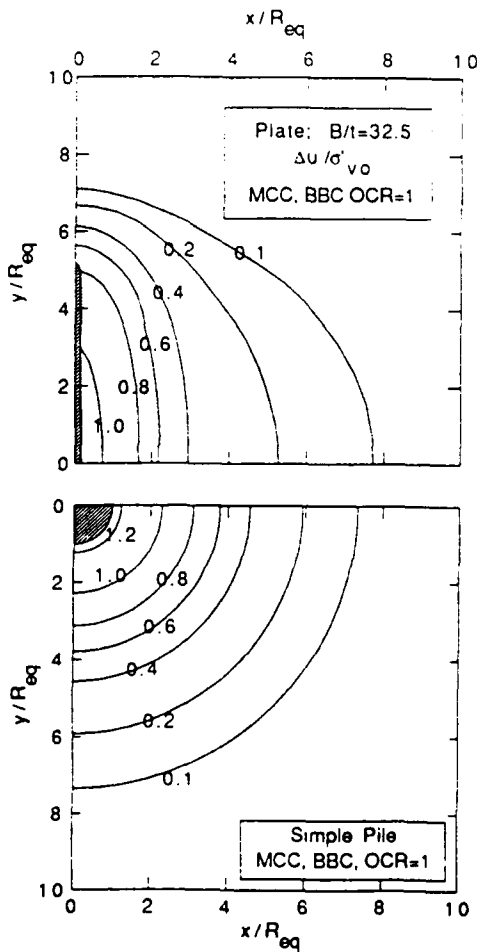
These results have important applications in the interpretation of soil properties from flat plate penetrometers and is estimating the disturbance around non-axisyemmetric section piles.

CONCLUSIONS

Using the Strain Path Method, reliable predictions of excess pore pressures during steady penetration can be achieved by satisfying equilibrium in the form of a Poisson equation. This method ameliorates the path dependence observed by integrating equilibrium equations directly, and provides a formulation which can be applied to general penetrometer geometries. Numerical solutions have been presented to illustrate the flexibility and applications of the proposed formulation.

REFERENCES

Aubeny, C.P. (1990) PhD Thesis in progress.

Azzouz, A.S. & Morrison, M.J. (1988) "Field measurements on model pile in two clay deposits," ASCE Journal of Geotechnical Engineering, 108, GT1, pp. 104-121.

Baligh, M.M. (1985), "Strain path method," ASCE, Journal of Geotechnical Engineering, 111, GT9, pp. 1108-1136.

Baligh, M.M. (1986a) "Undrained deep penetration: I. Shear stresses," Géotechnique, 36, No. 4, pp. 471-485.

Baligh, M.M. (1986b) "Undrained deep penetration: II. Pore pressures," Géotechnique, 36, No. 4, pp. 487-501.

Baligh, M.M., Vivatrat, V. & Ladd, C.C. (1980) "Cone penetration in soil profiling," ASCE Journal of Geotechnical Engineering, 106, GT4, pp. 447-461.

Bathe, K.J. (1982), Finite Element Procedures in Engineering Analysis, Prentice-Hall, N.J.

Elghaib, M.K. (1989) "Prediction and interpretation of piezocone data during undrained, drained and partially drained penetration," PhD Thesis, MIT.

Levadoux, J-N. & Baligh, M.M. (1980), "Pore pressures during cone penetration in clays," Research Report R80-15, Dept. of Civil Engrg., MIT, Cambridge, MA.

Roscoe, K.R. & Burland, J.B. (1968) "On the generalized stress-strain behaviour of wet clays," in Engineering Plasticity, eds. J. Heyman & F.A. Leckie, Cambridge University Press.

Teh, C-I (1987), "An analytical investigation of the cone penetration test," PhD Thesis, University of Oxford.

Teh, C-I & Houlsby, G.T. (1989) "An analytical study of the cone penetration test in clay," Oxford University Soil Mechanics Report, No. OUEL 1800/89.

Whittle, A.J. (1990), "A constitutive model for overconsolidated clays," MIT Sea Grant Report No. MITSG90-15.

Whittle, A.J. & Baligh, M.M. (1990), "Prediction and evaluation of pile shaft behaviour in lightly overconsolidated clays," submitted for publication.